U.PORTO

FEUP FACULDADE DE ENGENHARIA
UNIVERSIDADE DO PORTO

TiO$_2$ bioactive surfaces doped with Sr intended for orthopaedic applications

Ana Isabel Gomes Costa

Supervisor: Filomena Maria da Conceição Viana

Co-supervisor: Fatih Toptan

A dissertation to the fulfilment of doctoral degree in Advanced Materials and Processing

AdvaMTech
PhD Program in Advanced Materials and Processing

Porto, February 2021

NORTE2020
PROGRAMA OPERACIONAL REGIONAL DO NORTE

PORTUGAL 2020

UNIÃO EUROPEIA
Fundo Social Europeu

Title

TiO_2 bioactive surfaces doped with Sr intended for orthopaedic applications

Abstract

Ti-based implants currently on the market do not fully meet the expectation of patients. Infection, lack of bioactivity, wear debris and the biomechanical mismatch existent between the implant and the hosting bone are still the major problems in the prostheses field and can lead to aseptic loosening, fibrous encapsulation and osteolysis. Macro-porosity in the Ti implant is presented as a beneficial way to reduce the biomechanical mismatch, in order to match the value of Young's modulus of the implant to the one found in the bone. As follows, porous Ti is considered as a promising biomaterial for several orthopaedic applications, promoting the ingrowth of new bone tissue inside the pores, with the aim to achieve anchorage by enlarging the bone–implant interface area. However, the lack of bioactivity and wear resistance are yet to be improved. Surface modification by micro-arc oxidation (MAO) allows the bio-functionalization of the Ti surface with micro-porous oxide layers containing bioactive elements such as calcium (Ca), phosphorus (P) and strontium (Sr) with an improved biological response and tribocorrosion behaviour.

This thesis presents the study of multifunctional TiO_2 bioactive surfaces together with highly porous Ti. Ca and P as bioactive elements are already well reported in the literature, however, the knowledge on the effect of Sr is still limited. In the present work, the effect of several amounts of Sr was evaluated and the morphology, chemical composition and crystal structure of the oxide layer were investigated. Furthermore, *in vitro* studies were carried out using human osteoblast-like cells and it was revealed that lower concentrations of Sr did not compromise initial cell adhesion either viability and showed improved mineralization. However, the highest concentration of Sr (and consequent higher amount of rutile) revealed a superior amount of collagen secretion but with compromised mineralization, possibly due to a delayed mineralization process or due to induced precipitation of deficient hydroxyapatite. Results showed that the distribution of anatase and rutile in the porous oxide layer led to less visible damage and

lower values of coefficient of friction. The group containing more Sr presented the best tribocorrosion response mainly due to the increased amount of rutile.

Moreover, a bio-functionalized porous surface was obtained on Ti by a two-step anodic treatment. The first-step provided macro-porosity while the second-step, a bio-functionalization process by MAO, provided an oxide layer (anatase + rutile) with micro-pores and bioactive elements (Ca + P). Corrosion and tribocorrosion behaviour were enhanced due to the protective role of the oxide layer formed on the second-step. Tribocorrosion mechanisms for the bio-functionalized porous structures were presented.

Additionally, the electrochemical behaviour of highly porous Ti samples processed by powder metallurgy with space holder technique and bio-functionalized by MAO, was evaluated. Results showed that bio-functionalization improved the corrosion behaviour of highly porous Ti. Nevertheless, increased macro-porosity promoted a higher corrosion rate. Highly porous Ti was also studied under fretting-corrosion conditions as a function of load and amplitude. Fretting-corrosion mechanisms were presented and a fretting map was illustrated. There was a significant load- and amplitude-dependent response. The promising structure of highly porous Ti was preserved after 16 hours of fretting-corrosion under severe solicitations.

The outcome of this work deeply emphasizes the important role of biological and tribocorrosion characterizations in promising biomaterials structures such as TiO_2 bioactive surfaces doped with Sr.

Título

Superfícies bioativas de TiO$_2$ dopadas com Sr para aplicações ortopédicas

Resumo

Os implantes à base de Ti que se encontram atualmente no mercado não satisfazem as expectativas dos pacientes. Infeção, falta de bioatividade, produtos de desgaste e a incompatibilidade biomecânica existente entre o implante e o osso continuam a ser os principais problemas das próteses e podem levar ao descolamento asséptico, encapsulamento fibroso e osteólise. A macro-porosidade no implante de Ti é apresentada como uma forma benéfica de reduzir a incompatibilidade biomecânica, de modo a aproximar o módulo de Young do implante ao do osso. Desta forma, o Ti poroso é considerado um biomaterial promissor para diversas aplicações ortopédicas uma vez que permite o crescimento de novo tecido ósseo dentro dos poros, obtendo-se assim uma melhor ancoragem devido a uma maior área da interface osso–implante. No entanto, a falta de bioatividade e a baixa resistência ao desgaste ainda carecem de solução. A modificação da superfície por oxidação micro-arco (MAO) possibilita a bio-funcionalização da superfície de Ti com camadas de óxido micro-poroso com elementos bioativos, como cálcio (Ca), fósforo (P) e estrôncio (Sr), originando uma melhor resposta biológica e um melhor comportamento à tribocorrosão.

Esta tese tem como objetivo o estudo de superfícies multifuncionais bioativas de TiO$_2$ em conjunto com Ti altamente poroso. Ca e P, como elementos bioativos, já estão descritos na literatura, porém o conhecimento do efeito do Sr ainda é limitado. No presente trabalho, várias quantidades de Sr foram estudadas bem como a morfologia, composição química e estrutura cristalina da camada de óxido. Além disso, estudos realizados *in vitro* usando células semelhantes a osteoblastos humanos revelaram que concentrações mais baixas de Sr não comprometeram a adesão celular inicial nem a viabilidade e ainda melhoraram o processo de mineralização. Contudo, maior concentração de Sr (e consequente maior quantidade de rutilo) induziu a secreção de colagénio, mas com uma mineralização comprometida, possivelmente devido a um

processo de mineralização retardado ou precipitação de hidroxiapatita com défices. Os resultados mostraram que a distribuição de anatase e rutilo na camada de óxido poroso traduziu-se numa maior resistência ao desgaste, com menores valores de coeficiente de atrito. O grupo contendo maior quantidade de Sr apresentou a melhor resposta à tribocorrosão devido ao aumento da quantidade de rutilo.

Além disso, uma superfície porosa bio-funcionalizada foi obtida no Ti com tratamento anódico de duas etapas. A primeira etapa produziu macro-porosidade, enquanto a segunda etapa, um processo de bio-funcionalização por MAO, forneceu uma camada de óxido (anatase + rutilo) com micro-poros e elementos bioativos (Ca + P). O comportamento à corrosão e à tribocorrosão foi melhorado devido ao papel protetor desempenhado pela camada de óxido formada na segunda etapa. Os mecanismos de tribocorrosão para as estruturas porosas bio-funcionalizadas foram apresentados.

O comportamento eletroquímico de amostras de Ti altamente porosas processadas por metalurgia dos pós com técnica *space holder* e bio-funcionalizadas por MAO foi avaliado. Os resultados mostraram que a bio-funcionalização melhorou o comportamento à corrosão de Ti altamente poroso. No entanto, o aumento da macro-porosidade levou a um incremento da taxa de corrosão. Ti altamente poroso também foi investigado electroquimicamente em condições de *fretting* em função da carga e amplitude. Os mecanismos de corrosão por *fretting* foram apresentados e um mapa de *fretting* foi ilustrado. O comportamento sujeito a condições de *fretting* demonstrou uma dependência relativamente à carga e amplitude. A estrutura promissora de Ti altamente poroso foi preservada após 16 horas de corrosão por *fretting* sob severas solicitações.

Os resultados deste trabalho enfatizam a importância do papel essencial desempenhado pelas caracterizações biológicas e de tribocorrosão nos biomateriais com estruturas promissoras tais como superfícies bioativas de TiO_2 dopadas com Sr.

Acknowledgements

I consider myself very fortunate to have the opportunity to pursue a doctoral degree from the Faculty of Engineering at the University of Porto (FEUP) together with the University of Minho (UM). At the end of such long and laborious process, it is a great pleasure for me to express my gratitude for the given opportunities to develop this work in a multicultural and multidisciplinary environment across the world and for the motivation, love and friendship throughout this journey.

I am very grateful to my supervisors who allowed me to work under their supervision. I would like to thank Prof. Filomena Viana (FEUP) and Dr Fatih Toptan (UM) for their expertise, guidance, forward-thinking, patient and confidence in developing such a thesis. I truly thank them for the privilege to work with them and for the long scientific debates that have improved my scientific knowledge.

I would also like to thank Prof. Ana Maria Pinto and Dr Alexandra Alves (UM) for sharing their experience and broad knowledge as well as always being available to answer my doubts.

My gratitude to Dr Ana Ribeiro, Prof. Luis Rocha and Dr André Rossi (CBPF) that allowed me to develop part of my work abroad by giving me access to great facilities. I am very appreciative of the warm welcome I was given and the ideas I was inspired with that contributed to the successful development of the work.

I would like to thank Dr Sara Gimini-Piperni (CBPF) for her professional help and friendship. I want to acknowledge her creativity and endless help in developing experimental procedures that are part of this thesis. I will never forget the enthusiasm for science that we both share as well as the time we spent together.

I want to dedicate a special thanks to Dr Jean Geringer (Mines Saint-Étienne) who kindly received me in his lab and helped me produce experimental procedures. I express my deepest regard for his trust and shared scientific knowledge.

A thank you to Dr Edith Ariza and Prof. Aníbal Guedes (UM) for all the shared expertise, available help and suggestions. I also would like to say thanks to Leonor Carneiro, Miguel Abreu, Sérgio Carvalho, Filipe Marques and Fernando Araújo (UM) for all the help and support.

My sincere appreciation for all the contributing authors who took the time to teach me and added their valuable contribution to this work.

I thank Luís Sousa for the constant kind help, availability and support. I thank Ishan Çaha for the thoughtful support during this journey. I thank Aida Moreira for all the help and availability that together with Clarissa Melo e Bruno Oliveira made my first year of PhD, encouraging. Thank you to all of them for the hard-working spirit, optimistic attitude towards difficulties and commitment to success that has inspired me all along. I wish all the best to all of them in the future. My appreciation also goes out to past students and researchers that shared the laboratories with me and inspire me with their enthusiasm for discovery. A special thanks to Natalia Costa who filled my life with joy.

All my love to my dearest friends especially for all the company and support. Thank you for the laughs and all the love. A special thanks to my powerful and admirable dear friends Francisca and Catarina. We have been lucky to cross paths. Ana, Daniela, Joana, João, Luís, Mafalda, Rafael, Renato, Ricardo, Rita, Rodrigo, to them and their families, who taught me to own my story with pride and for the incredible phenomenon called true friendship that I am certain will last forever.

A special thanks to my dear Diogo and his family, for all the support, love and shared joy that have filled my days these past 4 years.

Last but not least, I would like to dedicate this work to my wonderful parents and my beautiful sister, Helena, Bernardino and Maria. I would like to thank them for their unwavering support in my life. I am forever grateful to them, for their unconditional love and for always taking exceptionally good care of me. I find in them my motivation to keep moving forward.

Table of contents

xvi

The structure of the thesis was summarised with a brief description of each chapter together with a diagram of the thesis outline. This thesis is composed of eight chapters:

Chapter 1 establish the significance of surface modification by micro-arc oxidation of porous titanium for orthopaedic applications in a general introduction. Subsequently, the problem statement, aims and specific objectives of this research were presented.

Chapter 2 covers the state-of-the-art in the area of biomaterials related to the development of the current research status in surface modification of porous Ti, mainly by micro-arc oxidation. This chapter was designed to provide a comprehensive literature review on the recent understanding of the topics. The main subjects were related to porous Ti, bio-functionalization by micro-arc oxidation and bio-functionalization of porous Ti. Firstly, biomaterials and the developments of porous metallic biomaterials were briefly reviewed, giving some considerations on the design and selection of such materials structure. The following sections review information related with bio-functionalization by micro-arc oxidation of Ti-based materials. The latter section focuses on the combination of porous Ti with bio-functionalization process by micro-arc oxidation. Moreover, this chapter highlights the challenges and the perspectives of such topics. This chapter was accepted for publication in the book *Tribology, Lubrication and Surface Engineering: Research and Applications, Two-Volume Set"* to be published by CRC Press in June 2021.

The following chapters compass five research reports that comprise contextualization, materials and methods, results, discussion and conclusions combining publications and a submitted manuscript. The experimental work was accomplished at Faculdade de Engenharia da Universidade do Porto (Portugal), Universidade do Minho (Portugal), Centro Brasileiro de Pesquisas Físicas (Brazil) and Centre Ingénierie et Santé from École Nationale Supérieure des Mines de Saint-Etienne (France).

Chapter 3 focuses on a detailed study of the effect of Sr as a bioactive element into a Sr-Ca-P-TiO$_2$ porous layer produced by micro-arc oxidation. Therefore, in this chapter, the effect of various amounts of Sr was evaluated and the morphology,

chemical composition and crystal structure of the TiO_2 layer were investigated. Furthermore, *in vitro* studies were carried out using human osteoblast-like cells, where cell adhesion, viability, mineralization and cytokine production were investigated. The results of this work were published in *Materials Science & Engineering C*.

Chapter 4 follows the previous chapter and presents added characterization to Sr-Ca-P-TiO_2 porous layers. Moreover, the influence of Sr addition on the tribocorrosion behaviour of the MAO layers was evaluated, using three different amounts of Sr. This chapter was published in *Materials Letters*.

A multiscale (macro-, micro- and nano-scale) porosity on the surface could be beneficial for mechanical interlocking, as well, for promoting cell adhesion and proliferation. By varying the parameters of two or more steps of anodic treatment, it was possible to obtain hierarchical porous surfaces on the macro-, micro- or nano-scale. In this way, hierarchical macro-, micro- to nano-topographies on the surface were produced and studied. Chapter 5 emphasizes the influence of micro-arc oxidation layers on the improved corrosion and tribocorrosion behaviour of porous surfaces produced by a two-step anodic treatment. The first-step provided macro-porosity only on the surface while the second-step, the bio-functionalization process by micro-arc oxidation provided a TiO_2 layer with micro-pores and bioactive elements such as Ca and P. Tribocorrosion mechanisms for the bio-functionalized porous surfaces were presented. The findings of this work were published in *Corrosion Science*.

Chapter 6 deals with bio-functionalized macro-porous Ti structures and their electrochemical characterization. In this chapter, macro-porous Ti structures were processed by powder metallurgy with space holder technique and then bio-functionalized by micro-arc oxidation, resulting in nano- and micro-structured TiO_2 surfaces containing bioactive elements such as Ca and P. This work was published in *Surface and Coating Technology*.

Chapter 7 devotes to the study of triboelectrochemical consequences of the micro-movements between macro-porous Ti against Ti alloy. In this investigation, fretting-corrosion behaviour of macro-porous Ti was studied as a function of normal load and displacement amplitude. A fretting map was illustrated and different fretting regimes were distinguished and identified from dynamic measurements of tangential

force and specimen displacement together with worn surfaces. This chapter was submitted to *Corrosion Science*.

Chapter 8 gives a general discussion of the outcomes of the experimental works reported in the previous chapters and concludes all the significant findings of this thesis with the subsequent suggestion for perspectives in the area.

A schematic diagram of the summarized objectives together with illustration and highlights for each chapter is presented in Figure 1.

Chapter 2
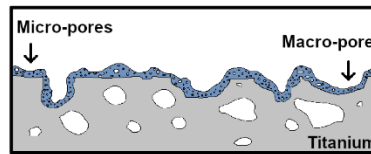
Highlights:
• The development of biomaterials with bio-functionalized macro-porous Ti structures is presented as a promising solution

Chapter 3   ## Chapter 4
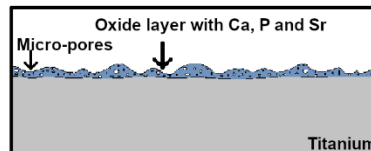
Highlights:
• A typical volcano-like micro-porous network rich in Ca, P and Sr was produced
• TiO_2 layers showed a triplex structure with distinct chemical and crystal structure
• *In vitro* cell culture showed a dose-dependent effect of Sr on TiO_2 surfaces
• Lowest amount of Sr improved osteoblasts mineralization

Highlights:
• Higher Sr concentration increased rutile phase in the Ca-P-Sr-doped TiO_2 layers
• EBSD showed a distribution of anatase and rutile that provided tribocorrosion resistance
• Less visible mechanical damage and lower COF values for group containing more Sr

Chapter 5   ## Chapter 6
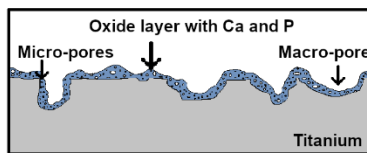
Highlights:
• Hierarchical porous structure was obtained by a two-step anodic treatment
• Surfaces presented improved wettability, corrosion and tribocorrosion resistance
• Wear-corrosion mechanisms involved in each bio-functionalization step were discussed
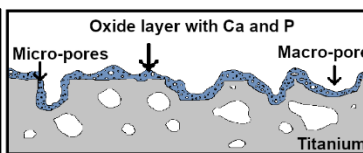
Highlights:
• Bio-functionalization was not influence by the level of porosity
• No significant differences were noticed on the triplex structure of the oxide layer formed on dense and porous Ti samples
• The corrosion resistance was improved by MAO

Chapter 7
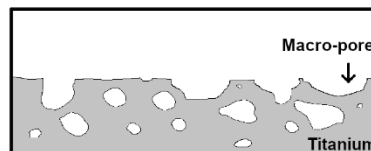
Highlights:
• Highly porous Ti was presented as a highly potential bone substitute
• Fretting-corrosion behaviour between highly porous Ti and Ti alloy was studied
• A load- and amplitude-dependent response was obtained
• Structure integrity of porous Ti was preserved after 16 hours of fretting-corrosion

Figure 1. Schematic diagram of the summarized objectives together with illustration and highlights for each chapter.

4

1.1. Motivation

Bone loss due to trauma or disease is a major problem of global public health. Unfortunately, surgeries are being performed on younger patients, which expose the implant to greater mechanical stress over a longer period of time due to their active lifestyle. The existing prostheses may be successful in restoring function, thereby increasing the quality of life of millions of people but in the medium/long-term present some concerns. The normal implant lifetime is from 10 to 15 years mainly due to the following problems: *i.* poor implant fixation due to the mismatch of the Young's modulus between the bone (10–30 GPa) and the metallic implant material (for example, 110 GPa for Ti) leading to a stress-shielding effect, and local resorption of the bone and consequently to aseptic loosening of the implant; *ii.* weak bond between the bone tissue and the implant metallic surface due to the bioinertness of its surface that causes fibrous encapsulation; *iii.* bio-tribocorrosion that implant suffers caused by the synergism of the physiologic aggressive environment and the tribological wear as a degradation process [1–5].

Through compositional or structural modification, it is possible to decrease Young's modulus of the implant to match that of the bone and at the same time to increase the interfacial bond between the biological part and the implant material. The use of porous metals for implants instead of fully dense materials can reduce the modulus mismatch, and consequently, the stress-shielding problem. Also, macro-porosity can improve the bone–implant interfacial bond by bone-ingrowth through the pores [4,6–8].

However, Ti implants cannot bond to living bone directly after implantation into the host body. To achieve improved osseointegration, the composition and topography of the implant surfaces need to be modified. Recent studies on the biological response of Ti implants have demonstrated that the micro-arc oxidation process is one of the best methods for modifying the implant's surface, by creating a nano- and micro-structured TiO_2 bioactive layer on the surface due to the incorporation of bioactive elements in the

oxide layer. Micro-arc oxidation can also increase the electrochemical and triboelectrochemical resistance and decrease the metal ion release [9–14].

One of the many advantages of micro-arc oxidation process is the possibility of doping bioactive elements to the porous oxide layer with the aim to improve the biological response by promoting bioactivity of the surface. The major chemical element found in the bone is Ca, followed by P, but there are at least a dozen of other chemical elements present there and one of them is Sr. 99% of the total amount of Sr in the human body is deposited in the bone due to its superior ability to bind with the mineral phase of bone, hydroxyapatite. Moreover, Sr preferably appears in the new bone: the amount of Sr is 3 to 4 times higher in a new cortical bone than that in an older one and about 2.5 times higher in a new cancellous bone than that in an older one. Sr presents a singular mechanism of action by increasing pre-osteoblast proliferation, osteoblast differentiation and replication, type I collagen synthesis and bone matrix mineralization. Sr also inhibits osteoclast differentiation and activation [15–22]. In this way, Sr with its dual action is a promising bioactive element to be incorporated on bio-functionalized porous Ti.

1.2. Objectives

Porous Ti is considered a promising biomaterial for several orthopaedic applications since it can allow ingrowth of new bone tissue inside of the pores. On the other hand, micro-arc oxidation allows modifying the Ti surface to obtain bioactive elements, such as Sr, incorporated in the micro-porous oxide layers yielding improved tribocorrosion behaviour and biological response. However, there is still a lack of knowledge in the literature about the combination of those two solutions, namely, a bio-functionalized macro-porous Ti structure. Accordingly, the present work hypothesises that Sr incorporated in a micro-porous Ti oxide layer formed on a macro-porous Ti can improve both the biological and triboelectrochemical response of the Ti implant. In order to test the proposed hypothesis, the main objectives are:

• To investigate the effect of Sr on the biological response and triboelectrochemical behaviour of the bio-functionalized Ti structures;

• To investigate the use of bio-functionalization processes like micro-arc oxidation to create bio-functionalized macro-porous Ti structures with improved behaviour to tribocorrosion;

• To investigate the influence of the macro-porous Ti and the bio-functionalization process on the electrochemical and triboelectrochemical (sliding tribocorrosion and fretting-corrosion) behaviour in simulated body conditions.

References

[1]   M. Geetha, A.K. Singh, R. Asokamani, A.K. Gogia, Ti based biomaterials, the ultimate choice for orthopaedic implants – A review, Prog. Mater. Sci. 54 (2009) 397–425.

[2]   W. Simka, A. Iwaniak, G. Nawrat, A. Maciej, J. Michalska, K. Radwański, J. Gazdowicz, Modification of titanium oxide layer by calcium and phosphorus, Electrochim. Acta. 54 (2009) 6983–6988.

[3]   H. Guleryuz, H. Cimenoglu, Surface modification of a Ti-6Al-4V alloy by thermal oxidation, Surf. Coatings Technol. 192 (2005) 164–170.

[4]   F.A. España, V.K. Balla, S. Bose, A. Bandyopadhyay, Design and fabrication of CoCrMo alloy based novel structures for load bearing implants using laser engineered net shaping, Mater. Sci. Eng. C. 30 (2010) 50–57.

[5]   H.J. Rack, J.I. Qazi, Titanium alloys for biomedical applications, Mater. Sci. Eng. C. 26 (2006) 1269–1277.

[6]   S.Y. Min, Y. Kim, T.K. Lee, S. Seo, H.S. Jung, D. Kim, J. Lee, B.J. Lee, The effect of porosity on the elasticity of pure titanium: An atomistic simulation, Met. Mater. Int. 16 (2010) 421–425.

[7]   O. Smorygo, A. Marukovich, V. Mikutski, A.A. Gokhale, G.J. Reddy, J.V. Kumar, High-porosity titanium foams by powder coated space holder compaction method, Mater. Lett. 83 (2012) 17–19.

[8]   A. Bansiddhi, D.C. Dunand, Titanium and NiTi foams for bone replacement, Woodhead Publishing Limited, 2014.

[9]   I. da S.V. Marques, V.A.R. Barão, N.C. da Cruz, J.C.C. Yuan, M.F. Mesquita, A.P. Ricomini-Filho, C. Sukotjo, M.T. Mathew, Electrochemical behavior of bioactive coatings on cp-Ti surface for dental application, Corros. Sci. 100 (2015) 133–146.

[10]   H.P. Felgueiras, L. Castanheira, S. Changotade, F. Poirier, S. Oughlis, M. Henriques, C. Chakar, N. Naaman, R. Younes, V. Migonney, J.P. Celis, P. Ponthiaux, L.A. Rocha, D. Lutomski, Biotribocorrosion (tribo-electrochemical) characterization of anodized titanium biomaterial containing calcium and phosphorus before and after osteoblastic cell culture, J. Biomed. Mater. Res. Part B Appl. Biomater. 103 (2015) 661–669.

8

[11]   M. Fazel, H.R. Salimijazi, M.A. Golozar, M.R. Garsivaz jazi, A comparison of corrosion, tribocorrosion and electrochemical impedance properties of pure Ti and Ti6Al4V alloy treated by micro-arc oxidation process, Appl. Surf. Sci. 324 (2015) 751–756.

[12]   A.C. Alves, A.I. Costa, F. Toptan, J.L. Alves, I. Leonor, E. Ribeiro, R.L. Reis, A.M.P. Pinto, J.C.S. Fernandes, Effect of bio-functional MAO layers on the electrochemical behaviour of highly porous Ti, Surf. Coatings Technol. 386 (2020) 125487.

[13]   A.I. Costa, L. Sousa, A.C. Alves, F. Toptan, Tribocorrosion behaviour of bio-functionalized porous Ti surfaces obtained by two-step anodic treatment, Corros. Sci. 166 (2020) 108467.

[14]   A.R. Ribeiro, F. Oliveira, L.C. Boldrini, P.E. Leite, P. Falagan-Lotsch, A.B.R. Linhares, W.F. Zambuzzi, B. Fragneaud, A.P.C. Campos, C.P. Gouvêa, B.S. Archanjo, C.A. Achete, E. Marcantonio, L.A. Rocha, J.M. Granjeiro, Micro-arc oxidation as a tool to develop multifunctional calcium-rich surfaces for dental implant applications, Mater. Sci. Eng. C. 54 (2015) 196–206.

[15]   Z.S. Tao, W.S. Zhou, X.W. He, W. Liu, B.L. Bai, Q. Zhou, Z.L. Huang, K.K. Tu, H. Li, T. Sun, Y.X. Lv, W. Cui, L. Yang, A comparative study of zinc, magnesium, strontium-incorporated hydroxyapatite-coated titanium implants for osseointegration of osteopenic rats, Mater. Sci. Eng. C. 62 (2016) 226–232.

[16]   J. Zhou, L. Zhao, Multifunction Sr, Co and F co-doped microporous coating on titanium of antibacterial, angiogenic and osteogenic activities, Acta Biomater. 43 (2016) 358–368.

[17]   K.C. Kung, T.M. Lee, T.S. Lui, Bioactivity and corrosion properties of novel coatings containing strontium by micro-arc oxidation, J. Alloys Compd. 508 (2010) 384–390.

[18]   W. Zhang, H. Cao, X. Zhang, G. Li, Q. Chang, J. Zhao, Y. Qiao, X. Ding, G. Yang, X. Liu, X. Jiang, A strontium-incorporated nanoporous titanium implant surface for rapid osseointegration, Nanoscale. 8 (2016) 5291–5301.

[19]   W. Liu, M. Cheng, T. Wahafu, Y. Zhao, H. Qin, J. Wang, X. Zhang, L. Wang, The in vitro and in vivo performance of a strontium-containing coating on the low-modulus Ti35Nb2Ta3Zr alloy formed by micro-arc oxidation, J. Mater. Sci. Mater. Med. 26 (2015) 203.

[20]   X. Lin, X. Yang, L. Tan, M. Li, X. Wang, Y. Zhang, K. Yang, Z. Hu, J. Qiu, In vitro degradation and biocompatibility of a strontium-containing micro-arc oxidation coating on the biodegradable ZK60 magnesium alloy, Appl. Surf. Sci. 288 (2014) 718–726.

[21]   M. Pilmane, K. Salma-Ancane, D. Loca, J. Locs, L. Berzina-Cimdina, Strontium and strontium ranelate: Historical review of some of their functions, Mater. Sci. Eng. C. 78 (2017) 1222–1230.

[22]   K.C. Kung, T.M. Lee, J.L. Chen, T.S. Lui, Characteristics and biological responses of novel coatings containing strontium by micro-arc oxidation, Surf. Coatings Technol. 205 (2010) 1714–1722.

A.I. Costa[a,b], J. Geringer[c], F. Toptan[a,d]

[a]CMEMS-UMinho – Center of MicroElectroMechanical Systems – Universidade do Minho, Campus de Azurém, Guimarães, Portugal

[b]DEMM – Department of Metallurgical and Materials Engineering, Faculty of Engineering of the University of Porto, Porto, Portugal

[c]Université de Lyon, IMT Mines Saint-Etienne, Centre CIS, INSERM SainBioSE U1059, F-42023, Saint-Etienne, France

[d]IBTN/Br – Brazilian Branch of the Institute of Biomaterials, Tribocorrosion and Nanomedicine, UNESP, Campus de Bauru, Bauru, São Paulo, Brazil

Abstract

Implants require long-term stability and rapid healing, however, Ti-based implants that are currently on the market do not meet entirely the existent expectation of patients. Infection, lack of bioactivity, wear debris and the biomechanical mismatch existent between the implant and the hosting bone are still the major problems in the prostheses field and can lead to aseptic loosening, fibrous encapsulation and osteolysis. Macro-porosity in the Ti implant is presented as a beneficial way to reduce the biomechanical mismatch, in order to approach the value of Young's modulus of the implant to the one found in the bone. As follows, porous Ti is considered a promising biomaterial for several orthopaedic applications, due to the capability of ingrowth of new bone tissue inside of pores with the aim to achieve anchorage by enlarging the bone–implant interface area. However, the lack of bioactivity and wear resistance are yet to be improved. Surface modification by micro-arc oxidation allows to bio-functionalize Ti surface with micro-porous oxide layers yields improved biological

response and tribocorrosion behaviour. In this way, the development of biomaterials with bio-functionalized macro-porous Ti structures is presented as a promising solution.

This chapter presents the main outcomes regarding those promising solutions based on their biocompatibility, mechanical properties, corrosion and tribocorrosion resistance. Although the current development in the research area of bio-functionalized macro-porous Ti is promising, further efforts should be applied to the study of essential long time investigations according to the clinic application.

Keywords: Bio-functionalization, Porous Ti, Micro-arc oxidation, Biomedical implants

2.1. Introduction

A remarkable increase in human life expectancy led to an unprecedented shift in the current patterns of disease, showing an increase in degenerative diseases, which causes degeneration of the bones. More than 50% of chronic diseases in patients with more 65 years old in Europe are related to bones and joints pathology. This brings a growing requirement for implants not only due to the people longer life but also due to the fact that more people at a younger age are injured from physical activity or trauma [1–4].

In most of the cases, the evolution of degenerative diseases, bring artificial prostheses as the sole solution with the demand for artificial bone implants increasing all over the world. Unfortunately, the available implants that are currently used have limited durability, most of the time, due to degradation in service. The products resulting from the degradation processes are bio-reactive species that, by interacting with the human tissues, provoke an adverse reaction that may lead to implant rejection and failure and consequently, a revision surgery. Nowadays, more hip replacements and dental implants are required for younger or more active patients, mainly due to traumas and diseases, making it essential and mandatory to improve their long-term longevity [2,5–9].

Each year, more than 2.2 million patients undergo to a hip or a knee replacement in OECD countries. Since the beginning of the 21st century, hip replacement rates have tripled. Currently, European countries like Germany, Austria, Switzerland, Finland,

Luxembourg and Belgium present the highest rates for hip and knee replacement while Mexico, Portugal, Israel, Ireland and Korea present the lowest rates. Differences in population structure may explain part of this variation across countries [1].

Health care quality is achieved by measuring what is important for people. However, just a few health systems in the world are asking and registering the patients' outcomes after their surgeries. In specific, after a hip replacement, according to OECD indicators, an individual's quality of life, regarding mobility, self-care, activity, pain and depression is improved around 20% [1].

The major clinical problems, illustrated in Figure 2.1, leading to the implant failures are:

▪ Infections that are caused by infectious agents, mainly bacteria and that challenging to treat orthopaedic implant infections due to a resistance of convention therapy and this may lead to revision surgeries and in the most severe cases can result in amputation and mortality. Infections are associated with patient health factors and it was found that aspects like chronic diseases as rheumatoid arthritis and diabetes, age, high body mass index are among the main reasons that increased their risks. Infections may also occur when the implant material provides surfaces with vulnerability for attachment and proliferation of bacteria, and consequently to biofilm formation, i.e., adherent bacteria that produce a protective and polymeric extracellular substance, making the treatment process more difficult. A revision surgery increases the risk of infections [10–13].

▪ Aseptic loosening of the implant initiated by Young's modulus mismatch existent between the bone (10–30 GPa) and the implant (for example, 110 GPa for Ti) leading to a stress-shielding effect and consequently to bone resorption. In this way, aseptic loosening reported the mechanical failure between the implant and the bone and appears primarily as a consequence of focal periprosthetic inflammatory bone loss occurring at the interface of the implant. At the present, aseptic loosening is the cause of more than 50% of the revision surgeries in hip arthroplasty. Specifically, early aseptic loosening may be related to the characteristics of the material and implant design that may affect osseointegration [7,14–18];

▪ Bioinertness of the implant surface resulting in a poor bond between the surrounding bone tissue and the implant that causes fibrous encapsulation, a layer of

13

connective tissue formed as part of the body's response to a foreign material [7,11,14,19];

▪ Osteolysis due to an inflammatory reaction caused by wear debris released for the surrounding tissue of the implant due to the bio-tribocorrosion process that material suffers caused by the synergism of the physiologic aggressive environment together with the tribological wear as a degradation process [2,7,14,20,21].
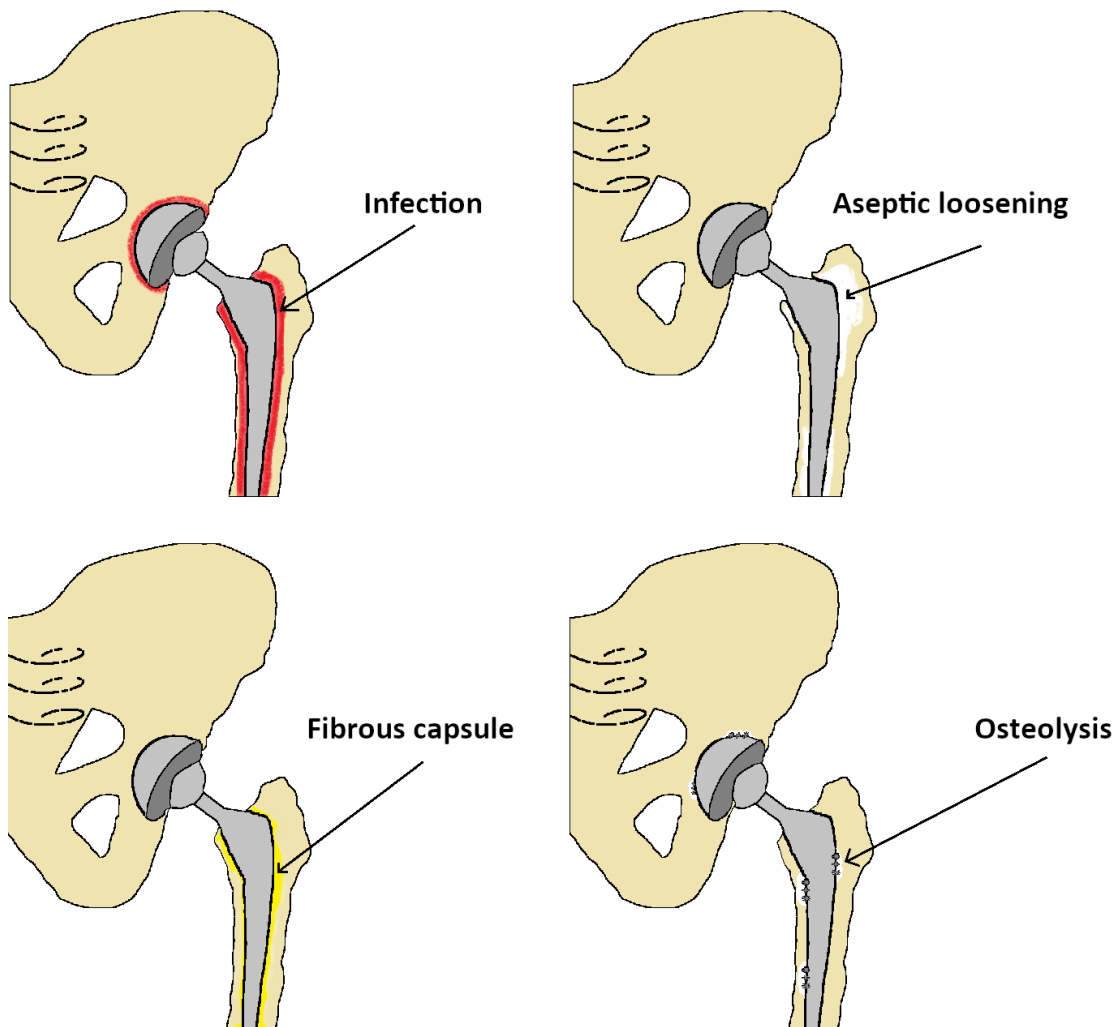
Figure 2.1. Schematic drawing of the major clinical problems leading to hip implant failures.

These problems will prevent the bone to heal and significantly reduce the quality of life of the patients. In this way, new investigations are demanded to improve clinical orthopaedic results [22]. Some of the solutions investigated are:

▪ By controlling the implant macro-porosity is possible to adjust the stiffness of the implant to match the one of the bone and consequently, reduce or eliminate the

14

stress-shielding effect caused by the stiffness mismatch between the prosthesis and the bone [23–25];

▪ Through surface modification, it is possible to improve bioactivity, corrosion and tribocorrosion performance of the implant by creating a micro-porous oxide layer with bioactive elements and this can enhance biological mechanisms and improve the long-term performance of implants by improving the wear resistance of the implant [26–28].

In order to succeed, implants require varied mechanical properties in different regions of their structure. The most common examples are the dental, hip, craniofacial and mandible implants. For each application, the functional requirements and aesthetics aspects must be considered. For load bearing implants, like hip and mandible, the mechanical properties change throughout the implant and the functionality requirements of the implant are heterogeneous through the implant. In the case of the hip, the head part should be dense while the stem can be porous. In the case of the mandible, the dental abutment must be a dense region while the body of the implant may be a porous part. These structures are described as Functionally Graded Materials (FGMs). FGMs are attracting attention in biomedical engineering due to the possibility to have exceptionally good mechanical and biological properties where they are most solicited. A more effective implant requires a gradient structure across it, with tailored size, shape and distribution of pores in each region. In this way, the part with a high level of porosity can stimulate elevated vascularization and direct formation of bone while the dense structure can provide mechanical stability. Somehow, it mimics the porous architecture of the bone because it presents a differentiated and graded structure [7,19,25,29,30]. Thus, the following aspects should be considered for designing implant surfaces: mimicking the natural bone structures at a macro-, micro- and nano-scales with an adequate chemical composition, wettability and rapid osseointegration ability. Osseointegration can be defined as the capability to produce bone from the osteoblasts that adhere to the substrates and rapid osseointegration is a critical factor for the success rate of orthopaedic implants. Osseointegration is a crucial stage for the success of implants and it has been showing that the biological fixation is closely related to the surface characteristics of the implant material. In this way, in order to fulfil such characteristic to achieve better outcomes, different materials together or not with coatings and surface modifications have been suggested to enhance biomechanical

behaviour in order to increase the performance of the implant–bone interface [22,31–34].

A biomaterial can be defined as a material designed to take a form that can direct, through interactions with living systems, the course of any therapeutic or diagnostic procedure [35]. Its production for implantology requires a multifaceted team composed of physicians, scientists and engineers that get involved in the creation of a new medical device in order to increase the quality of life of the patients. The development of new materials is constantly aiming the optimum balance between the biological, mechanical and triboelectrochemical performance as well as the surface properties since they can influence biological and mechanical compatibility. So, the desire is to develop biomaterials with mechanical properties that match the bone, without compromising its biocompatibility and bioactivity [14,25,36]. Biocompatibility can be defined as the ability of a material to perform with an appropriate host response in a specific application and it is controlled by the initial and successive reactions between the material and host body, where the most important are related with adsorption of molecules and proteins, cell and bacterial adhesion, activation of macrophage, formation of tissues and inflammation processes [37]. In this way, biocompatibility should be considered a characteristic of a biomaterial–host interface and not just from the biomaterial itself [38].

Several orthopaedic clinic applications, for example, knee, hip and shoulder joint implants, bone plates, screws, among others, have been used different biomaterials with the aim to improve performance for such applications. Currently, almost 80% of implants used are made of metallic biomaterials and the most metals used are Ti and its alloys, stainless steels and cobalt (Co)-chromium (Cr)-molybdenum (Mo) alloys. Among these, Ti exhibited the highest biocompatibility, corrosion resistance and specific strength (ratio of the tensile strength to density). Further metallic biomaterials, such as magnesium (Mg) alloys, iron (Fe), tantalum (Ta) and niobium (Nb) are also used in the field but with a much smaller presence [39].

One of the most abundant metals on Earth's crust and lithosphere is Ti, a transition metal within the group IV of Mendeleev's periodic table. Elements from this group present a partially filled *d* subshell and they are very reactive in the presence of oxygen and that is why an oxide (passive) film is immediately formed on their surfaces. Ti

16

presents the highest strength-to-weight ratio between the metals group. Ti is abundant and widely distributed in natural mineral deposits (ilmenite and rutile) making it more reachable than rare elements [22,32,40,41]. Ti is not usually used in the automotive industry due to the high cost of extraction and production. Therefore, Ti finds applications mainly in sectors with demands, such as the aerospace industry or biomedical devices, where the final high cost is not the principal concern [42]. More than 1000 tonnes of Ti are implanted into patients every year. Ti being non-magnetic presents the advantage of interferes less than, for example, steel and Co alloys with post-operative imaging methods such as magnetic resonance imaging (MRI) and computed tomography (CT) scanning, which are necessary to verify the position and health of the implant and the surrounding bone tissue. While Ti implants may have achieved high success rates, two major problems are still experienced: the lack of bone tissue integration and implant-centered infection. Ti is susceptible to crack propagation, that together with the other clinical problems associated with the implant failures, can limit the Ti implants lifetime to only 10 to 15 years [7–9,15,25,40,43,44]. Besides this, implants made of metallic materials, Ti included, are much stiffer when compared to bone, and this mismatch can cause stress-shielding effects under load-bearing leading to bone resorption and consequently, an eventual failure of implants. Therefore, metallic biomaterials with lower Young's modulus that can match the one from the bone are required in order to minimize the stress-shielding effects and to guarantee an optimal load transfer [17]. Among these, Ti and its alloys have been used extensively and there are studies on developing low Young's modulus implants, but they still could not reach the modulus of the bone [45–47]. Although new β-type alloys are recently emerging for biomedical applications with promising properties mainly in terms of their mechanical behaviour, they are still lack of exhaustedly completed studies, especially under *in vivo* evaluation.

In this way, another route of investigation that had progressively shifted the focus from an interface dense metallic–bone implant design is porous metallic structures that may present a Young's modulus that fits the one found in the bone. Besides this, a porous structure can promote a mechanical interlocking and a more area to contact with cells, leading to a bone-ingrowth inside of the pores [48–53], like it is schematized in Figure 2.2. Porous Ti maintains the already known properties of a material with the

possibility of osseointegration inside of the pores. This porosity gives the possibility of development of materials in accordance with the demands of specific situations encountered in the clinical practice. While factors controlling their biological and mechanical response have recently been a subject of research [48–52], the interplay between mechanical and triboelectrochemical properties, bone-ingrowth requirements and manufacturing constraints is still under study [26,54,55]. The processing of an implant with hierarchical porosity with macro- and micro-properties will determine its performance since they will control the physicochemical characteristics and topographical parameters that are the main communication with cells [56].
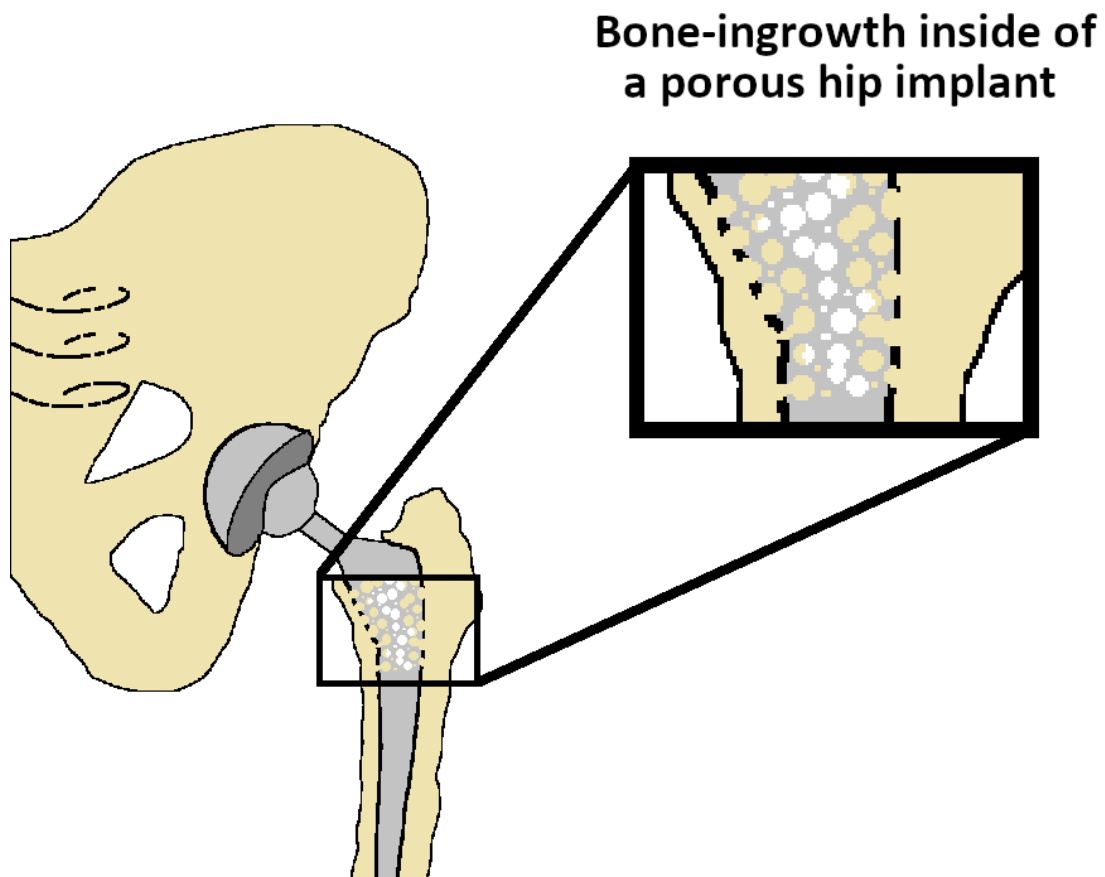
Figure 2.2. Schematic drawing of bone-ingrowth inside of a porous hip implant.

2.2. Porous Ti

With porosity, it is possible to obtain maintenance of the mechanical strength of the implant and at the same time provide the adequate pore size for bone-ingrowth. Porosity is the best way to achieve the required weight and density and it determines the final mechanical properties of the implants. Porosity may be defined by the percentage of void space in a solid and is a morphological property completely independent of the material. Pores provide the cells with the necessary space to migrate, to allow the vascularization and the proliferation and eventually to differentiate into the needed cell. Depending on the percentage of porosity and pore geometry, the surface area available to cell adhesion will be different and that will influence the vascularization process. In order to ensure ingrowth of bone inside of the pores, the optimum porosity may vary from about 30% to 60% [22,29,30,40,50,57].

A porous structure induces less time for the osseointegration process because it favours the contribution of adequate nutrients for the osteoblasts. Open pores are preferred for the increased ingrowth of tissue inside of the porous structure [36]. A complex structure is required with a wide range of pore size. Macro-pores of 50–300 µm are required for the fixation of the implants due to the interlocking between the tissue that grows inside of the pores [57,58]. However, an optimum range for the pore size required for implant fixation and osseointegration remains undetermined. From a biological point of view, some authors [30] prefer to consider a larger range and stated that an open porous structure with pore sizes from 50 to 800 µm should be the aim in order to favour bone ingrowth. On the other hand, other authors [40,59] follow a smaller range and consider that pore sizes between 100 and 500 µm are the most suitable for bone ingrowth and humoral transmission, whereas the minimum pore size for acceptable bone ingrowth may be in the range of 50–150 µm [57]. Baril *et al.* [60] used micro-computed tomography in order to quantify bone ingrowth inside of porous Ti. With this technique, the authors visualized and quantified the bone amount in different implant regions and planes and showed that bone ingrowth near cortical bone was around 28.9%, significantly greater than in cancellous that was found to be about 14.5%. The authors also presented mineralized tissue inside of the porous structures

and stated that a pore size larger than 28.5 μm did not affect bone formation, suggesting 28.5 μm as minimum pore size for efficient cell migration.

From a biological point of view, after the implantation, the response can be of two types. The worst type is related to the formation of a fibrous soft tissue capsule around the implant that does not provide biomechanical fixation and consequently, leads to the clinical failure of the implant. On the other hand, a better response involves the direct bone–implant contact, without having a connective tissue layer. The response is largely influenced by the surface chemical composition, hydrophilicity and roughness since such parameters play an important role in an implant–tissue interaction and osseointegration. Both bone anchoring and biomechanical stability are improved with implants with rough and porous surfaces [43,61,62]. Porosity, roughness and wettability are considered three major factors that contribute to the success of a cell-contacting biomaterial since the contacted area between the cells and the material is enlarged and in this way, cell growth is promoted [63]. Although it was accepted that a rough surface is considered beneficial for cell adhesion and proliferation, the interplay between roughness and mechanical properties need also to be taken into account, especially for porous structure. Wang *et al.* [64] showed that the best etching treatment in porous Ti for cell adhesion and proliferation presented a negative effect on the mechanical properties of such structures.

The production of porous Ti must provide high manufacturing rates and competitive prices so it is very important that porous structures present economically viable fabrication methods. Porous Ti implants will demand technologies that can concede economic mass production for standard implants while preserving flexible manufacturing options for custom-made implants and this market will sharply rise [25].

There are several ways to produce porous Ti structures. Powder metallurgy (PM) [26,49,55,65,66], additive manufacturing (AM) [29,67–70], freeze-casting [71,72], spark plasma sintering [73,74] and metal injection moulding [75,76] are some of the available techniques to produce porous structures. The high melting point of Ti (about 1670 °C) combined with its high reactivity makes liquid-based techniques not viable. Therefore, the production of porous Ti through powder-based processing routes is considered as an economic and flexible way to achieve the desired designed structures. PM presents several advantages such as high material yield, reduction of machining steps and the

possibility of designing alloys with tailored compositions. In addition, some of the above-mentioned methods provide limited porosity. PM can be combined with space holder technique and in this way, it is possible to obtain uniformity, adjustable porosity level, controlled pore shape and uniform pore size distribution with a not so expensive technology. Sintering temperature, porosity and pore size will condition yield strength and Young's modulus [24,49,55,59,65]. Several space holders can be used like urea or carbamide (CH_4N_2O) [24,26], sodium chloride (NaCl) [49], ammonium hydrogen carbonate $(NH_4)HCO_3$ [66], acrowax [66], sugar pellets ($C_{12}H_{22}O_{11}$) [77], tapioca [78] and rice husk [79].

AM offers freedom to design and a wide choice of materials and even multiple materials. Recently, AM techniques showed flexibility in constructing micro- and macro-scale structures based on computer models and analyses. AM can also be used for near-net-shape fabrication of complex-shaped parts with tailored properties [29,67–70]. Nowadays, AM had shown promising techniques to produce porous Ti structures, between them, the most common ones are electron beam melting (EBM) [29,69,70] and selective laser melting (SLM) [80–82]. EBM is a rapid manufacturing process in which an electron beam energy is applied on overlaying materials layer by layer based on CAD data. During the process, the electron beam passes over each successive layer of powder, which is gravity-fed from powder cassettes and raked into successive layers. SLM technique produces by melting selected areas of powder layers using a computer-controlled laser beam. Both techniques provided complex porous structures with freeform of shapes and porous structures with controlled pore size fraction. Usually, the properties achieved are comparable to the design parameters but the predictability at higher porosities seems to be better [29,69,70,80–82].

Impurities can seriously affect the mechanical properties of porous Ti, where the amount of oxygen and nitrogen present a crucial role. Increasing oxygen content develops an increase of the yield strength, hardness and fatigue resistance at a given stress level, whereas on the other hand, leads to a decrease of the ductility and impact resistance by restricting twinning and prismatic slip. When heated to a high temperature, Ti derives its strength from solution hardening because of oxygen and nitrogen and the presence of these interstitial elements lead to the brittleness of the material [40,83,84].

The oxygen content has an important impact on the compressive properties of dense and porous Ti. The yield strength and the ductility are significantly affected when the oxygen content increases from 0.24 to 0.51 $_{wt}$%. After the sintering stage in vacuum, the surface of Ti is repassivated when exposing to air and this is an additional oxygen pick-up. This effect is minimal for dense components but may be very relevant for porous components. This oxygen film contributes to the total oxygen content but its influence on the final mechanical properties is usually negligible. However, this oxide film provides to Ti improved corrosion resistance and biocompatibility [83–85].

The use of particles in most of the processes for the production of porous Ti provides a large surface area that is naturally covered with a thin oxide film that contributes to an increase in the oxygen content and consequently can affect the properties of the final materials. The large surface area of the powder provides also a large portion of the material to react with additives (i.e., binder, space holders) or with the atmosphere during processing. In addition, the high temperature processing of the powder leads to a dissolution of the oxide and/or nitride layers on the surface of the powder and, therefore, provides a fresh Ti surface to react with the atmospheric constituents. Then, a natural oxide layer reforms on the surface of the porous structure after exposure to air at low temperature. While the impact of interstitials on the properties of dense Ti-based materials has been widely studied and reported in the literature, their effect on the properties of porous Ti structures has been rarely reported [85,86].

Implants in the human body are usually under cyclic loading conditions during walking and running. The cortical bone suffers combined loading stress states that can involve tension, compression, shear and fatigue [87]. There have been several studies evaluating the compression behaviour [50,59,87–89], bending behaviour [90,91] and fatigue behaviour [84,87,92,93] of porous Ti. However, final results may present variations depending on the details of processing techniques, interstitial elements content and heat treatments, among other details.

The mechanical properties, especially Young's modulus, of porous Ti are mainly governed by the porosity. Xiang *et al.* [59] showed that the compressive strength and Young's modulus decreased as the porosity level increases. When the porosity was 70%, Young's modulus was 1.2 GPa, which is close to the one found in the human bone.

Imwinkelried *et al.* [90] stated that the typical yield strength of the porous Ti with 62.5% porosity is above 60 MPa in compression, bending and tension. In conclusion, Young's modulus, the yield strength and ultimate compressive strength decrease with an increase of porosity [40]. Nevertheless, the choice of the testing method for the evaluation of Young's modulus of porous material is critical. The most reported technique is compression test, however, dynamic methods like ultrasound technique have superior precision and repeatability. Hence, the literature shows that Young's modulus measurements from uniaxial compression tests are significantly lower than those obtained by dynamic measurements [94,95].

Bending combines tension and compression in a more complex stress distribution so that is why the values obtained by bending test differ from the ones obtained in pure tension or pure compression [96]. Amigó *et al.* [91] tested bending performance of porous Ti produced by PM with space holder technique and stated that the size of the space holder particles influences flexure strength. More specifically, a higher bending strength was obtained on the porous samples that had smaller particles size of the space holder. The results also showed that bending strength decreased as porosity increased. The same conclusion was found by Kashef *et al.* [97], where lower porosity provided a higher bending yield stress.

Fatigue may be defined by a progressive localized permanent structural change occurring in a material subjected to cyclic stresses that are often the principal cause of the premature mechanical failure of the metallic biomaterials. Under fatigue conditions, in the human body, fluids can accelerate the initiation of a surface flaw and can lead to propagation to its critical size that can start the fracture. The simultaneous action of fatigue stress and electrochemical dissolution is defined as corrosion fatigue. Fatigue strength presents remarkable changes when studied under corrosive action of simulated body fluids [87,92,98–100]. The reduction of fatigue life of Ti and its alloys under corrosion fatigue has been scarcely documented [101–105]. However, especially for porous structures, where it is possible to have interconnected porosity allowing fluids to penetrate through the structure, corrosion fatigue must be explored. Figure 2.3 presents surface and cross-section tomographic slice images showing a simulation of flooded pores by electrolyte, where porous Ti with a mixture of open and closed pores

was found to be crossed by the electrolyte, meaning that the top and bottom surfaces were linked by a void structure [26].
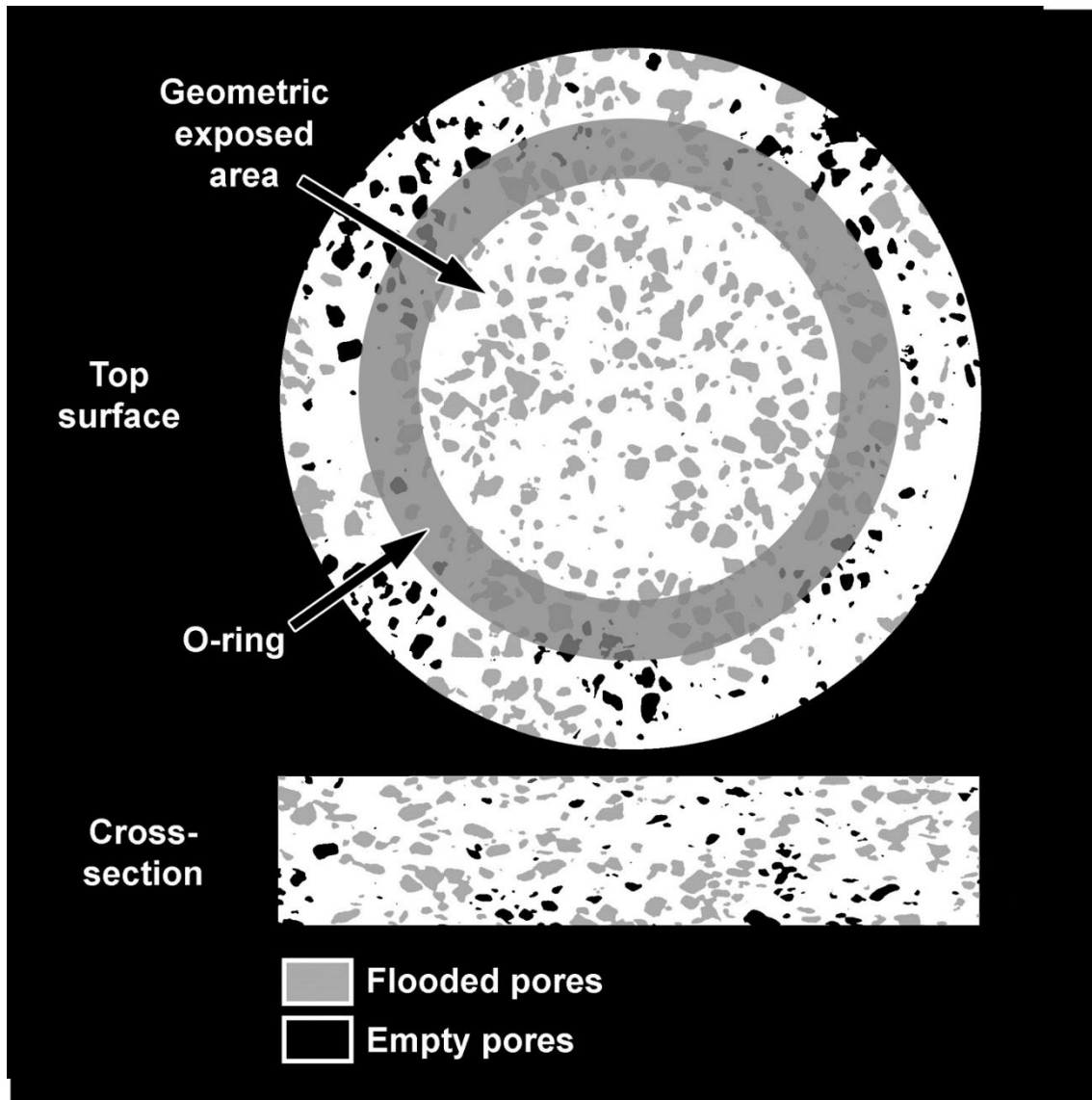
Figure 2.3. Top surface and cross-section tomographic slice images presenting a simulation of electrolyte penetrating the pores. Reproduced with permission from [26], Copyright (2020).

Porosity may be an efficient way to achieve the mechanical and biological characteristics that are needed, however, it may present a detrimental effect on the corrosion and tribocorrosion properties. The lifetime of an implant is crucial and it is conditioned by its degradation and this process is responsible for decreasing the structural integrity of the implant and the release of wear and corrosion products that may initiate some adverse biological reaction in the body and even lead to mechanical failure of the implant. Body fluids present a highly aggressive chemical environment for

the metals due to their high concentration of chloride ions that have an ability to induce localized corrosion [106–109]. The study of the electrochemical behaviour of Ti is well extended, whereas the same study on porous Ti is scarce. In general, studies indicate that pores may have strong effects on corrosion characteristics [110–112]. Xu *et al.* [110] fabricated porous NiTi and presented a decrease of the corrosion resistance on the porous samples that was attributed to a larger real contact surface area of the porous structures, as well as, the presence of crevice corrosion. Alves *et al.* [113] studied the corrosion behaviour of porous Ti having 30 and 50 $_{vol}$% of nominal porosity. Electrochemical studies revealed that samples presented a less stable oxide film at the inner pores at increased porosity. The lack of a well-defined passivation plateau in the potentiodynamic polarization curves was explained by the heterogeneities on the oxide film formed, especially on the most inner pores. The authors stated that the difference on the thickness and the nature of the oxide film between the porous structures was due to the difficulty on the electrolyte penetration through the pores as well as the difficulty on the oxygen diffusion. More recently, Alves *et al.* [26] developed corrosion studies on macro-porous Ti and stated that corrosion rate of macro-porous structures was influenced by the surface area.

Tribocorrosion, the phenomena caused by both the electrochemical and mechanical interactions on the materials, i.e. synergistic combination of corrosion processes and wear, is one of the most important aspects in biomedical industries. It appears as a threat to the quality of implant systems during and after the implantation surgery. There has been significant progress in this research area, however, the studies are significantly less when compared to the ones related to tribology and corrosion areas separately.

Hip implants as well as dental implants suffer different kinds of tribocorrosion phenomena. There are different interfaces in the hip implants: bone–cup (fretting-corrosion), head–cup (sliding-tribocorrosion), head-neck (modular junction: fretting-corrosion) and stem–bone (modular junction: fretting-corrosion), as presented in Figure 2.4. Dental implants are exposed to cyclic micro-movements at implant–abutment interface causing relative motion between contacting surfaces and leading to wear [114–116]. The wear behaviour of the implant depends on several properties, among them, with special emphasis on hardness, roughness, fracture toughness and Young's

modulus of the interacting materials. In this way, implants must have a good performance regarding degradation, that will not interfere in the bone–implant interface [117].
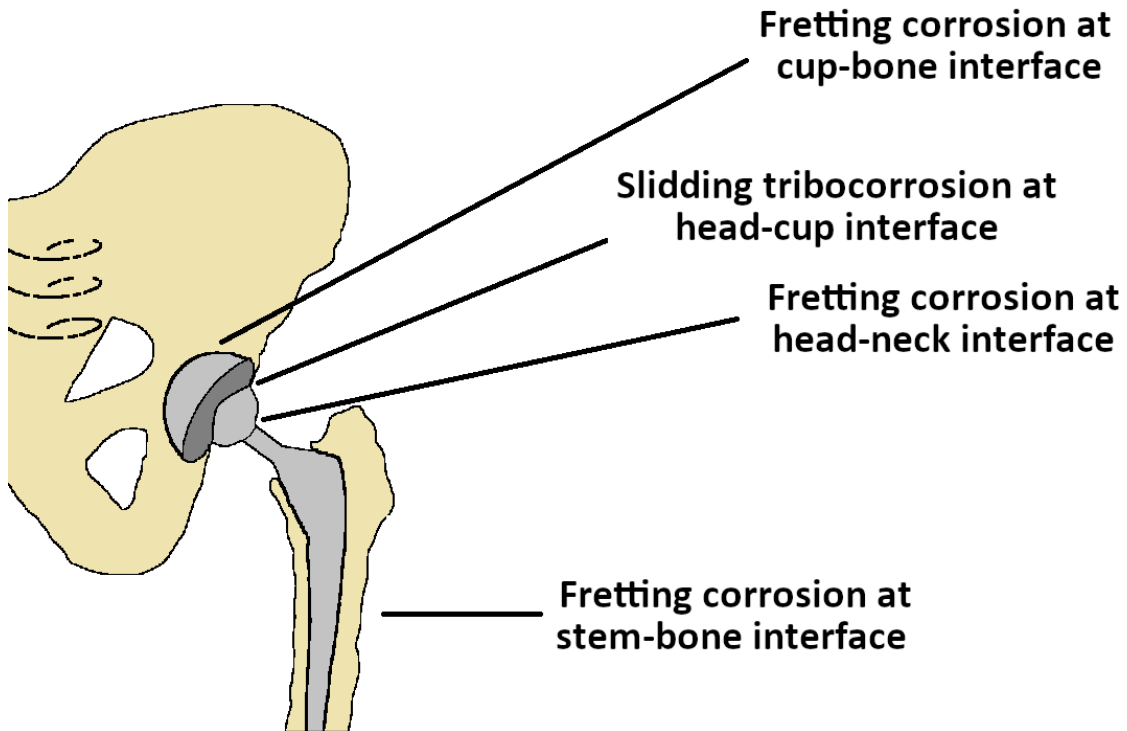
Figure 2.4. Schematic drawing showing the fretting-corrosion and sliding tribocorrosion interfaces in the hip implant.

Porous structures may present different wear behaviour compared with dense material. Studies [55,118–120] showed that porosity can either play a favourable or unfavourable role. Pores at the surface reduce the real nominal contact area and may trap the wear debris where they can be partly compacted in the pores. The presence or absence of debris can influence wear mechanisms and coefficient of friction. Porosity can also contribute to the initiation of microstructural defects, like cracks that may produce higher wear rates and decrease of the transition load. Toptan *et al.* [55] studied the tribocorrosion behaviour of macro-porous Ti and stated that the ejection of the wear debris into the macro-pores can decrease the third-body abrasion effect and may contribute to an improved tribocorrosion performance by macro-pores structures. A schematic draw of the suggested tribocorrosion mechanisms for porous Ti is presented in Figure 2.5.
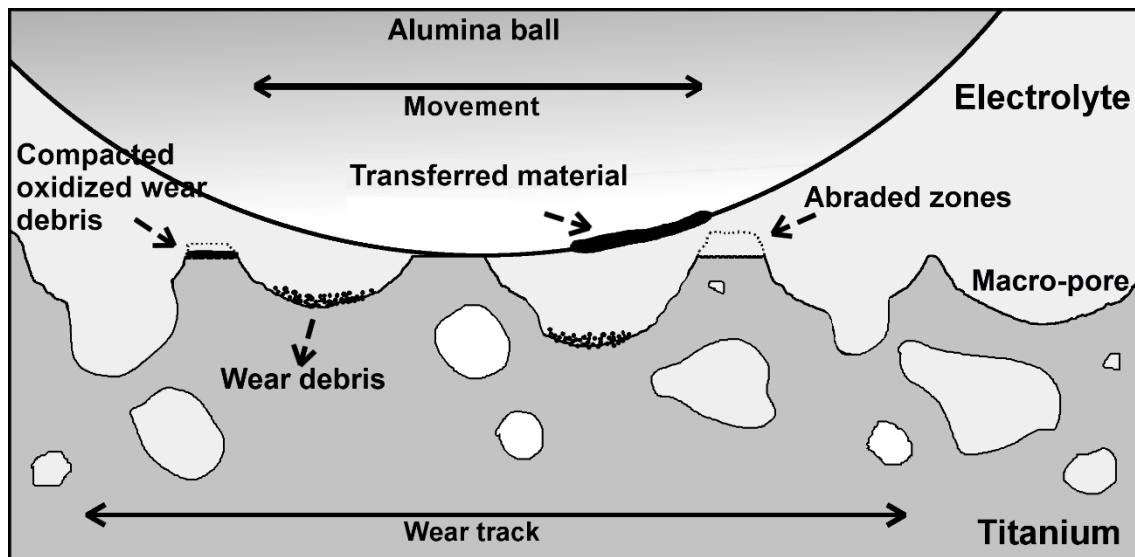
Figure 2.5. Schematic drawing for a possible wear scenario for porous Ti.

In contrast to what happens in static corrosion resistance, where the performance depends on a stable spontaneous passive film that was formed, under tribocorrosion evaluation, the behaviour relies on depassivation of the passive film and the formation of a tribofilm (including adsorbed proteins) [45,121,122]. It has been reported [5,123] that proteins affected the formation and the growth of the passive film and changed the variation in corrosion kinetics. Biological products (e.g. cells, proteins) can be a part of an extra layer that protects the implant from wear and therefore, may decrease the damage given by tribocorrosion.

Thus, the use of porous Ti instead of fully dense material may allow primary stability for the implant and a possibility to the living bone to grow inside of the structure. Although having these advantages, Ti is presented as a bioinert material, and after the implantation, Ti does not bond to the bone directly. Therefore, it is desirable to perform changes in the surfaces in order to add some bio-function without compromising the stable fixation. It is also pertinent to do improvement against long-term concerns such as the generation of metal debris from the implant. With surface modification, it is possible to achieve bioactivity, enhanced by the incorporation of bioactive elements and to achieve protection for both wear and corrosion [43,117,124].

Ti presents low resistance to wear and a high coefficient of friction, releasing metal ions under tribocorrosion solicitations [27,123,125,126]. However, there is still no consensus on how much amount of metal ions can be tolerable in the human body [127]. Recently, Costa *et al.* [128] showed that particles from tribological tests performed on Ti alloys increase the production of anti-inflammatory cytokines. Wear particles from Ti-based materials also exhibited the capability to penetrate osteoblast cell membranes and to become internalized [128]. In this way, it is required the use of an appropriate surface modification to improve the surface properties of the implant [14,20,21,27,125].

Ti implants are expected to detain high bone–implant contact. Briefly, there are four factors that can be considered being relevant in the contact between the bone and the structure: materials and surface treatments, topography, surface energy and bio-functionalization [32,129].

The main disadvantage of using metals, like Ti, as biomaterials is the fact that they have no bio-function. To solve this issue, surface modification is an effective way to bio-functionalize, altering the surface morphology and chemical composition of metals to be used as biomaterials where the tissue compatibility of the surface can be improved. Surface modification with nano- and micro-porous structures showed promising results at the implant–bone interface, with improved cell response, improved corrosion and wear resistance and, consequently, an increased implant lifetime [22,130–133].

There are several methods for surface modifications, where the most known ones are physical techniques like polishing, sandblasting and heat treatment, chemical approaches including acid-alkali etching, electrochemical methods like anodic treatment, among others. Nowadays, surface modification methods, such as anodic treatment [125,134], ion implantation [135], nitriding [135], laser-cladding [135], surface mechanical attrition treatment [136] and thermal oxidation [136] are widely applied to regulate the surface structure in order to improve the biological and the tribocorrosion behaviour of the Ti-based materials. Some of those techniques enforce the protective properties of the oxide film that is naturally formed on the surface that consists mainly of amorphous or low-crystalline and non-stoichiometric TiO_2. However, the passive film possesses poor tribological properties, thus, some of those techniques

can be applied in order to promote the growth of thick and adherent oxide layer on the surface and to enhance its tribocorrosion resistance [137].

At least four different types of titanium oxide can be formed on the surface of Ti. Under atmospheric pressure, the thermodynamically stable oxide is TiO_2 and it can exist in an amorphous natural state or one of three crystalline polymorphs phases: anatase (tetragonal), rutile (tetragonal) and brookite (orthorhombic). Rutile is the most stable crystallographic phase of TiO_2 but lower temperatures favour the formation of metastable anatase over the rutile [137].

Among the various available anodic treatments, micro-arc oxidation (MAO), that can also be called plasma electrolytic oxidation (PEO), generates a porous uniform hard TiO_2 layer that it is firmly adherent to the bulk material (Ti). This TiO_2 layer already proved to be a promising approach since it is capable of improving the surface aspects of materials intended for biomedical applications by presenting better roughness and wettability and promoting bioactivity. Consequently, these modifications bring better results on cells adhesion, proliferation and differentiation, blood compatibility, reduction of the haemolysis rate, among other properties [28,48,138,139]. In addition to improve bioactivity, many other studies refer to MAO as a suitable and economical method for improving the corrosion [140–145] and tribocorrosion [55,125,126,146,147] behaviours because this hard TiO_2 layer acts as a physical barrier against corrosion and wear.

MAO provides the possibility of combining the chemical and morphological modification of Ti implant surfaces in an effective single-step environmental friendly and fast process. Various electrolyte solutions are used to anodize Ti and the composition of the new layer is mainly determined by the electrolyte constituents [33,148,149].

There are several biological studies on anodized Ti surfaces [134,150,151]. Chen *et al.* [150] successfully applied MAO in order to grow TiO_2 (anatase- and rutile-rich) layers on β-Ti alloy for improved osseointegration. *In vitro* osteoblast activity and microscopic observations revealed that osteoblast grew well and completely fused to the micro-porous TiO_2 layer. Oliveira *et al.* [134] reported that the anodic treatment with Ca and P incorporation modulated positively the cell viability and osteoblast-related gene expression [152]. Ribeiro *et al.* [28] studied MAO layers formed on Ti surfaces and showed faster osteoblast adhesion and spreading when compared with Ti. Felgueiras *et*

al. [151] demonstrated that porous oxide surfaces promoted osteoblast attachment, differentiation and consequently osseointegration. These structures allowed a stronger bone anchorage on both animal and human experiments. The authors performed tribocorrosion tests in the presence of MG-63 osteoblast-like cells and results presented a resistant oxide layer and cells' capacity of regeneration after implant degradation [151].

Durdu *et al.* [153] studied the tribocorrosion behaviour of Ti-6Al-4V alloy modified by MAO and stated that the wear resistance and tribological properties of the treated samples were better than those of the untreated alloys. Alves *et al.* [125] stated that the presence of rutile decreased the mechanical damage after sliding, so the crystalline structure of the layer formed in the MAO process affected the tribocorrosion behaviour. In conclusion, several works studied the tribocorrosion behaviour of the porous oxide layer on Ti [125,151,154] showed that MAO contributes to an improvement of biomedical materials performance in tribocorrosion field.

On the electrochemical field, studies [140–144] have shown that micro-porous oxide layers produced by MAO demonstrated better corrosion behaviour when compared to Ti. Park *et al.* [140] evaluated the surface characteristics of Ti modified by MAO and reported an increased corrosion potential and decreased corrosion current density. Velten *et al.* [142] reported that the thickness of the TiO_2 layer increased with the increase of the oxidation voltage. As so, a higher thickness of the oxide porous layer can increase the corrosion performance as well as the surface roughness.

There are only a few reports [155–157] regarding the mechanical performance of MAO-treated Ti and its alloys. Gu *et al.* [156] evaluated the micro-hardness of treated Ti-6Al-4V samples by MAO and presented higher value for the treated samples when compared with the untreated ones. On the other hand, Santos *et al.* [157] studied the mechanical properties of MAO-treated Ti samples by nanoindentation and showed that the hardness of the oxide layer was reported as similar to the one found in the Ti bulk material. In opposite, Young's modulus of the oxide layer was 19% lower than the one for bulk Ti due to the porosity.

Hierarchical multiscale (macro-, micro- and nano-scale) porosity on a surface can be beneficial for promoting cell adhesion and proliferation and for mechanical interlocking [58]. Such approach can be easily obtained by changing the variables of two

or more steps of anodic treatment. Li *et al.* [58] created a super hydrophilic surface through a two-step MAO process. The authors stated that the first-step only changed the morphology, but the second-step changed both the morphology and the composition. The authors presented a triple hierarchical structure on Ti surface, in the macro- (macro-pores with 100–300 μm), micro- (micro-slots with 3–10 μm) and nano- (submicron/nano-pores with 80–200 nm) scales. It was also stated that the ability to induce hydroxyapatite increased due to the presence of the micro-slots and the nano-pores [58]. Zhou *et al.* [158] performed a three-step MAO on Ti with the incorporation of bioactive elements and biological results presented that good induction of apatite was closely related to the gouges, the structure that was formed in the second-step of MAO. More recently, a hierarchical bio-functionalized porous surface was obtained on Ti by a two-step anodic treatment [27] where the authors showed that with the first-step, it was possible to obtain macro-porosity while with the second-step, a bio-functionalization process by MAO, it was provided an oxide layer with micro-pores and bioactive elements, as presented in Figure 2.6. Corrosion and tribocorrosion behaviours were evaluated and the results showed improved performance due to the protective role given by the hard porous TiO_2 layer formed on the second-step (MAO).
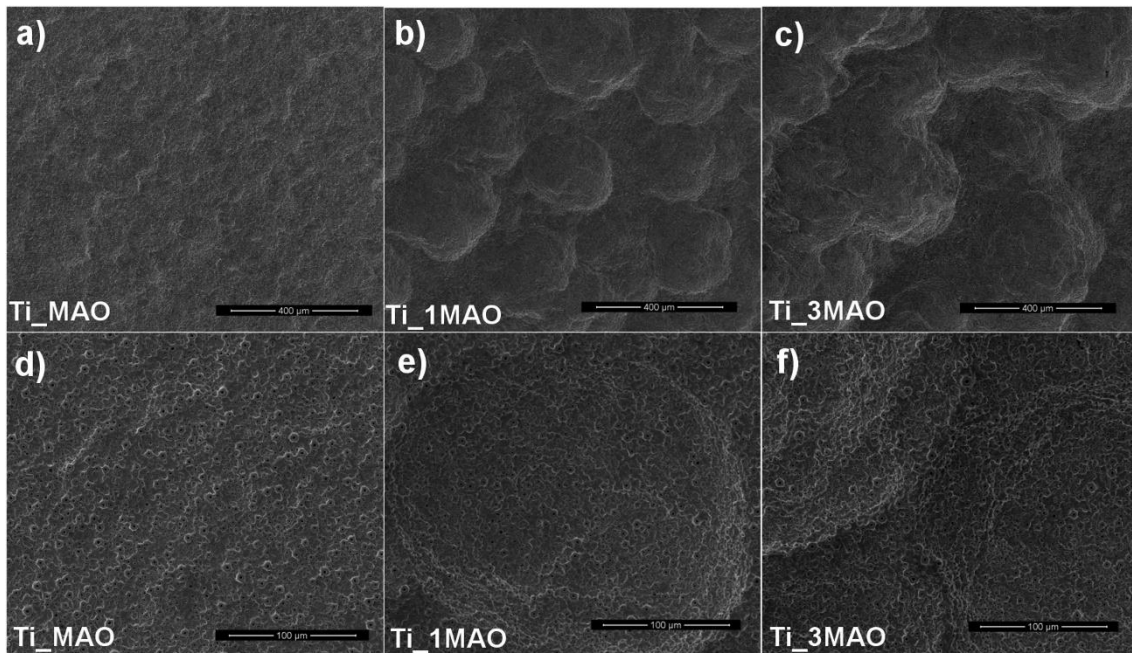
Figure 2.6. Hierarchical multiscale (macro-, micro- and nano-scale) porosity obtained by MAO process (a and d) and by a two-step anodic treatment (b to f). Reproduced with permission from [27], Copyright (2020).

One of the many advantages of MAO is the possibility of doping bioactive elements to the porous oxide layer with the aim to improve the biological response [28,48,148,159–166]. Calcium (Ca) is the most common mineral in the human body, the major structural component of bones and teeth. More than half of the mass of bone mineral is composed by phosphorus (P), which combined with calcium, forms hydroxyapatite crystals. Calcium phosphate showed to play a relevant role in order to enhance early-stage bone tissue integration [106,167,168]. Ishizawa and Ogino were the forerunners [169] to produced bioactive oxide layer containing Ca and P, as bioactive elements.

Strontium (Sr) as bioactive element presents a dual action since it showed beneficial effects on bone growth and reduction of bone resorption. In this way, Sr is reported to increase osteoblast differentiation and bone matrix mineralization [32,148,160–165]. Mg ions are naturally occurring within a human body and play a critical role to many essential cellular functions, such as activating adenosine triphosphate and synthesizing DNA and RNA. More than 60% of Mg in the human body is found in bone. Mg can be absorbed by the human body over time and this characteristic makes it particularly well-suited for applications that require malleable implant devices [22,160]. Another promising bioactive element is zinc (Zn) that presents a beneficial effect on bone growth and positively affects bone regeneration as well as antibacterial potential [160,170]. Fluor (F) is stored in teeth and bones and increases their structural stability. More recently, F incorporation as bioactive elements showed promising results since it enhanced the antibacterial activity of medical devices and also osteoblastic activity [168]. Silver (Ag) and copper (Cu) exhibit antimicrobial ability however their incorporation may lead to cytotoxicity [165,166,170,171]. Recently, it was reported that manganese (Mn) can have a significant role as a co-factor in the bone mineralization as well as bone cartilage and collagen formation showing promising results to be used as bioactive element [36]. Cerium (Ce) is a rare earth element that also has been used in biomaterials to stimulate antibacterial activity [159]. Co has been shown to be favourable for angiogenesis but also exhibits prolonged antibacterial effects [168]. Bioactive elements may play a role not only with biological effects but can also set performance on the tribocorrosion behaviour, playing or not a lubricant effect [172].

The main goal with the bio-functionalization process by surface modification using MAO for porous Ti is to achieve an efficient procedure that provides bioactivity for both the outer surface and inner parts of the surface implant, like Figure 2.7 illustrated. Such modification can increase the biological response and tribocorrosion without an alteration on its macro-pore size distribution, amount of porosity or 3D interconnection. However, the evaluation of bio-functionalized macro-porous Ti is still scarce in the literature [26,48,55,173–175] and most of the studies give a limited evaluation.
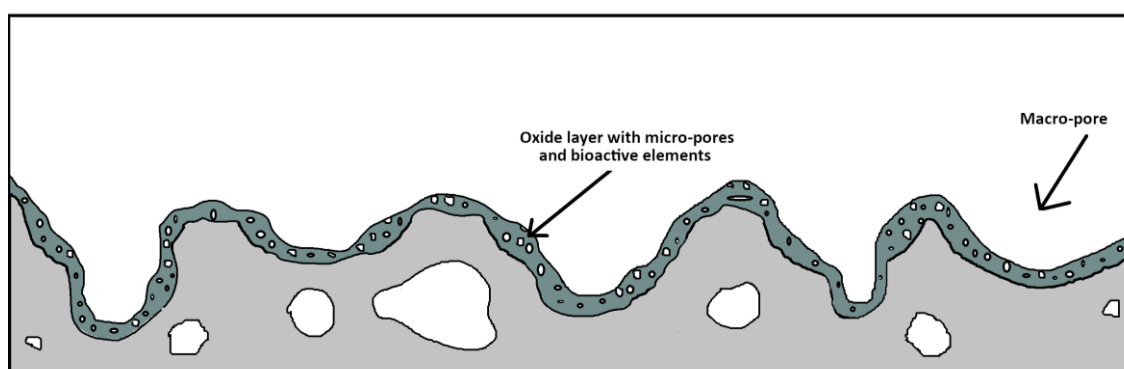
Figure 2.7. Schematic drawing of bio-functionalization of macro-porous Ti, where a micro-porous oxide layer with bioactive elements covers all the surface of the macro-pores.

Bio-functionalized macro-porous Ti showed apatite-forming abilities with apatite rapidly nucleates and grows on the porous structures [174,175]. Extensive biological studies were recently reported. Alves *et al.* [48] studied the biological response in terms of adhesion, spreading, viability and proliferation of pre-osteoblasts on bio-functionalized highly porous Ti. Representative lower and higher magnification SEM images of osteoblasts attached to bio-functionalized porous Ti are presented in Figure 2.8. The authors stated that bio-functionalization by MAO is an efficient way to incorporate bioactive elements on both outmost surfaces and inner pore surfaces, which may allow the supply of bioactive elements when necessary. Results showed that bio-functionalized porous Ti structures exhibited better cell adhesion and proliferation. Another study [170] with porous Ti implants that were bio-functionalized by MAO showed that bioactive elements such as Ag and Zn were released from the implant surfaces for at least 28 days resulting in antibacterial activity. Besides this, bio-

functionalized porous Ti generated reactive oxygen species and by this way, promoted antibacterial contact killing. Such surfaces also showed enhanced osteogenic behaviour of pre-osteoblasts after 3, 7, and 11 days [170].
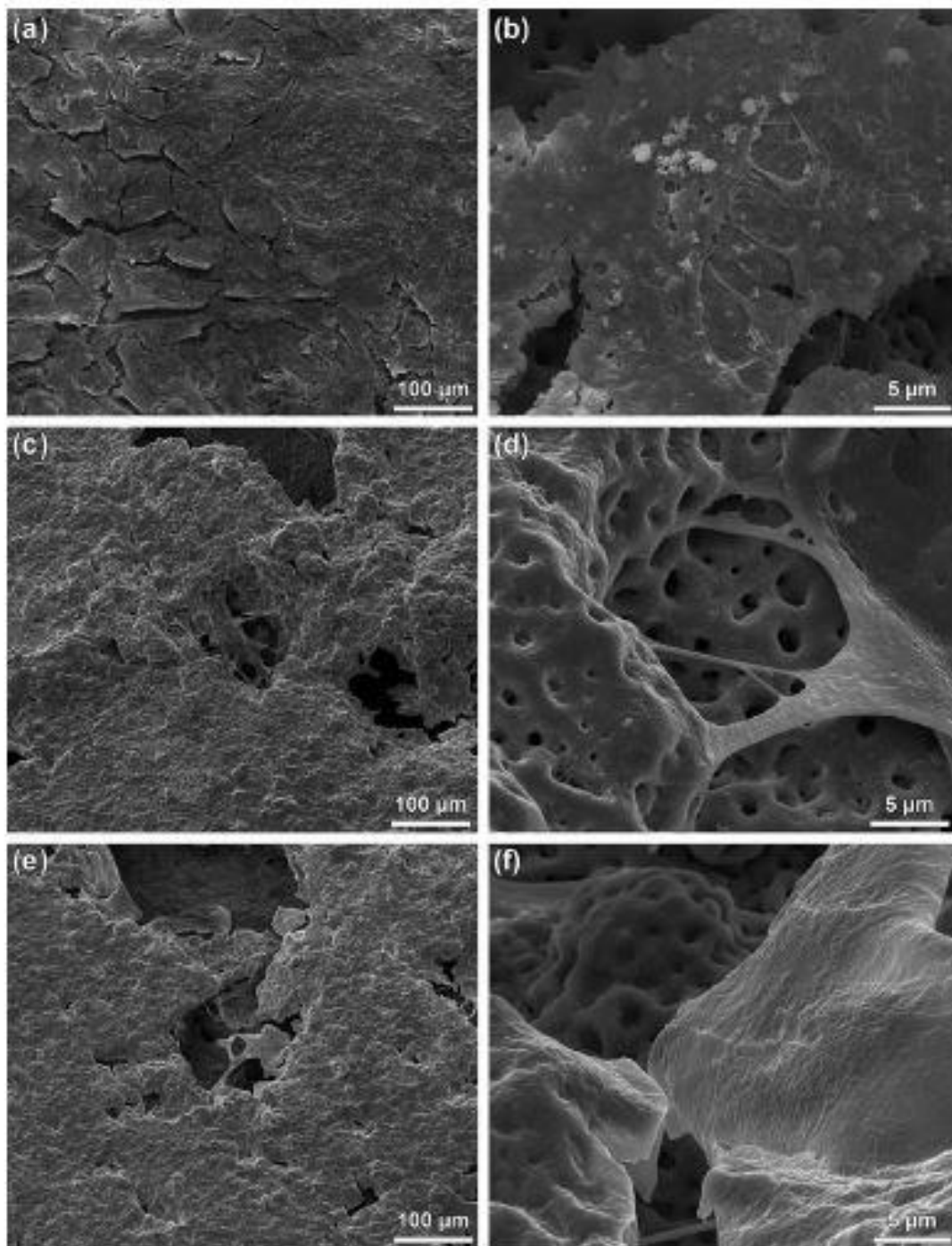
Figure 2.8. Representative lower (a, c and e) and higher (b, d and f) magnification SEM images of osteoblasts attached to bio-functionalized dense Ti (a,b) and bio-functionalized highly porous Ti (c–f). Reproduced with permission from [48], Copyright (2019).

Using a different bio-functionalization process than MAO, macro-porous Ti with TiO$_2$ nanotubes showed potential on the number of planktonic bacteria and hindering the formation of biofilms making them, according to the Yavari *et al*. [166], promising candidates for combating peri-operative implant-associated infections. Bose *et al.* [167] also studied the effect of TiO$_2$ nanotubes on porous Ti and stated that such an approach induced early-stage osteogenesis with enhanced defect healing and mechanical interlocking at the interface bone–implant.

On the other hand, surface modification methods should not deteriorate the final properties of macro-porous structures. Previously, surface techniques to improve the biological response of porous Ti showed promising results for cell response but mechanical response was seriously affected [176,177]. Korkmaz *et al*. [155] applied MAO to open-cell porous Ti-6Al-4V alloy and studied the mechanical properties by compression tests and stated that results of the MAO-treated porous samples were significantly improved when compared to the untreated porous materials, showing higher peak stress. Karaji *et al.* [178] studied the effect of MAO process on the mechanical properties of porous Ti processed by AM. The authors showed that when MAO was performed for 2 min, it did not influence most of the mechanical properties under studied like maximum stress, yield stress, plateau stress, energy absorption and Young's modulus. But when MAO treatment was applied for 5 minutes, a decrease on Young's modulus, yield stress and plateau stress was showed although no changes were found on the maximum stress and energy absorption.

The triboelectrochemical response is also an important aspect that will conditione the overall response of the material that will be implanted. The literature is still very scarce on the evaluation of corrosion and tribocorrosion of bio-functionalized porous Ti. Recently, Alves *et al.* [26] demonstrated that bio-functionalization process by MAO improved the corrosion behaviour of macro-porous Ti, in terms of thermodynamic and kinetics. The authors reported that an increase of the macro-porosity led to an increase on the corrosion rate, mostly due to the growth of the barrier film formed during MAO. Toptan *et al.* [55] evaluated the tribocorrosion behaviour of bio-functionalized macro-porous Ti and the results showed lower tendency to corrosion under sliding for bio-functionalized porous structures due to the load-carrying effect produced by the hard protruded porous TiO$_2$ surfaces formed by the MAO process.

Valuable insights are reported in the literature for bio-functionalized macro-porous Ti but most of the studies revealed limited information. The main limitation is related to the porous area that is exposed to the electrolyte, especially when MAO process is proceeding. The inner pores may not be reached during the surface treatment and therefore, the oxide layer formed at the surface might be different throughout the macro-porous structure [48,55]. Besides, a lot is yet to be explored since the overall and long-term responses are yet to be understood. A better understanding of the degradation mechanics under fatigue or fretting-corrosion solicitations for long times is not known for bio-functionalized macro-porous Ti. The effect of proteins, bio-organism or bone-ingrowth inside of the pores should also be understood.

2.5. Summary and concluding remarks

The search for an optimum solution to solve the clinical problems associated with the implants led to the manipulation of the implant structures in order to obtain hierarchical porosity. Bio-functionalized macro-porous Ti was presented as a promising solution in order to overcome the main problems of implant failures: infections, aseptic loosening, bioinertness of the implant surface and osteolysis. The combination of macro-porous Ti with a micro-porous bioactive Ti oxide layer as a hierarchical structure can have the adjusted Young's modulus to match the one of the bone by controlling the implant macro-porosity and increasing the surface area that may improve the osseointegration. Additionally, trough surface modification with micro-arc oxidation, it is possible to improve bioactivity, corrosion and tribocorrosion performance of the implant by creating a micro-porous oxide layer containing bioactive elements.

The biological, mechanical and triboelectrochemical performance of such combination of solutions, bio-functionalized macro-porous Ti structures, are on the way to be improved and optimized for future implant applications. However, further long-term investigations studies are needed to justify these approaches to be a candidate to substitute the current Ti-based implant materials. In addition to all the other mechanical properties of implant materials, the design of the implant should optimize the load transfer to the bone and such phenomena should not affect the osseointegration

process. After that, *in vivo* studies are necessary to validate such tailored materials to be used as an implant.

References

[1]   OECD, Health at a Glance 2019: OECD Indicators, Paris, 2019.

[2]   American Academy of Orthopaedic Surgeons, Total Hip Replacement, 2009.

[3]   L. Costa e Silva, M.I. Fragoso, J. Teles, Physical Activity–Related Injury Profile in Children and Adolescents According to Their Age, Maturation, and Level of Sports Participation, Sports Health. 9 (2017) 118–125.

[4]   Statistical Office of the European Communities, Population Structure and Ageing - Statistics Explained, (2019) 1–10.

[5]   M.T. Mathew, C. Nagelli, R. Pourzal, A. Fischer, M.P. Laurent, J.J. Jacobs, M.A. Wimmer, Tribolayer formation in a metal-on-metal (MoM) hip joint: An electrochemical investigation, J. Mech. Behav. Biomed. Mater. 29 (2014) 199–212.

[6]   Y. Liao, R. Pourzal, M.A. Wimmer, J.J. Jacobs, A. Fischer, L.D. Marks, Graphitic tribological layers in metal-on-metal hip replacements, Science (80-.). 334 (2011) 1687–1690.

[7]   F.A. España, V.K. Balla, S. Bose, A. Bandyopadhyay, Design and fabrication of CoCrMo alloy based novel structures for load bearing implants using laser engineered net shaping, Mater. Sci. Eng. C. 30 (2010) 50–57.

[8]   H.J. Rack, J.I. Qazi, Titanium alloys for biomedical applications, Mater. Sci. Eng. C. 26 (2006) 1269–1277.

[9]   R.J. Ferguson, A.J. Palmer, A. Taylor, M.L. Porter, H. Malchau, S. Glyn-Jones, Hip and knee replacement 1 - Hip replacement, Lancet. 392 (2018) 1662–1671.

[10]   S. Bilgen, G. Eken, Surgical Site Infection After Total Knee Arthroplasty : A Descriptive Study, Int. Multispecialty J. Heal. 2 (2016) 1–8.

[11]   U. Holzwarth, G. Cotogno, Total Hip Arthroplasty: State of the Art, Challenges and Prospects, JRC Sci. Policy Reports. (2012) 62.

[12]   G. Suzuki, S. Saito, T. Ishii, S. Motojima, Y. Tokuhashi, J. Ryu, Previous fracture surgery is a major risk factor of infection after total knee arthroplasty, Knee Surgery, Sport. Traumatol. Arthrosc. 19 (2011) 2040–2044.

[13]   M. Ribeiro, F.J. Monteiro, M.P. Ferraz, Infection of orthopedic implants with emphasis on bacterial adhesion process and techniques used in studying bacterial-material interactions, Biomatter. 2 (2012) 176–194.

[14]   M. Geetha, A.K. Singh, R. Asokamani, A.K. Gogia, Ti based biomaterials, the ultimate choice for orthopaedic implants – A review, Prog. Mater. Sci. 54 (2009) 397–425.

[15]   V. Goriainov, R. Cook, J. M. Latham, D. G. Dunlop, R.O.C. Oreffo, Bone and metal: an orthopaedic perspective on osseointegration of metals, Acta Biomater. 10 (2014) 4043–4057.

[16]   S.J. Macinnes, A. Gordon, J.M. Wilkinson, Risk Factors for Aseptic Loosening Following Total Hip Arthroplasty, (1960).

[17]   B. Zhao, A.K. Gain, W. Ding, L. Zhang, X. Li, Y. Fu, A review on metallic porous materials: pore formation, mechanical properties, and their applications, Int. J. Adv. Manuf. Technol. 95 (2018) 2641–2659.

[18]   S.D. Ulrich, T.M. Seyler, D. Bennett, R.E. Delanois, K.J. Saleh, I. Thongtrangan, M. Kuskowski, E.Y. Cheng, P.F. Sharkey, J. Parvizi, J.B. Stiehl, M.A. Mont, Total hip arthroplasties: What are the reasons for revision?, Int. Orthop. 32 (2008) 597–604.

[19]   A. Kumar, K. Biswas, B. Basu, Hydroxyapatite-titanium bulk composites for bone tissue engineering applications, (2014) 1–16.

[20]   W. Simka, A. Iwaniak, G. Nawrat, A. Maciej, J. Michalska, K. Radwański, J. Gazdowicz, Modification of titanium oxide layer by calcium and phosphorus, Electrochim. Acta. 54 (2009) 6983–6988.

[21]   H. Guleryuz, H. Cimenoglu, Surface modification of a Ti-6Al-4V alloy by thermal oxidation, Surf. Coatings Technol. 192 (2005) 164–170.

[22]   E.A. Lewallen, S.M. Riester, C.A. Bonin, H.M. Kremers, A. Dudakovic, S. Kakar, R.C. Cohen, J.J. Westendorf, D.G. Lewallen, A.J. Wijnen, Biological strategies for improved osseointegration and osteoinduction of porous metal orthopedic implants, Tissue Eng. Part B Rev. 2 (2015) 218–230.

[23]   S.Y. Min, Y. Kim, T.K. Lee, S. Seo, H.S. Jung, D. Kim, J. Lee, B.J. Lee, The effect of porosity on the elasticity of pure titanium: An atomistic simulation, Met. Mater. Int. 16 (2010) 421–425.

[24]   O. Smorygo, A. Marukovich, V. Mikutski, A.A. Gokhale, G.J. Reddy, J.V. Kumar, High-porosity titanium foams by powder coated space holder compaction method, Mater. Lett. 83 (2012) 17–19.

[25]   A. Bansiddhi, D.C. Dunand, Titanium and NiTi foams for bone replacement,

Woodhead Publishing Limited, 2014.

[26]   A.C. Alves, A.I. Costa, F. Toptan, J.L. Alves, I. Leonor, E. Ribeiro, R.L. Reis, A.M.P. Pinto, J.C.S. Fernandes, Effect of bio-functional MAO layers on the electrochemical behaviour of highly porous Ti, Surf. Coatings Technol. 386 (2020) 125487.

[27]   A.I. Costa, L. Sousa, A.C. Alves, F. Toptan, Tribocorrosion behaviour of bio-functionalized porous Ti surfaces obtained by two-step anodic treatment, Corros. Sci. 166 (2020) 108467.

[28]   A.R. Ribeiro, F. Oliveira, L.C. Boldrini, P.E. Leite, P. Falagan-Lotsch, A.B.R. Linhares, W.F. Zambuzzi, B. Fragneaud, A.P.C. Campos, C.P. Gouvêa, B.S. Archanjo, C.A. Achete, E. Marcantonio, L.A. Rocha, J.M. Granjeiro, Micro-arc oxidation as a tool to develop multifunctional calcium-rich surfaces for dental implant applications, Mater. Sci. Eng. C. 54 (2015) 196–206.

[29]   J. Parthasarathy, B. Starly, S. Raman, A design for the additive manufacture of functionally graded porous structures with tailored mechanical properties for biomedical applications, J. Manuf. Process. 13 (2011) 160–170.

[30]   C. Simoneau, P. Terriault, B. Jetté, M. Dumas, V. Brailovski, Development of a porous metallic femoral stem: Design, manufacturing, simulation and mechanical testing, Mater. Des. 114 (2017) 546–556.

[31]   L. Lin, H. Wang, M. Ni, Y. Rui, T.-Y. Cheng, C.-K. Cheng, X. Pan, G. Li, C. Lin, Enhanced osteointegration of medical titanium implant with surface modifications in micro/nanoscale structures, J. Orthop. Transl. 2 (2014) 35–42.

[32]   M. Bruschi, D. Steinmüller-Nethl, W. Goriwoda, M. Rasse, Composition and Modifications of Dental Implant Surfaces, J. Oral Implant. (2015) 1–14.

[33]   G. Li, H. Cao, W. Zhang, X. Ding, G. Yang, Y. Qiao, X. Liu, X. Jiang, Enhanced Osseointegration of Hierarchical Micro/Nanotopographic Titanium Fabricated by Microarc Oxidation and Electrochemical Treatment, ACS Appl. Mater. Interfaces. 8 (2016) 3840–3852.

[34]   X. Zhang, D. Williams, IV - Biocompatibility and immune responses to biomaterials, in: Defin. Biomater. Twenty-First Century, Elsevier, 2019: pp. 55–101.

[35]   X. Zhang, D. Williams, II - Biomaterials and biomedical materials, in: Defin. Biomater. Twenty-First Century, Elsevier, 2019: pp. 15–23.

[36]   C. Aguilar, C. Guerra, S. Lascano, D. Guzman, P.A. Rojas, M. Thirumurugan, L.

40

Bejar, A. Medina, Synthesis and characterization of Ti-Ta-Nb-Mn foams, Mater. Sci. Eng. C. 58 (2016) 420–431.

[37]   T. Hanawa, Titanium-tissue interface reaction and its control with surface treatment, Front. Bioeng. Biotechnol. 7 (2019).

[38]   D.F. Williams, Biocompatibility in clinical practice: predictable and unpredictable outcomes, Prog. Biomed. Eng. 1 (2019) 013001.

[39]   M. Niinomi, M. Nakai, J. Hieda, Development of new metallic alloys for biomedical applications, Acta Biomater. 8 (2012) 3888–3903.

[40]   A. Nouri, Titanium foam scaffolds for dental applications, Met. Foam Bone. (2017) 131–160.

[41]   Y. Kirmanidou, M. Sidira, M.E. Drosou, V. Bennani, A. Bakopoulou, A. Tsouknidas, N. Michailidis, K. Michalakis, New Ti-Alloys and Surface Modifications to Improve the Mechanical Properties and the Biological Response to Orthopedic and Dental Implants: A Review, Biomed Res. Int. (2016).

[42]   L. Bolzoni, E.M. Ruiz-Navas, E. Gordo, Processing of Elemental Titanium by Powder Metallurgy Techniques, Mater. Sci. Forum. 765 (2013) 383–387.

[43]   A. Nouri, P.D. Hodgson, C. Wen, W. Ponds, Biomimetic Porous Titanium Scaffolds for Orthopedic and Dental Applications, Biomimetics Learn. from Nat. (2010) 415–451.

[44]   O. Addison, A.J. Davenport, R.J. Newport, S. Kalra, M. Monir, Do 'passive' medical titanium surfaces deteriorate in service in the absence of wear?, J. R. Soc. Interface. 9 (2012) 3161–3164.

[45]   D.R.N. Correa, P.A.B. Kuroda, C.R. Grandini, L.A. Rocha, F.G.M. Oliveira, A.C. Alves, F. Toptan, Tribocorrosion behavior of β-type Ti-15Zr-based alloys, Mater. Lett. 179 (2016) 118–121.

[46]   Y. Tsutsumi, M. Ashida, K. Nakahara, A. Serizawa, H. Doi, C.R. Grandini, L.A. Rocha, T. Hanawa, Micro Arc Oxidation of Ti-15Zr-7.5Mo Alloy, Mater. Trans. 57 (2016) 2015–2019.

[47]   J.R.S. Martins Júnior, R.A. Nogueira, R.O. De Araújo, T.A.G. Donato, V.E. Arana-Chavez, A.P.R.A. Claro, J.C.S. Moraes, M.A.R. Buzalaf, C.R. Grandini, Preparation and characterization of Ti-15Mo alloy used as biomaterial, Mater. Res. 14 (2011) 107–112.

[48]   A.C. Alves, R. Thibeaux, F. Toptan, A.M.P. Pinto, P. Ponthiaux, B. David, Influence of macroporosity on NIH/3T3 adhesion, proliferation, and osteogenic differentiation of

MC3T3-E1 over bio-functionalized highly porous titanium implant material, J. Biomed. Mater. Res. - Part B Appl. Biomater. 107 (2019) 73–85.

[49]   Y. Torres, S. Lascano, J. Bris, J. Pavón, J.A. Rodriguez, Development of porous titanium for biomedical applications: A comparison between loose sintering and space-holder techniques, Mater. Sci. Eng. C. 37 (2014) 148–155.

[50]   S. Muñoz, J. Pavón, J.A. Rodríguez-Ortiz, A. Civantos, J.P. Allain, Y. Torres, On the influence of space holder in the development of porous titanium implants: Mechanical, computational and biological evaluation, Mater. Charact. 108 (2015) 68–78.

[51]   C. Domínguez-Trujillo, E. Peón, E. Chicardi, H. Pérez, J.A. Rodríguez-Ortiz, J.J. Pavón, J. García-Couce, J.C. Galván, F. García-Moreno, Y. Torres, Sol-gel deposition of hydroxyapatite coatings on porous titanium for biomedical applications, Surf. Coatings Technol. 333 (2018) 158–162.

[52]   C. Domínguez-Trujillo, F. Ternero, J.A. Rodríguez-Ortiz, J.J. Pavón, I. Montealegre-Meléndez, C. Arévalo, F. García-Moreno, Y. Torres, Improvement of the balance between a reduced stress shielding and bone ingrowth by bioactive coatings onto porous titanium substrates, Surf. Coatings Technol. 338 (2018) 32–37.

[53]   F. Matassi, A. Botti, L. Sirleo, C. Carulli, M. Innocenti, Porous metal for orthopedics implants, Clin. Cases Miner. Bone Metab. 10 (2013) 111–115.

[54]   S. Arabnejad, R. Burnett Johnston, J.A. Pura, B. Singh, M. Tanzer, D. Pasini, High-strength porous biomaterials for bone replacement: A strategy to assess the interplay between cell morphology, mechanical properties, bone ingrowth and manufacturing constraints, Acta Biomater. 30 (2016) 345–356.

[55]   F. Toptan, A.C. Alves, A.M.P. Pinto, P. Ponthiaux, Tribocorrosion behavior of bio-functionalized highly porous titanium, J. Mech. Behav. Biomed. Mater. 69 (2017) 144–152.

[56]   L. Yin, J. Zhou, L. Gao, C. Zhao, J. Chen, X. Lu, J. Wang, J. Weng, B. Feng, Characterization and osteogenic activity of SrTiO3/TiO2nanotube heterostructures on microporous titanium, Surf. Coatings Technol. 330 (2017) 121–130.

[57]   J.S. Ansari, T. Takahashi, H. Pandit, Uncemented hips: current status, Orthop. Trauma. 32 (2018) 20–26.

[58]   Y. Li, W. Wang, J. Duan, M. Qi, A super-hydrophilic coating with a macro/micro/nano triple hierarchical structure on titanium by two-step micro-arc

oxidation treatment for biomedical applications, Surf. Coatings Technol. 311 (2017) 1–9.

[59]   C. Xiang, Y. Zhang, Z. Li, H. Zhang, Y. Huang, H. Tang, Preparation and compressive behavior of porous titanium prepared by space holder sintering process, Procedia Eng. 27 (2012) 768–774.

[60]   E. Baril, L.P. Lefebvre, S.A. Hacking, Direct visualization and quantification of bone growth into porous titanium implants using micro computed tomography, J. Mater. Sci. Mater. Med. 22 (2011) 1321–1332.

[61]   K.-H. Kim, N. Ramaswamy, Electrochemical surface modification of titanium in dentistry, Dent. Mater. J. 28 (2009) 20–36.

[62]   L. Le Guéhennec, A. Soueidan, P. Layrolle, Y. Amouriq, Surface treatments of titanium dental implants for rapid osseointegration, Dent. Mater. 23 (2007) 844–854.

[63]   T. Yang, H. Shu, H. Chen, C. Chung, J. He, Interface between grown osteoblast and micro-arc oxidized bioactive layers, Surf. Coat. Technol. 259 (2014) 185–192.

[64]   D. Wang, G. He, Y. Tian, N. Ren, W. Liu, X. Zhang, Dual effects of acid etching on cell responses and mechanical properties of porous titanium with controllable open-porous structure, J. Biomed. Mater. Res. Part B Appl. Biomater. (2020) 1–10.

[65]   B.Q. Li, C.Y. Wang, X. Lu, Effect of pore structure on the compressive property of porous Ti produced by powder metallurgy technique, Mater. Des. 50 (2013) 613–619.

[66]   D.P. Mondal, M. Patel, S. Das, A.K. Jha, H. Jain, G. Gupta, S.B. Arya, Titanium foam with coarser cell size and wide range of porosity using different types of evaporative space holders through powder metallurgy route, Mater. Des. 63 (2014) 89–99.

[67]   D.K. Pattanayak, A. Fukuda, T. Matsushita, M. Takemoto, S. Fujibayashi, K. Sasaki, N. Nishida, T. Nakamura, T. Kokubo, Bioactive Ti metal analogous to human cancellous bone: Fabrication by selective laser melting and chemical treatments, Acta Biomater. 7 (2011) 1398–1405.

[68]   B. Zhang, X. Pei, C. Zhou, Y. Fan, Q. Jiang, A. Ronca, U. D'Amora, Y. Chen, H. Li, Y. Sun, X. Zhang, The biomimetic design and 3D printing of customized mechanical properties porous Ti6Al4V scaffold for load-bearing bone reconstruction, Mater. Des. 152 (2018) 30–39.

[69]   G. Li, L. Wang, W. Pan, F. Yang, W. Jiang, X. Wu, X. Kong, K. Dai, Y. Hao, In vitro and in vivo study of additive manufactured porous Ti6Al4V scaffolds for repairing bone

defects, Sci. Rep. 6 (2016) 34072.

[70]   S. Wang, R. Li, L. Dong, Z.-Y. Zhang, G. Liu, H. Liang, Y. Qin, J. Yu, Y. Li, Fabrication of bioactive 3D printed porous titanium implants with Sr ions-incorporated zeolite coatings for bone ingrowth, J. Mater. Chem. B. 6 (2018) 3254–3261.

[71]   Y. Chino, D.C. Dunand, Directionally freeze-cast titanium foam with aligned, elongated pores, Acta Mater. 56 (2008) 105–113.

[72]   H. Do Jung, S.W. Yook, T.S. Jang, Y. Li, H.E. Kim, Y.H. Koh, Dynamic freeze casting for the production of porous titanium (Ti) scaffolds, Mater. Sci. Eng. C. 33 (2013) 59–63.

[73]   A. Ibrahim, F. Zhang, E. Otterstein, E. Burkel, Processing of porous Ti and Ti5Mn foams by spark plasma sintering, Mater. Des. 32 (2011) 146–153.

[74]   Y. Sakamoto, S. Moriyama, M. Endo, Y. Kawakami, Mechanical property of porous titanium produced by spark plasma sintering, Key Eng. Mater. 385–387 (2008) 637–640.

[75]   N. Tuncer, M. Bram, A. Laptev, T. Beck, A. Moser, H.P. Buchkremer, Study of metal injection molding of highly porous titanium by physical modeling and direct experiments, J. Mater. Process. Technol. 214 (2014) 1352–1360.

[76]   L. jian Chen, T. Li, Y. min Li, H. He, Y. hua Hu, Porous titanium implants fabricated by metal injection molding, Trans. Nonferrous Met. Soc. China (English Ed. 19 (2009) 1174–1179.

[77]   Y. Chen, D. Kent, M. Bermingham, A. Dehghan-Manshadi, G. Wang, C. Wen, M. Dargusch, Manufacturing of graded titanium scaffolds using a novel space holder technique, Bioact. Mater. 2 (2017) 248–252.

[78]   A. Mansourighasri, N. Muhamad, A.B. Sulong, Processing titanium foams using tapioca starch as a space holder, J. Mater. Process. Technol. 212 (2012) 83–89.

[79]   X. Wang, Z. Lu, L. Jia, F. Li, Preparation and properties of low cost porous titanium by using rice husk as hold space, Prog. Nat. Sci. Mater. Int. 27 (2017) 344–349.

[80]   N. Taniguchi, S. Fujibayashi, M. Takemoto, K. Sasaki, B. Otsuki, T. Nakamura, T. Matsushita, T. Kokubo, S. Matsuda, Effect of pore size on bone ingrowth into porous titanium implants fabricated by additive manufacturing: An in vivo experiment, Mater. Sci. Eng. C. 59 (2016) 690–701.

[81]   B. Gorny, T. Niendorf, J. Lackmann, M. Thoene, T. Troester, H.J. Maier, In situ characterization of the deformation and failure behavior of non-stochastic porous

structures processed by selective laser melting, Mater. Sci. Eng. A. 528 (2011) 7962–7967.

[82]   S. Van Bael, Y.C. Chai, S. Truscello, M. Moesen, G. Kerckhofs, H. Van Oosterwyck, J.P. Kruth, J. Schrooten, The effect of pore geometry on the in vitro biological behavior of human periosteum-derived cells seeded on selective laser-melted Ti6Al4V bone scaffolds, Acta Biomater. 8 (2012) 2824–2834.

[83]   E. Baril, L.-P. Lefebvre, Y. Thomas, Interstitial elements in titanium powder metallurgy: sources and control, Powder Metall. 54 (2011) 183–186.

[84]   S. Özbilen, D. Liebert, T. Beck, M. Bram, Fatigue behavior of highly porous titanium produced by powder metallurgy with temporary space holders, Mater. Sci. Eng. C. 60 (2016) 446–457.

[85]   L.-P. Lefebvre, E. Baril, Effect of Oxygen Concentration and Distribution on the Compression Properties on Titanium Foams, Adv. Eng. Mater. 10 (2008) 868–876.

[86]   L.-P. Lefebvre, E. Baril, L. de Camaret, The effect of oxygen, nitrogen and carbon on the microstructure and compression properties of titanium foams, J. Mater. Res. 28 (2013) 2453–2460.

[87]   F. Li, J. Li, T. Huang, H. Kou, L. Zhou, Compression fatigue behavior and failure mechanism of porous titanium for biomedical applications, J. Mech. Behav. Biomed. Mater. 65 (2017) 814–823.

[88]   F. Li, J. Li, H. Kou, G. Xu, T. Li, L. Zhou, Anisotropic porous titanium with superior mechanical compatibility in the range of physiological strain rate for trabecular bone implant applications, Mater. Lett. 137 (2014) 424–427.

[89]   B. Lee, T. Lee, Y. Lee, D.J. Lee, J. Jeong, J. Yuh, S.H. Oh, H.S. Kim, C.S. Lee, Space-holder effect on designing pore structure and determining mechanical properties in porous titanium, Mater. Des. 57 (2014) 712–718.

[90]   T. Imwinkelried, Mechanical properties of open-pore titanium foam, InterScience. (2007).

[91]   V. Amigo, L. Reig, D. Busquets, J.L. Ortiz, J.A. Calero, Analysis of bending strength of porous titanium processed by space holder method, Powder Metall. 54 (2011) 67–70.

[92]   A. Zargarian, M. Esfahanian, J. Kadkhodapour, S. Ziaei-Rad, Numerical simulation of the fatigue behavior of additive manufactured titanium porous lattice structures, Mater. Sci. Eng. C. 60 (2016) 339–347.

[93]   S. Amin Yavari, R. Wauthle, J. Van Der Stok, A.C. Riemslag, M. Janssen, M. Mulier, J.P. Kruth, J. Schrooten, H. Weinans, A.A. Zadpoor, Fatigue behavior of porous biomaterials manufactured using selective laser melting, Mater. Sci. Eng. C. 33 (2013) 4849–4858.

[94]   M. Radovic, E. Lara-Curzio, L. Riester, Comparison of different experimental techniques for determination of elastic properties of solids, Mater. Sci. Eng. A. 368 (2004) 56–70.

[95]   Y. Torres, J.A. Rodríguez, S. Arias, M. Echeverry, S. Robledo, V. Amigo, J., Processing, characterization and biological testing of porous titanium obtained by space-holder technique, J. Mater. Sci. 47 (2012) 6553–6564.

[96]   R. Zdero, Experimental Methods in Orthopaedic Biomechanics, 2017.

[97]   S. Kashef, S.A. Asgari, P.D. Hodgson, W. Yan, Simulation of three-point bending test of Titanium foam for biomedical applications, Front. Mater. Sci. Technol. 32 (2008) 237–240.

[98]   R.A. Zavanelli, G.E.P. Henriques, I. Ferreira, J.M.D. De Almeida Rollo, Corrosion-fatigue life of commercially pure titanium and Ti-6Al-4V alloys in different storage environments, J. Prosthet. Dent. 84 (2000) 274–279.

[99]   M. Morita, T. Sasada, H. Hayashi, Y. Tsukamoto, The corrosion fatigue properties of surgical implants in a living body, J. Biomed. Mater. Res. 22 (1988) 529–540.

[100]   R.A. Antunes, M.C.L. De Oliveira, Corrosion fatigue of biomedical metallic alloys: Mechanisms and mitigation, Acta Biomater. 8 (2012) 937–962.

[101]   C. Leinenbach, C. Fleck, D. Eifler, The cyclic deformation behaviour and fatigue induced damage of the implant alloy TiAl6Nb7 in simulated physiological media, Int. J. Fatigue. 26 (2004) 857–864.

[102]   C. Leinenbach, D. Eifler, Fatigue and cyclic deformation behaviour of surface-modified titanium alloys in simulated physiological media, Biomaterials. 27 (2006) 1200–1208.

[103]   R.A. Zavanelli, A.S. Guilherme, G.E. Pessanha-Henriques, M. Antônio De Arruda Nóbilo, M.F. Mesquita, Corrosion-fatigue of laser-repaired commercially pure titanium and Ti-6Al-4V alloy under different test environments, J. Oral Rehabil. 31 (2004) 1029–1034.

[104]   Y. Okazaki, S. Rao, Y. Ito, T. Tateishi, Corrosion resistance, mechanical properties,

46

corrosion fatigue strength and cytocompatibility of new Ti alloys without Al and V., Biomaterials. 19 (1998) 1197–1215.

[105]   C. Fleck, D. Eifler, Corrosion, fatigue and corrosion fatigue behaviour of metal implant materials, especially titanium alloys, Int. J. Fatigue. 32 (2010) 929–935.

[106]   C.A.H. Laurindo, R.D. Torres, S.A. Mali, J.L. Gilbert, P. Soares, Incorporation of Ca and P on anodized titanium surface: Effect of high current density, Mater. Sci. Eng. C. 37 (2014) 223–231.

[107]   M.T. Mohammed, Z.A. Khan, A.N. Siddiquee, Surface Modifications of Titanium Materials for developing Corrosion Behavior in Human Body Environment: A Review, Procedia Mater. Sci. 6 (2014) 1610–1618.

[108]   J.E.G. González, J.C. Mirza-Rosca, Study of the corrosion behavior of titanium and some of its alloys for biomedical and dental implant applications, 471 (1999) 109–115.

[109]   S. Virtanen, I. Milošev, E. Gomez-Barrena, R. Trebše, J. Salo, Y.T. Konttinen, Special modes of corrosion under physiological and simulated physiological conditions, Acta Biomater. 4 (2008) 468–476.

[110]   J.L. Xu, X.F. Jin, J.M. Luo, Z.C. Zhong, Fabrication and properties of porous NiTi alloys by microwave sintering for biomedical applications, Mater. Lett. 124 (2014) 110–112.

[111]   R. Menini, M. Dion, S.K.V. So, M. Gauthier, L.-P. Lefebvre, Surface and Corrosion Electrochemical Characterization of Titanium Foams for Implant Applications, J. Electrochem. Soc. 153 (2006) 13–21.

[112]   J. Fojt, L. Joska, J. Málek, Corrosion behaviour of porous Ti-39Nb alloy for biomedical applications, Corros. Sci. 71 (2013) 78–83.

[113]   A.C. Alves, I. Sendão, E. Ariza, F. Toptan, P. Ponthiaux, A.M.P. Pinto, Corrosion behaviour of porous Ti intended for biomedical applications, J. Porous Mater. 23 (2016) 1261–1268.

[114]   S. KT, L. ME, M. MT, Failure Causes in Total Hip Replacements: A Review, Austin J. Orthop. Rheumatol. 5 (2018) 1064.

[115]   J. Villanueva, L. Trino, J. Thomas, D. Bijukumar, D. Royhman, M.M. Stack, M.T. Mathew, Corrosion, Tribology, and Tribocorrosion Research in Biomedical Implants: Progressive Trend in the Published Literature, J. Bio- Tribo-Corrosion. 3 (2017).

[116]   J. Geringer, K. Kim, B. Boyer, Fretting corrosion in biomedical implants, in:

Tribocorrosion Passiv. Met. Coatings, 2011: pp. 401–423.

[117]   A. Revathi, A. Dalmau, A. Igual, C. Richard, G. Manivasagam, Degradation mechanisms and future challenges of titanium and its alloys for dental implant applications in oral environment, 76 (2017) 1354–1368.

[118]   F. Živić, N. Grujović, S. Mitrović, D. Adamović, V. Petrović, A. Radovanović, S. Đurić, N. Pali, Tribology in Industry Friction and Adhesion in Porous Biomaterial Structure, Tribol. Ind. 38 (2016) 361–370.

[119]   M. Gui, S. Bong, J. Moo, Influence of porosity on dry sliding wear behavior in spray deposited Al–6Cu–Mn/SiCp composite, Mater. Sci. Eng. A. 293 (2000) 146–156.

[120]   D.P. Mondal, S. Das, N. Jha, Dry sliding wear behaviour of aluminum syntactic foam, Mater. Des. 30 (2009) 2563–2568.

[121]   Y. Yan, A. Neville, D. Dowson, Biotribocorrosion—an appraisal of the time dependence of wear and corrosion interactions: II. Surface analysis, J. Phys. D. Appl. Phys. 39 (2006) 3206–3212.

[122]   N. Diomidis, S. Mischler, N.S. More, M. Roy, Tribo-electrochemical characterization of metallic biomaterials for total joint replacement, Acta Biomater. 8 (2012) 852–859.

[123]   M.J. Runa, M.T. Mathew, M.H. Fernandes, L.A. Rocha, First insight on the impact of an osteoblastic layer on the bio-tribocorrosion performance of Ti6Al4V hip implants, Acta Biomater. 12 (2015) 341–351.

[124]   S. Banerjee, K. Issa, B.H. Kapadia, R. Pivec, H.S. Khanuja, M.A. Mont, Systematic review on outcomes of acetabular revisions with highly-porous metals, Int. Orthop. 38 (2014) 689–702.

[125]   A.C. Alves, F. Oliveira, F. Wenger, P. Ponthiaux, J.-P. Celis, L.A. Rocha, Tribocorrosion behaviour of anodic treated titanium surfaces intended for dental implants, J. Phys. D. Appl. Phys. 46 (2013) 404001.

[126]   F.G. Oliveira, A.R. Ribeiro, G. Perez, B.S. Archanjo, C.P. Gouvea, J.R. Araújo, A.P.C. Campos, A. Kuznetsov, C.M. Almeida, M.M. Maru, C.A. Achete, P. Ponthiaux, J.-P. Celis, L.A. Rocha, Understanding growth mechanisms and tribocorrosion behaviour of porous TiO2 anodic films containing calcium, phosphorous and magnesium, Appl. Surf. Sci. 341 (2015) 1–12.

[127]   M.T. Mathew, P. Srinivasa Pai, R. Pourzal, A. Fischer, M.A. Wimmer, Significance

of tribocorrosion in biomedical applications: Overview and current status, Adv. Tribol. 2009 (2009).

[128]   B.C. Costa, A.C. Alves, F. Toptan, A.M. Pinto, L. Grenho, M.H. Fernandes, D.Y. Petrovykh, L.A. Rocha, P.N. Lisboa-Filho, Exposure effects of endotoxin-free titanium-based wear particles to human osteoblasts, J. Mech. Behav. Biomed. Mater. 95 (2019) 143–152.

[129]   M. Kulkarni, Y. Patil-Sen, I. Junkar, C. V Kulkarni, M. Lorenzetti, A. Iglič, Wettability studies of topologically distinct titanium surfaces, Colloids Surf. B. Biointerfaces. 129 (2015) 47–53.

[130]   Y. Huang, H. Qiao, X. Nian, X. Zhang, X. Zhang, G. Song, Z. Xu, H. Zhang, S. Han, Improving the bioactivity and corrosion resistance properties of electrodeposited hydroxyapatite coating by dual doping of bivalent strontium and manganese ion, Surf. Coatings Technol. 291 (2016) 205–215.

[131]   M. Xiao, Y.M. Chen, M.N. Biao, X.D. Zhang, B.C. Yang, Bio-functionalization of biomedical metals, Mater. Sci. Eng. C. 70 (2017) 1057–1070.

[132]   T. Hanawa, Research and development of metals for medical devices based on clinical needs, Sci. Technol. Adv. Mater. 13 (2012) 64102.

[133]   T. Hanawa, A comprehensive review of techniques for biofunctionalization of titanium, J. Periodontal Implant Sci. 41 (2011) 263–272.

[134]   N.C.M. Oliveira, C.C.G. Moura, D. Zanetta-Barbosa, D.B.S. Mendonça, L. Cooper, G. Mendonça, P. Dechichi, Effects of titanium surface anodization with CaP incorporation on human osteoblastic response, Mater. Sci. Eng. C. 33 (2013) 1958–1962.

[135]   J. Dai, J. Zhu, C. Chen, F. Weng, High temperature oxidation behavior and research status of modifications on improving high temperature oxidation resistance of titanium alloys and titanium aluminides: A review, J. Alloys Compd. 685 (2016) 784–798.

[136]   M. Wen, C. Wen, P. Hodgson, Y. Li, Improvement of the biomedical properties of titanium using SMAT and thermal oxidation, Colloids Surfaces B Biointerfaces. 116 (2014) 658–665.

[137]   J.R. Birch, T.D. Burleigh, Oxides Formed on Titanium by Polishing, Etching, Anodizing, or Thermal Oxidizing, Corrosion. 56 (2000) 1233–1241.

[138]   L. Xu, K. Zhang, C. Wu, X. Lei, J. Ding, X. Shi, C. Liu, Micro-Arc Oxidation Enhances the Blood Compatibility of Ultrafine-Grained Pure Titanium, Materials (Basel). 10 (2017)

1446.

[139]   Y. Wang, H. Yu, C. Chen, Z. Zhao, Review of the biocompatibility of micro-arc oxidation coated titanium alloys, Mater. Des. 85 (2015) 640–652.

[140]   I.S. Park, T.G. Woo, W.Y. Jeon, H.H. Park, M.H. Lee, T.S. Bae, K.W. Seol, Surface characteristics of titanium anodized in the four different types of electrolyte, Electrochim. Acta. 53 (2007) 863–870.

[141]   M.D. Roach, R.S. Williamson, I.P. Blakely, L.M. Didier, Tuning anatase and rutile phase ratios and nanoscale surface features by anodization processing onto titanium substrate surfaces, Mater. Sci. Eng. C. 58 (2016) 213–223.

[142]   D. Velten, V. Biehl, F. Aubertin, B. Valeske, W. Possart, J. Breme, Preparation of TiO2 layers on cp-Ti and Ti6Al4V by thermal and anodic oxidation and by sol-gel coating techniques and their characterization, J Biomed Mater Res. 59 (2002) 18–28.

[143]   M. Fazel, H.R. Salimijazi, M.A. Golozar, M.R. Garsivaz jazi, A comparison of corrosion, tribocorrosion and electrochemical impedance properties of pure Ti and Ti6Al4V alloy treated by micro-arc oxidation process, Appl. Surf. Sci. 324 (2015) 751–756.

[144]   D. Quintero, O. Galvis, J.A. Calderón, J.G. Castaño, F. Echeverría, Control of the physical properties of anodic coatings obtained by plasma electrolytic oxidation on Ti6Al4V alloy, Surf. Coatings Technol. 283 (2015) 210–222.

[145]   L. Benea, E. Mardare-Danaila, M. Mardare, J.-P. Celis, Preparation of titanium oxide and hydroxyapatite on Ti–6Al–4V alloy surface and electrochemical behaviour in bio-simulated fluid solution, Corros. Sci. 80 (2014) 331–338.

[146]   I. da S.V. Marques, M.F. Alfaro, N.C. da Cruz, M.F. Mesquita, C. Sukotjo, M.T. Mathew, V.A.R. Barão, Tribocorrosion behavior of biofunctional titanium oxide films produced by micro-arc oxidation: Synergism and mechanisms, J. Mech. Behav. Biomed. Mater. 60 (2016) 8–21.

[147]   L. Benea, E. Danaila, P. Ponthiaux, Effect of titania anodic formation and hydroxyapatite electrodeposition on electrochemical behaviour of Ti-6Al-4V alloy under fretting conditions for biomedical applications, Corros. Sci. 91 (2015) 262–271.

[148]   K.C. Kung, T.M. Lee, T.S. Lui, Bioactivity and corrosion properties of novel coatings containing strontium by micro-arc oxidation, J. Alloys Compd. 508 (2010) 384–390.

[149] D.A. Torres-Cerón, F. Gordillo-Delgado, S.N. Moya-Betancourt, Effect of the voltage pulse frequency on the structure of TiO2 coatings grown by plasma electrolytic oxidation, J. Phys. Conf. Ser. 935 (2017).

[150] H.-T. Chen, C.-J. Chung, T.-C. Yang, C.-H. Tang, J.-L. He, Microscopic observations of osteoblast growth on micro-arc oxidized β titanium, Appl. Surf. Sci. 266 (2013) 73–80.

[151] H.P. Felgueiras, L. Castanheira, S. Changotade, F. Poirier, S. Oughlis, M. Henriques, C. Chakar, N. Naaman, R. Younes, V. Migonney, J.P. Celis, P. Ponthiaux, L.A. Rocha, D. Lutomski, Biotribocorrosion (tribo-electrochemical) characterization of anodized titanium biomaterial containing calcium and phosphorus before and after osteoblastic cell culture, J. Biomed. Mater. Res. Part B Appl. Biomater. 103 (2015) 661–669.

[152] N. Ohtsu, D. Ishikawa, S. Komiya, K. Sakamoto, Effect of phosphorous incorporation on crystallinity, morphology, and photocatalytic activity of anodic oxide layer on titanium, Thin Solid Films. 556 (2014) 247–252.

[153] S. Durdu, M. Usta, The tribological properties of bioceramic coatings produced on Ti6Al4V alloy by plasma electrolytic oxidation, Ceram. Int. 40 (2014) 3627–3635.

[154] S.A. Alves, R. Bayón, A. Igartua, V. Saénz de Viteri, L.A. Rocha, Tribocorrosion behaviour of anodic titanium oxide films produced by plasma electrolytic oxidation for dental implants, Lubr. Sci. 26 (2013) 7–8.

[155] K. Korkmaz, The effect of Micro-arc Oxidation treatment on the microstructure and properties of open cell Ti6Al4V alloy foams, Surf. Coatings Technol. 272 (2015) 72–78.

[156] Y. Gu, L. Chen, W. Yue, P. Chen, F. Chen, C. Ning, Corrosion behavior and mechanism of MAO coated Ti6Al4V with a grain-fined surface layer, J. Alloys Compd. 664 (2016) 770–776.

[157] E. Santos, G.B. de Souza, F.C. Serbena, H.L. Santos, G.G. de Lima, E.M. Szesz, C.M. Lepienski, N.K. Kuromoto, Effect of anodizing time on the mechanical properties of porous titania coatings formed by micro-arc oxidation, Surf. Coatings Technol. 309 (2017) 203–211.

[158] R. Zhou, D. Wei, J. Cao, W. Feng, S. Cheng, Q. Du, B. Li, Y. Wang, D. Jia, Y. Zhou, Conformal coating containing Ca, P, Si and Na with double-level porous surface structure on titanium formed by a three-step microarc oxidation, RSC Adv. 5 (2015) 28908–28920.

[159]   A.D. Anastasiou, M. Nerantzaki, E. Gounari, M.S. Duggal, P. V. Giannoudis, A. Jha, D. Bikiaris, Antibacterial properties and regenerative potential of Sr2+ and Ce3+ doped fluorapatites; a potential solution for peri-implantitis, Sci. Rep. 9 (2019) 1–11.

[160]   Z.S. Tao, W.S. Zhou, X.W. He, W. Liu, B.L. Bai, Q. Zhou, Z.L. Huang, K.K. Tu, H. Li, T. Sun, Y.X. Lv, W. Cui, L. Yang, A comparative study of zinc, magnesium, strontium-incorporated hydroxyapatite-coated titanium implants for osseointegration of osteopenic rats, Mater. Sci. Eng. C. 62 (2016) 226–232.

[161]   J. Zhou, L. Zhao, Multifunction Sr, Co and F co-doped microporous coating on titanium of antibacterial, angiogenic and osteogenic activities, Acta Biomater. 43 (2016) 358–368.

[162]   W. Zhang, H. Cao, X. Zhang, G. Li, Q. Chang, J. Zhao, Y. Qiao, X. Ding, G. Yang, X. Liu, X. Jiang, A strontium-incorporated nanoporous titanium implant surface for rapid osseointegration, Nanoscale. 8 (2016) 5291–5301.

[163]   W. Liu, M. Cheng, T. Wahafu, Y. Zhao, H. Qin, J. Wang, X. Zhang, L. Wang, The in vitro and in vivo performance of a strontium-containing coating on the low-modulus Ti35Nb2Ta3Zr alloy formed by micro-arc oxidation, J. Mater. Sci. Mater. Med. 26 (2015) 203.

[164]   X. Lin, X. Yang, L. Tan, M. Li, X. Wang, Y. Zhang, K. Yang, Z. Hu, J. Qiu, In vitro degradation and biocompatibility of a strontium-containing micro-arc oxidation coating on the biodegradable ZK60 magnesium alloy, Appl. Surf. Sci. 288 (2014) 718–726.

[165]   W.-B. C., U. S., B. R.B., S. D., Integration of strontium and copper species into calcium phosphate coatings and their cell biological characterization, 2017.

[166]   S. Amin Yavari, L. Loozen, F.L. Paganelli, S. Bakhshandeh, K. Lietaert, J.A. Groot, A.C. Fluit, C.H.E. Boel, J. Alblas, H.C. Vogely, H. Weinans, A.A. Zadpoor, Antibacterial Behavior of Additively Manufactured Porous Titanium with Nanotubular Surfaces Releasing Silver Ions, 2016.

[167]   S. Bose, D. Banerjee, A. Shivaram, S. Tarafder, A. Bandyopadhyay, Calcium phosphate coated 3D printed porous titanium with nanoscale surface modification for orthopedic and dental applications, Mater. Des. 151 (2018) 102–112.

[168]   J. Zhou, X. Wang, L. Zhao, Antibacterial, angiogenic, and osteogenic activities of Ca, P, Co, F, and Sr compound doped titania coatings with different Sr content, Sci. Rep. 9 (2019) 1–11.

52

[169]   H. Ishizawa, M. Ogino, Formation and characterization of anodic titanium oxide films containing Ca and P., J. Biomed. Mater. Res. 29 (1995) 65–72.

[170]   I.A.J. van Hengel, N.E. Putra, M.W.A.M. Tierolf, M. Minneboo, A.C. Fluit, L.E. Fratila-Apachitei, I. Apachitei, A.A. Zadpoor, Biofunctionalization of selective laser melted porous titanium using silver and zinc nanoparticles to prevent infections by antibiotic-resistant bacteria, Acta Biomater. 107 (2020) 325–337.

[171]   K. Glenske, P. Donkiewicz, A. Köwitsch, N. Milosevic-oljaca, Applications of metals for bone regeneration, M. Appl. Met. Bone Regen. (2018) 1–43.

[172]   S.A. Alves, A.L. Rossi, A.R. Ribeiro, F. Toptan, A.M. Pinto, T. Shokuhfar, J.P. Celis, L.A. Rocha, Improved tribocorrosion performance of bio-functionalized TiO2 nanotubes under two-cycle sliding actions in artificial saliva, J. Mech. Behav. Biomed. Mater. 80 (2018) 143–154.

[173]   Y. Yan, J. Sun, Y. Han, D. Li, K. Cui, Microstructure and bioactivity of Ca, P and Sr doped TiO2 coating formed on porous titanium by micro-arc oxidation, Surf. Coatings Technol. 205 (2010) 1702–1713.

[174]   X. Rao, J. Li, X. Feng, C. Chu, Bone-like apatite growth on controllable macroporous titanium scaffolds coated with microporous titania, J. Mech. Behav. Biomed. Mater. 77 (2018) 225–233.

[175]   J. Sun, Y. Han, K. Cui, Microstructure and apatite-forming ability of the MAO-treated porous titanium, Surf. Coatings Technol. 202 (2008) 4248–4256.

[176]   M. Khodaei, M. Meratian, O. Savabi, M. Fathi, H. Ghomi, The side effects of surface modification of porous titanium implant using hydrogen peroxide: Mechanical properties aspects, Mater. Lett. 178 (2016) 201–204.

[177]   S. Amin Yavari, S.M. Ahmadi, J. van der Stok, R. Wauthle, A.C. Riemslag, M. Janssen, J. Schrooten, H. Weinans, A.A. Zadpoor, Effects of bio-functionalizing surface treatments on the mechanical behavior of open porous titanium biomaterials, J. Mech. Behav. Biomed. Mater. 36 (2014) 109–119.

[178]   Z. Gorgin Karaji, R. Hedayati, B. Pouran, I. Apachitei, A.A. Zadpoor, Effects of plasma electrolytic oxidation process on the mechanical properties of additively manufactured porous biomaterials, Mater. Sci. Eng. C. 76 (2017) 406–416.

Chapter 3. TiO$_2$ bioactive implant surfaces doped with specific amount of Sr modulate mineralization

A.I. Costa[a,b], S. Gemini-Piperni[c,d], A.C. Alves[a], N.A. Costa[d,e], N.R. Checca[f], P.E. Leite[g,h], L.A. Rocha[d,i], A.M.P. Pinto[a,j], F. Toptan[a,d], A.L. Rossi[f], A.R. Ribeiro[c,d,h]

[a]CMEMS-UMinho – Center of MicroElectroMechanical Systems, University of Minho, Guimarães, Portugal

[b]DEMM – Department of Metallurgical and Materials Engineering, Faculty of Engineering of the University of Porto, Porto, Portugal

[c]Postgraduate Program of Translational Biomedicine, University Grande Rio, Duque de Caxias, Brazil

[d]IBTN/Br – Brazilian Branch of the Institute of Biomaterials, Tribocorrosion and Nanomedicine, São Paulo State University, Bauru, São Paulo, Brazil

[e]Postgraduate Program in Materials Science and Technology, São Paulo State University, Bauru, São Paulo, Brazil

[f]CBPF – Brazilian Centre for Research in Physics, Rio de Janeiro, Brazil

[g]Directory of Life Sciences Applied Metrology, National Institute of Metrology Quality and Technology, Xérem, Rio de Janeiro, Brazil

[h]Postgraduate Program in Biotechnology, National Institute of Metrology Quality and Technology, Xérem, Rio de Janeiro, Brazil

[i]Faculty of Science, Department of Physics, São Paulo State University, Bauru, São Paulo, Brazil

[j]DEM – Department of Mechanical Engineering, University of Minho, Guimarães, Portugal

Abstract

One of the main problems that remain in the implant industry is poor osseointegration due to bioinertness of implants. In order to promote bioactivity, calcium (Ca), phosphorus (P) and strontium (Sr) were incorporated into a TiO_2 porous layer produced by micro-arc oxidation. Ca and P as bioactive elements are already well reported in the literature, however, the knowledge of the effect of Sr is still limited. In the present work, the effect of various amounts of Sr was evaluated and the morphology, chemical composition and crystal structure of the oxide layer were investigated. Furthermore, *in vitro* studies were carried out using human osteoblast-like cells.

The oxide layer formed showed a triplex structure, where higher incorporation of Sr increased Ca/P ratio, amount of rutile and promoted the formation of $SrTiO_3$ compound. Biological tests revealed that lower concentrations of Sr did not compromise initial cell adhesion either viability and interestingly improved mineralization. However, higher concentration of Sr (and consequent higher amount of rutile) showed to induce collagen secretion but with compromised mineralization, possibly due to a delayed mineralization process or induced precipitation of deficient hydroxyapatite. Ca-P-TiO_2 porous layer with less concentration of Sr seems to be an ideal candidate for bone implants.

Graphical abstract
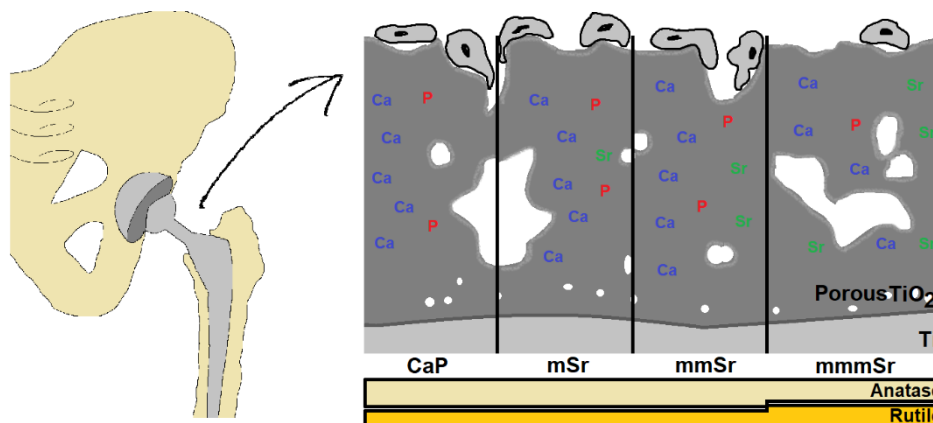
Keywords: Sr, Micro-arc oxidation, TiO_2, Orthopaedic implants

56

3.1. Introduction

In most OECD countries, the number of hip replacements has increased by 30% between 2000 and 2015 and currently, more than 1 million total hip replacements are performed every year in the world [1,2]. The existing prostheses may be successful in restoring function, thereby increasing the quality of life of millions of people, but present some concerns in the medium/long-term. Unfortunately, nowadays it was estimated that 75% of the hip implants had a lifetime of 15–20 years [3] mainly due to tendencies to fail after medium/long-term use because of various reasons, such as low wear resistance, lack of bioactivity and poor osseointegration due to the bioinertness of the implant surface [4–6]. In order to solve these problems and to improve the lifetime of implants, surface modification by anodic treatment under micro-arc oxidation (MAO) regime, also called plasma electrolytic oxidation (PEO), is presented as a favourable solution. MAO has shown capabilities to improve the most important surface characteristics of implants such as improving the bioactivity by the incorporation of bioactive elements, tailoring the oxide phases, roughness, porosity and topography that also eventually defines the wettability in a way to be more suitable for cells [7–10]. MAO contributed to an improved adhesion, proliferation and differentiation of cells, blood compatibility, reduction of the haemolysis rate, extended dynamic coagulation time, reduction of the amount of platelet adhesion and degree of deformation, among other properties [7–10], like improved corrosion [11–16] and tribocorrosion [17–21] behaviour.

MAO promotes the incorporation of bioactive elements in order to give bio-function to bioinert metal implants. Regarding bioactive elements, the major chemical element found in the bone is Ca, followed by P, but there are at least a dozen of other chemical elements in its constitution. For example, most Sr (99%) present in the human body is deposited in the bone due to its superior ability to bind with hydroxyapatite (HAP) i.e. with the mineral phase of bone [22–29]. New compact bone contains at least three times more Sr than old compact bone, while new cancellous bone contains at least two times more Sr than old cancellous bone. This can be explained by the fact that in the newly formed bone, Sr is not only incorporated into the crystals (as heteroionic substitutions) but it is also included onto their surface (adsorption and exchange). In

contrast in old bone, Sr is almost exclusively taken up onto the surface of crystals since almost no heteroionic substitution occurs afterwards [30]. Sr has an effect on osteoblast proliferation and osteoclast resorption with consequently stimulation of bone growth and inhibition of bone resorption [31,32]. Thus, Sr is accounted as a potential bioactive element showing promising results *in vitro* [31–34] and *in vivo* [25,33,35–37].

Nowadays Sr has been widely used in the biomedical field, as implants [31–34] and drug deliveries systems [34]. However, there are many concerns with its long-term effectiveness and performance because of possible Sr toxicity that has been shown to present a dose-dependent behaviour [30,38,39]. For example, some cardiovascular side effects were observed when strontium ranelate [28] was used as therapeutics to treat osteoporosis.

Sr on TiO_2 layers [29,35,40–43] showed promising results for biomedical applications. Kung *et al.* [29] studied the incorporation of Sr, Ca and P on anodized Ti and stated that the lowest Sr content provided a preferential surface for osteoblastic cell proliferation. Zhang *et al.* [41] showed that osteoblastic cell adhesion on Sr-incorporated TiO_2 was significantly enhanced compared with the Sr-free TiO_2. Sato *et al.* [42] studied the effect of the Sr addition along with Ca and P to a TiO_2 layer formed by MAO and the results showed a small inhibitory effect on pre-osteoblasts cell proliferation, however osteogenic differentiation and mineralization was observed. Based on our knowledge, few studies explored in in-depth the effect of Sr incorporation on Ca-P on TiO_2 layers and there is no consensus in which range of Sr is more beneficial for mineralization. There is still limited information regarding the effect of the amount of Sr on the composition, microstructure and long-term biological responses of Sr-TiO_2 surfaces.

A lot of studies that evaluated the effect of Sr in a layer with Ca are substituting Ca for Sr [31,35,42]. We combined the work of Kung *et al.* [24,29,44], where the authors used 0.0013 and 0.013 of strontium hydroxide to produce Ca-P-Sr TiO_2 porous surfaces, and a recent work that showed the behaviour of Sr can be promoted in a calcium-rich microenvironment [45]. Xie *et al.* [45] hypothesize that the effect of strontium on bone regeneration is related to the concentration of calcium and concluded that Sr is more potentially effective for bone regeneration in combination with an environment having a high concentration of calcium ions. In fact, strontium inhibits bone regeneration with

low dose calcium and promotes bone regeneration with a high dose of calcium *in vitro*. In addition, we also decide to work with 0.35 M of calcium acetate , since previous works showed that higher Ca concentration in the MAO electrolyte solution had a positive effect on the surface properties, chemical composition, cell evaluation and tribocorrosion behaviour [7,9,18,19,46]. In the end, we continued the studies with 0.35 M of calcium acetate and combined with the addition of 3 concentrations of strontium hydroxide (0.0013, 0.013 and 0.13 M).

Hence, in the present work, the effect of the incorporation of several concentrations of Sr on Ca-P-TiO_2 layers was evaluated and discussed. A detailed characterization of Sr-MAO oxide layer was performed with high-resolution techniques since there is a lack of information regarding their structure. Osteoblasts–Ca-P-Sr TiO_2 layers interface, cell adhesion, viability and mineralization was evaluated.

3.2. Materials and methods

3.2.1. Samples preparation and characterization

Prior to MAO treatment, Ti plates (1 x 1 cm) were ground with 320# SiC papers and then etched in a Kroll's reagent solution (1:1:1 for HF:HNO_3:H_2O) for 10 seconds. Then the samples were ultrasonically cleaned in propanol for 15 minutes followed by 10 minutes in distilled water and dried with warm air.

After surface pre-treatment, anodic treatment was carried out under MAO regime using 200 mL of a mixture of 0.02 M of β-glycerophosphate disodium salt pentahydrate (β-GP, Alfa Aesar), 0.35 M of calcium acetate monohydrate (CA, Alfa Aesar) and 0.0013 M, 0.013 M or 0.13 M of strontium hydroxide octahydrate (SH, Alfa Aesar). The electrolyte was chosen in order to incorporate bioactive species, namely P (from β-GP), Ca (from CA) and Sr (from SH). Electrical conductivity was measured (WTW Inolab conductivity meter Level 1) for the 4 conditions of electrolyte under study, at 22 ± 1 °C, with at least 5 measures per condition. Depending on the concentration of SH on the electrolyte, the groups of samples were named CaP (no SH added), mSr (0.0013 M of SH), mmSr (0.013 M of SH) and mmmSr (0.13 M of SH). Table 3.1 gives the details of the MAO process, presenting the electrolyte composition with the respective group code

and electrolyte conductivity (ms/cm). MAO treatment was performed at room temperature under a constant voltage of 300 V with a limiting current of 2.60 A during 1 minute (i.e. wait to reach 300 V and then count 1 minute) using a direct current (DC) power supply. The samples were connected as anode and a platinum sheet was used as cathode. The anode area was 2.8 cm^2 and the cathode area was 13 cm^2. The distance between the cathode and the anode was 8 cm and all the MAO treatments were carried out under turbulent regime at 200 rpm. After MAO treatment, the samples were cleaned with distilled water and air-dried. Each electrolyte was reused to produce a maximum of 5 samples after preliminary analyses ensuring the reproducibility in terms of morphology, oxide phases and chemical structure.

Table 3.1. Electrolyte composition with respective group nomenclature and electrolyte conductivity (ms/cm).

Electrolyte composition	Group nomenclature	Electrolyte Conductivity (ms/cm)
0.35 M CA + 0.02 M β-GP	CaP	21.5 ± 0.3
0.35 M CA + 0.02 M β-GP + 0.0013 M SrH	mSr	21.9 ± 0.1
0.35 M CA + 0.02 M β-GP + 0.013 M SrH	mmSr	22.6 ± 0.1
0.35 M CA + 0.02 M β-GP + 0.13 M SrH	mmmSr	33.6 ± 0.1

The topography, microstructure and chemical composition of the oxide layers formed on the surface were analysed by FEI Nova 200 field emission gun scanning electron microscope (FEG-SEM) equipped with energy dispersive X-ray spectroscopy (EDS). The distributions of pore size of the MAO layers were calculated using a point-counting method adapted from ASTM E562, where a grid (17 lines parallel to each other with a constant spacing of 0.03 mm) was superimposed on the micrographs. All the pores intersecting the lines had their diameters measured. Three SEM images were taken for each sample in at least 3 different zones of the surface and 3 samples were used per group. EDS mapping was performed using a silicon drift detector (SDD) (Oxford), equipped to scanning electron microscope, using AZtec (Oxford) software.

Crystalline structure was characterized by XRD (Cu Kα radiation, Bruker D8 Discover) with a scanning range (2Θ) of 20° to 100° at glancing incidence angle. At least three samples were evaluated per group in order to assure the reproducibility. Phase identification was performed with the help of the standard JCPDS database (JCPDS

database: 00-044-1294 for Ti, 01-089-4203 for anatase and 01-078-1508 for rutile) and the phase percentage of the oxide layer obtained by MAO was calculated following Equation (3.1):

$$\% \, phase_{\alpha} = \frac{\sum I_{\alpha peaks}}{\sum I_{allpeaks}} \qquad (3.1)$$

The elemental composition and chemical bonding of the top of the surface of the oxide layers were evaluated by X-ray photoelectron spectroscopy (XPS) using a SPECS PHOIBOS 100/150 spectrometer with a 150 mm hemispherical analyser operating with X-ray energy source of 1486.6 eV from a polychromatic Al (Kα) radiation in 30° as take-off angle, E_{pass} of 30.0 eV, using an energy step of 0.5 eV (for the survey spectra) and 0.02 eV (for the high-resolution spectra over each element peak). The energy band peak deconvolution was made using the CASA-XPS software and the NIST-XPS database for the envelope peaks C 1s, O 1s, Ti 2p, Ca 2p, P 2p and Sr 3d binding energies. C 1s (284.6 eV) was used as calibration energy.

3.2.2. Surface preparation and cell culture

Prior to cell culture experiments, Ti plates bio-functionalized (including their backsides) were sterilized in a sterile culture hood by 2 hours immersion in ethanol 70% (V/V) followed by 2 hours of UV light irradiation.

Human osteoblast-like MG-63 cells (ATCC number: CRL-1427™) were provided by Rio de Janeiro cell bank and were used for evaluation of cell–surface interactions. MG-63 osteoblastic cells were cultured at 37 °C and 5% CO_2 in a cell growth medium consisting of Dulbecco's modified Eagle's medium (DMEM, Gibco) supplemented with 10% (V/V) fetal bovine serum (FBS, Gibco) and 1% (V/V) of an antibiotic (100 U mL^{-1} of penicillin-streptomycin, BioReagent). Cell culture experiments were performed at approximately 80% confluence.

3.2.3. Cell adhesion

For adhesion experiments, MG-63 cells were seeded with a density of 1×10^4 cells per cm^2 on the surfaces placed in a 24-well plate and grown at 37 °C in fully humidified atmosphere containing 5% CO_2 alternatively for 4 and 24 hours. Evaluation of the cell adhesion experiments was performed by fluorescent staining of the actin cytoskeleton (using alexa fluor 546 phalloidin, Thermo Fisher Scientific, A22283) and the nucleus (4',6-diamidino-2-phenylindole-dihydrochloride, DAPI, Sigma-Aldrich, F6057). Cells adherent to the disks after 4 and 24 hours were fixed with 4% paraformaldehyde (PFA), permeabilized with 0.1% (V/V) Triton X-100 and the unspecific staining was blocked by incubation in 3% BSA before exposure to alexa fluor 546 phalloidin and DAPI. Samples were examined with a fluorescence microscope inverted with a digital camera Axio Observer A1 (Zeiss) equipped with AxioCAM MRm. For each testing condition and time point of experiment, at least four samples were used and two independent experiments were carried out.

3.2.4. Cell viability

For viability experiments, MG-63 cells were seeded (cell density of 2×10^4 cells per cm^2) on the surfaces placed in a 24-well plate. All the cell-containing samples were incubated at 37 °C in a fully humidified atmosphere containing 5% CO_2 for 24 hours. Then LIVE/DEAD® assay was performed to access the cytotoxicity of the surfaces and was used in accordance with the manufacturer's instructions (LIVE/DEAD® viability/cytotoxicity kit, Thermo Fisher Scientific, L3224). The kit contained two probes: calcein acetoxymethyl and ethidium homodimer. Active intracellular esterase of living cells converts calcein acetoxymethyl to calcein to generate green fluorescence. On the other hand, ethidium homodimer binds the nucleic acids but it is not permeable to cell membrane. In this way, it can only enter on the dead cells with a broken cell membrane producing red nuclear fluorescence. Finally, the total number of live and dead cells adhered on materials surfaces was determined by fluorescence microscope inverted with digital camera Axio Observer A1 (Zeiss) equipped with digital camera AxioCAM MRm (Zeiss). A total number of 12 images were acquired for each group, from which the

number of live (green) and dead (red) cells were counted. For each testing condition, at least three samples were used and two independent experiments were carried out.

3.2.5. Cell mineralization

For the 21 days cell culture experiments, in order to evaluate osteoblastic mineralization, MG-63 were seeded with a density of $1x10^5$ cells per cm^2 in incomplete osteogenic medium. The medium component are Dulbecco's modified Eagle's medium (DMEM, Gibco) high glucose, supplemented with 10% (V/V) fetal bovine serum (FBS, Gibco) and 1% (V/V) of an antibiotic (100 U mL^{-1} of penicillin-streptomycin, BioReagent), and 0.01 M β-glycerophosphate (Sigma-Aldrich) and 50 μg mL^{-1} of L-ascorbic acid (Sigma-Aldrich) to induce cell mineralization. The culture medium was replenished every 7 days. After 21 days, alizarin red-s staining (ARS) of MG-63 osteoblasts was conducted to detect the ability to form calcified deposits. All specimens were stained with 1% alizarin red-s (Sigma-Aldrich, A5533-25G) solution at room temperature and then rinsed with ultra-pure water. Alizarin red-s was dissolved using a solution of 0.5 N HCl with 5% SDS and the absorbance value of each well was quantified spectrophotometrically using a microplate reader (Biotek synergy 2 multi-mode detection with gen5 software) at a wavelength of 450 nm. Results were reported as optical density (OD) values. For each testing condition, at least four samples were used and two independent experiments were carried out.

Evaluation of the cell organic matrix was performed. Cells were fixed in PFA 4%, permeabilized with 0.1% (v/v) Triton X-100 and the unspecific staining was blocked by incubation in 1% BSA. Following triple staining for the actin cytoskeleton (using alexa fluor 546 phalloidin, Thermo Fisher Scientific, A22283), for the level of collagen type I (monoclonal anti-collagen type I, Sigma-Aldrich, C2456-2Ml) and for the nucleus (4',6-diamidino-2-phenylindole-dihydrochloride, DAPI, Sigma-Aldrich, F6057) was performed. Samples were then examined with a fluorescence microscope inverted with a digital camera Axio Observer A1 (Zeiss) equipped with AxioCAM MRm. For each testing condition, at least three samples were used and two independent experiments were carried out.

3.2.6. Cell morphology

In order to investigate cell morphology at different culture time points (4, 24 hours and 21 days), cells adhered to the surface were fixed with Karnovsky, post-fixed with 1% osmium tetroxide (OsO_4, Alpha Aesar), 0.8% potassium ferrocyanidethen dehydrated through a graded series of alcohol (50%, 60%, 70%, 80%, 90%, 95% and 100%), then dried using hexamethyldisilazane (HDMS, Sigma-Aldrich). Afterward, specimens were sputter-coated with gold and cell morphology was observed by SEM (FEG-SEM Tescan-Lyra 3 microscope).

An Auriga 40 Dual Beam instrument equipped with a Focused Ion Beam (FIB) using a gallium ion source and a SEM was used in order to analyse the interface between osteoblast and oxide layer. The samples were fixed and dehydrated as previously described. Cross-sections were performed on osteoblast adhered for 24. Slices and millings were performed using ion currents between 1 and 5 nA and beam energy of 30 keV. Lower ion beam currents (~ 200 pA) were used to polish and clean the cross-section surface. Images were recorded using the electron beam accelerated with 5 kV and a backscattered detector.

3.2.7. Cytokines expression

MG-63 cells were cultivated during 21 days on MAO-treated surfaces and 100 µL of the supernatants were collected for cytokine analysis for all the conditions. The supernatant was kept frozen at -80 °C. Analysis was performed following the manufactures' recommendations for the MAGPIX reagent kit for identification of cytokines (cytokines -plex panel, Biorad). IL-1β, IL-1Ra, IL-2, IL-4, IL-5, IL-6, IL-7, IL-8, IL-9, IL-10, IL-12p70, IL-13, IL-15, IL-17A, IP-10, IFN-γ, TNFα, VEGF, bFGF, MIP-1α, MIP-1β, MCP-1, PDGF-BB, RANTES, GM-CSF, G-CSF and Eotaxin were included in the analysis. Each step was preceded by washing using an automated washing station (BioPlex-MAGPIX, Biorad).

3.2.8. Statistical analysis

Statistical analysis was performed using one-way analysis of the variance (ANOVA) followed by Tuckey test in order to access the differences in the variance between the groups in the biological assays, using a significance level of $p < 0.05$.

3.3. Results and discussion

3.3.1. Surface characterization

Figure 3.1 shows the top surface of the MAO samples with a morphology that did not change through the studied conditions: a typical rough micro-porous network with volcano-like shape (also named as crater-like structure) resultant from the micro-discharges channels that occur during the MAO treatment [47]. It was observed that most of the holes were well separated and homogeneously distributed over the surface for all conditions. In this way, the incorporation of Sr was not influencing the morphology of the surface, either the pore size distribution or the average pore size (Figure 3.1). Sato *et al.* [42] also reported no significant effect of Sr concentrations in the morphology of MAO layers. The oxide layer presented a distribution of the pore size between 0.5 and 5 μm with an average size around 2 μm.
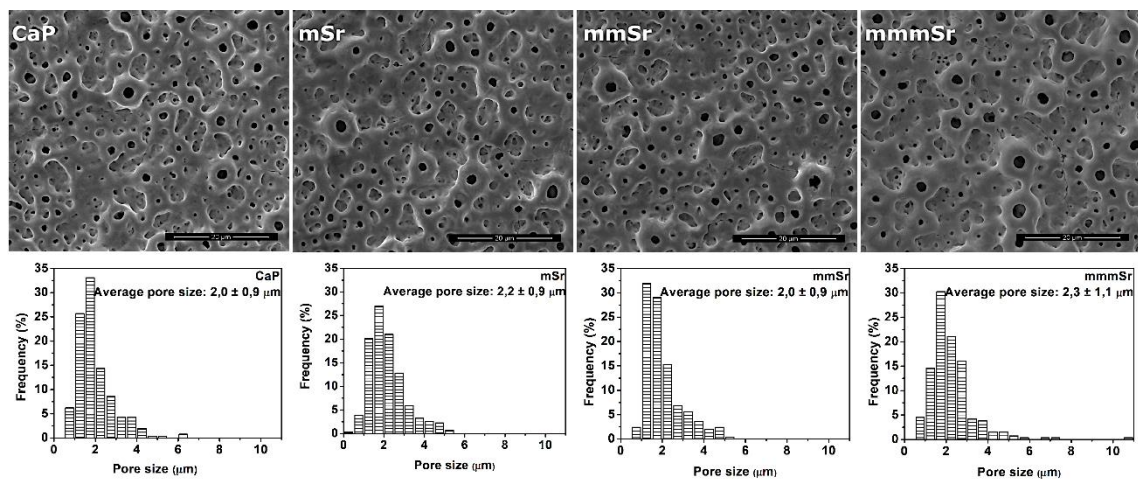
Figure 3.1. Representative SE-SEM images together with corresponding pore size distribution and average pore size for all conditions.

Supplementary video obtained by slice-and-view in a dual beam microscope shows a detailed look of the cross-section at the oxide layer produced by MAO treatment. Porosity along the cross-section showed interconnectivity between the pores along the oxide with some closed pores. Thickness of MAO layers was accessed by FIB cross-section cuts for all the groups under study and the mean value for thickness obtained was 4.7 ± 0.9 µm. The oxide layer presented the typical triplex structure composed by a compact and thin layer next to the bulk material, called barrier film, then an inner porous layer having small pores and an outer porous layer having bigger pores. A similar detailed cross-section was already presented by Alves *et al.* [46] and the authors stated that the barrier film was responsible for good corrosion protection. In this way, MAO treatments allow the formation of rough, porous titanium oxide layer with a wide range of pore size and distribution in the micro- and nano-scales, excellent conditions that influence bone cell behaviour [48].

During MAO treatments, high temperatures were reached promoting the localized melting of the oxide. In this way, bioactive elements present on the electrolyte were incorporated in the oxide layer during its formation [11]. Elements like Ti, O, Ca, P and especially Sr were detected in the elemental analysis by EDS, showing that the incorporation of Sr in the MAO layer was successful for the three conditions (Figure 3.2a). EDS confirmed the incorporation of Sr having an $_{at}$% content of 0.32 ± 0.03, 0.57 ± 0.04 and 2.66 ± 0.09 on mSr, mmSr and mmmSr groups, respectively. On the group with higher amount of Sr, Ca and P were incorporated less than in the other conditions, since Sr was highly available in the electrolyte. Despite that, Ca/P ratio obtained was above the one found in HAP (1.67) in all the conditions. Superior Ca/P ratio can be favourable since Ca presents a faster dissolution than P in physiologic solution, even though that dissolution is what promotes the formation of HAP [49–51]. Sr was distributed uniformly on the surface for all the conditions, as it can be observed in Figure 3.2a. According with Lu *et al.* [52], it is easier to incorporate Ca and Sr than P. The cationic elements as Ca^{2+} and Sr^{2+} in the electrolyte were more attracted to the cathode and repulsed from the anode during the MAO treatment because of the strong electric field. In fact, calcium acetate and strontium hydroxide were easily dissolved in the water and in this way, they combined with OH^- ions and moved towards the sparking areas incorporated in the oxide layer while the voltage increased.

X-ray diffraction patterns for all conditions are shown in Figure 3.2b. The major characteristic peaks presented corresponded to Ti and TiO_2 in the form of anatase and rutile. A large number of plasma discharges provided enough energy to reach temperatures to allow the formation of both metastable anatase and stable rutile [53]. The percentage of rutile phases were calculated by Equation (3.1) and the results obtained were 42 ± 3 for CaP, 40 ± 3 for mSr, 39 ± 3 for mmSr and 48 ± 2 for mmmSr. These results suggests that the condition with the highest level of Sr (mmmSr), led to an increase in the rutile phase. In fact, as it was shown in Table 3.1, the addition of Sr after a certain amount changed the conductivity of the electrolyte. It is known that the conductivity of the electrolyte influences the dielectric breakdown potential which may lead to differences in the oxide phases formed during MAO treatment. Hence, on mmmSr condition, the dielectric breakdown potential was probably reached sooner leading to higher temperatures for a longer period, facilitating the formation of more amount of rutile [53]. From literature, it is known that rutile is formed at higher temperatures and at higher voltages when compared with anatase [54,55]. Teng *et al.* [56] also reported the same trend in the MAO treatment where the relative intensity of the rutile peak increased with a higher amount of Sr. However, this phenomenon is dependent on the technique that is used to incorporate Sr. For instance, Xu *et al.* [38] incorporated Sr in TiO_2 by plasma spraying and stated that with the increased Sr amount in the coating, the relative amount of anatase increased, showing that Sr incorporation can suppress the anatase to rutile transformation.

The distribution of the oxide phases within the Sr-MAO-treated Ti oxide layers is not yet clarified. Previously, Ribeiro *et al.* [9] and Oliveira *et al.* [19] that produced MAO layers on Ti with similar processing parameters, including the Ca/P ratio stated that the oxide layer was a mixture of anatase and rutile phases where rutile was preferentially located on the top of the volcanoes-like structures, while the valleys of the oxide were mainly composed of anatase. In addition, wear and tribocorrosion resistance was also improved by the presence of rutile phases on the oxide layer [9,14,18–20].

XPS analysis was used to investigate the surface chemistry of the oxide layers formed by MAO in order to assess the effect of the Sr incorporation. The survey spectrum of the CaP specimen, presented in Figure 3.2c, revealed peaks associated with Ca 2s, Ti 3p, Ti 3s, P 2p, Sr 3d, P 2s, Sr 3p, C 1s, Ca 3p, Ti 2p, O 1s, O KLL, Ca LMM. The

addition of Sr resulted in a survey with peaks associated with the presence of Sr 3d and Sr 3p, confirming the incorporation of Sr into the oxide layer, as in accordance with the EDS analysis presented in Figure 3.2a. Figure 3.2c also shows the high-resolution spectra for P 2p and Sr 3d, Ti 2p and Ca 2p, regions, respectively, for CaP and mmmSr groups. P 2p envelope was fitted with two peaks. As presented, the binding energy found at 132.9 eV into the P 2p envelope reinforces that PO_4^{3-} groups were present on the surface of the different films [36,57–60]. On the mmmSr spectra, P 2p and Sr 3d peaks overlapped around 134/135 eV and the Sr $3d_{5/2}$ component detected at 133.8 eV might be assigned to strontium carbonate ($SrCO_3$) species, due to further oxidation of the metallic strontium with exposure to air [25,61]. In Figure 3.2c, high-energy resolution analysis of individual peaks for Ca 2p are presented, where the significant contributions at 347.0 and 346.8 eV for CaP and mmmSr groups could be attributed to the presence of $CaCO_3$ compounds, as well as Ca-O compounds [36,57–59,62]. It is also suggested that the minor Ca $2p_{3/2}$ contributions at 345.5 and 345.0 eV for CaP and mmmSr groups, respectively, corresponded to metallic Ca species [57,63]. As depicted in Figure 3.2c, four major peaks were fitted for each condition in the Ti 2p region, decomposing into two doublets, where the major one (represented by the Ti $2p_{3/2}$ peaks at 458.3 and 458.1 eV for CaP and mmmSr groups, respectively) corresponded to TiO_2 [57,58,64]. For CaP group, the Ti $2p_{3/2}$ peak found at 457.7 eV with a doublet separation of 5.2 eV may be associated with the Ti^{3+} valence state from Ti_2O_3 [57,58,64]. On the other hand, for the mmmSr group, the additional doublet with spin-orbit splitting of 5.7 eV could be related to the $SrTiO_3$ compound, which is identified by Ti $2p_{3/2}$ peak at 457.0 eV.
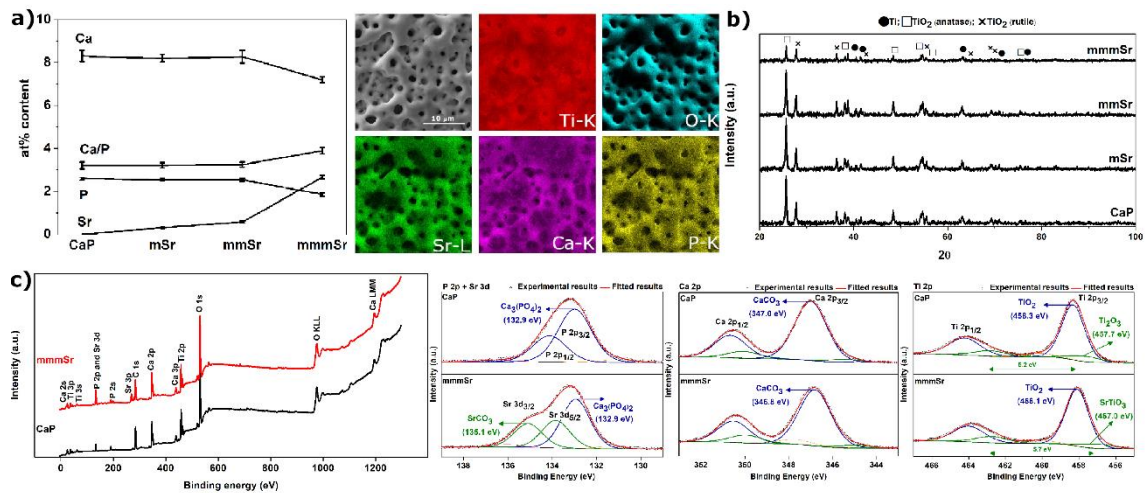
Figure 3.2. Surface characterization: a) elemental concentrations (_at_%) by EDS analysis for all conditions and SE-SEM and EDS mapping images (without overlay) for mmmSr group; b) crystal structure obtained by XRD analysis for all conditions; c) XPS spectra with the respective high-resolution spectra and respective deconvolution for P 2p and Sr 3d, Ca 2p and Ti 2p for CaP and mmmSr groups.

3.3.2. Biological assays

The behaviour of MG-63 osteoblast cells was evaluated in terms of cell adhesion, viability and mineralization. It is known from the literature that biological results are due to the combination of several physicochemical characteristics of the surfaces, hence, we suppose that the biological results are the combined action of Sr within the coating as well as the Sr leached, together with oxide morphology, chemical composition and crystal structure. Figure 3.3a presents the initial cell adhesion area (4 h after seeding) where no significant differences between all the conditions were observed. However, after 24 h, a statistically significant difference in the cell adhesion area was observed between mSr and mmmSr. Figure 3.3b shows the fluorescence microscope images after 24 h of cell adhesion, where it was possible to see a significant enhancement of cell adhesion and spreading only for CaP and mSr groups. Cells presented an organised actin cytoskeleton with a spindle morphology. Hence, these results showed that higher amount of Sr (mmmSr) may have a detrimental effect on cell adhesion after 24 h (Figure 3.3a). This poor cell adhesion may be due to the combined action of chemical composition (higher quantity of Sr) and different quantities of crystal structures (higher amount of rutile in mmmSr) on the oxide layer. He _et al._ [65] showed that the crystal structure influence osteoblastic cells grown, with osteoblasts presenting the largest

69

spreading on the anatase phase, behaviour that was not observed in the rutile phases structures. In this way, probably the poor osteoblast adhesion on mmmSr may be due to the combined action of higher amount of Sr and rutile phase that can possibly compromise cell adhesion. Ribeiro *et al.* [9] previously reported the interface osteoblast–CaP cross-section after 2 h of osteoblast adhesion and showed that cells are well adhered to the surface when the amorphous nanometric film rich in Ca and P is present, but not when the surface is made of a mixture of rutile and amorphous phases. The authors presented a TEM image of the cross-section showing that the inner part of the oxide was composed of a mixture of crystalline and amorphous structures, while the top of the oxide was mainly composed of an amorphous phase rich in Ca and P that enter in direct contact with cells stimulating their adhesion [19].

Osteoblastic-like cells adhered to the oxide layers were viable, indicating that although higher concentrations of Sr compromise cell adhesion their viability was not disturbed (see Figure 3.3c–d). These results are consistent with the literature where no appreciable Sr effects on pre-osteoblastic [43] and mesenchymal stem [66] cells cytotoxicity were reported. MAO surfaces are extremely porous and rough which can mislead the cell density on different fields due to the peculiarity ridges and valleys present on the surfaces.
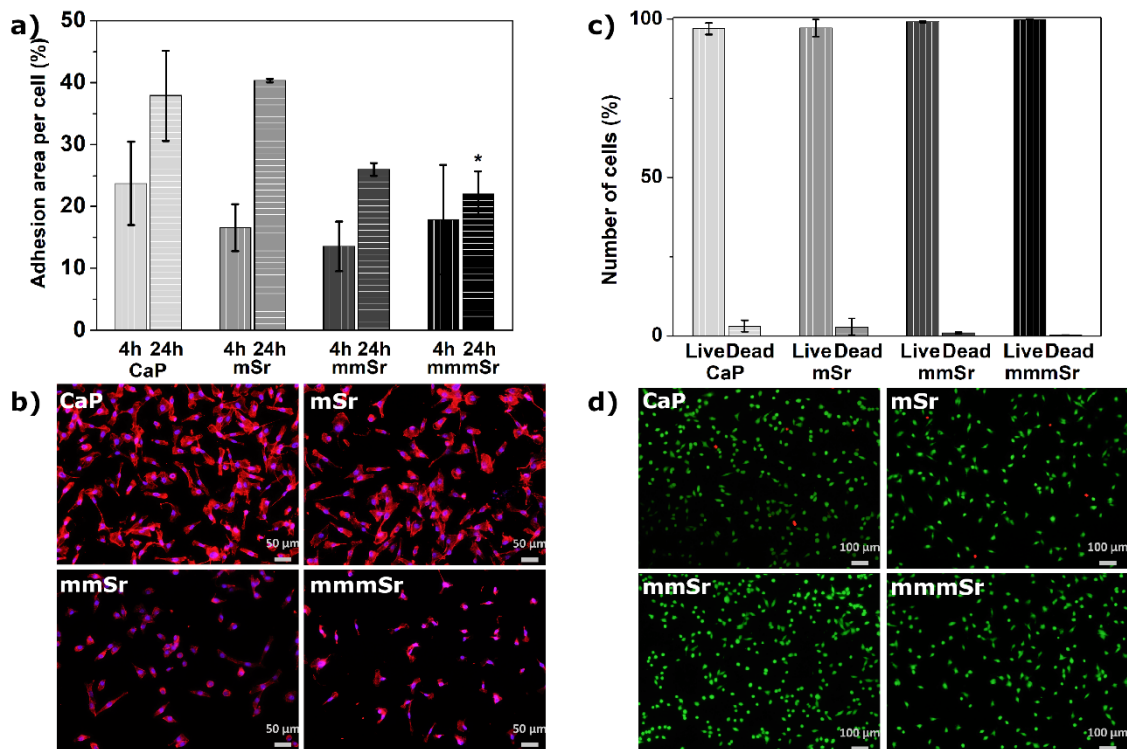
Figure 3.3. a) Adhesion area (%) of MG-63 cells cultured for 4 and 24 hours (* p<0.05 indicates a significant difference compared with the mSr 24 hours) and **b)** fluorescence images of MG-63 cells cultured after 24 h with F-actin stained with phalloidin in red and the cell nuclei stained with DAPI in blue; **c)** Number of live and dead cells (%) and **d)** fluorescence images of LIVE/DEAD® staining of MG-63 cells after 24 h of incubation.

Osteoblast morphology was examined by SEM after 4 h, 24 h and 21 days of culture (Figure 3.4). No significant differences were seen in cell morphologies between all the conditions and between the studied time-points. According to the results presented in Figure 3.4c and d, osteoblasts on Ca-P-Sr TiO$_2$ porous layer were well attached to their surfaces. It was also possible to see osteoblasts spreading on the surface, with extended filopodia covering the porous oxide surface, attached to the edges of the pores, penetrating and crossing the pores (see Figure 3.4a–f after 4 and 24 h). After 21 days, osteoblasts continued to be well adhered to the oxide layer and it was possible to observe a thin lamellipodia on the top of some parts of the oxide layer, with cell processes extending over other neighbouring cells indicated the formation of cell monolayer (Figure 3.4g). No differences were obtained in the cell morphology between all the conditions after 21 days of incubation. On the other hand, superficial and cross-sectional observations of the cell–oxide layer interface revealed osteoblasts penetration in the pores, as illustrated on Figure 3.4i.
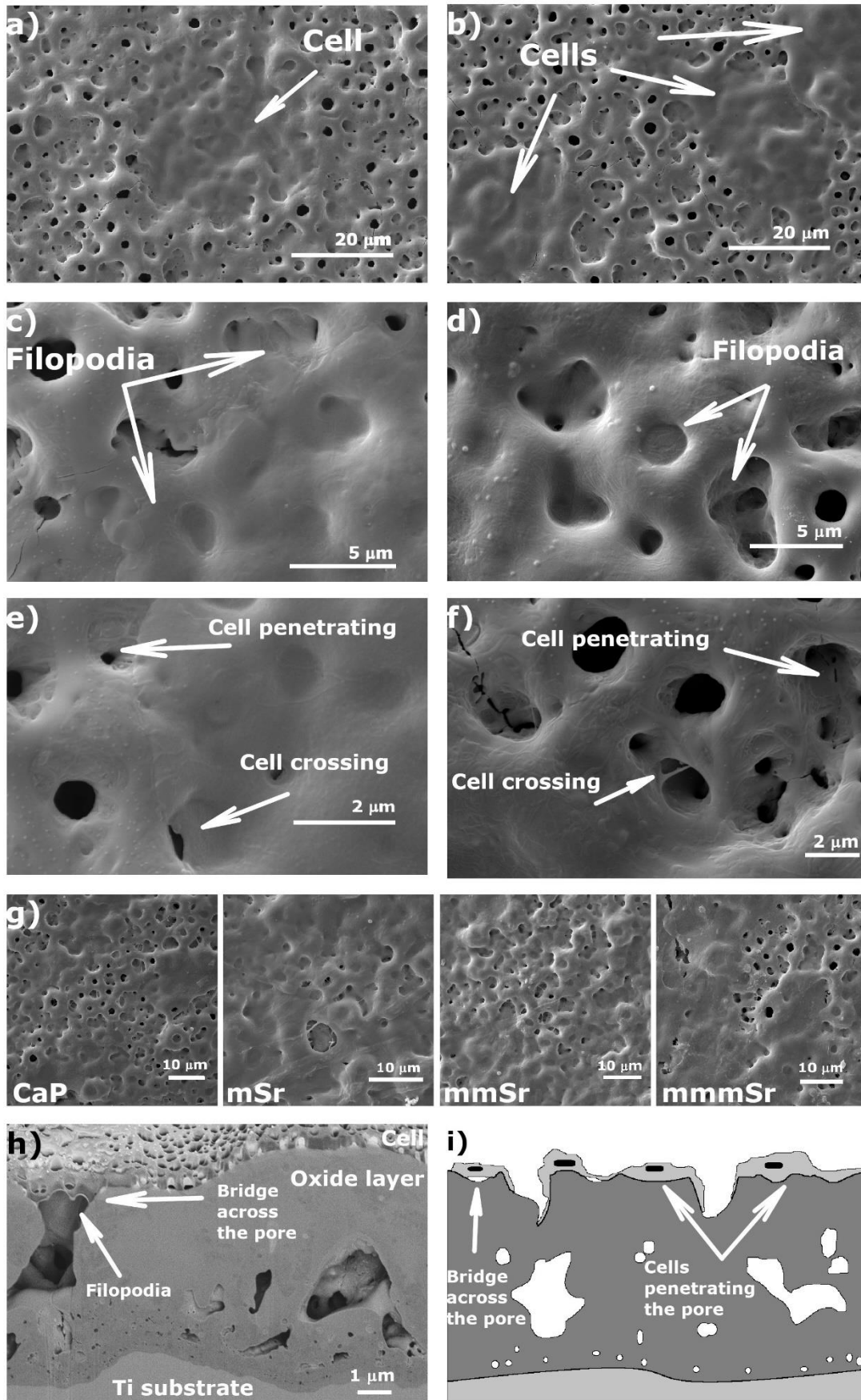
Figure 3.4. SE-SEM images presenting cell morphology after a, c and e) 4 h of seeding and b), d) and f) 24 h of seeding; g) SE-SEM images presenting cell morphology after 21 days of culture; h) SE-SEM image of the cross-section of the oxide layer with a cell on top 24 h after seeding; i) illustration of the interface between cells and the oxide layer [Figures a, c, e, f and h are from mmmSr condition, b from mSr condition and d from mmSr condition. No significant differences were seen in cell adhesion morphologies by SEM analysis between the studied conditions and time-points].

Bone is a living organ maintained by living cells such as osteoblasts, osteoclasts, osteocytes, among others. It is composed by an inorganic component that is predominantly hydroxyapatite ($Ca_5(PO_4)_3(OH)$), together with an organic matrix of type I collagen and small quantities of osteonectin and osteocalcin that promote bone regeneration [67–70]. Bone mineralization is the result of complex biological processes in which deposition of inorganic salts is induced by a template of collagen type I network. Collagen provides the template for mineral deposition, where the size and the organization of the collagen fibrils determine the dimensions that mineral crystals can attain [67–70]. Figure 3.5a presents the fluorescence microscope images of MG-63 cells cultured after 21 days (stained with DAPI for nucleus, phalloidin for actin and collagen type I for collagen secretion) where it was possible to observe the presence of collagen network in all conditions. Figure 3.5b shows the results of the semi-quantitative analysis of collagen deposition, where a statistically significant increase on collagen secretion was observed in mmSr and mmmSr conditions compared with the control group. Previous studies using Sr for other applications showed that Sr was promoting the collagen secretion [71]. Naruphontjirakul *et al.* [71] evaluated the biological behaviour of human stem cells on bioactive glass and the biological effect of Sr ions released. The presence of Sr-bioactive glass induced a higher amount of mature extracellular matrix formation and expression of proteins associated with collagen production.

Alizarin red-s was used to stain matrix calcium phosphates deposits and results presented in Figure 3.5c. As it is possible to observe a clear statistically significant decrease in the amount of calcium deposits was observed for the mmmSr group. It is possible that the combined action of higher content of Sr with rutile phase, can be what is delaying the mineralization process. Previously, Verberckmoes *et al.* [72] showed a multiphasic interference of Sr ions with osteoblast cells mineralization. Particularly, it was shown by the authors that a Sr dose between 2–5 ppm was promoting cell

mineralization, while a Sr dose between 20–100 ppm showed the opposite effect. Studies [39,73,74] indicated that Sr ions can activate signalling pathways particularly, through a calcium-sensing receptor, stimulating or inhibit cell mineralization. On the other hand, Xu *et al.* [38] showed that higher amount of Sr presented an adverse effect on the osteogenic function of bone marrow mesenchymal stem cells and reported that more amount of rutile might be influencing their mineralization.

Interestingly, the group with a higher amount of Sr showed higher secretion of collagen matrix despite the decrease in mineralization processes. Mineralization of calcium phosphates in bone has been proposed to proceed through an initial collagen secretion and deposition of the mineralized matrix via amorphous precursor phase which transforms into nanocrystalline hydroxyapatite [75–77]. Possibly, the higher amount of Sr can be delaying the mineralization process. Another possibility is that the surface with a higher amount of Sr is inducing a mineralization process with a deficient HAP structure and/or an amorphous precipitate as stated by Verberckmoes *et al.* [78]. The authors showed that low Sr amount did not affect either HAP crystal solubility or mineralization. On the contrary, when the Sr content increased, a physicochemical interference of Sr in the HAP formation was observed resulting in defective mineralization. The authors presented an XRD of the deposited mineral that revealed a diffuse pattern, characteristic for a non-crystalline (amorphous) HAP precipitate [78].
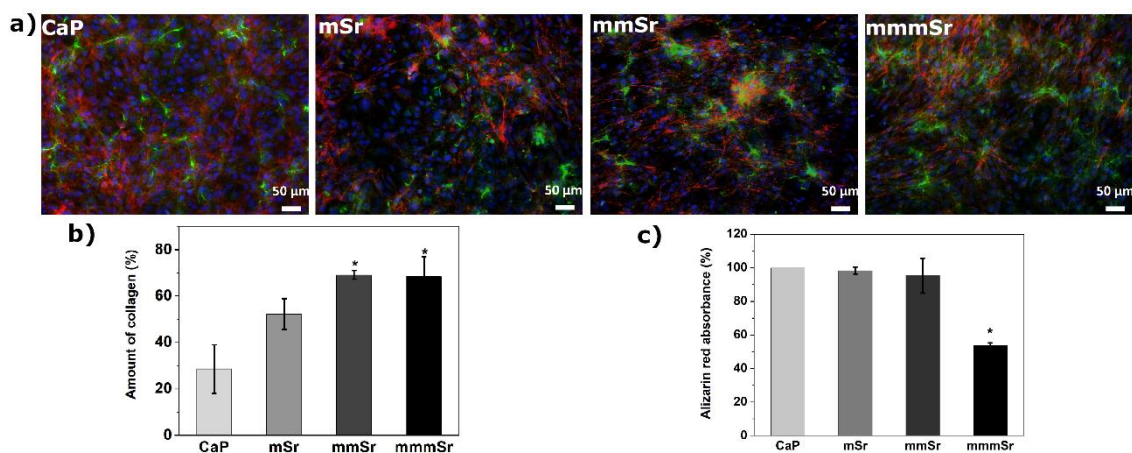
Figure 3.5. a) Fluorescence images of MG-63 cells cultured after 21 days with F-actin stained with phalloidin in red, the cell nuclei stained with DAPI in blue and collagen stained in green and b) amount of collagen (%) of MG-63 cells cultured for 21 days (* p<0.05 indicates a significant difference compared with the CaP); c) quantitative mineralization results of alizarin red-s absorbance (%) after 21 days of incubation (* p<0.05 indicates a significant difference compared with the CaP, mSr and mmmSr).

The mineralization and differentiation of osteoblasts are processes regulated by complex interactions among different molecules like hormones, cytokines and local growth factors, among others. The cytokines secretion plays a crucial role in bone remodelling since these factors appear to have crucial roles in both normal and pathologic bone cell functions [79,80]. The amount of the cytokines, chemokines and growth factors were quantified in the supernatant after 21 days of cell culture and results are presented in Figure 3.6. Although almost 30 soluble secreted mediators were quantified, it was only observed significant differences in interleukin-1 receptor antagonist (IL-1Ra), granulocyte colony-stimulating factor (G-CSF) and IL-15 cytokines.

Comparing with CaP control surfaces, mSr and mmmSr groups promoted reduced secretion levels of IL-1Ra, whereas mmSr increased its levels. IL-1Ra is a member of the IL-1 family involved in modulation of immune and inflammatory responses. In specific events where IL-1β levels are increased in the microenvironment, the reduction of IL-1Ra levels leads to a greater IL-1β ability that activates its signalling cascades and induces inflammation [81–83]. Indeed, increased levels of IL-1Ra have been associated with the inhibition of bone formation *in vivo* [84]. In this sense, our data suggested that mmSr possibly induce inhibition of bone formation and that mSr and mmmSr could turn the microenvironment more susceptible to inflammation. However, in a complex system, several secreted proteins are able to promote a balance in order to maintain homeostasis.

Lower amount of Sr (mSr) on the oxide layer seemed to induce the secretion of higher levels of G-CSF, whereas higher amount of Sr (mmSr and mmmSr) do not alter G-CSF levels, being comparable to control group CaP. G-CSF is considered an endogenous hematopoietic growth factor that induces proliferation, differentiation and release of neutrophils from bone marrow [85]. Despite these relevant effects, overexpression of G-CSF may also lead to bone resorption in mice [86]. Resuming mSr induced the secretion of G-CSF that is an important growth factor that stimulates the bone marrow to produce stem cells and releases them into the bloodstream stimulating osteogenesis [87].

Regarding the cytokine IL-15, mmSr promotes its increase in secretion, but not mSr and mmmSr. IL-15 is widely known for its role in osteoclast differentiation [80] and

consequent osteoclastogenesis [79,86]. Possibly the reduced secretion of this cytokine for mSr and mmmSr indicates that these surfaces inhibit osteoclastogenesis.

All the surfaces induced osteoblasts to secrete vascular endothelial growth factor (VEGF) and interferon gamma (IFN-γ) since no significant differences were observed when comparing to CaP. VEGF, a potent mediator of angiogenesis displaying an important role in bone development and regeneration [70,88], and IFN-γ, that presents variable effects on many immunological functions as well as in inflammation, seemed to have a similar secretion pattern between groups. In bone, studies showed that IFN-γ plays an important role in bone homeostasis and increases alkaline phosphatase activity in osteoblast-like cells. However, it also plays important roles in osteoclastogenesis [89]. So, depending on the circumstances, IFN-γ may contribute to a reduce inflammation but may also promote bone resorption and formation [9,80,85,86,90].

Resuming, mSr and mmmSr induced the secretion of lower levels of IL-1Ra, with mSr inducing G-CSF secretion. In addition, mmSr induced increased levels of IL-1Ra and seemed to increase IL-15 secretion. It is important to disclose that increased levels of a secreted protein in mSr experimental group do not mean that mmSr or mmmSr (or vice-versa) would result in its increased levels in a concentration dependent manner. Eukaryotic cells display different mechanisms for maintaining their microenvironment balance. Then, it is common that the challenged cells respond, altering the levels of many secreted proteins and activating or deactivating intracellular signalling pathways, always searching for survival and homeostasis. It is conceivable that it was occurring in this study. Taken together, our data suggested that although mSr surfaces possibly secrete cytokines involved in inflamation, they also secrete growth factors that contribute to osteogenesis and other cytokines that inhibit osteoclast formation and consequent bone resorption.
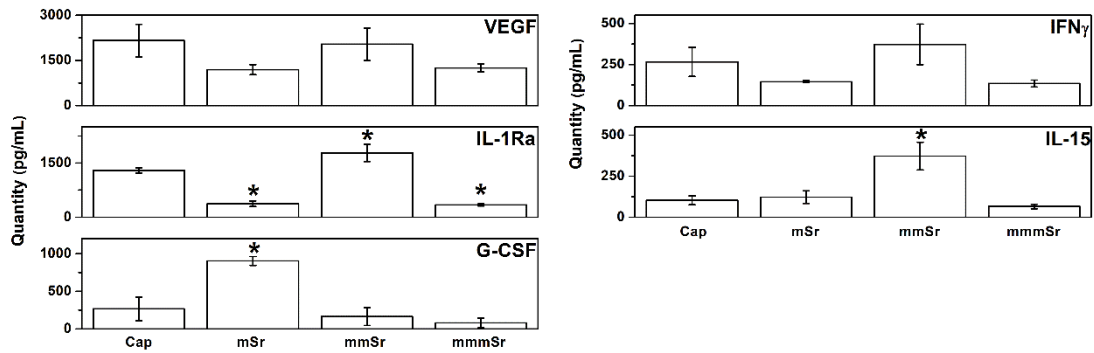
Figure 3.6. VEGF, IL-1Ra, G-CSF, IFN-γ and IL-15 cytokines secreted by osteoblasts after 21 days of incubation (* p<0.05 indicates a significant difference compared with the CaP).

This work gives an insight into the effect of Sr amount in the oxide layer on osteoblast culture. It is shown that the presence of Sr, with a dose-depending effect, influences the behaviour of osteoblast adhesion, mineralization and cytokines released. Sr is a unique element showing promising results in its dual action in the bone cells, osteoblasts and osteoclasts. So, as future work, the effect of Sr amount on osteoclast behaviour should be evaluated. The real magnitude of the effect of Sr amount cannot be easily evaluated and there may be some synergistic relationships coming into account, mainly between osteoblast and osteoclast independent and dependent responses. The optimal material that will promote the enhancement of bone formation osseointegration as well as a reduction of bone resorption should be a result of the synergistic effect exerted by the hierarchical surface topography (micro- and nano-porous), chemical composition (TiO_2 with Ca-P-Sr) and crystal structure (anatase + rutile) together, and as it was studied and presented, the amount of Sr can be in the range of mSr and mmSr groups.

3.4. Conclusion

This study has outlined the effect of the Sr amount in porous Ca- and P-rich TiO_2 layers processed by MAO, evaluated in terms of surface characteristics and *in vitro* biological response. Incorporation of Sr did not affect the pore size and morphology in the TiO_2 layer, although, changed the chemical composition and the oxide crystal

structure. Cell viability was not compromised, however, the combination of higher amount of Sr with the higher amount of rutile impaired osteoblast adhesion, induced collagen secretion and mineralization compromised. Possibly Sr is delaying the mineralization process or inducing the formation of a deficient HAP structure. More studies are necessary to clarify these phenomena however we can conclude that lower amount of Sr presented an overall good biological outcome which is likely to be a beneficial surface to be used as implants and other bone regeneration applications.

Acknowledgments

References

[1]   OECD, Health at a Glance 2017: OECD Indicators, Paris, 2017.

[2]   R.J. Ferguson, A.J. Palmer, A. Taylor, M.L. Porter, H. Malchau, S. Glyn-Jones, Hip and knee replacement 1 - Hip replacement, Lancet. 392 (2018) 1662–1671.

[3]   J.T. Evans, J.P. Evans, R.W. Walker, A.W. Blom, M.R. Whitehouse, A. Sayers, How long does a hip replacement last? A systematic review and meta-analysis of case series and national registry reports with more than 15 years of follow-up, Lancet. 393 (2019) 647–654.

[4]   M. Bruschi, D. Steinmüller-Nethl, W. Goriwoda, M. Rasse, Composition and Modifications of Dental Implant Surfaces, J. Oral Implant. (2015) 1–14.

[5]   M. Geetha, A.K. Singh, R. Asokamani, A.K. Gogia, Ti based biomaterials, the ultimate choice for orthopaedic implants – A review, Prog. Mater. Sci. 54 (2009) 397–425.

[6]   H.J. Rack, J.I. Qazi, Titanium alloys for biomedical applications, Mater. Sci. Eng. C. 26 (2006) 1269–1277.

[7]   A.C. Alves, R. Thibeaux, F. Toptan, A.M.P. Pinto, P. Ponthiaux, B. David, Influence of macroporosity on NIH/3T3 adhesion, proliferation, and osteogenic differentiation of MC3T3-E1 over bio-functionalized highly porous titanium implant material, J. Biomed. Mater. Res. - Part B Appl. Biomater. 107 (2019) 73–85.

[8]   L. Xu, K. Zhang, C. Wu, X. Lei, J. Ding, X. Shi, C. Liu, Micro-Arc Oxidation Enhances the Blood Compatibility of Ultrafine-Grained Pure Titanium, Materials (Basel). 10 (2017) 1446.

[9]   A.R. Ribeiro, F. Oliveira, L.C. Boldrini, P.E. Leite, P. Falagan-Lotsch, A.B.R. Linhares, W.F. Zambuzzi, B. Fragneaud, A.P.C. Campos, C.P. Gouvêa, B.S. Archanjo, C.A. Achete, E. Marcantonio, L.A. Rocha, J.M. Granjeiro, Micro-arc oxidation as a tool to develop multifunctional calcium-rich surfaces for dental implant applications, Mater. Sci. Eng. C. 54 (2015) 196–206.

[10]   Y. Wang, H. Yu, C. Chen, Z. Zhao, Review of the biocompatibility of micro-arc oxidation coated titanium alloys, Mater. Des. 85 (2015) 640–652.

[11]   I.S. Park, T.G. Woo, W.Y. Jeon, H.H. Park, M.H. Lee, T.S. Bae, K.W. Seol, Surface characteristics of titanium anodized in the four different types of electrolyte, Electrochim. Acta. 53 (2007) 863–870.

[12]   M.D. Roach, R.S. Williamson, I.P. Blakely, L.M. Didier, Tuning anatase and rutile phase ratios and nanoscale surface features by anodization processing onto titanium substrate surfaces, Mater. Sci. Eng. C. 58 (2016) 213–223.

[13]   D. Velten, V. Biehl, F. Aubertin, B. Valeske, W. Possart, J. Breme, Preparation of TiO2 layers on cp-Ti and Ti6Al4V by thermal and anodic oxidation and by sol-gel coating techniques and their characterization, J Biomed Mater Res. 59 (2002) 18–28.

[14]   M. Fazel, H.R. Salimijazi, M.A. Golozar, M.R. Garsivaz jazi, A comparison of corrosion, tribocorrosion and electrochemical impedance properties of pure Ti and Ti6Al4V alloy treated by micro-arc oxidation process, Appl. Surf. Sci. 324 (2015) 751–756.

[15]   D. Quintero, O. Galvis, J.A. Calderón, J.G. Castaño, F. Echeverría, Control of the physical properties of anodic coatings obtained by plasma electrolytic oxidation on Ti6Al4V alloy, Surf. Coatings Technol. 283 (2015) 210–222.

[16]   L. Benea, E. Mardare-Danaila, M. Mardare, J.-P. Celis, Preparation of titanium oxide and hydroxyapatite on Ti–6Al–4V alloy surface and electrochemical behaviour in bio-simulated fluid solution, Corros. Sci. 80 (2014) 331–338.

[17]   F. Toptan, A.C. Alves, A.M.P. Pinto, P. Ponthiaux, Tribocorrosion behavior of bio-functionalized highly porous titanium, J. Mech. Behav. Biomed. Mater. 69 (2017) 144–152.

[18]   A.C. Alves, F. Oliveira, F. Wenger, P. Ponthiaux, J.-P. Celis, L.A. Rocha, Tribocorrosion behaviour of anodic treated titanium surfaces intended for dental implants, J. Phys. D. Appl. Phys. 46 (2013) 404001.

80

[19]   F.G. Oliveira, A.R. Ribeiro, G. Perez, B.S. Archanjo, C.P. Gouvea, J.R. Araújo, A.P.C. Campos, A. Kuznetsov, C.M. Almeida, M.M. Maru, C.A. Achete, P. Ponthiaux, J.-P. Celis, L.A. Rocha, Understanding growth mechanisms and tribocorrosion behaviour of porous TiO2 anodic films containing calcium, phosphorous and magnesium, Appl. Surf. Sci. 341 (2015) 1–12.

[20]   I. da S.V. Marques, M.F. Alfaro, N.C. da Cruz, M.F. Mesquita, C. Sukotjo, M.T. Mathew, V.A.R. Barão, Tribocorrosion behavior of biofunctional titanium oxide films produced by micro-arc oxidation: Synergism and mechanisms, J. Mech. Behav. Biomed. Mater. 60 (2016) 8–21.

[21]   L. Benea, E. Danaila, P. Ponthiaux, Effect of titania anodic formation and hydroxyapatite electrodeposition on electrochemical behaviour of Ti-6Al-4V alloy under fretting conditions for biomedical applications, Corros. Sci. 91 (2015) 262–271.

[22]   Z.S. Tao, W.S. Zhou, X.W. He, W. Liu, B.L. Bai, Q. Zhou, Z.L. Huang, K.K. Tu, H. Li, T. Sun, Y.X. Lv, W. Cui, L. Yang, A comparative study of zinc, magnesium, strontium-incorporated hydroxyapatite-coated titanium implants for osseointegration of osteopenic rats, Mater. Sci. Eng. C. 62 (2016) 226–232.

[23]   J. Zhou, L. Zhao, Multifunction Sr, Co and F co-doped microporous coating on titanium of antibacterial, angiogenic and osteogenic activities, Acta Biomater. 43 (2016) 358–368.

[24]   K.C. Kung, T.M. Lee, T.S. Lui, Bioactivity and corrosion properties of novel coatings containing strontium by micro-arc oxidation, J. Alloys Compd. 508 (2010) 384–390.

[25]   W. Zhang, H. Cao, X. Zhang, G. Li, Q. Chang, J. Zhao, Y. Qiao, X. Ding, G. Yang, X. Liu, X. Jiang, A strontium-incorporated nanoporous titanium implant surface for rapid osseointegration, Nanoscale. 8 (2016) 5291–5301.

[26]   W. Liu, M. Cheng, T. Wahafu, Y. Zhao, H. Qin, J. Wang, X. Zhang, L. Wang, The in vitro and in vivo performance of a strontium-containing coating on the low-modulus Ti35Nb2Ta3Zr alloy formed by micro-arc oxidation, J. Mater. Sci. Mater. Med. 26 (2015) 203.

[27]   X. Lin, X. Yang, L. Tan, M. Li, X. Wang, Y. Zhang, K. Yang, Z. Hu, J. Qiu, In vitro degradation and biocompatibility of a strontium-containing micro-arc oxidation coating on the biodegradable ZK60 magnesium alloy, Appl. Surf. Sci. 288 (2014) 718–726.

[28]   M. Pilmane, K. Salma-Ancane, D. Loca, J. Locs, L. Berzina-Cimdina, Strontium and strontium ranelate: Historical review of some of their functions, Mater. Sci. Eng. C. 78 (2017) 1222–1230.

[29]   K.C. Kung, T.M. Lee, J.L. Chen, T.S. Lui, Characteristics and biological responses of novel coatings containing strontium by micro-arc oxidation, Surf. Coatings Technol. 205 (2010) 1714–1722.

[30]   G. Boivin, P. Deloffre, B. Perrat, G. Panczer, M. Boudeulle, Y. Tsouderos, P.J. Meunier, Strontium distribution and interreactions with bone mineral in male monkey iliac bone after strontium salt (S 12911) administration, Osteoporos. Int. 6 (1996) 251–251.

[31]   C. Chung, H. Long, Systematic strontium substitution in hydroxyapatite coatings on titanium via micro-arc treatment and their osteoblast/osteoclast responses, Acta Biomater. 7 (2011) 4081–4087.

[32]   L. Yin, J. Zhou, L. Gao, C. Zhao, J. Chen, X. Lu, J. Wang, J. Weng, B. Feng, Characterization and osteogenic activity of SrTiO3/TiO2 nanotube heterostructures on microporous titanium, Surf. Coat. Technol. 330 (2017) 121–130.

[33]   Q. Zhao, L. Yi, L. Jiang, Y. Ma, H. Lin, J. Dong, Surface functionalization of titanium with zinc/strontium-doped titanium dioxide microporous coating via microarc oxidation, Nanomedicine NBM. 16 (2019) 149–161.

[34]   M. Khodaei, A. Valanezhad, I. Watanabe, Controlled gentamicin- strontium release as a dual action bone agent: Combination of the porous titanium scaffold and biodegradable polymers, J. Alloys Compd. 720 (2017) 22–28.

[35]   J. Yan, J.F. Sun, P.K. Chu, Y. Han, Y.M. Zhang, Bone integration capability of a series of strontium-containing hydroxyapatite coatings formed by micro-arc oxidation, J. Biomed. Mater. Res. - Part A. 101 A (2013) 2465–2480.

[36]   J. Wen, J. Li, H. Pan, W. Zhang, D. Zeng, L. Xu, Q. Wu, X. Zhang, X. Liu, X. Jiang, Strontium delivery on topographical titanium to enhance bioactivity and osseointegration in osteoporotic rats, J. Mater. Chem. B. 3 (2015) 4790–4804.

[37]   D. Bellucci, V. Cannillo, A. Anesi, R. Salvatori, L. Chiarini, T. Manfredini, D. Zaffe, Bone Regeneration by Novel Bioactive Glasses Containing Strontium and/or Magnesium: A Preliminary In-Vivo Study, Materials (Basel). 11 (2018) 2223.

[38]   Z. Xu, H. Lu, J. Lu, C. Lv, X. Zhao, G. Wang, Enhanced osteogenic activity of Ti alloy

implants by modulating strontium configuration in their surface oxide layers, RSC Adv. 8 (2018) 3051–3060.

[39]   P.J. Marie, P. Ammann, G. Boivin, C. Rey, Mechanisms of action and therapeutic potential of strontium in bone, Calcif. Tissue Int. 69 (2001) 121–129.

[40]   J.-W. Park, Increased bone apposition on a titanium oxide surface incorporating phosphate and strontium, Clin. Oral Impl. Res. 22 (2011) 230–234.

[41]   Z. Zhang, Osteoblastic cell adhesion on Strontium- incorporated porous nanostructured TiO2 coating prepared by micro-arc oxidation, J. Clin. Exp. Orthop. 1 (2015) 1–7.

[42]   M. Sato, P. Chen, Y. Tsutsumi, M. Shiota, T. Hanawa, S. Kasugai, Effect of strontium ions on calcification of preosteoblasts cultured on porous calcium- and phosphate-containing titanium oxide layers formed by micro-arc oxidation, Dent. Mater. J. 35 (2016) 627–634.

[43]   X. He, X. Zhang, L. Bai, R. Hang, X. Huang, L. Qin, X. Yao, B. Tang, Antibacterial ability and osteogenic activity of porous Sr/Ag-containing TiO2 coatings, Biomed. Mater. 11 (2016) 045008.

[44]   K.-C. Kung, K. Yuan, T.-M. Lee, T.-S. Lui, Effect of heat treatment on microstructures and mechanical behavior of porous Sr–Ca–P coatings on titanium, J. Alloys Compd. 515 (2012) 68–73.

[45]   H. Xie, Z. Gu, Y. He, J. Xu, C. Xu, L. Li, Q. Ye, Microenvironment construction of strontium-calcium-based biomaterials for bone tissue regeneration: The equilibrium effect of calcium to strontium, J. Mater. Chem. B. 6 (2018) 2332–2339.

[46]   A.C. Alves, F. Wenger, P. Ponthiaux, J.-P. Celis, A.M. Pinto, L.A. Rocha, J.C.S. Fernandes, Corrosion mechanisms in titanium oxide-based films produced by anodic treatment, Electrochim. Acta. 234 (2017) 16–27.

[47]   A.E.R. Friedemann, T.M. Gesing, P. Plagemann, Electrochemical rutile and anatase formation on PEO surfaces, Surf. Coatings Technol. 315 (2017) 139–149.

[48]   J.I. Rosales-Leal, M.A. Rodríguez-Valverde, G. Mazzaglia, P.J. Ramón-Torregrosa, L. Díaz-Rodríguez, O. García-Martínez, M. Vallecillo-Capilla, C. Ruiz, M.A. Cabrerizo-Vílchez, Effect of roughness, wettability and morphology of engineered titanium surfaces on osteoblast-like cell adhesion, Colloids Surfaces A Physicochem. Eng. Asp. 365 (2010) 222–229.

[49]   O. Banakh, T. Journot, P.A. Gay, J. Matthey, C. Csefalvay, O. Kalinichenko, O. Sereda, M. Moussa, S. Durual, L. Snizhko, Synthesis by anodic-spark deposition of Ca- and P- containing films on pure titanium and their biological response, Appl. Surf. Sci. 378 (2016) 207–215.

[50]   L. Wang, G.H. Nancollas, Calcium Orthophosphates: Crystallization and Dissolution, Chem. Rev. 108 (2008) 4628–4669.

[51]   S. Kim, H. Ryu, H. Shin, H.S. Jung, K.S. Hong, In situ observation of hydroxyapatite nanocrystal formation from amorphous calcium phosphate in calcium-rich solutions, Mater. Chem. Phys. 91 (2005) 500–506.

[52]   Y. Lu, P. Wan, L. Tan, B. Zhang, K. Yang, J. Lin, Preliminary study on a bioactive Sr containing Ca-P coating on pure magnesium by a two-step procedure, Surf. Coat. Technol. 252 (2014) 79–86.

[53]   G. Mortazavi, J. Jiang, E.I. Meletis, Investigation of the plasma electrolytic oxidation mechanism of titanium, Appl. Surf. Sci. 488 (2019) 370–382.

[54]   D.A.H. Hanaor, C.C. Sorrell, Review of the anatase to rutile phase transformation, J. Mater. Sci. 46 (2011) 855–874.

[55]   N. Wetchakun, S. Phanichphant, Effect of temperature on the degree of anatase-rutile transformation in titanium dioxide nanoparticles synthesized by the modified sol-gel method, Curr. Appl. Phys. 8 (2008) 343–346.

[56]   H. Teng, H. Lin, Y. Huang, F. Lu, Formation of strontium-substituted hydroxyapatite coatings on bulk Ti and TiN-coated substrates by plasma electrolytic oxidation, Surf. Coat. Technol. (2018).

[57]   L.P. Qiao, J. Lou, S.F. Zhang, B. Qu, W.H. Chang, R.F. Zhang, The entrance mechanism of calcium and phosphorus elements into micro arc oxidation coatings developed on Ti6Al4V alloy, Surf. Coatings Technol. 285 (2016) 187–196.

[58]   S.A. Alves, A.R. Ribeiro, S. Gemini-Piperni, R.C. Silva, A.M. Saraiva, P.E. Leite, G. Perez, S.M. Oliveira, J.R. Araujo, B.S. Archanjo, M.E. Rodrigues, M. Henriques, J.P. Celis, T. Shokuhfar, R. Borojevic, J.M. Granjeiro, L.A. Rocha, TiO2 nanotubes enriched with calcium, phosphorous and zinc: Promising bio-selective functional surfaces for osseointegrated titanium implants, RSC Adv. 7 (2017) 49720–49738.

[59]   G.C. Gomes, F.F. Borghi, R.O. Ospina, E.O. López, F.O. Borges, A. Mello, Nd:YAG (532 nm) pulsed laser deposition produces crystalline hydroxyapatite thin coatings at

84

room temperature, Surf. Coatings Technol. 329 (2017) 174–183.

[60]   E.O. López, A. Mello, M. Farina, A.M. Rossi, A.L. Rossi, Nanoscale analysis of calcium phosphate films obtained by RF magnetron sputtering during the initial stages of deposition, Surf. Coatings Technol. 279 (2015) 16–24.

[61]   Y. Huang, X. Zhang, H. Zhang, H. Qiao, X. Zhang, T. Jia, S. Han, Y. Gao, H. Xiao, H. Yang, Fabrication of silver- and strontium-doped hydroxyapatite/TiO2 nanotube bilayer coatings for enhancing bactericidal effect and osteoinductivity, Ceram. Int. 43 (2017) 992–1007.

[62]   Q. Liu, J. Li, Z. Zhou, J. Xie, J.Y. Lee, Hydrophilic Mineral Coating of Membrane Substrate for Reducing Internal Concentration Polarization (ICP) in Forward Osmosis, Sci. Rep. 6 (2016) 1–10.

[63]   S. Yamaguchi, S. Nath, T. Matsushita, T. Kokubo, Controlled release of strontium ions from a bioactive Ti metal with a Ca-enriched surface layer, Acta Biomater. 10 (2014) 2282–2289.

[64]   M.C. Biesinger, B.P. Payne, A.P. Grosvenor, L.W.M. Lau, A.R. Gerson, R.S.C. Smart, Resolving surface chemical states in XPS analysis of first row transition metals, oxides and hydroxides: Cr, Mn, Fe, Co and Ni, Appl. Surf. Sci. 257 (2011) 2717–2730.

[65]   J. He, E. Zhou, X. Zhou, X. Zhong, X. Zhang, P. Wan, B. Zhu, W. Chen, The anatase phase of nanotopography titania plays an important role on osteoblast cell morphology and proliferation, J Mater Sci Mater Med. 19 (2008) 3465–3472.

[66]   S. Wang, R. Li, L. Dong, Z.-Y. Zhang, G. Liu, H. Liang, Y. Qin, J. Yu, Y. Li, Fabrication of bioactive 3D printed porous titanium implants with Sr ions-incorporated zeolite coatings for bone ingrowth, J. Mater. Chem. B. 6 (2018) 3254–3261.

[67]   F. Yang, D. Yang, J. Tu, Q. Zheng, L. Cai, L. Wang, Strontium enhances osteogenic differentiation of mesenchymal stem cells and in vivo bone formation by activating Wnt/catenin signaling, Stem Cells. 29 (2011) 981–991.

[68]   P. Proff, P. Römer, The molecular mechanism behind bone remodelling: A review, Clin. Oral Investig. 13 (2009) 355–362.

[69]   A. Nather, H.J.C. Ong, Z. Aziz, Structure of Bone, in: Bone Grafts Bone Substitutes, World Scientific Publishing Co Pte Ltd., 2005: pp. 3–17.

[70]   H.C. Blair, Q.C. Larrouture, Y. Li, H. Lin, D. Beer-Stoltz, L. Liu, R.S. Tuan, L.J. Robinson, P.H. Schlesinger, D.J. Nelson, Osteoblast Differentiation and Bone Matrix

Formation In Vivo and In Vitro, Tissue Eng. Part B Rev. 23 (2017) 268–280.

[71]   P. Naruphontjirakul, O. Tsigkou, S. Li, A.E. Porter, J.R. Jones, Human mesenchymal stem cells differentiate into an osteogenic lineage in presence of strontium containing bioactive glass nanoparticles, Acta Biomater. 90 (2019) 373–392.

[72]   S.C. Verberckmoes, M.E. De Broe, P.C. D'Haese, Dose-dependent effects of strontium on osteoblast function and mineralization, Kidney Int. 64 (2003) 534–543.

[73]   N. Chattopadhyay, S.J. Quinn, O. Kifor, C. Ye, E.M. Brown, The calcium-sensing receptor (CaR) is involved in strontium ranelate-induced osteoblast proliferation, Biochem. Pharmacol. 74 (2007) 438–447.

[74]   J. Park, H. Kim, Y. Kim, J. Jang, H. Song, T. Hanawa, Osteoblast response and osseointegration of a Ti–6Al–4V alloy implant incorporating strontium, Acta Biomater. 6 (2010) 2843–2851.

[75]   A. Lotsari, A.K. Rajasekharan, M. Halvarsson, M. Andersson, Transformation of amorphous calcium phosphate to bone-like apatite, Nat. Commun. 9 (2018).

[76]   Y. Han, X. You, W. Xing, Z. Zhang, W. Zou, Paracrine and endocrine actions of bone - The functions of secretory proteins from osteoblasts, osteocytes, and osteoclasts, Bone Res. 6 (2018) 1–11.

[77]   S. Boonrungsiman, E. Gentleman, R. Carzaniga, N.D. Evans, D.W. McComb, A.E. Porter, M.M. Stevens, The role of intracellular calcium phosphate in osteoblast-mediated bone apatite formation, Proc. Natl. Acad. Sci. U. S. A. 109 (2012) 14170–14175.

[78]   S.C. Verberckmoes, G.J. Behets, L. Oste, A.R. Bervoets, L. V. Lamberts, M. Drakopoulos, A. Somogyi, P. Cool, W. Dorriné, M.E. De Broe, P.C. D'Haese, Effects of strontium on the physicochemical characteristics of hydroxyapatite, Calcif. Tissue Int. 75 (2004) 405–415.

[79]   J.-M. Zhang, J. An, Cytokines, Inflammation and Pain, Int Anesth. Clin. 45 (2007) 27–37.

[80]   M.C. Horowitz, J.A. Lorenzo, Local Regulators of Bone - IL- 1, TNF, Lymphotoxin, Interferon-y, IL-8, IL-10, IL-4, the LIF/IL-6 Family, and Additional Cytokines, in: Princ. Bone Biol., Second Edi, Academic Press, 2002: pp. 961–977.

[81]   P.E.C. Leite, M.R. Pereira, G. Harris, D. Pamies, L.M.G. Dos Santos, J.M. Granjeiro, H.T. Hogberg, T. Hartung, L. Smirnova, Suitability of 3D human brain spheroid models to distinguish toxic effects of gold and poly-lactic acid nanoparticles to assess

biocompatibility for brain drug delivery, Part. Fibre Toxicol. 16 (2019) 1–20.

[82]   J. Liao, C. Li, Y. Wang, M.H. Ten, X. Sun, A. Tian, Q. Zhang, X. Liang, Meta-analysis of the association between common interleukin-1 polymorphisms and dental implant failure, Mol. Biol. Rep. 41 (2014) 2789–2798.

[83]   M. Hurme, S. Santtila, IL-1 receptor antagonist (IL-1Ra) plasma levels are co-ordinately regulated by both IL-1Ra and IL-1β genes, Eur. J. Immunol. 28 (1998) 2598–2602.

[84]   T. Ma, K. Miyanishi, M.C.D. Trindade, M. Genovese, D. Regula, R.L. Smith, S.B. Goodman, Interleukin 1 Receptor Antagonist Inhibits Localized Bone Formation in Vivo, J. Rheumatol. 30 (2003) 2547–2552.

[85]   S.-H. Lee, T.-S. Kim, Y. Choi, J. Lorenzo, Osteoimmunology: cytokines and the skeletal system, BMB Rep. 41 (2008) 495–510.

[86]   J. Lorenzo, The effects of immune cell products (Cytokines and Hematopoietic Cell Growth Factors) on Bone Cells, in: Osteoimmunology Interact. Immune Skelet. Syst., Academic Press, 2015: pp. 143–167.

[87]   K. Ishida, T. Matsumoto, K. Sasaki, Y. Mifune, K. Tei, S. Kubo, T. Matsushita, K. Takayama, T. Akisue, Y. Tabata, M. Kurosaka, R. Kuroda, Bone regeneration properties of granulocyte colony-stimulating factor via neovascularization and osteogenesis, Tissue Eng. - Part A. 16 (2010) 3271–3284.

[88]   J. Street, M. Bao, L. DeGuzman, S. Bunting, F. V. Peale, N. Ferrara, H. Steinmetz, J. Hoeffel, J.L. Cleland, A. Daugherty, N. Van Bruggen, H.P. Redmond, R.A.D. Carano, E.H. Filvaroff, Vascular endothelial growth factor stimulates bone repair by promoting angiogenesis and bone turnover, Proc. Natl. Acad. Sci. U. S. A. 99 (2002) 9656–9661.

[89]   M. Tang, L. Tian, G. Luo, X. Yu, Interferon-gamma-mediated osteoimmunology, Front. Immunol. 9 (2018).

[90]   F.-C. Lin, H.A. Young, The talented interferon-gamma, Adv. Biosci. Biotechnol. 04 (2013) 6–13.

Chapter 4. Preliminary tribocorrosion evaluation of bio-functionalized Ti doped with Ca-P-Sr

Published in *Materials Letters 283 (2021) 128775*

A.I. Costa[a,b], F. Viana[b,c,d], F. Toptan[a,e]

[a]CMEMS-UMinho – Center for MicroElectroMechanical Systems, Universidade do Minho, Portugal

[b]DEMM – Department of Metallurgical and Materials Engineering, Faculdade de Engenharia da Universidade do Porto, Portugal

[c]LAETA – Associate Laboratory of Energy, Transports and Aeronautics, Faculdade de Engenharia da Universidade do Porto, Portugal

[d]INEGI – Institute of Science and Innovation in Mechanical and Industrial Engineering, Porto, Portugal

[e]IBTN/Euro – European Branch of the Institute of Biomaterials, Tribocorrosion and Nanomedicine, Dept. Eng. Mecânica, Universidade do Minho, Guimarães, Portugal

Abstract

Micro-arc oxidation is being applied to overcome the poor wear resistance of Ti that also enables to give bio-functions with the incorporation of bioactive agents such as Ca, P and Sr. In the present work, micro-arc oxidation was used to obtain Ca-P-Sr-doped hard TiO_2 porous layers with three different amounts of Sr and tribocorrosion behaviour was investigated. Results showed that the distribution of anatase and rutile in the porous oxide layer led to a less visible damage and lower COF values, where the group containing more Sr presented the best tribocorrosion response mainly due to the increased amount of rutile.

Graphical abstract

Ca-P-Sr-doped TiO$_2$ layers

Wear tracks

Less visible damage

Amount of Sr
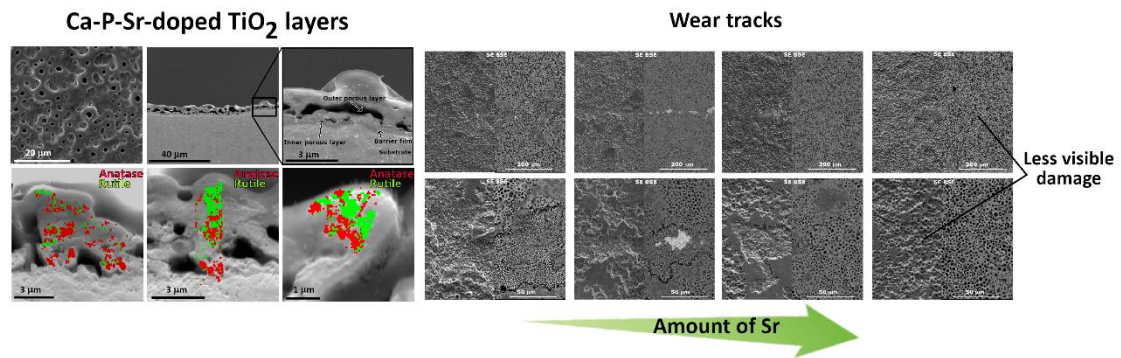
Keywords: Ti, MAO, Tribocorrosion, Strontium

4.1. Introduction

Ti presents an attractive combination of chemical, mechanical and electrochemical properties for biomedical implants, however, presents poor wear resistance and bioinertness [1,2]. In order to overcome such problems, micro-arc oxidation (MAO) can create TiO$_2$ layers with the incorporation of bioactive elements [3–5]. The most common ones, being the main constituents of the bone, are Ca and P, but there are other important elements like Sr [6]. Sr showed promising results on bone formation and healing due to its dual-action by promoting bone formation and reduction of bone resorption [7,8].

Although biological response of Sr in bioactive surfaces is studied, studies on materials degradation involving wear and corrosion are still very scarce. Since tribocorrosion is an important concern for implants, the influence of Sr on the tribocorrosion behaviour of the bio-functionalized Ti should be understood. The present work aimed at having a first insight on the tribocorrosion behaviour of Ti having Ca-P-Sr-doped TiO$_2$ layers.

90

4.2. Materials and methods

MAO was applied to Ti (Grade 2) plates for 1 min at 300 V. An electrolyte composed by 0.35 M calcium acetate monohydrate, 0.02 M β-glycerophosphate disodium salt pentahydrate and strontium hydroxide octahydrate (Sr(OH)$_2$) was used as a source of bioactive species (Ca, P and Sr, respectively). Testing groups were labelled as CaP, mSr, mmSr and mmmSr, containing 0, 0.0013, 0.013 and 0.13 M of Sr(OH)$_2$, respectively.

Energy dispersive X-ray spectroscopy (EDS) analysis was performed at 15 keV accelerating voltage (EDAX Pegasus). Crystalline structure was characterized by X-ray diffraction (XRD, Cu Kα radiation, Bruker D8 Discover). For electron backscatter diffraction (EBSD, FEI QUANTA 400 FEG-SEM having a TSL-EDAX EBSD Unit), samples were embedded in epoxy resin, cut and then cross-sections were mechanically grinded and polished with a final polishing step of 0.2 μm fumed silica.

For tribocorrosion evaluation, a linear reciprocating ball-on-plate tribometer (CETR-UMT-2) coupled with a potentiostat (Gamry Reference 600) was used with Ag/AgCl as reference electrode and samples as a working electrode (0.38 cm^2 as exposed area). 10 mm diameter alumina balls were used as counter-body. Tests were performed with 3 mm of amplitude, 1 Hz and a normal load of 0.50 N for 30 min with 9 g/L of NaCl as electrolyte at body temperature by following open circuit potential (OCP) and coefficient of friction (COF). Before sliding, all samples were immersed in the electrolyte for 1 h to stabilize OCP. To guarantee the reproducibility, all tests were triplicated. Wear tracks were analysed with FEI Nova 200 FEG-SEM.

4.3. Results and discussion

In the beginning of MAO, high current contributes to the fast growth of the oxide layer and sparks can be visible on the surface. The dielectric breakdown potential occurs when the applied voltage exceeds the critical voltage of original naturally formed insulating layer of the material and after that, the number of sparks started to decrease even though in the final moments, they can be more energetic than the previous ones promoting large pores [5,9]. Figure 4.1a presents the current evolution during MAO.

$t_{(gal/pot)}$ corresponds to the time where current remains at its maximum value, delimitating the end of galvanostatic control and the begging of potentiostatic control. Higher Sr concentration possibly contributed to higher electrolyte conductivity, thus, the $t_{(gal/pot)}$ was delayed. EDS confirmed the incorporation of Sr having an $_{at}$% content of 0.32 ± 0.03, 0.57 ± 0.04 and 2.66 ± 0.09 on mSr, mmSr and mmmSr groups, respectively. Ca/P ratio was 3.23 ± 0.02 for CaP, mSr and mmSr groups and increased to 3.89 ± 0.15 on mmmSr group. Figure 4.1b presents the XRD spectra showing that TiO_2 layers were composed by anatase and rutile. The phase percentages were calculated by dividing the total intensity of the selected peaks by the total intensity of all peaks [4] and found that mmmSr surfaces had 38% of rutile whereas the other bio-functionalized groups had 34%. Roughness (R_a) was calculated and presented in Table 4.1, showing no differences between the conditions.
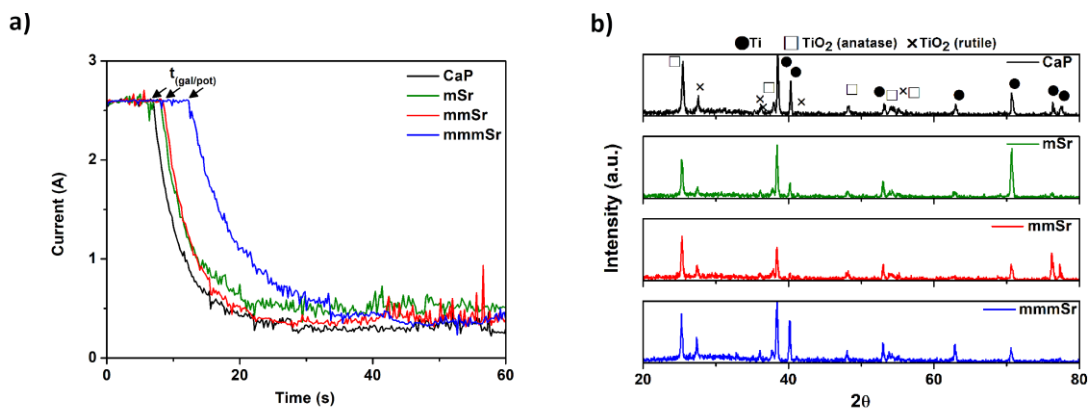
Figure 4.1. a) Evolution of current during MAO and b) resulting XRD spectra after MAO.

Table 4.1. Roughness of MAO layers.

	CaP	mSr	mmSr	mmmSr
R_a (μm)	1.24 ± 0.60	1.30 ± 0.38	1.12 ± 0.20	1.09 ± 0.20

Surfaces presented a typical porous volcano-like structure of MAO composed of a thin barrier film next to Ti followed by inner and outer porous layers having small and big pores, respectively (Figures 4.2a–c). Addition of Sr did not lead to a noticeable difference in terms of morphology or pore size (data not shown).

Figures 4.2d–f represent phase maps overlaid on the corresponding cross-sectional images of the samples without and with the highest Sr concentration. While Ti

has a hexagonal close-packed crystal structure, anatase and rutile phases have a tetragonal crystal structure with different lattice parameters and in this way, they can be distinguished by EBSD. EBSD phase maps indicated that the oxide layer contained relatively higher amount of anatase phase near the inner porous layer whereas relatively higher amount of rutile was observed on the outer surfaces. Porosity and remaining roughness that was not possible to remove by polishing can contribute to a reduced electron diffraction signal. This combined with the nano-sized grain sizes of anatase and rutile resulted in maps that are not continuous in all surface [10]. Besides, amorphous phases were presented through the entire oxide layer. It has been shown recently for MAO-treated Ti that TiO_2 phases were irregularly distributed as result of the higher energy input on the uppermost side of the layer and amorphous TiO_2 phases were observed next to pores due to the rapid cooling of gas phase and the distribution of discharges during MAO [11,12].
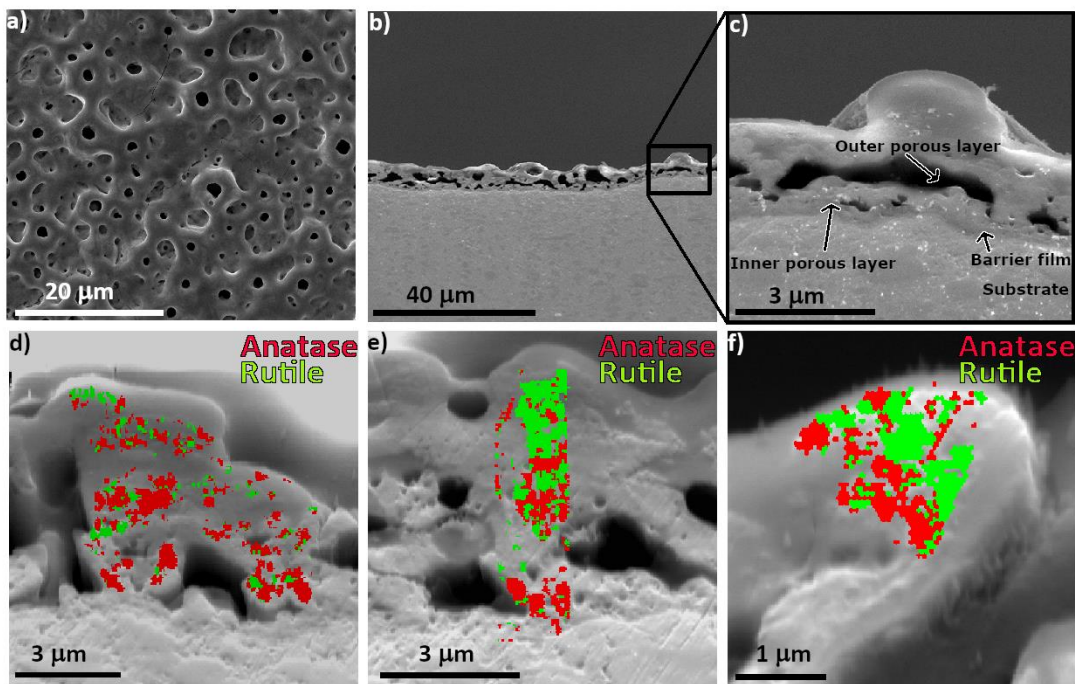
Figure 4.2. SEM images of MAO a) top surface, b) cross-sectional surface and c) cross-sectional detailed image; d), e) and f) EBDS maps overlapped on cross-sectional detailed images (a, d and e from CaP group; b, c and f from mmmSr group).

Figure 4.3 presents worn surfaces for all bio-functionalized groups together with OCP and COF evolution during tribocorrosion tests. It was observed that the protrusions of the oxide layers were smoothed while the bottom part of the porous structure seemed to remain undamaged. Pores were filled and compacted with the debris removed from the protrusions. Interestingly, worn mmmSr surfaces exhibited noticeably less damage. Although some damage was observed mainly on the outmost surfaces of the oxide layer, no significant variation of the potential values was noticed during sliding. For the untreated Ti, naturally formed passive film was easily removed when the sliding started, indicated by the abrupt decrease on OCP. The excellent tribocorrosion properties of MAO layers can be attributed to the presence of an oxide layer, mixture of anatase and rutile, where the increased percentage of rutile may be the reason for obtaining less visible mechanical damage on mmmSr group within the testing conditions. Similar wear mechanism of MAO layers was previously reported elsewhere [4] by some of the authors. Besides, the average COF values were lower for mmmSr group (0.47 ± 0.04), than the other groups (0.60 ± 0.03), and that can be related to the increased rutile percentage and/or increased Sr concentration, that needs further studies for deeper understanding. COF values for MAO layers are in accordance with previous studies [4,13,14].
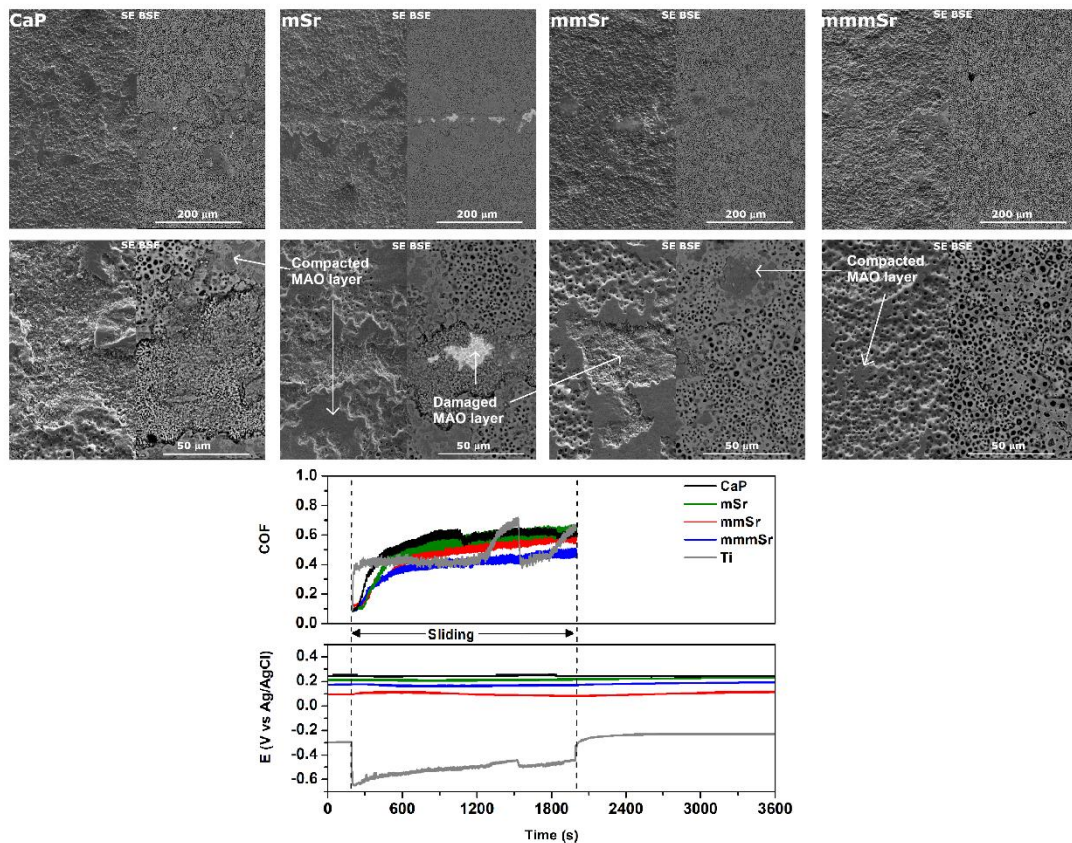
Figure 4.3. Lower (upper row, the tracks are in the centre) and higher (lower row) magnification SEM images of the wear tracks together with the evolution of COF and OCP on tribocorrosion tests.

4.4. Conclusions

Influence of Sr on Ca-P-Sr-doped TiO_2 layers was investigated by means of microstructural, chemical and triboelectrochemical evaluation. The results revealed that higher Sr concentration in the MAO electrolyte led to an increase of rutile phase within the MAO surfaces resulting in less visible mechanical damage and lower COF during tribocorrosion tests.

Acknowledgements

References

[1]   M. Saini, Y. Singh, P. Arora, V. Arora, K. Jain Monika Saini, K. Jain, Implant biomaterials: A comprehensive review, World J Clin Cases. 3 (2015) 52.

[2]   S. Prasad, M. Ehrensberger, M.P. Gibson, H. Kim, E.A. Monaco, Biomaterial properties of titanium in dentistry, J. Oral Biosci. 57 (2015) 192–199.

[3]   A.C. Alves, A.I. Costa, F. Toptan, J.L. Alves, I. Leonor, E. Ribeiro, R.L. Reis, A.M.P. Pinto, J.C.S. Fernandes, Effect of bio-functional MAO layers on the electrochemical behaviour of highly porous Ti, Surf. Coatings Technol. 386 (2020) 125487.

[4]   A.I. Costa, L. Sousa, A.C. Alves, F. Toptan, Tribocorrosion behaviour of bio-functionalized porous Ti surfaces obtained by two-step anodic treatment, Corros. Sci. 166 (2020) 108467.

[5]   F.G. Oliveira, A.R. Ribeiro, G. Perez, B.S. Archanjo, C.P. Gouvea, J.R. Araújo, A.P.C. Campos, A. Kuznetsov, C.M. Almeida, M.M. Maru, C.A. Achete, P. Ponthiaux, J.-P. Celis, L.A. Rocha, Understanding growth mechanisms and tribocorrosion behaviour of porous TiO2 anodic films containing calcium, phosphorous and magnesium, Appl. Surf. Sci. 341 (2015) 1–12.

[6]   S.G. Dahl, P. Allain, P.J. Marie, Y. Mauras, G. Boivin, P. Ammann, Y. Tsouderos, P.D. Delmas, C. Christiansen, Incorporation and distribution of strontium in bone, Bone. 28 (2001) 446–453.

[7]   J. Park, H. Kim, Y. Kim, J. Jang, H. Song, T. Hanawa, Osteoblast response and osseointegration of a Ti–6Al–4V alloy implant incorporating strontium, Acta Biomater. 6 (2010) 2843–2851.

[8]   M. Khodaei, A. Valanezhad, I. Watanabe, Controlled gentamicin- strontium release as a dual action bone agent: Combination of the porous titanium scaffold and

biodegradable polymers, J. Alloys Compd. 720 (2017) 22–28.

[9]   Y. Wang, T. Lei, B. Jiang, L. Guo, Growth, microstructure and mechanical properties of microarc oxidation coatings on titanium alloy in phosphate-containing solution, Appl. Surf. Sci. 233 (2004) 258–267.

[10]   M.D. Roach, R.S. Williamson, I.P. Blakely, L.M. Didier, Tuning anatase and rutile phase ratios and nanoscale surface features by anodization processing onto titanium substrate surfaces, Mater. Sci. Eng. C. 58 (2016) 213–223.

[11]   A.E.R. Friedemann, K. Thiel, U. Haßlinger, M. Ritter, T.M. Gesing, P. Plagemann, Investigations into the structure of PEO-layers for understanding of layer formation, Appl. Surf. Sci. 443 (2018) 467–474.

[12]   G. Mortazavi, J. Jiang, E.I. Meletis, Investigation of the plasma electrolytic oxidation mechanism of titanium, Appl. Surf. Sci. 488 (2019) 370–382.

[13]   I. da S.V. Marques, M.F. Alfaro, N.C. da Cruz, M.F. Mesquita, C. Sukotjo, M.T. Mathew, V.A.R. Barão, Tribocorrosion behavior of biofunctional titanium oxide films produced by micro-arc oxidation: Synergism and mechanisms, J. Mech. Behav. Biomed. Mater. 60 (2016) 8–21.

[14]   E.E. Sukuroglu, H. Farzi, S. Sukuroglu, Y. Totik, E. Arslan, I. Efeoglu, The effect of plasma electrolytic oxidation process parameters on the tribocorrosion properties of TiO2 coatings, J. Adhes. Sci. Technol. 31 (2017) 1361–1373.

Chapter 5. Tribocorrosion behaviour of bio-functionalized porous Ti surfaces obtained by two-step anodic treatment

A.I. Costa[a,b], L. Sousa[a,b], A.C. Alves[a], F. Toptan[a,c,d]

[a]CMEMS-UMinho – Center of MicroElectroMechanical Systems – Universidade do Minho, Campus de Azurém, Guimarães, Portugal
[b]DEMM – Department of Metallurgical and Materials Engineering – Faculdade de Engenharia da Universidade do Porto, Porto, Portugal
[c]DEM – Department of Mechanical Engineering – Universidade do Minho, Campus de Azurém, Guimarães, Portugal
[d]IBTN/Br – Brazilian Branch of the Institute of Biomaterials, Tribocorrosion and Nanomedicine, UNESP, Campus de Bauru, Bauru, SP, Brazil

Abstract

A bio-functionalized porous surface was obtained on Ti by a two-step anodic treatment and its corrosion and tribocorrosion behaviour were evaluated. The first-step provided macro-porosity while the second-step, a bio-functionalization process by micro-arc oxidation (MAO), provided an oxide layer (anatase + rutile) with micro-pores and bioactive elements (Ca + P). Corrosion and tribocorrosion behaviour were improved due to the protective role given by the oxide layer formed on the second-step. Tribocorrosion mechanisms for the bio-functionalized porous structures are presented.

Graphical abstract
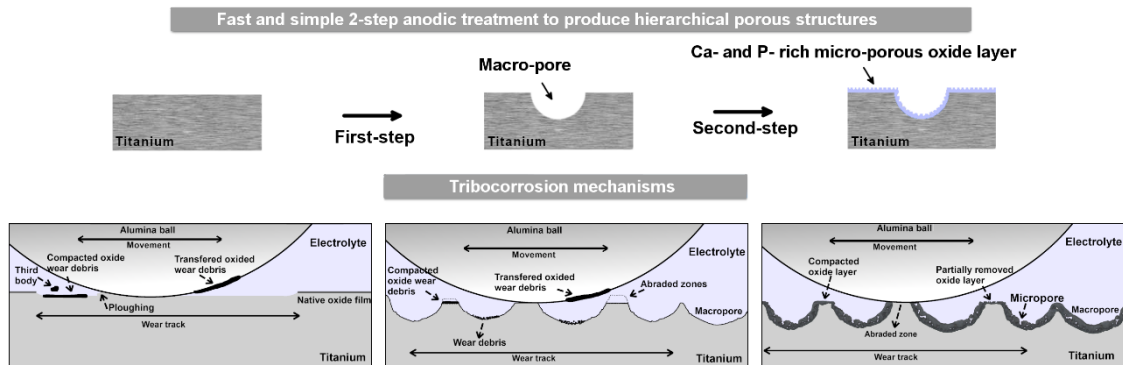
Keywords: Titanium, Anodic treatment, Micro-arc oxidation (MAO), Corrosion, Tribocorrosion

5.1. Introduction

Chronic diseases such as osteoarthritis, cardiovascular diseases and old age-related traumas together with the ageing population worldwide are set to increase the demand for medical implants in the next following years. By 2022, the medical implants market is expected to garner 116 billion USD [1]. Several types of materials are used to fulfil the needs of the implants market, and among the metallic materials, Ti is widely used mainly due to its high strength, lower Young's modulus compared to Co-Cr alloys and stainless steel, lower density and a good combination of mechanical properties and outstanding corrosion resistance [2–4]. However, Ti presents three major concerns as an implant material, such as poor wear resistance, bioinertness and higher Young's modulus compared to bone, that can result in stress-shielding effect [5].

A multiscale (macro-, micro- and nano-scale) porosity on the surface could be beneficial for mechanical interlocking, as well, for promoting cell adhesion and proliferation [6]. By varying the parameters of two or more steps of anodic treatment, it is possible to obtain hierarchical porous surfaces on the macro-, micro- or nano-scale. In order to give bio-functions, a specific anodic treatment, micro-arc oxidation (MAO), can be applied. MAO has shown tremendous potential as a process to improve the surface characteristics of materials intended for biomedical applications since it can

improve the roughness, create better wettability and promote bioactivity. Consequently, these modifications bring better results regarding adhesion, proliferation and differentiation of cells, blood compatibility, reduction of the haemolysis rate, extended dynamic coagulation time, reduction of the amount of platelet adhesion and degree of deformation, among other properties [7–10]. In addition to improved bioactivity, the tailored MAO layer also improves the corrosion [11–16] and tribocorrosion [17–21] behaviours by acting as a physical barrier against corrosion and wear. Moreover, it is also possible to have a further increase on tribocorrosion resistance by optimizing the electrolyte concentrations or compositions in a way to increase the rutile to anatase ratio [17–19].

Hierarchical porous surfaces have already been reported in the literature [6,22–24]. Through a one-step anodic treatment process, Xie *et al.* [22] obtained a multi-level porous structure with craters sized from 2 to 20 μm that were covered by pores with 50 to 500 nm. Zhou *et al.* [23] obtained macro-pores in the range of 50 to 1000 μm and micro-pores from 0.6 to 2 μm on the surface through a two-step anodic treatment. Then some of the same authors, by a three-step anodic treatment, obtained pores with 80 to 200 μm and with 0.6 to 2 μm with the incorporation of bioactive elements, such as Ca, P, Si and Na [24]. More recently, Li *et al.* [6] obtained surfaces with macro-pores in the range of 100 to 300 μm, micro-pores with 3 to 10 μm and also submicron/nano-pores in the range of 80 to 200 nm by a two-step anodic treatment.

Although macro-porous structures present many advantages as biomaterial, studies regarding their tribocorrosion performance are very scarce [21] and their wear mechanisms are yet to be fully understood. Wear studies on porous materials showed that porosity may play a beneficial role by reduced contact area, reduced third-body abrasive wear after ejection of wear debris to the pores [25], or in an aqueous environment, by promoting a self-lubricant effect [26]. However, porosity may also play a disadvantageous role due to higher effective stresses applied to the outmost surfaces [25], or due to cracks that are originated from pores [25,27].

Bio-functionalized multi-scale porous surfaces may be a promising cost-effective solution to improve bioactivity as well as corrosion and tribocorrosion resistance of Ti. Thus, the present work aimed to study the corrosion and tribocorrosion behaviour of bio-functionalized hierarchical porous surfaces obtained by a two-step anodic

treatment. In the first-step, superficial macro-porosity was created and in the second-step, by MAO, a micro-porous oxide layer was obtained with the incorporation of bioactive elements (Ca and P), in order to bio-functionalize the macro-porous surface obtained on the first-step.

5.2. Materials and methods

5.2.1. First-step anodic treatment

Prior to the anodic treatments, Ti (Grade 2) plates (20 x 20 x 2 mm) were ground down to 800 mesh with SiC papers and etched in a dilute acid mixture ($V_{HF}:V_{HNO_3}:V_{H_2O} =$ 1:1:18) for 5 min in an ultrasonic bath, to remove all impurities, grinding marks and the native oxide film. Cleaning was performed with propanol and distilled water in an ultrasonic bath for 10 and 5 min, respectively.

All anodic treatments were performed using a DC power supply (Agilent technologies N5772A), under agitation in a turbulent regime by using a magnetic stirrer rotating at 200 rpm in an acrylic electrochemical cell. The exposed anodic area was 1.50 cm^2 and a platinum sheet with an exposed area of 7 cm^2 was used as a cathode, positioned 8 cm away from the sample. The first-step was carried out at room temperature using 200 mL of an electrolyte mixture (pH=14) of 0.50 M sodium hydroxide (NaOH, Eka) and 0.10 M sodium nitrate (NaNO$_3$, Sigma-Aldrich) under a constant voltage of 45 V with a limiting current of 2.60 A for 1, 2, 3, 4 and 5 minutes (Table 5.1). In order to remove the oxide products formed in the first-step and to reveal the macro-pores, the samples were etched with a dilute acid mixture ($V_{HF}:V_{HNO_3}:V_{H_2O} =$ 1:1:18) in ultrasonic bath for 10 min. After, the samples were ultrasonically cleaned in propanol for 10 min followed by distilled water for 5 min and then dried with warm air.

Table 5.1. Groupings of samples after the first- and the second-step anodic treatment.

Duration of the first-step anodic treatment (min)	0	1	2	3	4	5
Grouping after the first-step anodic treatment	Ti	Ti_1	Ti_2	Ti_3	Ti_4	Ti_5
Grouping after the second-step anodic treatment	Ti_MAO	Ti_1MAO	-	Ti_3MAO	-	-

Pore size distribution was obtained by measuring the diameters of the pores on 9 images of 1.14 x 0.86 mm frames captured from each 3 different samples per each group. Considering the pores size distribution and morphology, just the groups treated for one and three minutes were chosen for the second-step anodic treatment.

Superficial area (the area exposed to electrolyte on corrosion tests) was calculated on optical microscope (OM, Leica DM2500) images using ImageJ 1.51j8 software through 3 combined cross-sections images per group with a total area of 0.20 cm^2. The superficial area obtained for Ti_1 was 0.47 cm^2 and for Ti_3 was 0.51 cm^2. These areas were used for normalizing electrochemical data.

5.2.2. Second-step anodic treatment under MAO regime

The second-step anodic treatment was performed under MAO regime using 200 mL of a mixture of 0.02 M of β-glycerophosphate disodium salt pentahydrate (β-GP, Alfa Aesar) and 0.35 M of calcium acetate monohydrate (CA, Sigma-Aldrich) electrolyte. This electrolyte was chosen in order to incorporate bioactive species, namely P (from β-GP) and Ca (from CA). The treatment was performed at room temperature under a constant voltage of 300 V with a limiting current of 2.60 A during 1 min. The setup was the same as the one used on the first-step, including the electrochemical cell, cathode, exposed areas and power supply. Finally, the samples were ultrasonically cleaned in distilled water for 5 min and then dried with warm air. This second-step was identified by MAO on sample grouping presented on Table 5.1.

The topography, microstructure and chemical composition of the modified surfaces were analysed by FEI Nova 200 field emission gun scanning electron microscope (FEG-SEM) equipped with energy dispersive X-ray spectroscopy (EDS). EDS analysis was performed at an accelerating voltage of 15 keV, using conventional ZAF correction procedure included in the EDAXPegasus software. Crystalline structure was characterized by XRD (Cu Kα radiation, Bruker D8 Discover) with a scanning range (2Ө) of 20° to 100°. The phase percentage of the oxide layer obtained by MAO was calculated by following Equation (5.1):

$$\% \, phase_\alpha = \frac{\sum I_{\alpha peaks}}{\sum I_{allpeaks}}$$
(5.1)

In order to obtain cross-section images by OM, the samples were embedded in a hard-resin, cut with a diamond disc, ground with 1200 mesh SiC papers and polished with a colloidal silica suspension (Struers, OP-S) down to 0.04 mm.

Surface roughness measurements were carried out by a non-contact profilometer (Veeco Dektak 150). In total, 10 profiles (2 mm in length) were taken per each condition, on different samples to calculate the average roughness values (Ra). In the case of macro-porous samples, the roughness values were taken from the outermost surfaces.

5.2.3. Wettability

Hydrophilicity of each group was examined by contact angle measurements through a sessile drop method using an optical tensiometer Theta Lite controlled by OneAttension software. C.a. 5 µl droplet of ultra-pure water was dropped on the surface and the contact angle was considered after 10 s. The evaluation was performed at room temperature in air. Five different samples per group were analysed with three valid measurements per sample. One-way analysis of the variance (ANOVA) followed by Tuckey test was used in order to access the differences in the variance within the groups after the first- and the second-step anodic treatments, using a significance level of $p < 0.05$.

5.2.4. Corrosion tests

Corrosion tests consisted of open circuit potential (OCP) measurement and potentiodynamic polarization were performed using a three-electrode setup at body temperature (37 ± 2 °C) in 200 mL NaCl solution (9 g/L). Samples with geometric exposed area of 0.38 cm^2 were used as working electrode (WE), a Pt electrode was used as a counter electrode (CE), while a saturated Ag/AgCl electrode was used as a reference electrode (RE). All the potentials were given with respect to saturated Ag/AgCl electrode. Corrosion tests were performed with a Reference 600+ potentiostat/galvanostat/ZRA from Gamry Instruments. OCP was monitored for a period of 180 minutes to evaluate the corrosion potential of the material in contact with the electrolyte and to stabilize the system. The system was considered stable if OCP values

did not present a variation higher than 60 mV in the last hour of measurement. Potentiodynamic polarization tests were performed from -0.25 V to 1.50 V using a scanning rate of 0.50 mV/s. At least three samples were evaluated per group in order to assure the reproducibility.

5.2.5. Tribocorrosion tests

Tribocorrosion tests were carried out in a triboelectrochemical cell, containing 25 mL of NaCl solution (9 g/L) at 37 ± 2 °C. The cell was installed in a tribometer with a reciprocating ball-on-disk configuration (CETR-UMT-2), against an alumina ball with 10 mm of diameter (Ceratec). A three-electrode configuration (RE-Ag/AgCl, CE-Pt and WE-samples) connected to a Reference 600 potentiostat/galvanostat/ZRA from Gamry Instruments was used for the triboelectrochemical measurements. Before sliding, the samples were immersed for 180 minutes in the electrolyte in order to stabilize the system. OCP values were monitored before, during and after sliding. Coefficient of friction (COF) values were also monitored during sliding. Tribocorrosion tests were performed with a total stroke length of 3 mm, frequency of 1 Hz, normal load of 0.50 N (corresponding to a maximum Hertzian contact pressure of 330 MPa for Ti) and total sliding time of 60 min. All groups had at least three tests in order to assure the reproducibility. After each tribocorrosion test, the electrolyte was collected, stored in 2 mL plastic container and kept at 4 °C for posterior analyses. The released ions of Ti, Ca and P were quantified by inductively coupled plasma-atomic emission spectrometer (ICP-AES, Horiba Jobin-Yvon Ultima). Three measurements were performed for each group, however for Ti quantification, in the groups after the second-step, only two numeric ion concentration values were obtained due to a detection limit of 1 μg/L.

5.3. Results and discussion

5.3.1. First-step anodic treatment

Figure 5.1a presents a macro-pore formed after 2 minutes of the first-step anodic treatment. The formation of macro-pores covered by oxides (corrosion products) may be explained by the pitting mechanism that Ti suffers randomly across the surface, as a result of the corrosion capacity of NO_3^- and its predisposition to react with bulk Ti [6,28]. Previously, Zhou *et al.* [23] suggested that OH^- promotes the reaction of NO_3^- with Ti, in this way, a higher amount of OH^- leads to higher amount of macro-pores due to the formation of more pitting sites on the surface. The first-step anodic treatment was only applied to form macro-pores and this treatment is known to not to affect the outmost surface [6]. The oxides or corrosion products formed on the macro-pores were removed after etching in a dilute acid mixture (Figure 5.1b and c).
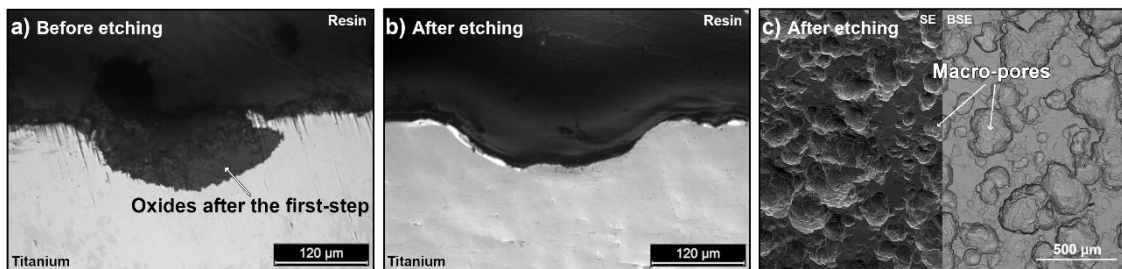
Figure 5.1. a) and b) OM images of the cross-sections after first-step of anodic treatment before and after etching, respectively and c) secondary electron (SE) and backscattered electron (BSE) SEM images of the porous surface after etching.

The morphology and distribution of the pores can be seen on the OM images given in Figure 5.2 with the respective time of the first-step anodic treatment. The samples shown in Figure 5.2 were slightly polished with 4000 mesh SiC paper to improve the contrast between the macro-pores and the outmost surface in order to reveal the morphology of the macro-pores. With the increasing time, pores grew larger in all directions and became interconnected. All conditions presented a homogeneous distribution of macro-pores through all surface which is in accordance with the literature [6,23,24] stating that a NaOH concentration of 0.50 M in the electrolyte was suitable to obtain a homogeneous distribution of macro-pores.
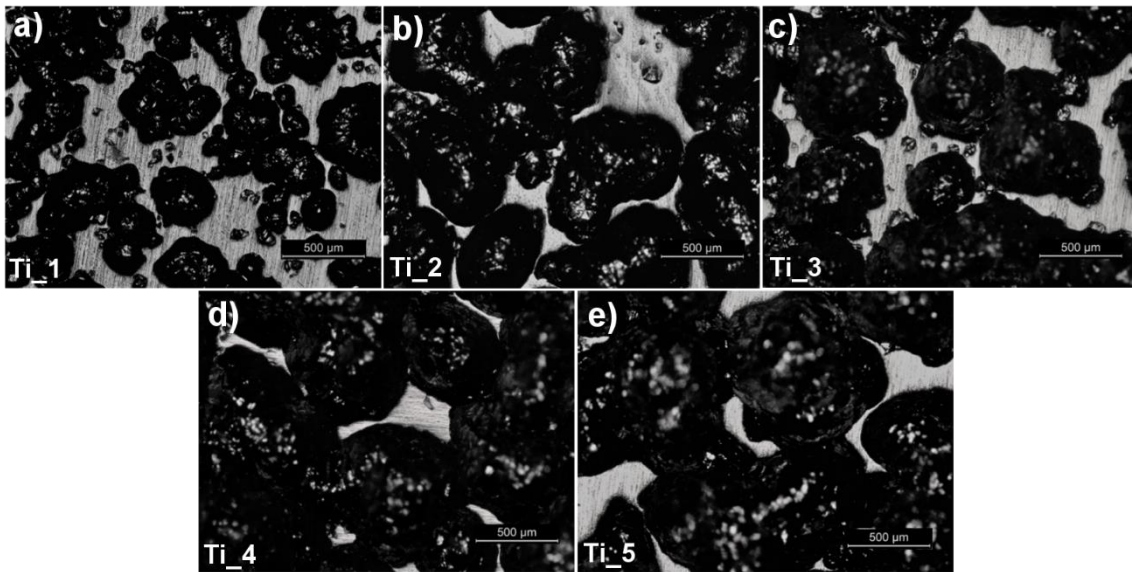
Figure 5.2. OM images after the first-step anodic treatment performed for a) 1, b) 2, c) 3, d) 4 and e) 5 minutes.

Pore size distribution after the first-step anodic treatment is presented in Figure 5.3 together with the percentage of superficial macro-porosity and average pore size values. With the increasing time, the pore size distribution was shifted to higher values of pore dimensions due to more time given to the macro-pores to be enlarged. Consequently, both the average pore size and surface porosity increased with treatment time. An optimum pore size or pore size distribution are still undefined but it is known that if the pores are very small, cells may not migrate inside of the pores and if the pores are too big, cell attachment may be difficult [29]. Pores around 100 μm are reported to facilitate optimal attachment for cell proliferation, differentiation and bone remodelling [30,31]. On the other hand, macro-pores in the range of 300–600 μm are also required, especially to facilitate the bone formation, bone-ingrowth and vascularization [32–34]. When the first-step was performed for more than three minutes, the favourable range of pores stated before was lost. Thus, Ti_4 and Ti_5 were discarded due to the presence of pores with dimensions well above to the ones intended. Within the remaining groups, Ti_1 and Ti_3 were selected to carry forward representing the surfaces having mostly isolated round pores and mostly interconnected porosity, respectively. Eventually, the second-step anodic treatment, MAO, was only performed on three groups: Ti as control, Ti_1 and Ti_3.

The average deepness of the pores for Ti_1 and Ti_3 groups was accessed, and the values were 74 ± 23 μm and 149 ± 48 μm, respectively. Consequently, the mass loss after Ti_1 was lower than Ti_3 (11 ± 3% and 16 ± 3%, respectively) due to a lower number of pores with smaller dimensions.
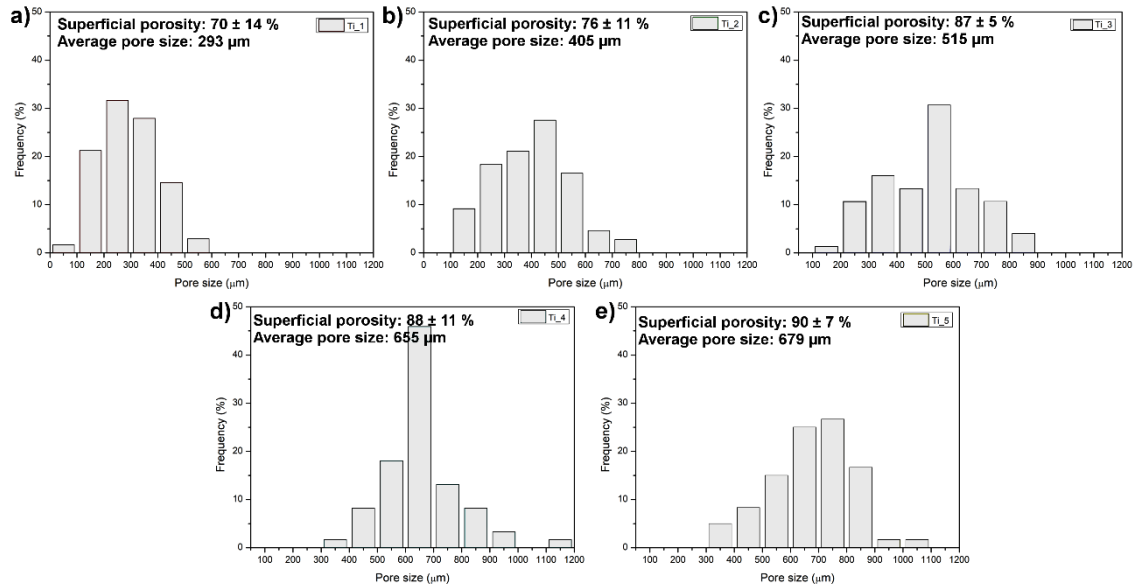
Figure 5.3. Pore size distribution after the first-step anodic treatment for Ti_1 to Ti_5 groups, respectively.

5.3.2. Second-step anodic treatment under MAO regime

After the second-step anodic treatment (MAO), surfaces were covered by a uniform micro-porous anodic layer with the typical volcano-like structure, as shown in the SE-SEM images presented in Figure 5.4a to c and in more detail in Figure 5.4d to f. No discontinuities or differences in morphology were observed between the pore surfaces and the outmost surfaces.

108
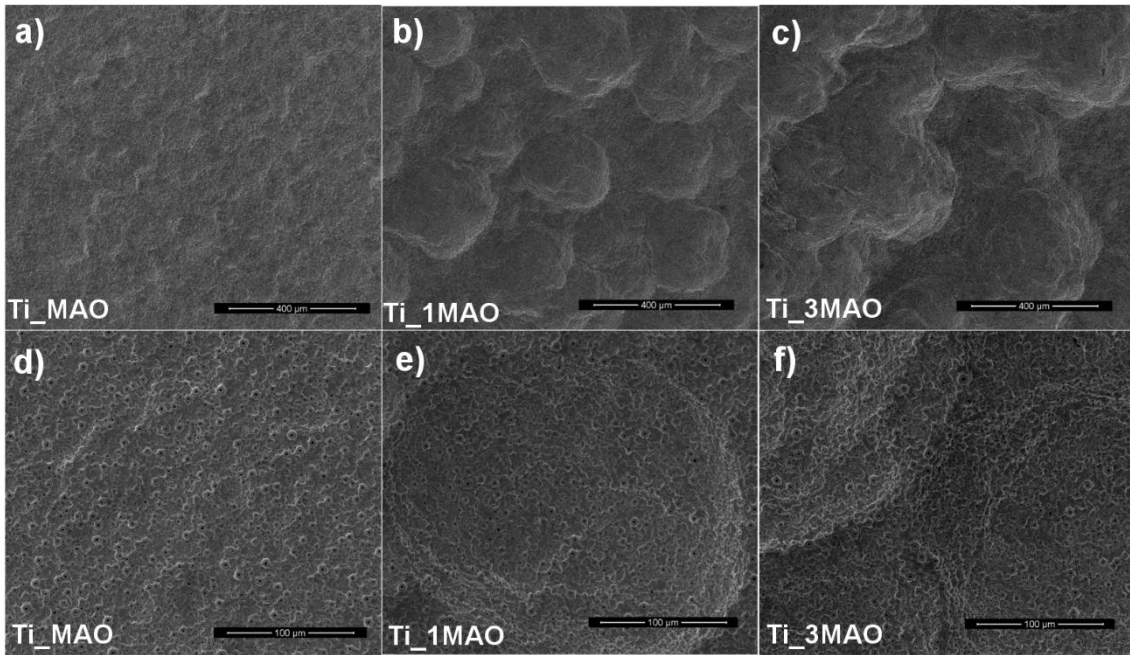
Figure 5.4. Representative SE-SEM images obtained after the second-step anodic treatment for Ti_MAO (a and d), Ti_1MAO (b and e) and Ti_3MAO (c and f).

The cross-sectional morphology of Ti_MAO, Ti_1MAO and Ti_3MAO groups are shown in Figure 5.5a, b and c, respectively, revealing a similar oxide layer with a thickness of 5.20 ± 1.00 μm, 5.27 ± 1.26 μm and 5.41 ± 1.06 μm, respectively. Alves *et al.* [35] had previously presented the detailed cross-section of a MAO layer obtained with the same processing parameters on a bulk Ti, having a triplex structure composed of a compact and thin layer next to the bulk material followed by an inner porous layer having small pores and an outer porous layer having bigger pores.

During MAO process, the applied voltage exceeded the dielectric breakdown of the oxide layer and a micro-porous structure was formed because of the micro-arc discharges [36]. The initial moments were attributed to the formation of a thin and compact oxide layer. Then, as a result of the higher applied voltage, the oxide layer started to get thicker as a consequence, the measured current dropped to lower values [6]. The evolution of current during the MAO treatment did not reveal significant differences between the testing groups (Figure 5.5d). These results confirmed that the macro-pores formed at the first-step did not have a noticeable effect on the micro-porous oxide layer formed at the second-step. Furthermore, no significant differences in the cross-section morphology or thickness were observed between the oxide layer inside and out of the pores.
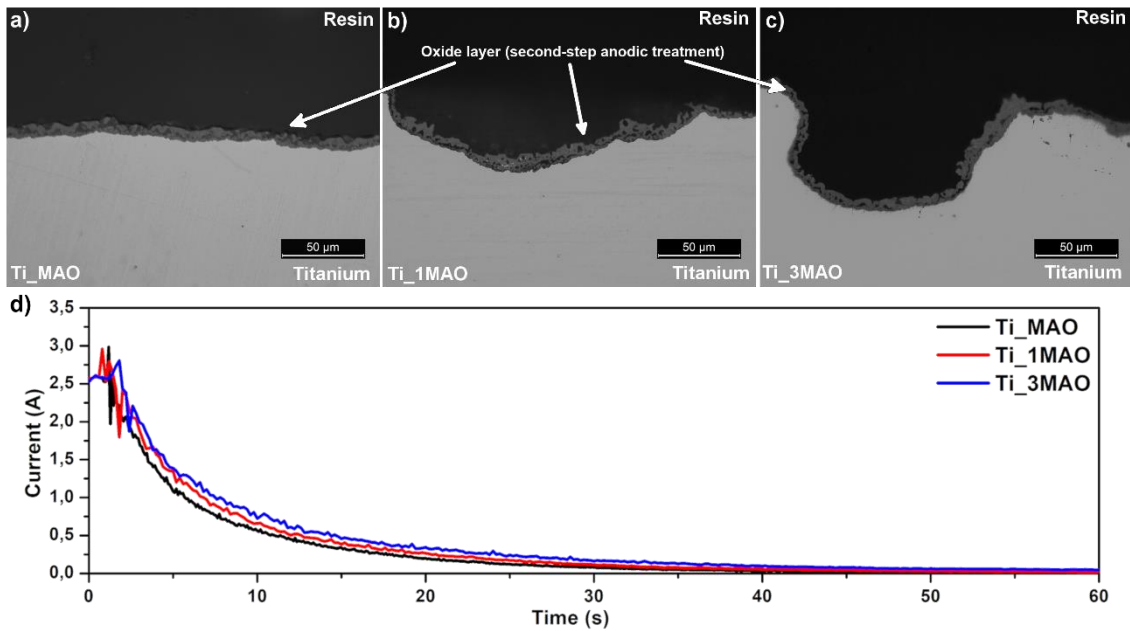
Figure 5.5. Cross-sectional OM images of a) Ti_MAO, b) Ti_1MAO and c) Ti_3MAO and d) respective current evolution during MAO treatment.

Due to localized melting of the oxide, Ca and P elements presented in the electrolyte were incorporated in the micro-porous anodic layer [19], giving a bio-function since they are the main constituents of bone [37]. Figure 5.6a shows the EDS spectra of MAO-treated groups, confirming the incorporation of Ca and P during MAO treatment. The Ca/P as atomic ratio was 2.91 ± 0.13, 2.99 ± 0.15 and 2.99 ± 0.11 for Ti_MAO, Ti_1MAO and Ti_3MAO, respectively. In the bone, the stoichiometric atomic ratio of Ca/P for hydroxyapatite (HAP) is about 1,67 [37]. It was favourable to have Ca/P ratio above the one in HAP since Ca presents a faster dissolution than P [38–40].

The XRD patterns of MAO-treated groups are shown in Figure 5.6b where characteristic peaks of Ti and TiO_2 (as anatase and rutile) were obtained as in accordance with the literature [17,21,35]. The percentage of anatase and rutile phases were calculated by Equation (5.1) and the results showed around 70% of anatase and 30% of rutile for all the conditions. A mixture of anatase and rutile may play an important role on the tribocorrosion behaviour and biological properties of the implant. It is well reported that MAO treatment improves the wear resistance of Ti, mainly attributed to the increase in hardness due to the presence of mixture of hard anatase and rutile phases [14,17–19]. Hardness of anatase and rutile are around 8 and 17 GPa, respectively [41]. Oliveira *et al.* [19] studied similar structures on bulk Ti surfaces and reported that

110

anatase was evenly distributed through all the surface while rutile was mostly presented at higher zones around the micro-pores with volcano-like structures. Recently, Alves *et al.* [7] showed that bio-functionalization process by MAO, with the same parameters used in the second-step anodic treatment described in this work, improved adhesion and proliferation of NIH/3T3 cells when compared to untreated Ti due to chemical composition, nature of the TiO_2 films (a mixture of anatase and rutile) and topography of the anodic layers formed by MAO.
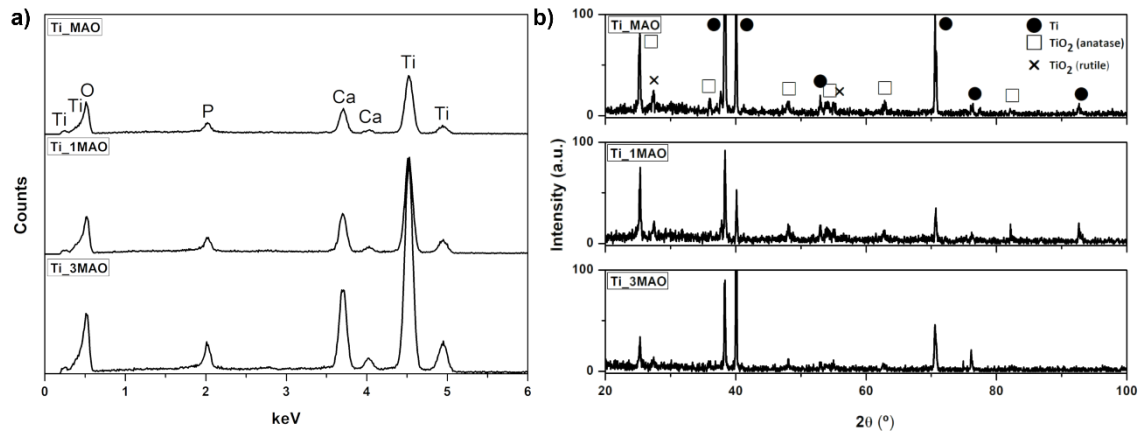
Figure 5.6. a) EDS and b) XRD spectra after the two-step anodic treatment.

5.3.3. Roughness

Another important surface characteristic influencing the interactions between the implant and the biological material is surface roughness. After the first-step anodic treatment, the acid etched surfaces (just before MAO treatment) presented Ra values of 1.48 ± 0.35 µm, 1.47 ± 0.78 µm and 1.41 ± 0.89 µm for Ti, Ti_1 and Ti_3, respectively. After the MAO treatment, a slight increase on Ra values was observed, leading to values of 1.88 ± 0.49, 1.85 ± 0.52 µm and 1.90 ± 0.60 µm for Ti_MAO, Ti_1MAO and Ti_3MAO, respectively. These results suggest that the roughness created by etching governed the global roughness after two-step treatment. For biomedical applications, the material response does not necessarily depend on the degree of the surface roughness but rough surfaces usually presents better biological response [42,43] since cell growth and a better adsorption of proteins can be promoted by an increase in the surface area available for cells [43].

Wettability may control four important phenomena between the biological organisms and the surface: adhesion of proteins and other macro-molecules, hard and soft tissue cell interactions, adhesion of bacteria and bio-film formation, and rate of osseointegration [44]. Therefore, wettability of the treated surfaces was defined and the results of the contact angle measurements are presented in Figure 5.7, together with the representative images for each group under water contact angle evaluation test. After the first-step, the average values of contact angle for Ti, Ti_1 and Ti_3 were 71 ± 9°, 80 ± 8° and 70 ± 7°, respectively. These values pointed a less hydrophilic behaviour after the first-step. Statistical analysis was performed in order to access if the type of porosity influenced the wettability within the groups after the first-step anodic treatment. Results showed statically significant differences for the values obtained for Ti_1 as compared to Ti and Ti_3, indicating that the type of macro-porosity had an effect on the wettability. When the macro-pores were mostly isolated (Ti_1), the contact angle was higher, and consequently, the wettability decreased when compared with the control group. But, if the interconnected porosity increased, then the wettability increased and the value was closer to the one found in the control group, Ti. After the second-step, Ti_MAO, Ti_1MAO and Ti_3MAO presented average contact angles of 26 ± 9°, 27 ± 8° and 19 ± 11°, respectively. These values showed that a shift for the hydrophilic regime occurred after the second-step, due to chemical as well as topographical changes on the surface, with the formation of a micro-porous oxide layer. Regarding the MAO groups, there were no statistically significant differences in the average values between the testing groups.

A hydrophilic surface is more prone to interact with the fluids in a biological environment, promoting protein adsorption to the surface, while a hydrophobic one can promote the entrapment of air bubbles that can affect the interaction between the surface and the proteins or the cells, leading to a worse adsorption or adhesion/activation, respectively [44]. Therefore, the second-step anodic treatment under MAO regime may also promote beneficial interactions in a biological environment by transforming the surfaces from hydrophobic to hydrophilic.
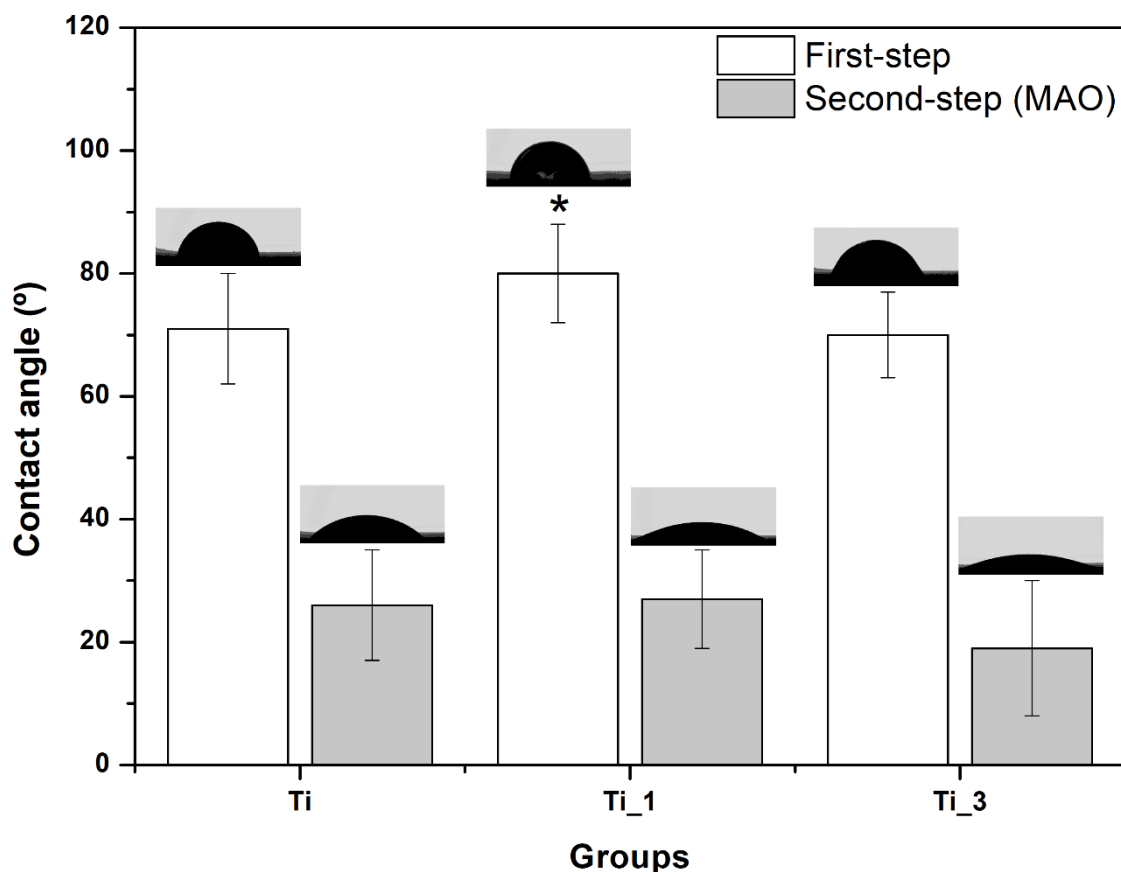
Figure 5.7. Contact angle values for each group and the respective representative images (* Significant difference within the first-step group (p<0.05)).

5.3.5. Corrosion behaviour

Figure 5.8 shows the representative potentiodynamic polarization curves for all groups and Table 5.2 gives the average values for open circuit potential (E_{OCP}), corrosion potential ($E_{(i=0)}$) and passivation current density (i_{pass}). All polarization curves exhibited a direct transition from the active region to passive region. It was also possible to see a well-defined passivation plateau for Ti (starting around 0.25 V), that was not lost after the first-step. There was no significant difference between Ti and porous surfaces of Ti_1 and Ti_3 as also can be seen more clearly on E_{OCP}, $E_{(i=0)}$, and i_{pass} values presented in Table 5.2, thus, it can be stated that the corrosion behaviour was not affected significantly by the macro-porosity obtained after the first-step. It was clear that the corrosion resistance was improved after the second-step (MAO) since it can be observed that the polarization curves in Figure 5.8 shifted to the left-upper area of the graph, exhibiting lower values of current density as well as higher corrosion potential as it is confirmed in

Table 5.2. There were no significant differences between Ti_MAO, Ti_1MAO and Ti_3MAO on i_{pass} (values considered at 0.60 V), E_{OCP} or $E_{(i=0)}$. Improvement of corrosion behaviour after MAO had already been reported in the literature for dense Ti and Ti-6Al-4V surfaces and it was attributed to the formation of oxide layers with higher corrosion resistance, mainly by the contribution of the barrier layer that was formed in the MAO treatment [14,19,35].
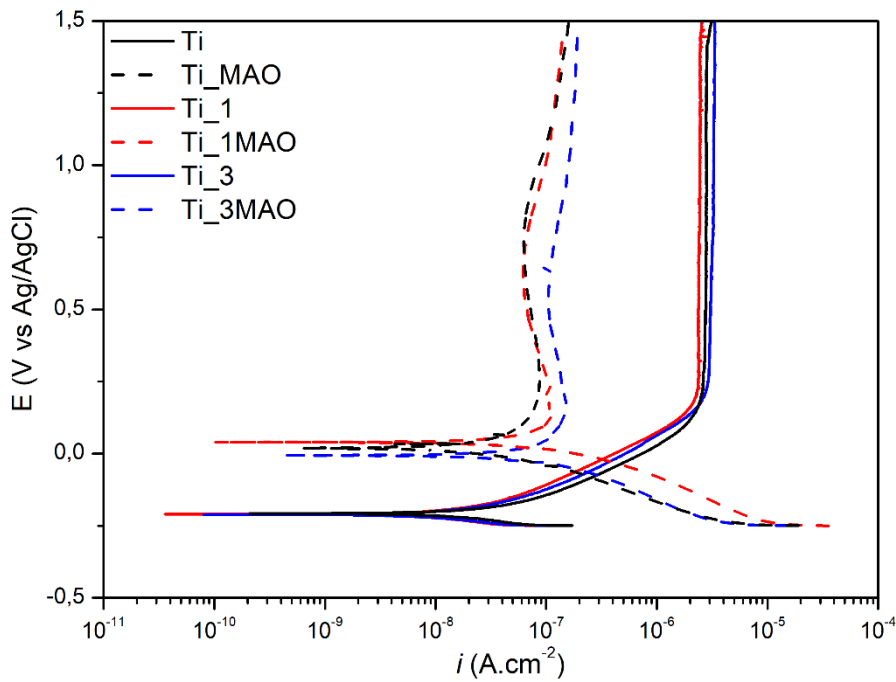
Figure 5.8. Potentiodynamic polarization curves before (Ti_1 and Ti_3) and after (Ti_1MAO and Ti_3MAO) the second-step anodic treatments, in comparison with their control groups (Ti and Ti_MAO, respectively).

Table 5.2. Open circuit potential (E_{OCP}), corrosion potential ($E_{(i=0)}$) and passivation current density (i_{pass}) values for all testing groups.

	Ti	Ti_1	Ti_3	Ti_MAO	Ti_1MAO	Ti_3MAO
E_{OCP} (V)	-0.16 ± 0.03	-0.20 ± 0.05	-0.17 ± 0.05	0.36 ± 0.05	0.34 ± 0.06	0.38 ± 0.08
$E_{(i=0)}$ (V)	-0.20 ± 0.05	-0.15 ± 0.06	-0.23 ± 0.01	0.01 ± 0.03	0.04 ± 0.02	0.00 ± 0.01
i_{pass} ($\mu A\ cm^{-2}$)	2.97 ± 0.63	2.37 ± 0.34	2.92 ± 0.53	0.06 ± 0.02	0.07 ± 0.02	0.09 ± 0.02

114

Figure 5.9 presents the representative OM and SEM images of the worn sample and counter-body surfaces, together with the EDS spectra taken from the worn counter-body surfaces after the first- and the second-step anodic treatment. Parallel grooves to the sliding direction were dominant on the samples tested after the first-step anodic treatment, which is a characteristic feature of abrasive wear. MAO-treated samples presented smaller worn areas (more evident on the OM images) and less visible wear damage (more evident on the SEM images) compared to samples tested after the first-step anodic treatment. Additionally, SEM images revealed oxidized patches formed due to repetitive transfer of material between the two mating surfaces, as well, loose oxidized wear debris in the macro-pores. In MAO-treated samples, both worn and unworn areas can be seen on the wear tracks since the counter-body was carried by the most protruded surfaces. On the other hand, material transfer from samples to the counter-body (alumina ball) was confirmed for all conditions, evidenced by EDS spectra taken from the worn counter-body surfaces.
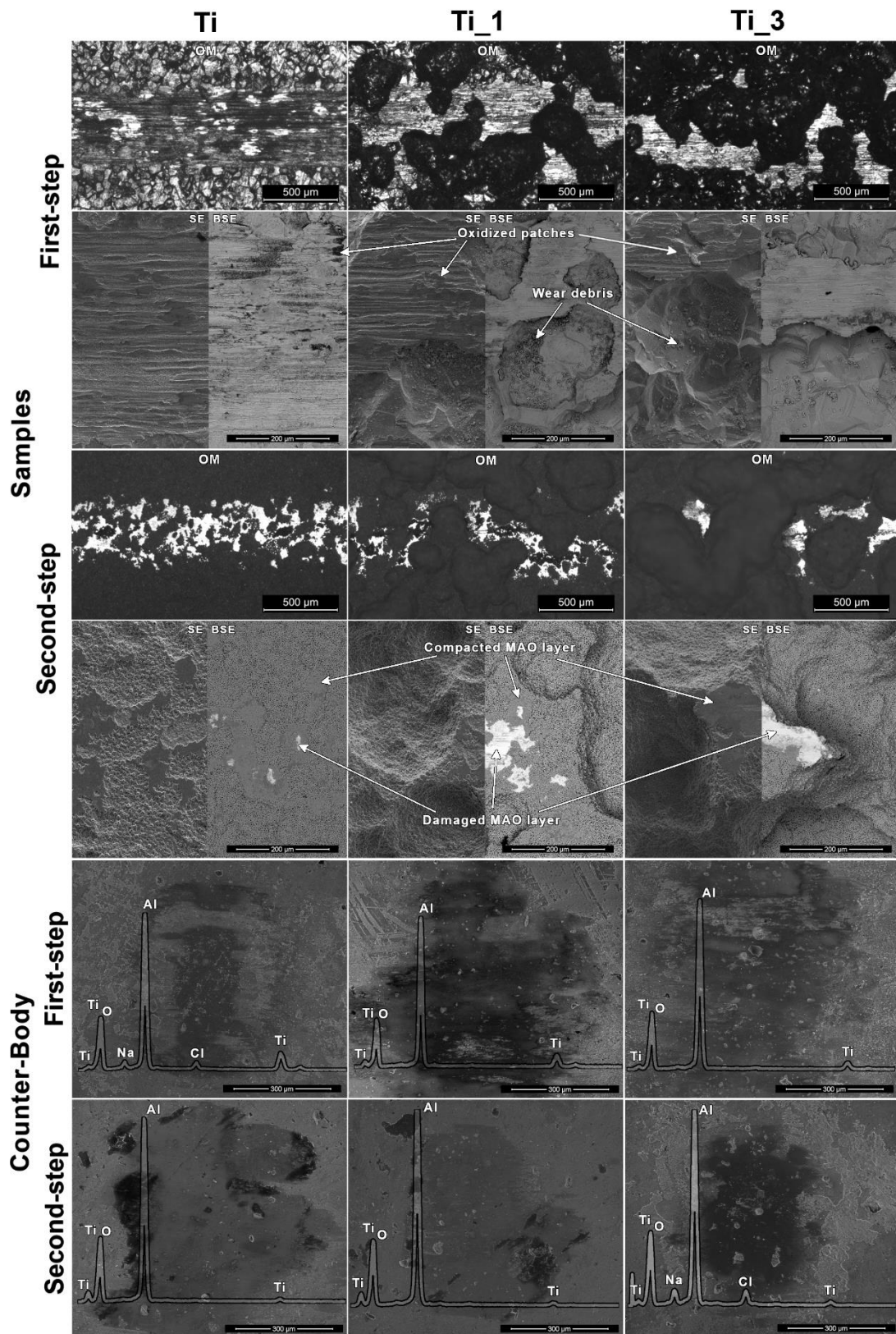
Figure 5.9. OM and SEM images of the worn sample surfaces, together with the SEM images and the respective EDS spectra taken from the worn counter-body surfaces after the first- and the second-step anodic treatments.

BSE-SEM images taken from Ti_1MAO sample presented in Figure 5.10 give a closer look to the worn MAO-treated surfaces, showing some typical key worn surface features observed on all MAO-treated surfaces, together with the respective EDS spectra. As it can be seen on Figures 5.10a and b, the zones marked as Z1, Z3 and Z6 presented different atomic contrast, pointing severe local damage on the MAO layer, as also evidenced by the EDS spectra where no distinguishable peaks of Ca and/or P were registered. Nevertheless, some differences were observed within these three zones as Z1 and Z6 presented sharp grooves or scratches parallel to the sliding direction and Z3 presented an uneven morphology. In Z2 and Z7, the outmost part of the MAO layer was damaged due to contact with the counter-body and these zones presented a smooth surface with some areas presenting a darker tone that were probably the micro-pores being filled with wear debris. In Z4, the oxide layer was only partially damaged and Ca and P peaks were still presented in the EDS spectrum (Figure 5.10c). The zones marked as Z5 and Z8 represented unaffected areas, where the structure was not changed and therefore, similar morphology and similar EDS spectra were observed to the ones already shown in Figure 5.4d and Figure 5.6a, respectively.
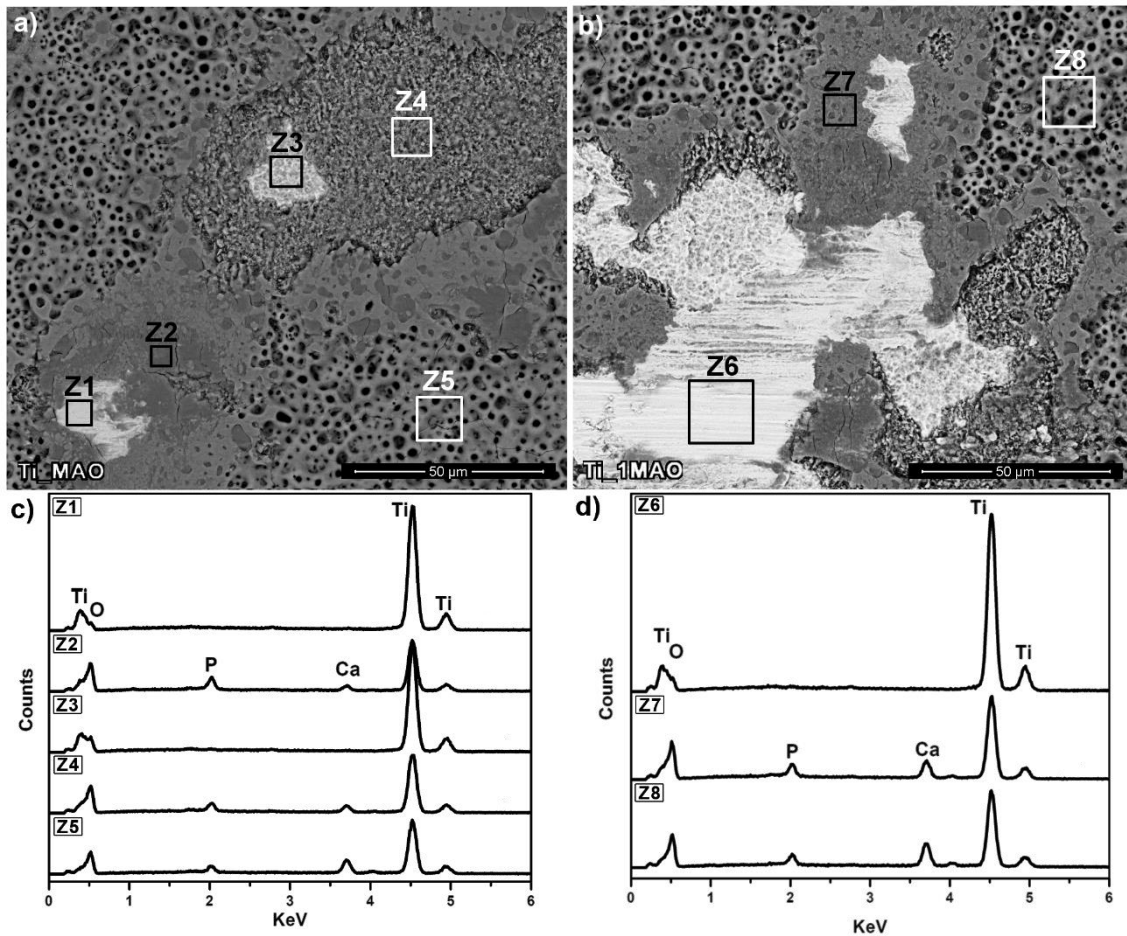
Figure 5.10. Higher magnification SEM images of the worn surfaces after the second-step anodic treatment (a and b), together with EDS spectra taken from the marked zones (c and d).

The evolution of OCP before, during and after sliding together with the evolution of COF during sliding are presented in Figure 5.11. As general, groups before (Figure 5.11a) and after (Figure 5.11b) the second-step anodic treatment exhibited significantly different behaviour. Before sliding Ti, Ti_1 and Ti_3 presented stable and very similar potential values due to the presence of the native oxide film. This film was immediately damaged with the starting of sliding as it was evident by a sharp decrease in OCP values. The lowest OCP values were observed on the run-in period and afterwards, OCP values increased and remained relatively stable for the remaining time of sliding. During sliding, simultaneous increases and decreases were observed in both OCP and COF values that were more pronounced on Ti as compared to the porous samples. These variations on OCP and COF can be linked with the adhered oxidized patches. In the presence of macro-pores, some part of the wear debris was ejected into the pores resulting with less dense oxidized patches on the worn Ti_1 and Ti_3 surfaces, as compared to Ti (Figure 5.9). On

118

Ti, on the absence of the macro-pores, it was possible that adhered oxidized patches got denser during sliding time, however, after getting a certain thickness, these wear debris might be broken by the counter-body. As patches were getting thicker, due to their physical barrier role, they can give a limited protection against corrosion that can explain the local increments on OCP. In the same time, as they were getting thicker, surface roughness was also getting higher, therefore simultaneous increments on COF values were recorded [45].

After the second-step anodic treatment, all groups presented an improvement on the tribocorrosion behaviour, characterized by higher OCP values under sliding, together with more stable COF values (Figure 5.11). It was also observed that within the MAO-treated groups, an increase in macro-porosity led to lower OCP values under sliding, with OCP values slightly decreasing as sliding proceeded. Considering that there were no significant differences in terms of morphology, chemical and phase composition between the MAO layers for each condition, and that there were no significant differences on the corrosion behaviour from potentiodynamic polarization curves, it is reasonable to assume that these differences were related to the distinct tribological contact due to different levels of macro-porosity. As the level of macro-porosity increased, the contact area with the counter-body decreased, leading to higher local contact pressures on the contact zones. In this way, higher contact pressures translated into higher mechanical damage on the contact points with the counter-body. On the other hand, since the contact with the counter-body was only on the protruded hard oxide zones on the MAO-treated surfaces, more stable evolution of COF values was observed.
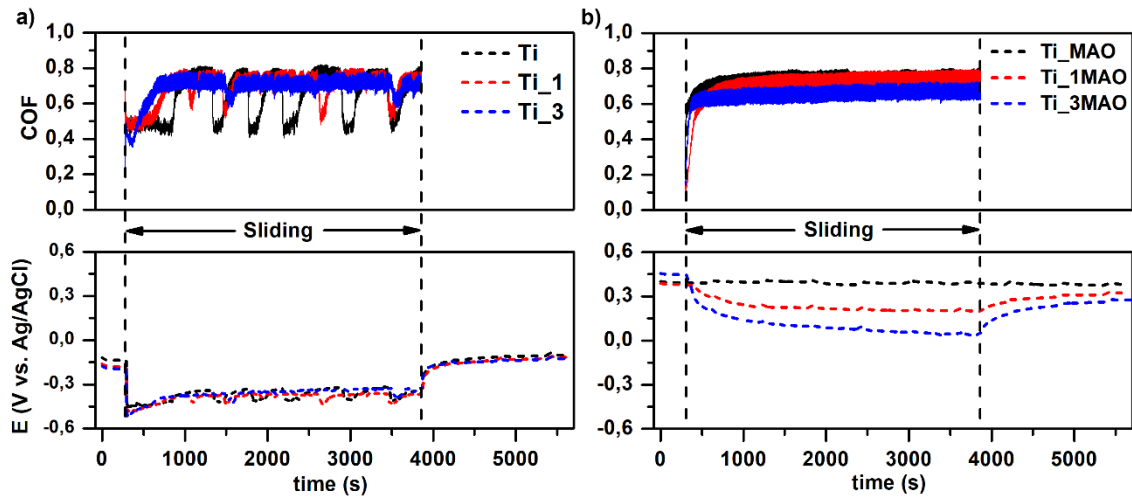
Figure 5.11. Evolution of OCP before, during and after sliding on the samples before (a) and after the second-step anodic treatments (b), with the respective COF values.

Metal ion release in the body may significantly alter several biological processes like osteoblastic cell viability and apoptosis as well as regulation of bone resorbing mediators [46]. The average ICP-AES results of the Ti ion concentration in the electrolyte after the tribocorrosion tests for Ti, Ti_1 and Ti_3 groups were 0.06, 0.10 and 0.11 mg/L, respectively. After the second-step, the results obtained for Ti ion concentration were 0.01, 0.02 and 0.03 mg/L for Ti_MAO, Ti_1MAO and Ti_3MAO, respectively. Results showed that metal ion release after the second-step anodic treatment was much lower than the one after the first-step. Decreased metal ion release on the bio-functionalized porous surfaces indicated that the oxide layer formed on the second-step protected the metal substrate. ICP-AES results for Ca ion concentration were 1.39, 1.54 and 1.92 mg/L, for Ti_MAO, Ti_1MAO and Ti_3MAO, respectively, whereas the values obtained for P ion concentration were 0.41, 0.46 and 0.66 mg/L for Ti_MAO, Ti_1MAO and Ti_3MAO, respectively. These results suggest that as the level of macro-porosity increased, the released amount of ions increased most probably due to the increased damage given at the contact zones due to the higher local contact pressures.

The tribocorrosion mechanisms proposed based on the microstructural, electrochemical and triboelectrochemical analysis of the worn surfaces are illustrated in Figure 5.12. Due to high reactivity of Ti, as well as due to its low tensile and shear strength, during sliding, micro-fractures may occur on the surface and consequently, large amounts of metal may be pulled out (adhesive wear) [47]. As sliding proceeds, pulled-out debris can be work hardened, as well, can be mixed with the oxidized wear debris (third-bodies). Afterwards, these mixed debris can be compacted on the worn surfaces, forming oxidized patches, whereas some of these debris may adhere on counter-body surfaces (Figure 5.9) that can abrade the metal leading to the formation of grooves on the worn surfaces (Figure 5.9), or move freely on the sliding surfaces, acting as third-body particles (Figure 5.12a). As also discussed above, it is suggested that oxidized patches gave a limited protection against corrosion, but as well, led to an increase in COF values. Evolution of COF and OCP values during sliding suggested that thickening and removal of the oxidized patches repeated several times during sliding.

After the first-step anodic treatment, similar mechanisms were also observed on the macro-porous surfaces, however, oxidized patches were less dense and the effect of third-body abrasive wear was reduced due to ejection of wear debris into the macro-pores, but at the same time, higher local contact pressures on the contact surfaces seemed to increase the severity of abrasive wear (Figure 5.12b).

Figure 5.12c presents the proposed wear mechanism for the MAO-treated Ti surfaces. As discussed above with the detailed SEM images, local damages were observed on the most pultruded zones of the MAO layer that had direct contact with the counter-body. A similar mechanism was also observed on the samples after two-step anodic treatment (Figure 5.12d). Due to the reduced contact area of the macro-porous surfaces, which was further reduced by the increased roughness of the anodic layer, higher contact pressures were obtained on the contact zones leading to more severe local damage, evidenced mainly by lower OCP under sliding, as compared to Ti_MAO samples. Ti_1MAO and Ti_3MAO samples presented a gradual decrease in OCP values during sliding, suggesting a gradual increase on the damage given to the MAO layer, whereas overall lower OCP values were observed on Ti_3MAO samples. Even

though, it is worthy to stress that Ti_3MAO samples still exhibited better tribocorrosion behaviour as compared to the samples after the first-step anodic treatment in terms of less visible total wear damage, less amount of released metallic ions and more positive OCP values during sliding.
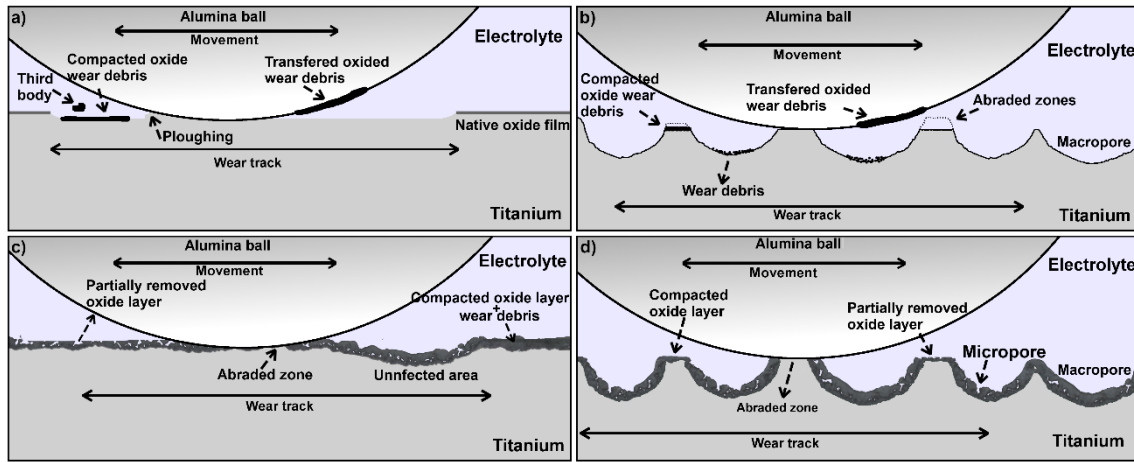
Figure 5.12. Schematic draws of the suggested tribocorrosion mechanisms for a) Ti, b) Ti after the first-step, c) Ti after the second-step and d) Ti after two-step anodic treatments.

5.4. Conclusions

A fast and simple two-step anodic treatment was used to obtain a macro-porous surface structure covered with a micro-porous Ca- and P-rich anodic layer. By increasing the treatment time of the first-step anodic treatment, bigger and more interconnected macro-porosity was obtained. After the second-step anodic treatment by MAO, multi-scale (micro- and macro-) porous surfaces exhibited a lower tendency to corrosion and more stable COF values under sliding, together with improved wettability. Therefore, this two-step anodic treatment can be considered as a versatile and low-cost technique to obtain multi-scale porous surfaces having potential of improved bioactivity and mechanical interlocking, along with their improved resistance to tribocorrosion. Nevertheless, before considering this treatment for biomedical implants, biomechanical stability and biological response of these surfaces should be explored.

Acknowledgements

References

[1]   Medical Implants Market- Global Opportunity Analysis and Industry Forecast, 2014 - 2022, (2016) 216.

[2]   A. Nouri, Titanium foam scaffolds for dental applications, Met. Foam Bone. (2017) 131–160.

[3]   G. Manivasagam, D. Dhinasekaran, A. Rajamanickam, Biomedical Implants: Corrosion and its Prevention - A Review, Recent Patents Corros. Sci. 2 (2010) 40–54.

[4]   M. Bruschi, D. Steinmüller-Nethl, W. Goriwoda, M. Rasse, Composition and Modifications of Dental Implant Surfaces, J. Oral Implant. (2015) 1–14.

[5]   F.A. España, V.K. Balla, S. Bose, A. Bandyopadhyay, Design and fabrication of CoCrMo alloy based novel structures for load bearing implants using laser engineered net shaping, Mater. Sci. Eng. C. 30 (2010) 50–57.

[6]   Y. Li, W. Wang, J. Duan, M. Qi, A super-hydrophilic coating with a macro/micro/nano triple hierarchical structure on titanium by two-step micro-arc oxidation treatment for biomedical applications, Surf. Coatings Technol. 311 (2017) 1–9.

[7]   A.C. Alves, R. Thibeaux, F. Toptan, A.M.P. Pinto, P. Ponthiaux, B. David, Influence of macroporosity on NIH/3T3 adhesion, proliferation, and osteogenic differentiation of MC3T3-E1 over bio-functionalized highly porous titanium implant material, J. Biomed. Mater. Res. - Part B Appl. Biomater. 107 (2019) 73–85.

[8]   L. Xu, K. Zhang, C. Wu, X. Lei, J. Ding, X. Shi, C. Liu, Micro-Arc Oxidation Enhances the Blood Compatibility of Ultrafine-Grained Pure Titanium, Materials (Basel). 10 (2017) 1446.

[9]   A.R. Ribeiro, F. Oliveira, L.C. Boldrini, P.E. Leite, P. Falagan-Lotsch, A.B.R.

Linhares, W.F. Zambuzzi, B. Fragneaud, A.P.C. Campos, C.P. Gouvêa, B.S. Archanjo, C.A. Achete, E. Marcantonio, L.A. Rocha, J.M. Granjeiro, Micro-arc oxidation as a tool to develop multifunctional calcium-rich surfaces for dental implant applications, Mater. Sci. Eng. C. 54 (2015) 196–206.

[10]   Y. Wang, H. Yu, C. Chen, Z. Zhao, Review of the biocompatibility of micro-arc oxidation coated titanium alloys, Mater. Des. 85 (2015) 640–652.

[11]   I.S. Park, T.G. Woo, W.Y. Jeon, H.H. Park, M.H. Lee, T.S. Bae, K.W. Seol, Surface characteristics of titanium anodized in the four different types of electrolyte, Electrochim. Acta. 53 (2007) 863–870.

[12]   M.D. Roach, R.S. Williamson, I.P. Blakely, L.M. Didier, Tuning anatase and rutile phase ratios and nanoscale surface features by anodization processing onto titanium substrate surfaces, Mater. Sci. Eng. C. 58 (2016) 213–223.

[13]   D. Velten, V. Biehl, F. Aubertin, B. Valeske, W. Possart, J. Breme, Preparation of TiO2 layers on cp-Ti and Ti6Al4V by thermal and anodic oxidation and by sol-gel coating techniques and their characterization, J Biomed Mater Res. 59 (2002) 18–28.

[14]   M. Fazel, H.R. Salimijazi, M.A. Golozar, M.R. Garsivaz jazi, A comparison of corrosion, tribocorrosion and electrochemical impedance properties of pure Ti and Ti6Al4V alloy treated by micro-arc oxidation process, Appl. Surf. Sci. 324 (2015) 751–756.

[15]   D. Quintero, O. Galvis, J.A. Calderón, J.G. Castaño, F. Echeverría, Control of the physical properties of anodic coatings obtained by plasma electrolytic oxidation on Ti6Al4V alloy, Surf. Coatings Technol. 283 (2015) 210–222.

[16]   L. Benea, E. Mardare-Danaila, M. Mardare, J.-P. Celis, Preparation of titanium oxide and hydroxyapatite on Ti–6Al–4V alloy surface and electrochemical behaviour in bio-simulated fluid solution, Corros. Sci. 80 (2014) 331–338.

[17]   A.C. Alves, F. Oliveira, F. Wenger, P. Ponthiaux, J.-P. Celis, L.A. Rocha, Tribocorrosion behaviour of anodic treated titanium surfaces intended for dental implants, J. Phys. D. Appl. Phys. 46 (2013) 404001.

[18]   I. da S.V. Marques, M.F. Alfaro, N.C. da Cruz, M.F. Mesquita, C. Sukotjo, M.T. Mathew, V.A.R. Barão, Tribocorrosion behavior of biofunctional titanium oxide films produced by micro-arc oxidation: Synergism and mechanisms, J. Mech. Behav. Biomed. Mater. 60 (2016) 8–21.

124

[19]   F.G. Oliveira, A.R. Ribeiro, G. Perez, B.S. Archanjo, C.P. Gouvea, J.R. Araújo, A.P.C. Campos, A. Kuznetsov, C.M. Almeida, M.M. Maru, C.A. Achete, P. Ponthiaux, J.-P. Celis, L.A. Rocha, Understanding growth mechanisms and tribocorrosion behaviour of porous TiO2 anodic films containing calcium, phosphorous and magnesium, Appl. Surf. Sci. 341 (2015) 1–12.

[20]   L. Benea, E. Danaila, P. Ponthiaux, Effect of titania anodic formation and hydroxyapatite electrodeposition on electrochemical behaviour of Ti-6Al-4V alloy under fretting conditions for biomedical applications, Corros. Sci. 91 (2015) 262–271.

[21]   F. Toptan, A.C. Alves, A.M.P. Pinto, P. Ponthiaux, Tribocorrosion behavior of bio-functionalized highly porous titanium, J. Mech. Behav. Biomed. Mater. 69 (2017) 144–152.

[22]   L. Xie, X. Liao, H. Xu, G. Yin, Z. Huang, Y. Yao, X. Chen, J. Gu, A facile one-step anodization treatment to prepare multi-level porous titania layer on titanium, Mater. Lett. 72 (2012) 141–144.

[23]   R. Zhou, D. Wei, W. Feng, S. Cheng, H. Yang, B. Li, Y. Wang, D. Jia, Y. Zhou, Bioactive coating with hierarchical double porous structure on titanium surface formed by two-step microarc oxidation treatment, Surf. Coatings Technol. 252 (2014) 148–156.

[24]   R. Zhou, D. Wei, J. Cao, W. Feng, S. Cheng, Q. Du, B. Li, Y. Wang, D. Jia, Y. Zhou, Conformal coating containing Ca, P, Si and Na with double-level porous surface structure on titanium formed by a three-step microarc oxidation, RSC Adv. 5 (2015) 28908–28920.

[25]   D.P. Mondal, S. Das, N. Jha, Dry sliding wear behaviour of aluminum syntactic foam, Mater. Des. 30 (2009) 2563–2568.

[26]   M. Gradzka-Dahlke, J.R. Dabrowski, B. Dabrowski, Characteristic of the porous 316 stainless steel for the friction element of prosthetic joint, Wear. 263 (2007) 1023–1029.

[27]   M. Gui, S. Bong, J. Moo, Influence of porosity on dry sliding wear behavior in spray deposited Al–6Cu–Mn/SiCp composite, Mater. Sci. Eng. A. 293 (2000) 146–156.

[28]   N. Cassillas, S. Charlebois, W. Smyrl, H. White, Pitting Corrosion of Titanium, Br. Corros. J. 7 (1972) 59–60.

[29]   C.M. Murphy, F.J. O'Brien, Understanding the effect of mean pore size on cell activity in collagen-glycosaminoglycan scaffolds, Cell Adhes. Migr. 4 (2010) 377–381.

[30]   R.F. do Prado, G.C. Esteves, E.L.D.S. Santos, D.A.G. Bueno, C.A.A. Cairo, L.G.O. De

Vasconcellos, R.S. Sagnori, F.B.P. Tessarin, F.E. Oliveira, L.D. De Oliveira, M.F.L. Villaça-Carvalho, V.A.R. Henriques, Y.R. Carvalho, L.M.R. De Vasconcellos, In vitro and in vivo biological performance of porous Ti alloys prepared by powder metallurgy, PLoS One. 13 (2018) e0196169.

[31]   H.E. Götz, M. Müller, A. Emmel, U. Holzwarth, R.G. Erben, R. Stangl, Effect of surface finish on the osseointegration of laser-treated titanium alloy implants, Biomaterials. 25 (2004) 4057–4064.

[32]   G. Li, L. Wang, W. Pan, F. Yang, W. Jiang, X. Wu, X. Kong, K. Dai, Y. Hao, In vitro and in vivo study of additive manufactured porous Ti6Al4V scaffolds for repairing bone defects, Sci. Rep. 6 (2016) 34072.

[33]   N. Taniguchi, S. Fujibayashi, M. Takemoto, K. Sasaki, B. Otsuki, T. Nakamura, T. Matsushita, T. Kokubo, S. Matsuda, Effect of pore size on bone ingrowth into porous titanium implants fabricated by additive manufacturing: An in vivo experiment, Mater. Sci. Eng. C. 59 (2016) 690–701.

[34]   C.M. Murphy, M.G. Haugh, F.J. O'Brien, The effect of mean pore size on cell attachment, proliferation and migration in collagen-glycosaminoglycan scaffolds for bone tissue engineering, Biomaterials. 31 (2010) 461–466.

[35]   A.C. Alves, F. Wenger, P. Ponthiaux, J.-P. Celis, A.M. Pinto, L.A. Rocha, J.C.S. Fernandes, Corrosion mechanisms in titanium oxide-based films produced by anodic treatment, Electrochim. Acta. 234 (2017) 16–27.

[36]   A.L. Yerokhin, X. Nie, A. Leyland, A. Matthews, S.J. Dowey, Plasma electrolysis for surface engineering, Surf. Coatings Technol. 122 (1999) 73–93.

[37]   N. Eliaz, N. Metoki, N. Eliaz, N. Metoki, Calcium Phosphate Bioceramics: A Review of Their History, Structure, Properties, Coating Technologies and Biomedical Applications, Materials (Basel). 10 (2017) 334.

[38]   O. Banakh, T. Journot, P.A. Gay, J. Matthey, C. Csefalvay, O. Kalinichenko, O. Sereda, M. Moussa, S. Durual, L. Snizhko, Synthesis by anodic-spark deposition of Ca- and P- containing films on pure titanium and their biological response, Appl. Surf. Sci. 378 (2016) 207–215.

[39]   L. Wang, G.H. Nancollas, Calcium Orthophosphates: Crystallization and Dissolution, Chem. Rev. 108 (2008) 4628–4669.

[40]   S. Kim, H. Ryu, H. Shin, H.S. Jung, K.S. Hong, In situ observation of hydroxyapatite

126

nanocrystal formation from amorphous calcium phosphate in calcium-rich solutions, Mater. Chem. Phys. 91 (2005) 500–506.

[41]   O. Zywitzki, T. Modes, H. Sahm, P. Frach, K. Goedicke, D. Glöß, Structure and properties of crystalline titanium oxide layers deposited by reactive pulse magnetron sputtering, Surf. Coatings Technol. 180–181 (2004) 538–543.

[42]   E. Anitua, R. Prado, G. Orive, R. Tejero, Effects of calcium-modified titanium implant surfaces on platelet activation, clot formation, and osseointegration., J. Biomed. Mater. Res. A. 103A (2015) 969–980.

[43]   J.I. Rosales-Leal, M.A. Rodríguez-Valverde, G. Mazzaglia, P.J. Ramón-Torregrosa, L. Díaz-Rodríguez, O. García-Martínez, M. Vallecillo-Capilla, C. Ruiz, M.A. Cabrerizo-Vílchez, Effect of roughness, wettability and morphology of engineered titanium surfaces on osteoblast-like cell adhesion, Colloids Surfaces A Physicochem. Eng. Asp. 365 (2010) 222–229.

[44]   R.A. Gittens, L. Scheideler, F. Rupp, S.L. Hyzy, J. Geis-Gerstorfer, Z. Schwartz, B.D. Boyan, A review on the wettability of dental implant surfaces II: Biological and clinical aspects, Acta Biomater. 10 (2014) 2907–2918.

[45]   J.I. Silva, A.C. Alves, A.M. Pinto, F. Toptan, Corrosion and tribocorrosion behavior of Ti–TiB–TiNx in-situ hybrid composite synthesized by reactive hot pressing, J. Mech. Behav. Biomed. Mater. 74 (2017) 195–203.

[46]   G.O. Alrabeah, P. Brett, J.C. Knowles, H. Petridis, The effect of metal ions released from different dental implant-abutment couples on osteoblast function and secretion of bone resorbing mediators, J. Dent. 66 (2017) 91–101.

[47]   B.R. Waterhouse, M.H. Wharton, Titanium and Tribology, Ind. Lubr. Tribol. 26 (1974) 20–23.

Chapter 6. Effect of bio-functional MAO layers on the electrochemical behaviour of highly porous Ti

A.C. Alves[a], **A.I. Costa**[a], F. Toptan[a,b,c], J.L. Alves[a,b], I. Leonor[d,e], E. Ribeiro[d,e], R.L. Reis[d,e], A.M.P. Pinto[a,b], J.C.S. Fernandes[f,g]

[a]CMEMS-UMinho – Center of MicroElectroMechanical Systems – Universidade do Minho, Campus de Azurém, Guimarães, Portugal

[b]DEM – Department of Mechanical Engineering – Universidade do Minho, Campus de Azurém, Guimarães, Portugal

[c]IBTN/Br – Brazilian Branch of the Institute of Biomaterials, Tribocorrosion and Nanomedicine, UNESP, Campus de Bauru, Bauru, SP, Brazil

[d]3B's Research Group – Biomaterials, Biodegradables and Biomimetics, Universidade do Minho, Guimarães, Portugal

[e]ICVS/3B's-PT Government Assoc. Laboratory, Universidade do Minho, Campus de Azurém, Braga/Guimarães, Portugal

[f]Department of Chemical Engineering – Instituto Superior Técnico, Universidade de Lisboa, Lisboa, Portugal

[g]CQE – Instituto Superior Técnico, Lisboa, Portugal

Abstract

Ti foams are attractive for orthopaedic applications due to reduced Young's modulus and ability of bone-ingrowth. However, poor corrosion behaviour and lack of bioactivity are yet to be overcome. In the present work, highly porous Ti samples were processed by powder metallurgy with space holder technique and bio-functionalized by micro-arc oxidation, resulting in nano- and micro-structured TiO_2 surfaces containing bioactive elements. The electrochemical behaviour of these bio-functionalized highly porous Ti surfaces was evaluated through potentiodynamic polarization and EIS in physiological solution at body temperature. Results showed that bio-functionalization

improved the corrosion behaviour of highly porous Ti. However, increased macro-porosity led to an increased corrosion rate.

6.1. Introduction

Ti-based materials are commonly used as orthopaedic and dental implant materials due to their properties, as excellent biocompatibility, high specific strength, high corrosion resistance, low density and relatively low Young's modulus [1–6]. However, these materials still present the risk of implant aseptic loosening or bone failure, mainly due to stress-shielding effect that is caused by the inefficient load transfer from the implant to the bone [7–9]. The stress-shielding effect occurs due to the mismatch of Young's modulus between the implant material (Ti: 100–110 GPa, Ti-6Al-4V: 114 GPa) and human bones (4–30 GPa) [3,7,8].

Porous Ti structures presenting open-cellular structure are being developed in order to decrease this mismatch but also to allow the new bone-ingrowth and the transport of body fluids [10–14]. Moreover, as reported by Jha *et al.* [15], open-cellular structures also show potential for drug delivery applications. One of the most suitable methods for processing Ti foams is space holder technique. This method is cost-effective and allows to adjust the porosity level, pores geometry and pores size distribution [15–18].

Studies regarding characterization of porous metallic implants in terms of microstructural, mechanical and biological properties are widely reported in the literature [19–24]. However, reports on their electrochemical behaviour are still scarce [1,22,23]. Some studies showed that the corrosion behaviour of porous materials may be different from dense materials, mainly due to the existence of localized corrosion as a result of the stagnation of the electrolyte inside the pores [22,23], or due to the differences in the nature and quality of the passive films formed on the outermost surfaces and on the inner pore surfaces [1].

Although Ti is the most biocompatible metallic material, it is also bioinert thus, it cannot induce bone growth. With the aim of addressing this issue, several surface

130

modification approaches have been developed such as micro-arc oxidation (MAO) [24–34]. MAO does not only lead to a better corrosion behaviour but also can improve the bioactivity of Ti through the creation of tailored surfaces in terms of chemical composition, nano- and micro-porosity and topography [24–26,28–36]. Furthermore, during MAO treatment it is possible to incorporate bioactive elements, as Ca and/or P, allowing to reach a Ca/P ratio similar to hydroxyapatite (HAP) on the anodic layers. After MAO treatment, HAP may be precipitated by a hydrothermal treatment, which is reported to improve the bioactivity [27–30,37–39]. Nevertheless, the studies on the bio-functionalization of highly porous Ti surfaces by anodic treatment are still very limited [3,20,40,41]. Yavari *et al.* [20] studied the effect of alkali-acid heat and acid-alkali treatments on compression and fatigue behaviour of porous Ti-6Al-4V alloy processed by selective laser melting. The authors stated that the acid-alkali treatment leads to substantial mass loss when compared with alkali-acid heat treatment, and thus it notably modify the porous Ti-6Al-4V structures mechanical properties. On the other hand, Fan *et al.* [41] processed porous Ti scaffolds by powder metallurgy using space holder technique followed by anodic and heat treatments. The authors stated that anatase nanotubes were successfully produced on Ti scaffold, which improved the biocompatibility due to their apatite-formation ability.

The present study is a following work of these authors. Previous studies on bio-functionalized highly porous Ti showed that both outermost and inner pore surfaces were successfully covered by MAO layers leading to a lower corrosion susceptibility, both under static conditions and under sliding. The authors attributed this behaviour not only to the improved corrosion resistance provided by the MAO layers but also to the increased hardness, leading to higher wear resistance, of those layers [3]. Moreover, although no clear effect of bio-functionalization was found on cell viability, enhanced cell proliferation and activity was reported for bio-functionalized highly porous Ti having 22% of porosity [42]. Although it is well reported that MAO treatment on Ti surfaces improves the corrosion behaviour, the electrochemical response of bio-functionalised highly-porous Ti is yet to be known. Therefore, this study aimed at understanding the electrochemical behaviour of 3D macro-porous architecture having bio-functionalized surfaces developed by MAO with the incorporation of Ca and P.

6.2. Experimental procedure

6.2.1. Processing

Dense Ti samples were produced using angular shaped Ti powders (Grade 2, Alfa Aesar, D50 = 36 μm) and as a binder it was used polyvinyl alcohol (PVA, Sigma Aldrich Chemistry). For highly porous Ti samples, angular shaped urea particles (Scharlau, <500 μm) were used as a space holder.

Firstly, Ti powders and PVA (0.4 $_{vol}$%) were manually mixed, then 0, 30 or 50 $_{vol}$% of urea was added to the mixture. In order to get a homogeneous mixture, the powders were mixed in a ball mill rotating with Al_2O_3 spheres at 130 rpm for 4 h. The blended powders were then uniaxially pressed in a zinc stearate lubricated nitrided stainless steel die under 350 MPa for 2 min. The green compacts (12 mm in diameter and 3 mm in thickness) were subjected to two thermal cycles. The first one at 450 °C during 3 h under Ar atmosphere was performed to remove the binder and the space holder. Then, the samples were sintered in vacuum (better than 10^{-5} mbar at 1100 °C during 3 h). The heating and cooling rates were set to 5 °C min^{-1}. Thermal analysis/thermal gravimetric (DTA/TG) and dilatometric tests were carried out to select the binder and space holder as well as sintering temperatures and this analysis was presented elsewhere [1].

6.2.2. Bio-functionalization by micro-arc oxidation

In order to achieve similar surface roughness to the highly porous samples, dense Ti samples were grounded using SiC papers with 180 mesh. Both dense and highly porous samples were ultrasonically cleaned in acetone for 3 min and etched in Kroll's reagent (V_{HF}:V_{HNO_3}:V_{H_2O} = 2:10:88) for 1 min. After the etching procedure, the samples were immediately cleaned ultrasonically in propanol for 10 min followed by 5 min in distilled water and dried with warm air.

The bio-functionalization treatment by MAO was performed in an electrolyte consisting of a mixture of 0.02 M of β-glycerophosphate disodium salt pentahydrate, (β-GP; Alfa Aesar) and 0.35 M of calcium acetate monohydrate (CA; Alfa Aesar), as P and

Ca ions source, respectively. Dense and highly porous Ti samples were used as anode (geometric area of 3.39 cm^2) and completely immersed in the electrolyte, while a Pt plate was used as cathode (exposed area 12.57 cm^2). The anode and cathode were placed 8 cm apart and connected to a DC power supply (GPR-30H10D). The total MAO treatment time was 1 min with a selected voltage of 300 V. A magnetic stirrer rotating at 200 rpm was used to create a turbulent flow regime. After the bio-functionalization, all samples were cleaned in an ultrasonic bath in propanol and distilled water and dried as described previously.

6.2.3. Electrochemical tests

Open circuit potential (OCP), potentiodynamic polarization and electrochemical impedance spectroscopy (EIS) tests were performed to assess the electrochemical behaviour of all groups of samples. All electrochemical tests were performed in a physiological solution consisting of 9 g/L of NaCl at body temperature (37 ± 2 °C) as presented in Figure 6.1. The electrochemical cell was placed in a climate chamber, which kept the temperature constant and acted as a Faraday cage in order to avoid any external currents. Sample surfaces were used as working electrode, a platinum wire was used as a counter electrode while a saturated calomel electrode (SCE) was used as reference electrode, connected to a Reference 600 potentiostat/galvanostat/ZRA from Gamry Instruments. All potentials are given with respect to SCE.

All samples were immersed in the electrolyte and allowed to rest for 24 h. OCP, EIS and potentiodynamic polarization measurements were performed sequentially. OCP was continuously measured and was considered stable when ΔE<60 mV h^{-1}. Then, at 24 h, EIS was performed at the last registered OCP with frequencies ranging from 10^5 till 10^{-2} Hz, with 7 points per frequency decade. A sinusoidal signal with an amplitude of 10 mV was chosen in order to ensure the linearity of the electrode response. After EIS measurements, the OCP was measured during 10 min, followed by the potentiodynamic polarization tests that started at -0.250 V$_{OCP}$ and went up to 1 V$_{SCE}$ with a scanning rate of 1 mV s^{-1}. The potentiodynamic polarization parameters were chosen in a way to determine the passivation current densities and to understand the stability of the anodic

layers within the range of potentials that are reported to be relevant in human body [43,44].

To guarantee the repeatability of the results, all these experiments were repeated at least three times and the results are presented as average ± standard deviation.
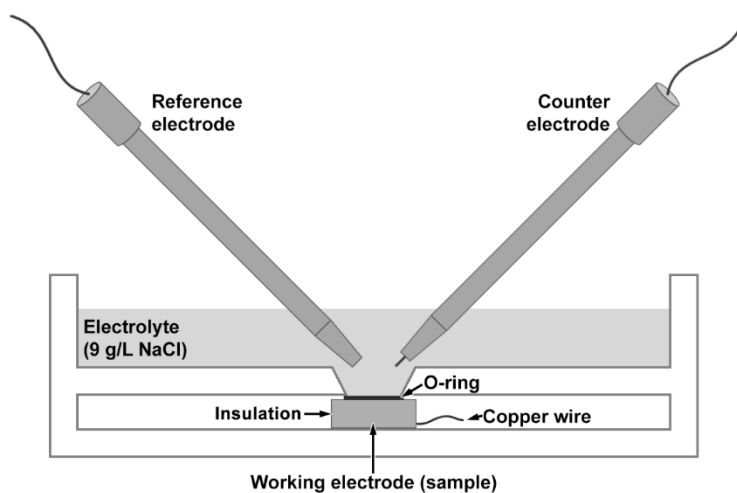
Figure 6.1. Schematic representation of the electrochemical test setup.

6.2.4. Characterization

The topography, microstructure and chemical composition of as-processed and bio-functionalized samples were analysed by SEM using a FEI Nova 200 equipped with energy dispersive X-ray spectroscopy (EDS).

The porosity morphology and distribution of pores of highly porous Ti samples were characterized by micro-computed tomography (micro-CT) by using X-view X 50-CT (North Star Imaging) micro-CT system, under the accelerating voltage of 50 KV and a tube current of 400 µA. For each bulk sample, 1200 projections were taken over 360° (0.3° range) with an exposure time of 3 s for each projection. A CMOS image sensor (3888 × 3072 pixels) coupled to CsI scintillator was used for detecting the transmission beam. The samples were scanned with 17 µm × 17 µm pixel size, allowing a field of view of around 3 cm. Reconstruction was done with 2400 TIFF projections, where the average scanning time was 90 min per sample.

A point-counting technique based on ASTM E562 was used to calculate the number and pores size distribution of the anodic layers. This method consisted in a grid having 17 lines parallel to each other with a constant distance between them of 0.03

mm that was superimposed on a SEM micrograph. All the pores intersecting the lines were counted and their diameters were measured. From each group of bio-functionalized samples, three SEM micrographs were taken in different zones of the surface's samples and five samples were used per group of samples. The groups of samples are presented in Table 6.1 together with the nominal porosity, real porosity and surface treatment.

Table 6.1. Samples under study, nominal porosity, real porosity and surface treatment.

Group	Nominal Porosity (as urea vol%)	Real Porosity (%) [1]	Surface Treatment
Ti	-	0.4	Etched
Ti22	30	22	Etched
Ti37	50	37	Etched
Ti-AT	-	0.4	Bio-functionalized
Ti22-AT	30	22	Bio-functionalized
Ti37-AT	50	37	Bio-functionalized

The cross-section of the anodic layers was analysed using a FIB-SEM (Auriga Compact, ZEISS). Gallium ions at 30 keV were used to section the surface, with a 5 nA current up to a depth of approximately 20 μm and to clean the edge of the cross-section, with 1 nA currents.

The real exposed metallic area to the electrolyte for highly porous samples was determined from the voxelized true geometry of the porous sample derived from the raw data acquired by micro-CT. After the 3D reconstruction, grayscale data of the voxels was submitted to the following procedure: *i.* denoising by a Gaussian technique; *ii.* segmentation of the full 3D domain between (0) world (outside domain), (1) matrix (Ti) and (2) void (pores), based on a simple threshold technique, with the threshold value determined from the histogram of images from the material + voids domain. After segmentation and being known the 3D geometry of the porous sample, an arbitrary flat surface was selected. Following the experimental procedure, the free subsurface area delimited by the o-ring is numerically flooded, as well as all void voxels in contact with the flooded region. By the end, the area of the interface between the void flooded

region and the matrix was simply integrated by counting the number of elementary surfaces (voxel faces) of the flooded region–matrix interface.

6.3. Results

6.3.1. As-processed surfaces

Previous results [1] had shown that, for the same processing conditions, approximately 80% of the pores in both highly porous Ti samples ranged from 50–350 μm. Although Ti22 group presented an average pore size of 230 μm, the average pore size of Ti37 samples was slightly lower, around 200 μm. Microstructural and 3D tomographic investigations revealed that Ti22 samples mainly presented closed pores, while Ti37 samples showed a mixture of open (interconnected) and closed pores. Considering its importance on the electrochemical tests, the real metallic area exposed to the electrolyte was calculated using the micro-CT data. For a geometric area of 0.38 cm^2 the real metallic area exposed to electrolyte was 1.18 cm^2 and 14.8 cm^2 for Ti22 and Ti37, respectively. It was observed on the 3D reconstructions that the flooded region did not pass completely through the sample on Ti22. However, since Ti37 samples contained a mixture of open and closed pores, whatever the first flat surface selected on 3D reconstructions, the flooded region always crossed completely the sample, meaning that the upper and lower surfaces were always linked by the void region (Figure 6.2). Thus, these calculated real exposed areas were used to normalize the electrochemical data.
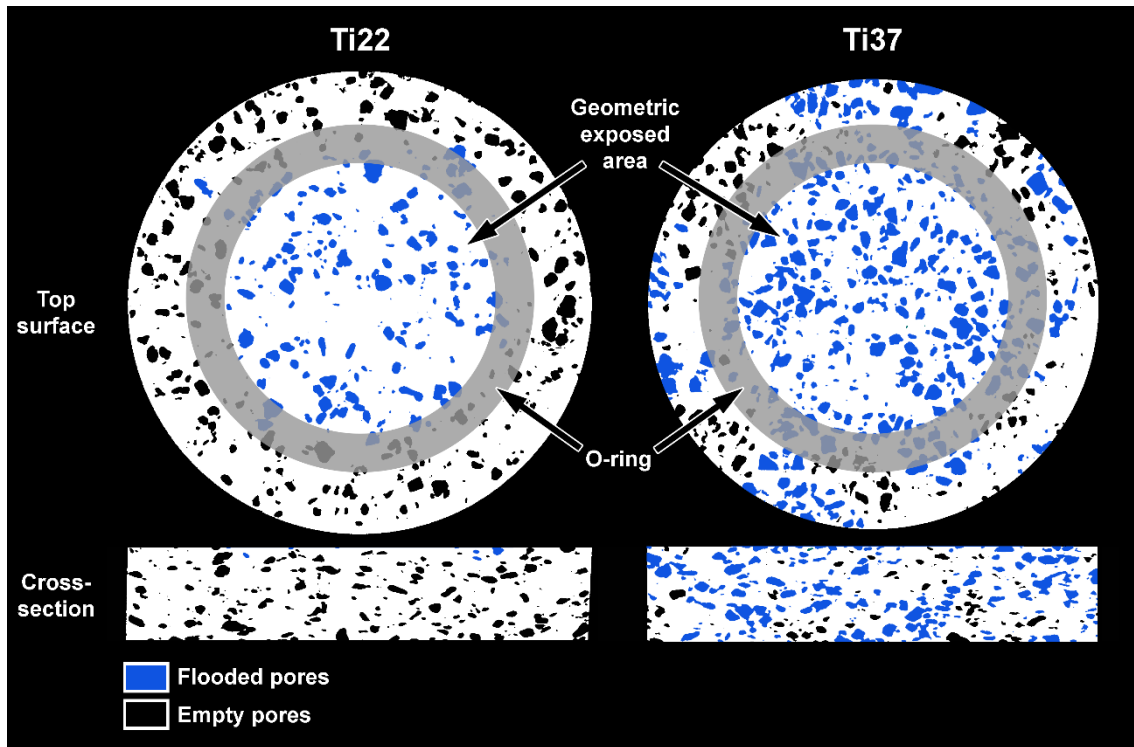
Figure 6.2. Surface and cross-section tomographic slice images showing the exposed geometric area for the electrochemical tests and the simulation of flooded pores by electrolyte.

6.3.2. Current density evolution with anodic treatment time

The current density evolution during the MAO treatment at 300 V is given in Figure 6.3. All curves showed two different regions: In region I, the current was constant (limiting current of 2.6 A, which was the maximum current provided by the power supply) until the system reached the selected potential (300 V). When 300 V was reached (moment indicated as $t_{gal/pot}$), the anodic treatment turned to constant voltage control and a decrease on current values was observed (region II), thus, the formation of micro-arcs and evolution of gas in the system started [34]. Moreover, it was observed that the density of micro-arcs decreased while the current fell. The parameter $t_{gal/pot}$ corresponds to the time at which the final potential is reached, being 13 ± 1, 23 ± 1 and 48 ± 1 seconds for Ti, Ti22 and Ti37, respectively. Higher levels of porosity led $t_{gal/pot}$ to increase probably due to the increased exposed metallic area. However, the current density is not significantly different for all group of samples.
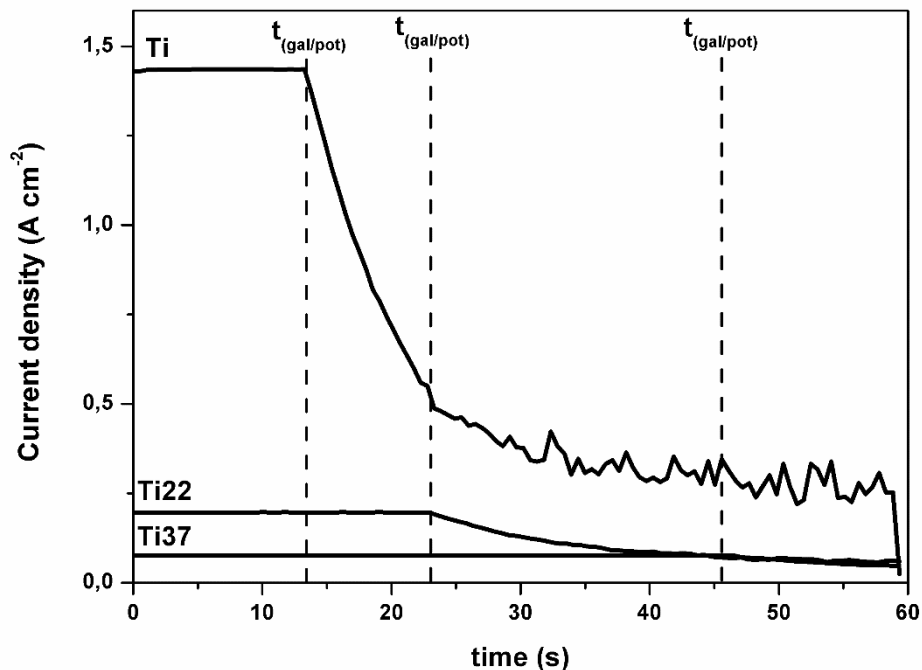
Figure 6.3 Current density evolution during the anodic treatment at 300 V.

6.3.3. As-etched and bio-functionalized surfaces

Figure 6.4 presents the SEM micrograph of as-etched and bio-functionalized surfaces. As previously reported by some of the present authors [1,3], along with the induced porosity, residual porosity was presented in all etched surfaces (Figures 6.4b and 6.4c), being typical on the conventional powder metallurgy processing method. On the other hand, as already reported by some of the present authors [1], the difference between the nominal porosity (30 and 50%) and the measured porosity (22 and 37%, respectively) is attributed to shrinkage, which increased as the amount of the space holder was increased. The grinding marks on the as-etched Ti surfaces (Figure 6.4a) were still visible after etching. However, after anodic treatment, those grinding marks were disappeared (Figure 6.4d) and a multiscale porous structure was obtained. It has also been previously reported that after anodic treatment the surface roughness had increased from 0.63 to 1.27 μm [3]. The volcano-like porous structure, typical of micro-arc treated surfaces, was observed in all samples. Moreover, in the case of Ti22-AT and Ti37-AT (Figures 6.4e–f), the uppermost pore surfaces were successfully covered by the

anodic layers formed during the bio-functionalization process. The size of the pores of the anodic layers ranged from approximately 0.6 to 2.9 μm, in accordance with the values reported in the literature [34,35].

The ratio of Ca/P ($_{wt}$%), based on EDS analysis, is 3.44 ± 0.15, 3.38 ± 0.23 and 3.46 ± 0.40 for Ti-AT, Ti22-AT and Ti37-AT, respectively. Moreover, the crystalline structure of the anodic layers processed under identical conditions was previously characterized as a mixture of anatase and rutile [3].
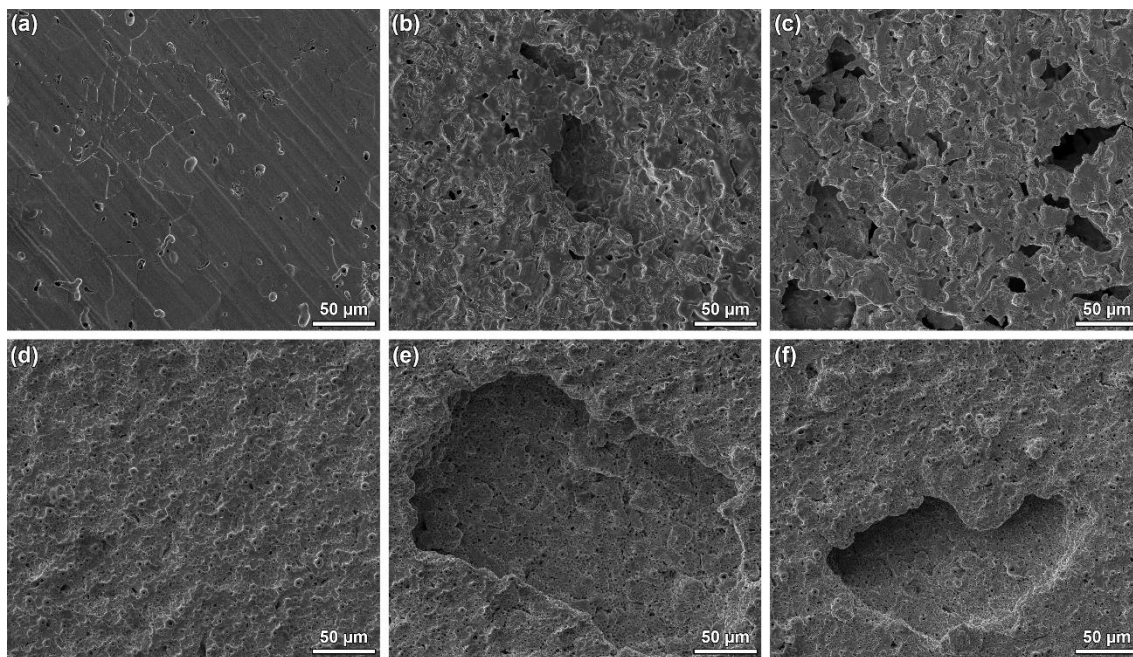
Figure 6.4. Secondary electron SEM images of the as-etched (a–c) and bio-functionalized (d–f) Ti, Ti22 and Ti37 samples, respectively.

In this study, Ti-AT samples presented the largest pores size distribution, ranging from 0.60 to 3.68 μm, while for porous bio-functionalized samples it ranged from 0.24 to 2.91 and from 0.21 to 2.58 μm for Ti22-AT and Ti37-AT, respectively (Figure 6.5). Most of the pores on Ti-AT had a diameter between 1.0 and 1.5 μm. In the case of Ti22-AT and Ti37-AT, the pore sizes decreased, with diameters between 0.5 and 1.0 μm. Also, the number of pores per geometric surface area was different comparing Ti-AT and Ti22-AT/Ti37-AT groups, namely $(9.2 ± 2.3) \times 10^3$ pores mm^{-2} for Ti-AT and $(11.7 ± 1.6) \times 10^3$ and $(11.9 ± 1.7) \times 10^3$ pores mm^{-2} for Ti22-AT and Ti37-AT, respectively. Thus, within the bio-functionalized samples, there was a slight increase on the number of pores from

dense to porous samples. However, no significant differences were observed between Ti22-AT and Ti37-AT.
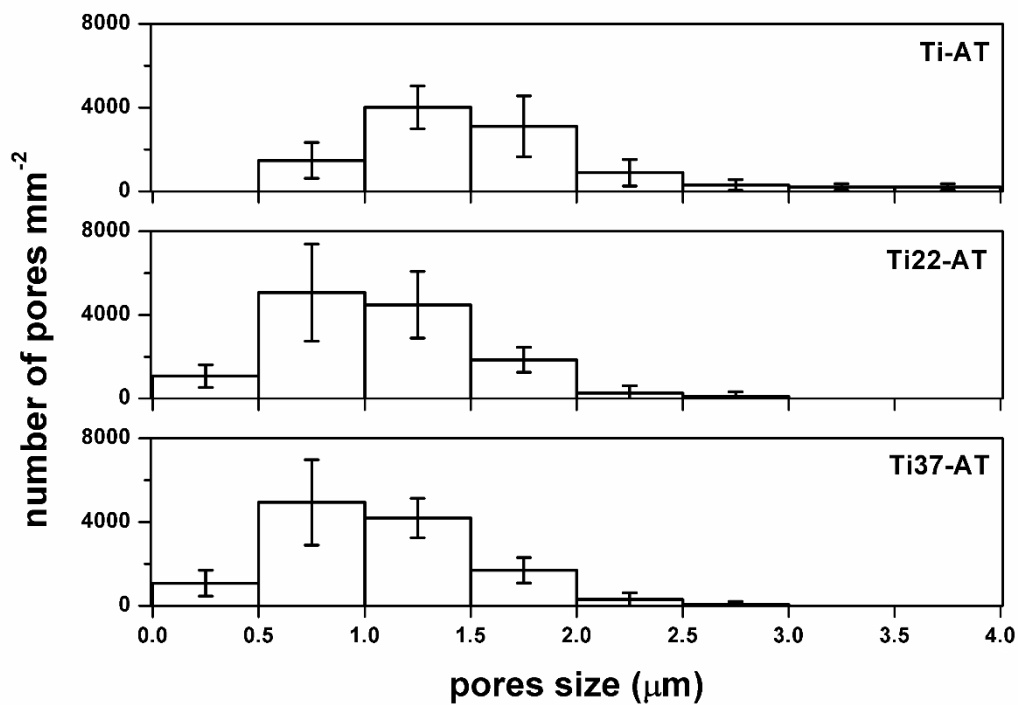
Figure 6.5. Pores size distribution on the bio-functionalized samples.

Representative SEM micrographs of FIB-prepared cross-sections of the anodic layers formed on the outermost surfaces are presented in Figure 6.5. The anodic layer formed in both dense and highly porous Ti samples presented a triplex structure, where no significant differences were observed, at least on the outermost surface. The barrier film is formed at metal–oxide interface in the first seconds of the anodic treatment. This barrier film is followed by two porous layers, an inner porous layer that is characterized by small pores and an outer porous layer that presents larger pores [35]. All anodic layers with the triplex structure presented an average overall thickness of approximately 2.50 μm. However, in the most inner pores, the formed anodic layer may present some heterogeneities, most probably due to the difficulty of the electrolyte to wet all the exposed metallic area in the case of highly porous samples.

140
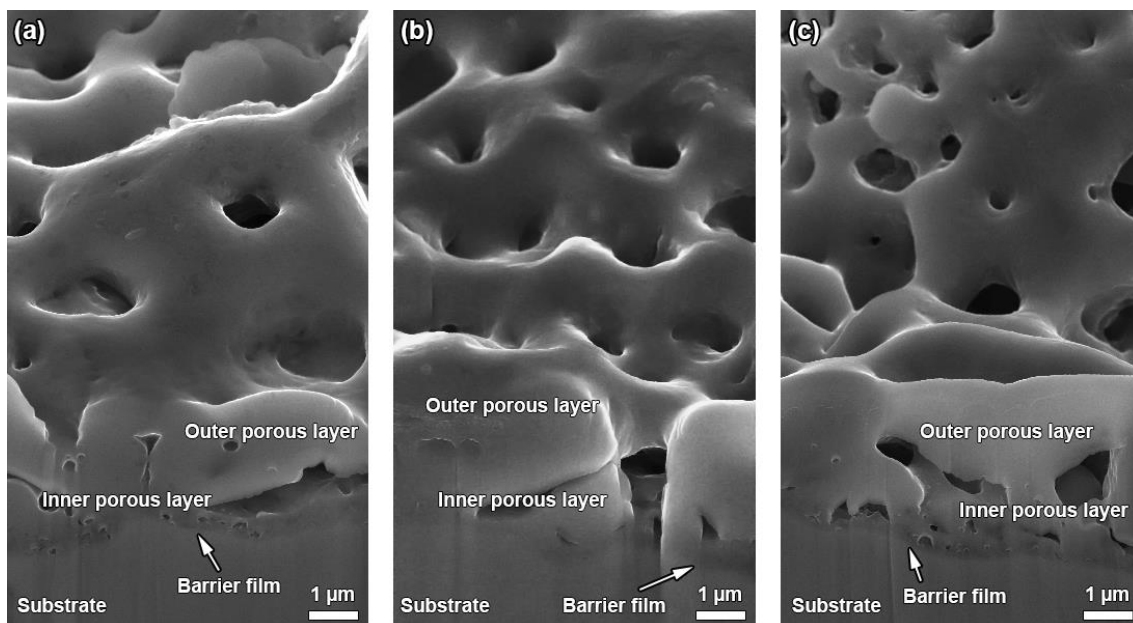
Figure 6.6. SE-SEM images of FIB-prepared cross-sections of the anodic layers for: a) Ti-AT, b) Ti22-AT and c) Ti37-AT samples.

6.3.4. Electrochemical behaviour

OCP, EIS and potentiodynamic polarization measurements were performed sequentially. After the immersion of each sample, the evolution of its OCP was monitored for 24 h and a stable condition was assumed when the potential drift became lower than 60 mV.h^{-1}. The OCP values recorded during the last hour of monitoring, just before the EIS measurement, are presented in Figure 6.7. It was observed on the as-etched samples that increased porosity led to a decrease on the corrosion susceptibility by presenting values of OCP less negative for the highest level of porosity (Ti37). On the other hand, the bio-functionalized samples presented nobler values than as-etched samples, showing a lower tendency to corrosion, although this difference samples was not significant on Ti37.
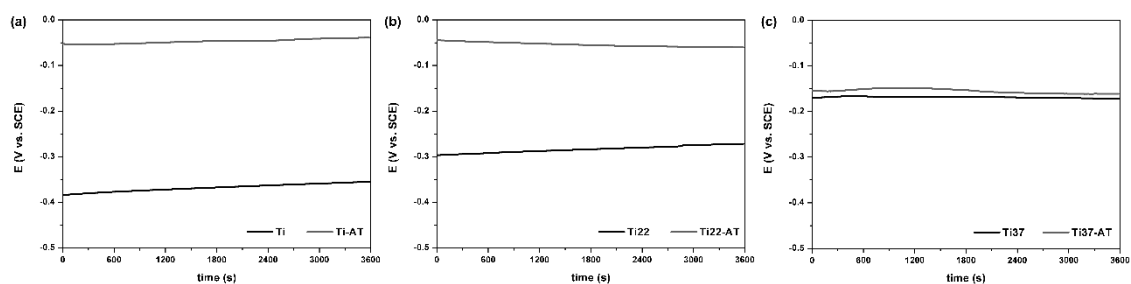
Figure 6.7. OCP evolution with immersion time for all samples in NaCl (9 g/L) at body temperature.

Figure 6.8 shows the representative potentiodynamic polarization curves of as-etched and bio-functionalized samples and Table 6.2 presents the average OCP (average of the last 10 min of monitoring), corrosion potential (E_{corr}) and passivation current density (i_{pass}) taken as the respective current density at 0.4 V_{SCE}. As-etched Ti showed the lowest corrosion potential and a well-defined passivation plateau starting at approximately 0.1 V_{SCE}. The E_{corr} showed a clear improvement from Ti to Ti-AT samples. Bio-functionalized Ti showed a passivation plateau starting from *ca* -0.1 V_{SCE} to 0.39 V_{SCE}, followed by a slight increase of the current, which may be related to the dissolution of calcium and phosphorus on the MAO layer. The passivation current density showed a decrease of almost two orders of magnitude from Ti to Ti-AT samples. As-etched highly porous Ti samples presented E_{corr} slightly nobler than Ti. Even though no well-defined passivation plateau was recorded, these groups of samples presented a passivation region, where a slow increase of the current density rate on the anodic domain around 10^{-5} A cm^{-2} was observed.
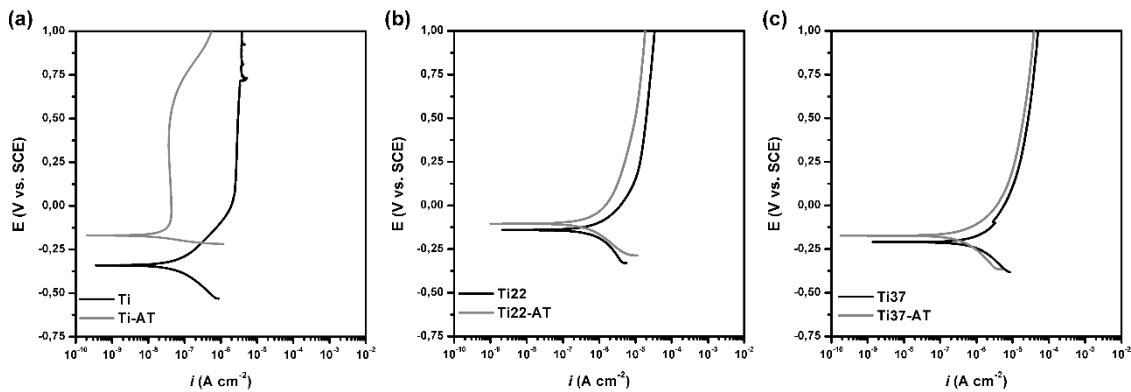
Figure 6.8. Potentiodynamic polarization curves of a) Ti, b) Ti22 and c) Ti37 as-etched and bio-functionalized samples immersed in NaCl (9 g/L) at body temperature.

Table 6.2. Open circuit potential, corrosion potential E_{corr} and passivation current density (i_{pass}) values for all groups of samples.

	Ti	Ti-AT	Ti22	Ti22-AT	Ti37	Ti37-AT
E_{OCP} (mV$_{SCE}$)	-354 ± 9	-32 ± 22	-174 ± 90	-82 ± 57	-157 ± 34	-136 ± 30
E_{corr} (mV$_{SCE}$)	-356 ± 12	-152 ± 41	-170 ± 96	-109 ± 29	-186 ± 40	-196 ± 36
i_{pass} (µA cm^{-2})	3.24 ± 0.95	0.05 ± 0.02	13.33 ± 3.62	5.89 ± 1.72	26.50 ± 5.05	17.97 ± 1.90

Figure 6.9 shows the electrochemical impedance spectra for as-etched and bio-functionalized samples in the forms of Bode (Figures 6.9a–c) and Nyquist (Figures 6.9d–f) diagrams, respectively. Comparing the Nyquist diagrams, an increase can be observed on the diameter of the semicircle from as-etched to bio-functionalized samples. This behaviour suggests a better corrosion resistance of bio-functionalized samples. Constant values of |Z| and phase angles close to 0° were obtained in the Bode diagrams for all as-etched samples at the high frequencies range, being the typical response of the electrolyte resistance. Independently of the porosity level, just one time constant was observed. In low and middle frequency range, the typical capacitive behaviour of a compact oxide film was observed by the phase angle values approaching -90° for Ti. Regarding Ti22 and Ti37, the phase angle approached to -70° and -50°, respectively. This is an effect of the decrease of exponent n_{ox} of the CPE, in agreement with the higher heterogeneity of an increasingly porous material.

Concerning the bio-functionalized samples, all groups presented three time constants, two corresponding to middle-high frequencies, where the phase angle approached to -40°, -30° and -20° for Ti-AT, Ti22-AT and Ti37-AT, respectively. The third one (low frequencies) was characterized by an increase of the phase angle (-80° and -60° for Ti-AT and Ti22-AT, respectively) with the exception of Ti37-AT, where no significant difference was observed on the phase angle from high to low frequencies, due to the larger values of the electrolyte resistance.
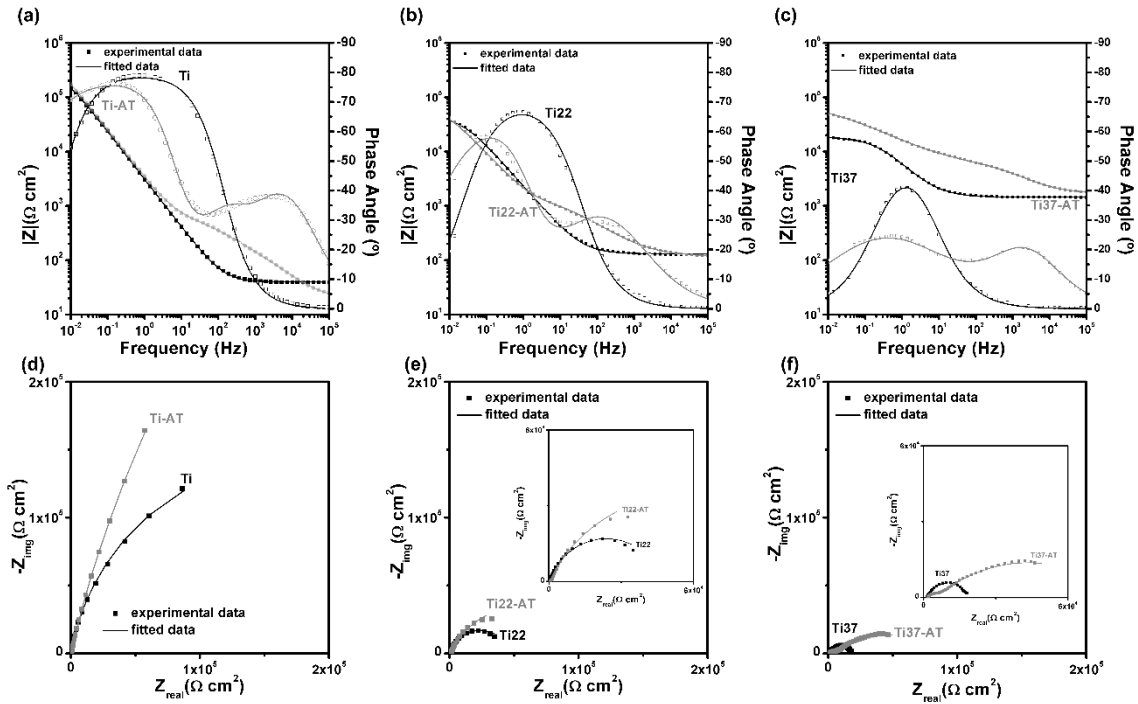
Figure 6.9. EIS spectra in the form: (a–c) Bode and (e–f) Nyquist diagrams recorded on as-etched and bio-functionalized Ti, Ti22 and Ti37 samples immersed in NaCl (9 g/L) at body temperature.

Figure 6.10a gives the schematic representation of the electrical equivalent circuit (EEC) used for fitting the EIS results of as-etched samples. An $R_e(R_{ox}Q_{ox})$ circuit was used to represent the native oxide film formed on exposed sample surfaces, where R_e is the electrolyte resistance, R_{ox} is the native oxide film resistance and Q_{ox} is a constant phase element (CPE), considering a non-ideal capacitance of the native oxide film. The schematic representation of the EEC used for fitting the EIS results of bio-functionalized samples is presented in Figure 6.9b. The presented EEC was recently proposed by some of the present authors to fit EIS results for commercial pure Ti, bio-functionalized by MAO under conditions similar to those used in the present study [35]. In this EEC, the barrier film is represented by a resistor R_{bf} and a constant phase element Q_{bf}. Regarding the porous layers, the intact porous wall (outer porous layer, Figures 6.6 and 6.10) and the porous wall under the outer pores (inner porous layer, Figure 6.6 and 6.10) are represented by Q_{wall} and $Q_{1/2wall}$, respectively. No resistor was considered in parallel with these CPEs as the thickness of the corresponding layers was too high, leading to a very high resistance, as electronic conduction is almost impossible. Moreover, the overall electrolyte resistance was represented by R_e, together with the additional resistances of the electrolyte inside the outer pores ($R_{e'}$) and inner pores ($R_{e''}$).

144

R$_e$: Electrolyte resistance
R$_e$' and R$_e$": Additional electrolyte resistances
R$_{ox}$: Native oxide film resistance
R$_{bf}$: Barrier film resistance

Q$_{ox}$: CPE of the native oxide film
Q$_{1/2\ wall}$: CPE of the inner porous wall
Q$_{wall}$: CPE of the outer porous wall
Q$_{bf}$: CPE of the barrier film
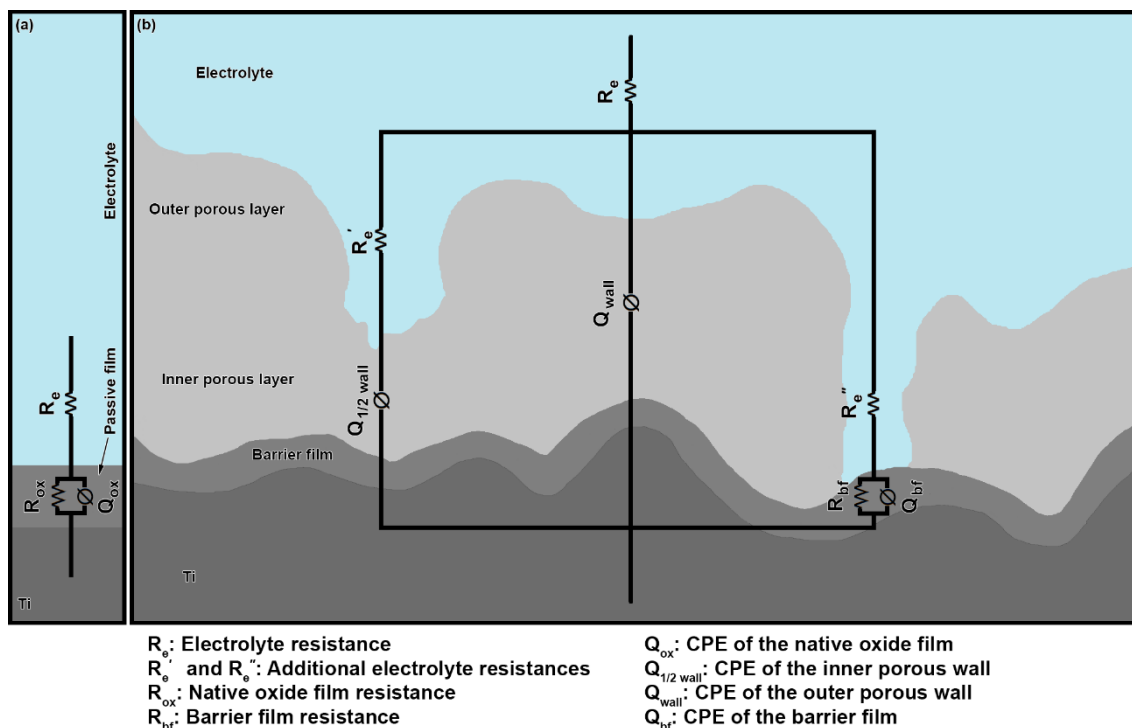
Figure 6.10. Equivalent circuit for fitting EIS results for a) as-etched and b) bio-functionalized samples.

In order to allow the representation of a non-ideal capacitor, a CPE was used in the fitting. The impedance of CPE is defined as: $Z_{CPE} = [Y_0(j\omega)^n]^{-1}$, where $-1 \leq n \leq 1$. For $n = 1$, $n = 0$, or $n = -1$ the CPE response corresponds to a capacitor, a resistor or an inductor, respectively. A non-ideal capacitor may be described by a CPE if $n \sim 1$. However, it is known that the surface roughness and its heterogeneities influence the n values. All as-etched samples presented n values higher than 0.90 in the case of dense Ti, while for porous samples the n values were always higher than 0.74. Regarding the bio-functionalized samples, the lowest n was 0.71. All the impedance spectra were fitted to these circuits using Zview software (version 2.9) and the quality of the fittings was evaluated by their chi-square values. All as-etched samples presented chi-square below 10^{-4} and in the case of the bio-functionalized samples the chi-square was below 10^{-3}. The EEC parameters obtained from EIS data for as-etched and bio-functionalized samples are presented in Table 6.3.

Table 6.3. Equivalent circuit parameters obtained from EIS data for all groups of samples.

Samples	R_{ox} (MΩ cm^2)	Q_{ox} (x10^{-5} F cm^{-2} s^{n-1})	n_{ox}	Q_{bf} (x10^{-5} F cm^{-2} s^{n-1})	n_{bf}	$Q_{1/2wall}$ (x10^{-6} F cm^{-2} s^{n-1})	$n_{1/2wall}$	Q_{wall} (x10^{-6} F cm^{-2} s^{n-1})	n_{wall}
Ti	0.52 ± 0.16	4.25 ± 1.84	0.91 ± 0.03	-		-		-	
Ti22	0.16 ± 0.14	7.03 ± 3.69	0.80 ± 0.01	-		-		-	
Ti37	0.02 ± 0.01	4.21 ± 0.97	0.74 ± 0.02	-		-		-	
Ti-AT	-	-		1.26 ± 0.09	0.85 ± 0.08	9.59 ± 2.17	0.80 ± 0.04	5.74 ± 2.87	0.71 ± 0.01
Ti22-AT	-	-		2.06 ± 0.38	0.73 ± 0.09	38.81 ± 3.70	0.82 ± 0.09	5.43 ± 0.38	0.72 ± 0.05
Ti37-AT	-	-		0.52 ± 0.06	0.84 ± 0.01	31.87 ± 1.05	0.76 ± 0.01	5.73 ± 0.07	0.73 ± 0.04

6.4. Discussion

6.4.1. Bio-functionalization

MAO treatment has two distinct stages. In the first stage, anodic layer formation proceeds as the conventional anodic treatment mechanism where a compact and thin oxide film is formed. Then, when the dielectric breakdown potential is reached, oxide phases such as anatase and rutile are formed as a result of the extremely high temperatures that are locally reached at the metal–electrolyte interface due to the micro-arcs that occur at that interface [45]. Moreover, the transformation of metastable anatase to stable rutile is facilitated by the frequent micro-discharges. On the other hand, the formed oxides present low thermal conductivity, which increases the local temperature, thus further transformation of anatase to rutile is also promoted, as reported by Wang *et al.* [46]. However, some studies [32,35] show that decreased electrolyte conductivity may increase the amount of rutile phase. Although increased macro-porosity level led to an increase on the galvanostatic control, no differences were observed on the anatase/rutile ratio. During the galvanostatic control, the highest current was reached and kept constant until the selected voltage was reached. However, the remaining sparks were probably more energetic than the previous ones and therefore, the transformation of anatase to rutile occurred.

By increasing the duration of galvanostatic control (i.e. for longer $t_{gal/pot}$), it is considered that the thickness of the barrier film (thin and compact oxide film) increased, as shown by the decrease of Q_{bf} values (Table 6.3) from Ti-AT to Ti22-AT and Ti37-AT. In theory, longer galvanostatic regions lead to an increase on the total charge of the system ($Q = I \times t$), which would influence the amount of oxide formed during this stage of the process. On the other hand, on the second stage (when currents fall), higher currents are usually associated to thinner oxide films [32]. However, the increase of total charge did not account for a significant difference in the thickness of the MAO layer (at least on the outermost surface, Figure 6.5). Also, from the cross-sections obtained for the samples from each group, it was not possible to observe any visible effects in the compactness of the oxide. On the other hand, micro-pores were formed at high voltages (exceeding the electrochemical breakdown potential) and the species present in the

electrolyte were incorporated into the porous oxide layer [27–31]. Consequently, MAO process resulted in porous surfaces with a wide range of pore sizes [33,37] presenting the well-known volcano-like structures. Furthermore, it is known that using a mixture of CA and β-GP as electrolyte in MAO leads to incorporation of elements as Ca and P in the porous oxide layers, being one advantage of the MAO treatment since the presence of bioactive elements as Ca and P may improve the bioactivity of Ti [24–31,38].

6.4.2. Electrochemical behaviour

Results showed that porosity affected the corrosion behaviour of highly porous Ti samples where increased i_{corr} values were observed for Ti22 and Ti37 samples, in accordance with the literature [1,47–49]. Some of the present authors [1] have previously explained these differences by the effect of porosity on the formation rate of the passive oxide layer. Moreover, several authors working on the corrosion behaviour of porous metallic materials have stated the difficulties on calculating the real metallic area exposed to the electrolyte solution [50–55]. In the present work, a model has been used for the accurate calculation of the real metallic exposed area. However, this model does not consider the oxygen/air entrapped in the most inner pores either the difficulty of electrolyte penetration into these pores, which may lead to different passive states on the native oxide film. Nevertheless, the corrosion rate of highly porous structures is not just influenced by the surface area. Although Ti is known for its high resistance to localized corrosion, and the localized breakdown of its passive film occurs at relatively higher potentials [56], the effect of the highly porous architecture on localized corrosion is yet to be fully understood. Some authors [50–53] stated that the increased corrosion density with the increased porosity level is due to the larger surface area in contact with the electrolyte, but crevices or restrictions to the flow of species into the interconnected pores can result in corrosion rates that are not proportional to the real contact surface area. In this respect, Blackwood *et al.* [53] stated that the attempts to accurately assess the true effective surface area directly wetted by the electrolyte are not enough to understand the corrosion behaviour of the highly porous metallic structures, since they do not take into account the restrictions on the flow of species. Although these difficulties may result in increased corrosion kinetics, excellent passivation

148

characteristics are still reported in the literature for porous Ti structures [50–52,55]. On the other hand, Seah *et al.* [50] also reported decreased corrosion susceptibility (less negative values of E_{corr}) with increasing amount of porosity, since the interconnected pores promoted the free flow of ionic species, whereas isolated pores trapped the electrolyte and exhausted the oxygen supply, resulting in a thinner oxide film. Apart from electrolyte penetration, entrapped air and free flow of species, as Damborenea *et al.* [43] reported for the Ti-6Al-4V scaffolds processed by direct metal laser sintering (DMLS), that the three-dimensional architecture of the scaffolds might also have an influence on their corrosion behaviour, due to the presence of edges and vertices in the samples that may lead to different corrosion response when compared with flat surfaces.

The decreased values on |Z| and phase angle from Ti to Ti22 and Ti37 were probably due to the difference in the nature of the passive film. Recently, some of the present authors [1] reported two time constants for porous Ti samples: the first on middle frequencies representing the response of the most external pores and the second time constant on the low frequencies characterizing the inner pores. Due to their complex geometry, the most inner surfaces may lead to a slower and more difficult penetration of the electrolyte. In the referred study [1], the authors used a conventional three-electrode electrochemical cell (adapted from ASTM G3-89), where the samples were placed vertically. In order to overcome the difficulty of removal of entrapped oxygen, which limits the electrolyte penetration into the inner pores, and to facilitate the formation of a more homogeneous passive film, the testing set-up was changed, and the samples were placed horizontally, as shown in Figure 6.1. The average values of the native oxide film capacitance were increased from Ti to Ti22 samples, but no relevant differences were found between Ti and Ti37 samples. On the other hand, R_{ox} values decreased with increased porosity, independently of the porosity level. These results showed that although a passive film was formed on Ti surfaces and inside pores, it presented different corrosion resistance. In principle, this behaviour would be assigned to a deterioration of the protective nature of the oxide film, but in the present case it is important to stress that a huge increase in the surface area occurred in the porous materials leading to different passive states at the surface and inside the pores, as

evidenced by the differences on the phase angles for the highly porous samples (Figure 6.9).

Research on porous materials is not new and, in particular, there has been previous research published on the general topic of porosity and about its effect on the electrochemical results [1,22,23]. This work departs from previously existing knowledge and tries to obtain a deeper insight on the behaviour of these materials. Impedance results for complex systems may be difficult to interpret just based on the visual analysis of Nyquist or Bode spectra. This has led to a large number of analysis strategies whose discussion was not intended in this manuscript and that may include the use of special-purpose graphics or the modification of the data. As an example, the methodology, recently proposed by Tribollet [57], where the Bode plots were obtained after subtracting the ohmic impedance, leads to a complete modification of the phase plot at high frequencies, revealing processes (and corresponding time constants) that might be hidden in the original spectrum. This has happened in the present work with the as-etched samples, where a fine analysis has shown that, instead of the proposed one time constant equivalent circuit, a ladder model with two time constants could be more appropriated to account for the effect of porosity. However, this effect was so subtle that the corresponding time constant was not evident in the spectrum and, for the sake of simplicity in the analysis, the one-time constant circuit was maintained. On the other hand, the evolution of the parameters of a three or four time constant system may not reflect easily on the corresponding spectra. Thus, just a discussion of the effects of porosity on the Bode plots is not straightforward. Moreover, several degenerated equivalent circuits may be used for three time constants, resulting in similar spectra, even if they have no physical meaning. Thus, for the choice of an equivalent circuit, there is a need for more information than that exclusively provided by the impedance spectra, in particular that originating from the morphology and structure of the system. Therefore, in the present work it is not easy to establish a cause-effect relationship between the analysis of the spectra and the choice of the proposed equivalent circuits. The strategy is then to propose a circuit that leads to an appropriate fitting of the results, with meaningful parameters, in the expected orders of magnitude, and that, by establishing the correspondence of each circuit element with a physical process, may explain the behaviour of the sample.

It is very well reported in the literature that MAO treatment improves the corrosion behaviour of Ti, along with bioactivity [29,31–34,37,58]. In the present study, a clear improvement was observed on the dense Ti, whereas the improvement was relatively limited on the highly porous samples. This behaviour may be explained by the complexity of the system, having a highly porous structure including interconnected pores. It is acceptable to assume that the most inner pores might not be reached by the electrolyte during the anodic treatment [3]. Consequently, the most inner pores might not be uniformly covered by the typical anodic layers. Even though, a slight improvement was obtained on the porous samples after bio-functionalization, namely on the corrosion potential and corrosion current density.

The lowest Q_{bf} values were found for Ti37-AT samples, while a slight increase from Ti-AT to Ti22-AT samples was observed (Table 6.3). This behaviour may be explained by the increased galvanostatic conditions where the barrier film was formed. Ikonopisov [59] stated that the breakdown voltage is practically independent of the current density. Recently, Mathis *et al.* [45] showed that, under galvanostatic conditions, micro-arc initiation voltages observed were similar to the ones obtained during potentiodynamic scans. The authors also suggested three stages of galvanostatic conditions: *i.* the formation of an inner barrier inner layer leading to a sharp increase of voltage with time; *ii.* increase of the voltage and formation of first micro-arcs; and finally, *iii.* the stabilization of the voltage and transformation of the micro-arcs into large energetic arcs. Thus, the lower values of Q_{bf} for Ti37-AT were probably due to the increased $t_{gal/pot}$ giving longer time for barrier film formation. Moreover, due to the complexity of the porous sample geometry, the Q values might be affected as the surface area significantly increased with increased porosity. Nevertheless, the Q_{wall} values were always lower when compared with $Q_{1/2wall}$, which may result from the lower thickness of the oxide corresponding to $Q_{1/2wall}$. Assuming a parallel plate capacitor, the dependence of the capacitance with thickness is given as $C = \varepsilon\varepsilon_0 A/d$, where ε is the dielectric constant, ε_o the vacuum permittivity, A is the surface area and d is the thickness, so a thinner layer will lead to higher capacitances. Furthermore, no relevant differences were found for Q_{wall} values with increased porosity, showing the ability to form the anodic layers on the outermost porous surfaces. However, an increase on $Q_{1/2wall}$ values was found for bio-functionalized porous samples, probably due to the fact that the anodic layer might not

be homogenously formed on the most inner pores. When the Q_{bf} of the bio-functionalized samples was compared with the as-etched Q_{ox} values, it was noticed that the Q_{bf} values were always lower than Q_{ox}, showing the improvement in the corrosion behaviour by the anodic treatment.

Although the anodic layers formed on the outermost surfaces did not exhibit significant differences between dense and highly porous Ti (Figure 6.6), there is still a lack of knowledge on the structure of the inner pores, where the anodic layer may not be fully formed. Anyway, the present values seem to be easily explained considering the above factors. Nevertheless, to get a deeper understanding on the electrochemical behaviour of bio-functionalized highly porous Ti, long-time immersion tests involving OCP monitoring and periodic EIS measurements in physiological solution should be performed on samples having more levels of macro-porosity, together with potentiodynamic tests after different immersion times. On the other hand, there is a need to understand the morphology, composition and homogeneity of the anodic layers formed on the most inner pores, as a function of macro-porosity.

6.5. Conclusions

The effect of macro-porosity on the composition, structure and electrochemical behaviour of the bio-functionalized highly porous Ti was studied. Within the limitations of this work, it is concluded that the presence of macro-porosity did not deteriorate the bio-functionalization treatment, on which regards chemical composition (Ca/P ratio) and layer structure. The electrochemical behaviour of highly porous samples was improved by the bio-functionalization treatment in terms of thermodynamic and kinetics. The improved corrosion behaviour of bio-functionalized highly porous samples was mostly due to the barrier film formed under longer galvanostatic control during the anodic treatment.

Acknowledgments

References

[1]   A.C. Alves, I. Sendão, E. Ariza, F. Toptan, P. Ponthiaux, A.M.P. Pinto, Corrosion behaviour of porous Ti intended for biomedical applications, J. Porous Mater. 23 (2016) 1261–1268.

[2]   E. Butev, Z. Esen, S. Bor, In vitro bioactivity investigation of alkali treated Ti6Al7Nb alloy foams, Appl. Surf. Sci. 327 (2015) 437–443.

[3]   F. Toptan, A.C. Alves, A.M.P. Pinto, P. Ponthiaux, Tribocorrosion behavior of bio-functionalized highly porous titanium, J. Mech. Behav. Biomed. Mater. 69 (2017) 144–152.

[4]   M. Zuldesmi, A. Waki, K. Kuroda, M. Okido, High Osteoconductive Surface of Pure Titanium by Hydrothermal Treatment, J. Biomater. Nanobiotechnol. 04 (2013) 284–290.

[5]   Y. Torres, S. Lascano, J. Bris, J. Pavón, J.A. Rodriguez, Development of porous titanium for biomedical applications: A comparison between loose sintering and space-holder techniques, Mater. Sci. Eng. C. 37 (2014) 148–155.

[6]   A. Mansourighasri, N. Muhamad, A.B. Sulong, Processing titanium foams using tapioca starch as a space holder, J. Mater. Process. Technol. 212 (2012) 83–89.

[7]   Y. Torres, P. Trueba, J.J. Pavón, E. Chicardi, P. Kamm, F. García-Moreno, J.A. Rodríguez-Ortiz, Design, processing and characterization of titanium with radial graded porosity for bone implants, Mater. Des. 110 (2016) 179–187.

[8]   G.G. Lima, G.B. Souza, C.M. Lepienski, N.K. Kuromoto, Mechanical properties of anodic titanium films containing ions of Ca and P submitted to heat and hydrothermal treatment, J. Mech. Behav. Biomed. Mater. 64 (2016) 18–30.

[9]   C. Simoneau, P. Terriault, B. Jetté, M. Dumas, V. Brailovski, Development of a porous metallic femoral stem: Design, manufacturing, simulation and mechanical testing, Mater. Des. 114 (2017) 546–556.

[10]   Q. Fu, Y. Hong, X. Liu, H. Fan, X. Zhang, A hierarchically graded bioactive scaffold bonded to titanium substrates for attachment to bone, Biomaterials. 32 (2011) 7333–7346.

[11]   M.A. Lopez-Heredia, E. Goyenvalle, E. Aguado, P. Pilet, C. Leroux, M. Dorget, P. Weiss, P. Layrolle, Bone growth in rapid prototyped porous titanium implants., J. Biomed. Mater. Res. A. 85 (2008) 664–73.

[12]   L. Mullen, R.C. Stamp, W.K. Brooks, E. Jones, C.J. Sutcliffe, Selective Laser Melting: a regular unit cell approach for the manufacture of porous, titanium, bone in-growth constructs, suitable for orthopedic applications., J. Biomed. Mater. Res. B. Appl. Biomater. 89 (2009) 325–34.

[13]   B. Li, Z. Li, X. Lu, Effect of the macro-pore structure on the anodic polarization behavior of porous titanium, Anti-Corrosion Methods Mater. 59 (2012) 57–62.

[14]   Y. Tian, S. Ding, H. Peng, S. Lu, G. Wang, L. Xia, P. Wang, Osteoblast growth behavior on porous-structure titanium surface, Appl. Surf. Sci. 261 (2012) 25–30.

[15]   N. Jha, D.P. Mondal, J. Dutta Majumdar, A. Badkul, A.K. Jha, A.K. Khare, Highly porous open cell Ti-foam using NaCl as temporary space holder through powder metallurgy route, Mater. Des. 47 (2013) 810–819.

[16]   L. Bolzoni, T. Weissgaerber, B. Kieback, E.M. Ruiz-Navas, E. Gordo, Mechanical behaviour of pressed and sintered CP Ti and Ti-6Al-7Nb alloy obtained from master alloy addition powder, J. Mech. Behav. Biomed. Mater. 20 (2013) 149–161.

[17]   M. Sharma, G.K. Gupta, O.P. Modi, B.K. Prasad, A.K. Gupta, Titanium foam through powder metallurgy route using acicular urea particles as space holder, Mater. Lett. 65 (2011) 3199–3201.

[18]   B.Q. Li, C.Y. Wang, X. Lu, Effect of pore structure on the compressive property of porous Ti produced by powder metallurgy technique, Mater. Des. 50 (2013) 613–619.

[19]   B. Lee, T. Lee, Y. Lee, D.J. Lee, J. Jeong, J. Yuh, S.H. Oh, H.S. Kim, C.S. Lee, Space-holder effect on designing pore structure and determining mechanical properties in porous titanium, Mater. Des. 57 (2014) 712–718.

[20]   S. Amin Yavari, S.M. Ahmadi, J. van der Stok, R. Wauthle, A.C. Riemslag, M.

154

Janssen, J. Schrooten, H. Weinans, A.A. Zadpoor, Effects of bio-functionalizing surface treatments on the mechanical behavior of open porous titanium biomaterials, J. Mech. Behav. Biomed. Mater. 36 (2014) 109–119.

[21]   K. Kato, S. Ochiai, A. Yamamoto, Y. Daigo, K. Honma, S. Matano, K. Omori, Novel multilayer Ti foam with cortical bone strength and cytocompatibility., Acta Biomater. 9 (2013) 5802–9.

[22]   R. Menini, M. Dion, S.K.V. So, M. Gauthier, L.-P. Lefebvre, Surface and Corrosion Electrochemical Characterization of Titanium Foams for Implant Applications, J. Electrochem. Soc. 153 (2006) 13–21.

[23]   F.X. Xie, X.B. He, S.L. Cao, X. Lu, X.H. Qu, Structural characterization and electrochemical behaviour of a laser-sintered porous Ti-10Mo alloy, Corros. Sci. 67 (2013) 217–224.

[24]   S.A. Alves, R. Bayón, V.S. de Viteri, M.P. Garcia, A. Igartua, M.H. Fernandes, L.A. Rocha, Tribocorrosion Behavior of Calcium- and Phosphorous-Enriched Titanium Oxide Films and Study of Osteoblast Interactions for Dental Implants, J. Bio- Tribo-Corrosion. 1 (2015) 23.

[25]   H.P. Felgueiras, L. Castanheira, S. Changotade, F. Poirier, S. Oughlis, M. Henriques, C. Chakar, N. Naaman, R. Younes, V. Migonney, J.P. Celis, P. Ponthiaux, L.A. Rocha, D. Lutomski, Biotribocorrosion (tribo-electrochemical) characterization of anodized titanium biomaterial containing calcium and phosphorus before and after osteoblastic cell culture, J. Biomed. Mater. Res. Part B Appl. Biomater. 103 (2015) 661–669.

[26]   A.R. Ribeiro, F. Oliveira, L.C. Boldrini, P.E. Leite, P. Falagan-Lotsch, A.B.R. Linhares, W.F. Zambuzzi, B. Fragneaud, A.P.C. Campos, C.P. Gouvêa, B.S. Archanjo, C.A. Achete, E. Marcantonio, L.A. Rocha, J.M. Granjeiro, Micro-arc oxidation as a tool to develop multifunctional calcium-rich surfaces for dental implant applications, Mater. Sci. Eng. C. 54 (2015) 196–206.

[27]   H. Ishizawa, M. Fujino, M. Ogino, Mechanical and histological investigation of hydrothermally treated and untreated anodic titanium oxide films containing Ca and P, J. Biomed. Mater. Res. 29 (1995) 1459–68.

[28]   H. Ishizawa, M. Fujino, M. Ogino, Histomorphometric evaluation of the thin hydroxyapatite layer formed through anodization followed by hydrothermal treatment.,

J. Biomed. Mater. Res. 35 (1997) 199–206.

[29]   H. Ishizawa, M. Ogino, Characterization of thin hydroxyapatite layers formed on anodic titanium oxide films containing Ca and P by hydrothermal treatment, J. Biomed. Mater. Res. 29 (1995) 1071–9.

[30]   H. Ishizawa, M. Ogino, Hydrothermal precipitation of hydroxyapatite on anodic titanium oxide films containing Ca and P, J. Mater. Sci. 34 (1999) 5893–5898.

[31]   H. Ishizawa, M. Ogino, Formation and characterization of anodic titanium oxide films containing Ca and P., J. Biomed. Mater. Res. 29 (1995) 65–72.

[32]   F.G. Oliveira, A.R. Ribeiro, G. Perez, B.S. Archanjo, C.P. Gouvea, J.R. Araújo, A.P.C. Campos, A. Kuznetsov, C.M. Almeida, M.M. Maru, C.A. Achete, P. Ponthiaux, J.-P. Celis, L.A. Rocha, Understanding growth mechanisms and tribocorrosion behaviour of porous TiO2 anodic films containing calcium, phosphorous and magnesium, Appl. Surf. Sci. 341 (2015) 1–12.

[33]   I.S. Park, T.G. Woo, W.Y. Jeon, H.H. Park, M.H. Lee, T.S. Bae, K.W. Seol, Surface characteristics of titanium anodized in the four different types of electrolyte, Electrochim. Acta. 53 (2007) 863–870.

[34]   D. Quintero, O. Galvis, J.A. Calderón, J.G. Castaño, F. Echeverría, Effect of electrochemical parameters on the formation of anodic films on commercially pure titanium by plasma electrolytic oxidation, Surf. Coatings Technol. 258 (2014) 1223–1231.

[35]   A.C. Alves, F. Wenger, P. Ponthiaux, J.-P. Celis, A.M. Pinto, L.A. Rocha, J.C.S. Fernandes, Corrosion mechanisms in titanium oxide-based films produced by anodic treatment, Electrochim. Acta. 234 (2017) 16–27.

[36]   A.C. Alves, F. Oliveira, F. Wenger, P. Ponthiaux, J.-P. Celis, L.A. Rocha, Tribocorrosion behaviour of anodic treated titanium surfaces intended for dental implants, J. Phys. D. Appl. Phys. 46 (2013) 404001.

[37]   I.S. Park, T.S. Bae, K.W. Seol, Surface Characteristics of Anodized and Hydrothermally Treated Titanium with an Increasing Concentration of Calcium Ion, Met. Mater. Int. 12 (2006) 399–406.

[38]   L.-H. Li, Y.-M. Kong, H.-W. Kim, Y.-W. Kim, Improved biological performance of Ti implants due to surface modification by micro-arc oxidation, Biomaterials. 25 (2004) 2867–2875.

[39]   L. Benea, E. Mardare-Danaila, M. Mardare, J.-P. Celis, Preparation of titanium

156

oxide and hydroxyapatite on Ti–6Al–4V alloy surface and electrochemical behaviour in bio-simulated fluid solution, Corros. Sci. 80 (2014) 331–338.

[40]   M. Teixeira, A.C. Alves, F.S. Silva, A.M. Pinto, F. Toptan, Microstructural Characterization of Biofunctionalized Titanium Foams, Microsc. Microanal. 21 (2015) 55–56.

[41]   X. Fan, B. Feng, J. Weng, J. Wang, X. Lu, Processing and properties of porous titanium with high porosity coated by bioactive titania nanotubes, Mater. Lett. 65 (2011) 2899–2901.

[42]   A.C. Alves, R. Thibeaux, F. Toptan, A.M.P. Pinto, P. Ponthiaux, B. David, Influence of macroporosity on NIH/3T3 adhesion, proliferation, and osteogenic differentiation of MC3T3-E1 over bio-functionalized highly porous titanium implant material, J. Biomed. Mater. Res. - Part B Appl. Biomater. 107 (2019) 73–85.

[43]   J.J. de Damborenea, M.A. Larosa, M.A. Arenas, J.M. Hernández-López, A.L. Jardini, M.C.F. Ierardi, C.A.C. Zavaglia, R.M. Filho, A. Conde, Functionalization of Ti6Al4V scaffolds produced by direct metal laser for biomedical applications, Mater. Des. 83 (2015) 6–13.

[44]   S. Virtanen, I. Milosev, E. Gomez-Barrena, R. Trebse, J. Salo, Y.T. Konttinen, Special modes of corrosion under physiological and simulated physiological conditions., Acta Biomater. 4 (2008) 468–76.

[45]   A. Mathis, E. Rocca, D. Veys-Renaux, J. Tardelli, Electrochemical behaviour of titanium in KOH at high potential, Electrochim. Acta. 202 (2016) 253–261.

[46]   Y. Wang, T. Lei, B. Jiang, L. Guo, Growth, microstructure and mechanical properties of microarc oxidation coatings on titanium alloy in phosphate-containing solution, Appl. Surf. Sci. 233 (2004) 258–267.

[47]   F. Xie, X. He, S. Cao, M. Mei, X. Qu, Influence of pore characteristics on microstructure, mechanical properties and corrosion resistance of selective laser sintered porous Ti-Mo alloys for biomedical applications, Electrochim. Acta. 105 (2013) 121–129.

[48]   G. Xie, F. Qin, S. Zhu, D. V. Louzguine-Lugzin, Corrosion behaviour of porous Ni-free Ti-based bulk metallic glass produced by spark plasma sintering in Hanks' solution, Intermetallics. 44 (2014) 55–59.

[49]   J. Fojt, L. Joska, J. Málek, Corrosion behaviour of porous Ti-39Nb alloy for

biomedical applications, Corros. Sci. 71 (2013) 78–83.

[50]   K.H.W. Seah, R. Thampuran, S.H. Teoh, The influence of pore morphology on corrosion, Corros. Sci. 40 (1998) 547–556.

[51]   K.H.W. Seah, X. Chen, A comparasion between the corrosion characteristics of 316 stainless steel, soldi titanium and porous titanium, Corros. Sci. 34 (1993) 1841–1851.

[52]   X. Chen, Q. Fu, Y. Jin, M. Li, R. Yang, X. Cui, M. Gong, In vitro studying corrosion behavior of porous titanium coating in dynamic electrolyte, Mater. Sci. Eng. C. 70 (2017) 1071–1075.

[53]   D.J. Blackwood, A.W.C. Chua, K.H.W. Seah, R. Thampuran, S.H. Teoh, Corrosion behaviour of porous titanium-graphite composites designed for surgical implants, Corros. Sci. 42 (2000) 481–503.

[54]   B.J. Edwards, P. Higham, Anodic polarisation of porous coated vitalhum alloy - effect of passivation, ASTM-STP. (1987) 115–123.

[55]   B. Dabrowski, W. Swieszkowski, D. Godlinski, K.J. Kurzydlowski, Highly porous titanium scaffolds for orthopaedic applications, J. Biomed. Mater. Res. Part B Appl. Biomater. 95B (2010) 53–61.

[56]   S.B. Basame, H.S. White, Pitting corrosion of titanium the relationship between pitting potential and competitive anion adsorption at the oxide film/electrolyte interface, J. Electrochem. Soc. 147 (2000) 1376–1381.

[57]   M.E. Orazem, B. Tribollet, Electrochemical Impedance Spectroscopy, 2nd Ed., Jonh Wiley & Sons, New Jersey, 2017.

[58]   E.M. Szesz, B.L. Pereira, N.K. Kuromoto, C.E.B. Marino, G.B. de Souza, P. Soares, Electrochemical and morphological analyses on the titanium surface modified by shot blasting and anodic oxidation processes, Thin Solid Films. 528 (2013) 163–166.

[59]   S. Ikonopisov, Theory of electrical breakdown during formation of barrier anodic films, Electrochim. Acta. 22 (1977) 1077–1082.

Chapter 7. Highly porous Ti as a bone substitute: triboelectrochemical characterization of highly porous Ti against Ti alloy under fretting-corrosion conditions

A.I. Costa[a,b], F. Viana[b,c,d], F. Toptan[a,e], J. Geringer[f]

[a]CMEMS-UMinho – Center of MicroElectroMechanical Systems – Universidade do Minho, Campus de Azurém, Guimarães, Portugal

[b]DEMM – Department of Metallurgical and Materials Engineering – Faculdade de Engenharia da Universidade do Porto, Portugal

[c]LAETA – Associate Laboratory of Energy, Transports and Aeronautics – Faculdade de Engenharia da Universidade do Porto, Portugal

[d]INEGI – Institute of Science and Innovation in Mechanical and Industrial Engineering – Porto, Portugal

[e]IBTN/Euro – European Branch of the Institute of Biomaterials, Tribocorrosion and Nanomedicine – Departamento de Engenharia Mecânica, Universidade do Minho, Campus de Azurém, Guimarães, Portugal

[f]Université de Lyon, IMT Mines Saint-Etienne, Centre CIS, INSERM SainBioSE U1059, F-42023, Saint-Etienne, France

Abstract

Highly porous Ti was investigated under fretting-corrosion conditions as a function of load and amplitude.

To obtain a correlation between mechanical and electrochemical responses according to amplitude, a new representative master curve was suggested: the A ratio (dissipated energy over total energy) vs. 1st OCP drop that fitted well the fretting-corrosion behaviour.

Fretting-corrosion mechanisms were presented and a fretting map was illustrated. There was a significant load- and amplitude-dependent response, showing gross slip and partial slip regimes can occur with expected OCP variations.

The promising structure of highly porous Ti was preserved after 16 hours of fretting-corrosion under severe solicitations.

Graphical abstract
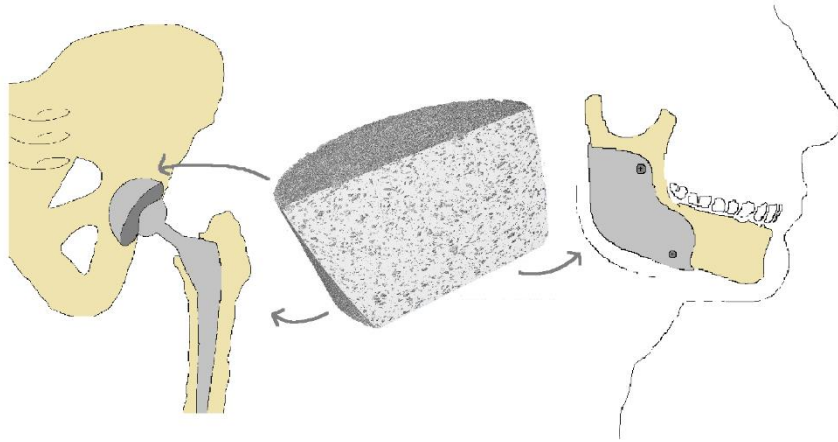
7.1. Introduction

The elderly population is increasing and together with lack of proper physical activity resulting in trauma or disease, the rate of implants used is rising. Implants require long-term stability and rapid healing however the existing Ti-based implant materials do not meet completely the current expectation [1,2].

Macro-porosity in the Ti implant was presented as a beneficial way to reduce the biomechanical mismatch, in order to approach the value of Young's modulus of the implant to the one found in the bone. It also gives the opportunity of ingrowth of new bone tissue inside of the pores [3–5].

Depending on the target implant application that can be dedicated for dental, hip, craniofacial or mandible, the functional requirements and aesthetics aspects should be considered where the mechanical properties can change throughout the implant and consequently, the functionality requirements will be heterogeneous through the implant. Macro-porosity can be combined with dense regions in order to achieve an implant structure that will fulfil the specified requirements for every section. Porosity may promote high vascularization and direct osteogenesis while the dense structure

160

may promote mechanical stability. For example, in the case of the hip, the head part should be dense while the stem may be partly porous. In the case of the mandible, the dental abutment should be a dense region while the body of the implant may have porosity [3,6–9]. These approaches, with tailored design, can lead to several complications due to the introduction of additional interfaces, which are subjected to various loading conditions and micro-motions.

The study of simultaneous wear and corrosion (tribocorrosion) is one of the most important aspects of load-bearing systems. A hip implant is affected by sliding contact between the femoral and the tibial or acetabular component and it is immersed in body fluids, therefore it is susceptible to tribocorrosion. There are micro-motions in the points of the implant fixation. On the other hand, dental implants are also exposed to cyclic micro-motions at the implant–abutment and implant–bone interfaces. These micro-motions are leading to debris and consequently to ions released by fretting-corrosion [2,10].

A very limited number of tribocorrosion studies on porous structures [11,12] have been published, leaving a lack of understanding of the evaluation of the contacts between porous-dense Ti-based structures. This work aims at investigating, to the best of the authors' knowledge for the first time, the triboelectrochemical consequences of the micro-movements between the highly porous Ti against Ti alloy structures under fretting-corrosion solicitations. The fretting-corrosion behaviour of highly porous Ti in foetal bovine serum solution was studied as a function of normal load and according to displacement amplitude.

7.2. Materials and methods

Powder metallurgy with space holder technique was used to produce highly porous Ti samples (Ø = 12 mm). Angular shaped Ti powders (Grade 2, Alfa Aesar, D50 = 36 μm) and angular shaped urea particles (Scharlau, <500 μm), 50 $_{vol}$%, were prepared in a ball mill for 4 hours at 130 rpm with alumina balls, in an argon atmosphere. Then the procedure continued with the pressing stage where a zinc stearate lubricated nitrided stainless steel die was used to uniaxially press the power blends under 350 MPa for 2 minutes. Then, green compacts were subjected to a thermal cycle for space holder

removal, performed at 450 °C for 3 hours under argon atmosphere. Afterwards, the sintering step was performed at 1100 °C, for 3 hours under high vacuum (<10^{-5} mbar). Highly porous Ti was characterized by tomography using a Nanotom 180 (Phoenix|X-ray, GE) equipment, with an accelerating voltage of 160 kV and a current of 75 µA. The sample was scanned in continuous mode and 2000 projections were performed around 360° with an exposure time of 500 ms for each projection.

Ti alloy (Ti-6Al-4V) samples were manufactured according to ASTM F136. For fretting-corrosion experiments, Ti alloy samples were electrically insulated with oxidized zirconium (Zircalloy) alloy plates and varnished, exposing to the electrolyte the surfaces facing each other.

Fretting-corrosion tests were carried out at room temperature (25 ± 2 °C) in normal air atmosphere using a fretting-corrosion set-up (details described elsewhere [13–15]) during 57600 cycles, i.e. 16 hours. Metal surfaces were electrically insulated from the experimental device. Electrochemical data was continuously monitored with a potentiostat (Parstat 2263) connected to the device of fretting-corrosion. During electrochemical measurements, a three-electrode configuration was used with highly porous Ti sample as working electrode and platinum and saturated calomel electrodes (SCE) as counter and reference electrodes, respectively. The protocol started with a cathodic polarization at −1 V_{SCE} for 5 minutes followed by open circuit potential (OCP) monitorization, before, during and after fretting solicitation.

A substantial range of loads (no load applied, 22.5, 42.5, 85, 127.5, 170 and 200 N) was applied where linear voltage displacement transducer sensors on the device were in charge of controlling a displacement of ± 10, 40, 70 and 100 µm sinusoidal displacement. Tests were repeated to a minimum of 3 times (5 times max.) to ensure the reproducibility for ± 40 µm sinusoidal displacement. For the rest of the amplitudes under study, only one test per load was carried out in order to obtain a fretting map. For each test, new samples of porous Ti and Ti alloy were used. It was not possible to apply the higher loads (170 N and 200 N) when higher amplitudes (± 70 and 100 µm) were imposed because the tangential load limit exceeded the limit that the tangential transducer was able to measure.

The usual master curve used in tribology is wear volume vs. total dissipated energy [16,17]. Due to corrosion phenomena in solution, the wear volume is not only the

162

consequence of some mechanical degradations (friction). This statement provides the opportunity to combine both effects, i.e. electrochemistry and mechanics. In order to build and suggest a new master curve for each amplitude under study according to the load, 1st OCP drop vs the A ratio (dissipated energy over total energy) was calculated. After 1 hour of stabilization, fretting started and 1st OCP drop was obtained by the difference between the potential before and after fretting started. The schematic representation of the fretting-corrosion protocol was illustrated in Figure 7.1. The A ratio (dissipated energy over total energy) was obtained with a mean of the last hour under fretting solicitation. Dissipated energy is the area of every tangential load vs. imposed displacement cycle.
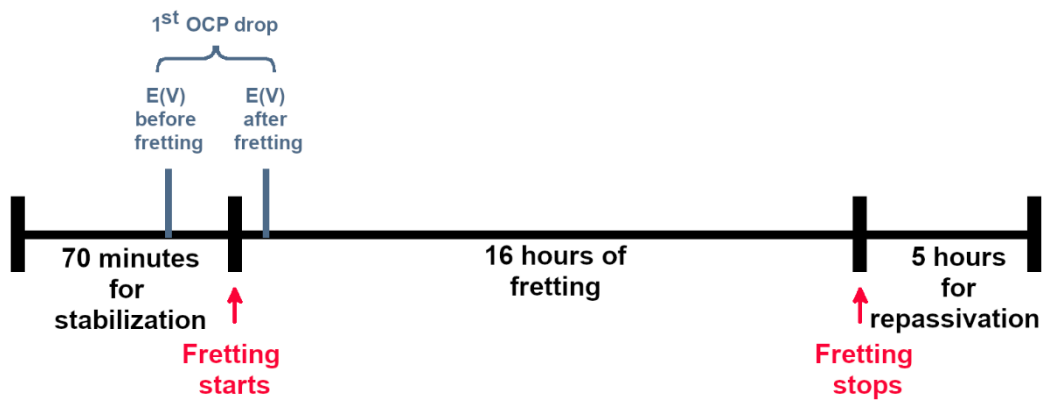
Figure 7.1. Schematic representation of the fretting-corrosion protocol.

3D profilometry (NT9100 ex. Veeco, Bruker^{TM}) was used in order to obtain 3D roughness, wear volume and 3D wear profile for all the samples under study. The morphological features of the fretted corroded zones were assessed using scanning electron microscopy (SEM, Zeiss™Supra 55, 20 kV of voltage). Special attention was paid on the conduction of the holder in order to avoid some electrical charges accumulation, especially on porous titanium that exhibits non uniform oxide films.

7.3.   Results and discussion

Figure 7.2 presented the three-dimensional tomographic reconstructions of highly porous Ti sample together with the optical microscope (OM) images of the top surfaces. Supplementary video obtained by tomographic analysis and Figure 7.2 showed a general look of the macro-porosity of highly porous Ti structures, presented closed and open (interconnected) pores well distributed through the sample. Induced (nominal) porosity was 50%, but previous studies [18,19] with identical processing conditions showed that real porosity obtained by image analysis was around 37%. About 80% of the pores were in the range 50 to 350 μm, with an average pore size of around 200 μm [18,19].
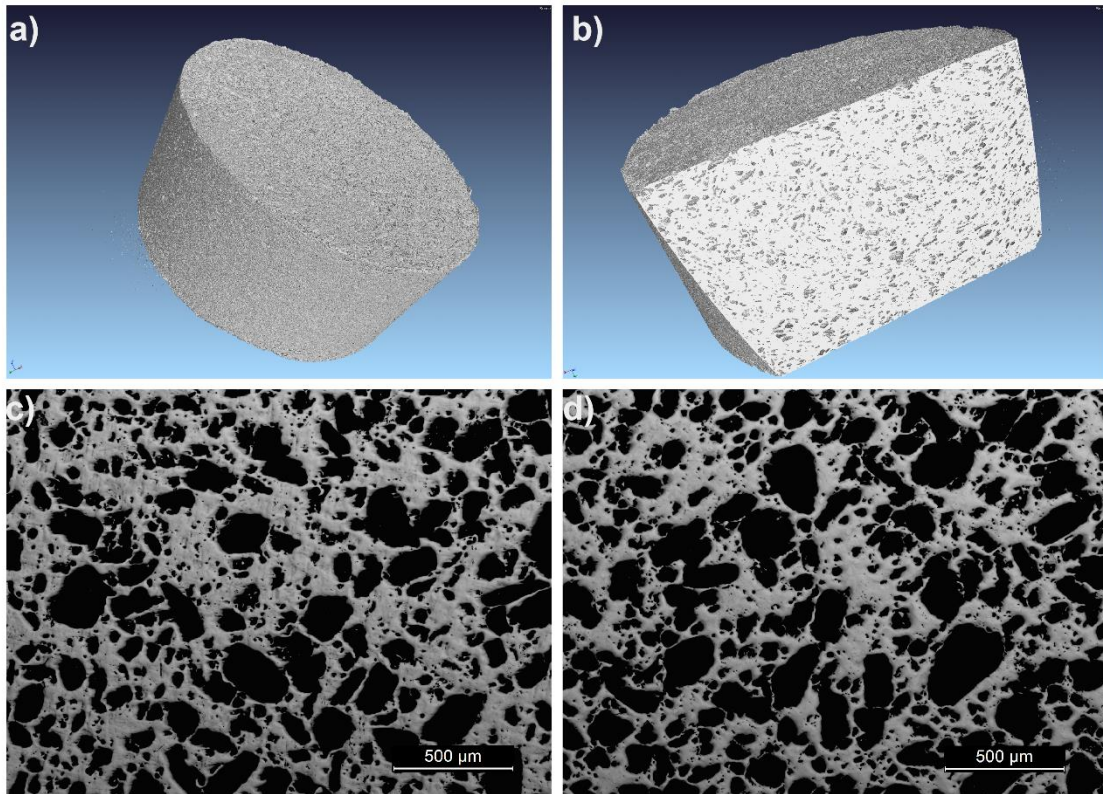
Figure 7.2. Three-dimensional tomographic reconstructions of highly porous Ti sample with Ø = 12 mm: a) top surface and b) cross-sectional view; c) and d) OM images from the top surface.

Maximum Hertzian contact pressure for dense Ti/Ti alloy contact was calculated for all the loads under study (22.5, 42.5, 85, 127.5, 170 and 200 N) and results showed 210, 280, 400, 490, 570, 620 MPa respectively. A dense structure was assumed for contact pressure calculations, thus, it is reasonable to assume that the values during the tests were much higher due to reduced contact area because of porosity. These values of contact pressure were considerably above to the ones found in the human body for most of the cases in implant materials that are lower than 10 MPa [20–22]. For example, on the femoral structure (acetabulum cavity), the peak pressure for normal walking can be 3.26 MPa while standing up is 8.97 MPa [23].

Micro-movements occurring during the healing phase may lead to fibrous encapsulation of the implant and usually, they were in the range 3 to 50 μm, showed a maximum displacement of 71.9 μm [24–29]. According to this, 0.08 mm of displacement amplitude was investigated and representative curves from the results regarding fretting-corrosion tests for 16 hours were presented in Figure 7.3. Coefficient of friction (COF) values presented in Figure 7.3a, showed a trend since values were decreasing with the increase of the load, with the exception for 127.5 N. For lower loads, 22.5 and 42.5 N, oscillations can be seen during the 16 hours of the tests. On another way, for the rest of the loads, the COF was relatively stable through the duration of the test. The decreasing of the COF values, while the load was increasing, may be related with several factors, creating a complex system under study, where lubrication by the electrolyte, tribolayer formation and adhesive wear from the metal/metal contact can contribute. For instance, highly porous Ti presented protrusions that may be flattened while the load was increasing, promoting a decreased of COF. In order to evaluate tribocorrosion and fretting-corrosion behaviours as well as wear damages, COF evolution is widely used but following the results, in this study, an isolated COF evolution did not present a valuable contribution regarding fretting regimes and their transition. In this work, COF evolution was considered to compare the behaviour between the loads under study.

The representative curves for the evolution of OCP with time during fretting solicitations were presented in Figure 7.3b. These OCP values were mixed potential values of highly porous Ti and Ti alloy, as well, mixed potential values of both the active (worn) and passive (unworn) surfaces of both materials. Highly porous Ti consisted of a mixture of open and closed pores (as presented in Figure 7.2) and previous 3D

reconstructions samples [18] showed that electrolyte can cross completely the samples. Although samples were isolated to prevent leaking of the electrolyte, a more extensive metallic area from the porous samples was exposed to the electrolyte than from Ti alloy. When fretting solicitations were starting, a decrease in the potential was observed for all the loads under study. The highest OCP drop was related to the test under 22.5 N indicating a higher perturbation of the native oxide film and more exposure of the underlying metal surface to the electrolyte. After fretting stopped, all samples recovered their potential values up to the ones registered before fretting soliciting. This may indicate that the repassivation process and growth of the oxide film happened once fretting finished.

Depending on the applied load, different characteristics are highlighted between the conditions in the acquired fretting hysteresis loops (tangential load vs. displacement) as observed in Figures 7.3c and d. While fretting-corrosion was occurring, modifications of the contact parameters were happening depending on the load, and consequently, fretting hysteresis loops presented a dynamic response [30]. In this way, the response at cycle 10, correspondent to 3 hours and 20 minutes of fretting solicitations (Figure 7.3c) and cycle 240, correspondent to 16 hours of fretting solicitations (Figure 7.3d) were presented in order to show the main differences in the evolution between the fretting hysteresis loops at the beginning and the end of the experiments, respectively. While 22.5 N was being applied, gross slip was occurring for all the cycles. This behaviour was promoted by a contact that was characterised by a constant friction force associated with a pure dissipative behaviour and that was why the fretting hysteresis loops presented a quadratic shape [31]. For 42.5, 85, 127.5, 170 and 200 N fretting hysteresis loops, an elliptic shape was obtained. However, for 42.5 N, the final loop presented a different shape than the one presented in the beginning, and that can mean a mixed slip regime, starting with partial slip and then became more close to a gross slip regime [31]. The area of the fretting hysteresis loops corresponds to the mechanical energy dissipated during the cycle [14,30] and it was presented its evolution during the fretting tests in Figure 7.3e. The lowest loads under study (22.5 and 42.5 N) presented considerable high values of dissipated energy, followed by 200 N condition. For the intermediate loads, 85, 127.5 and 170 N, the values obtained for dissipated energy were close to 0. Another mechanical parameter than can access the fretting

166

regimes is the ratio obtained between the dissipated energy over the total energy called the A ratio [15]. This energy ratio, defined by Mindlin and Deresiewicz [32] approach, followed by Fouvry *et al.* [17], allows accessing the transition between partial and gross slip regimes. If the A ratio (in a cylinder vs. plane contact) is below 0.2, a partial slip regime is occurring as presented by Figure 7.3f for 42.5, 85, 127.5, 170 and 200 N. For 22.5 N, it was possible to see that the first cycles were under a gross slip regime (energy ratio > 0.2), in accordance with the fretting hysteresis loops shown in Figure 7.3c, followed by a transition for the partial slip regime. On the other hand, 42.5 N presented an evaluation of the A ratio that followed the opposite trend, showing lower values, in the beginning, increasing the values at the end of the test, being closer to a gross slip regime, as in accordance with the fretting hysteresis loops presented in Figure 7.3d.
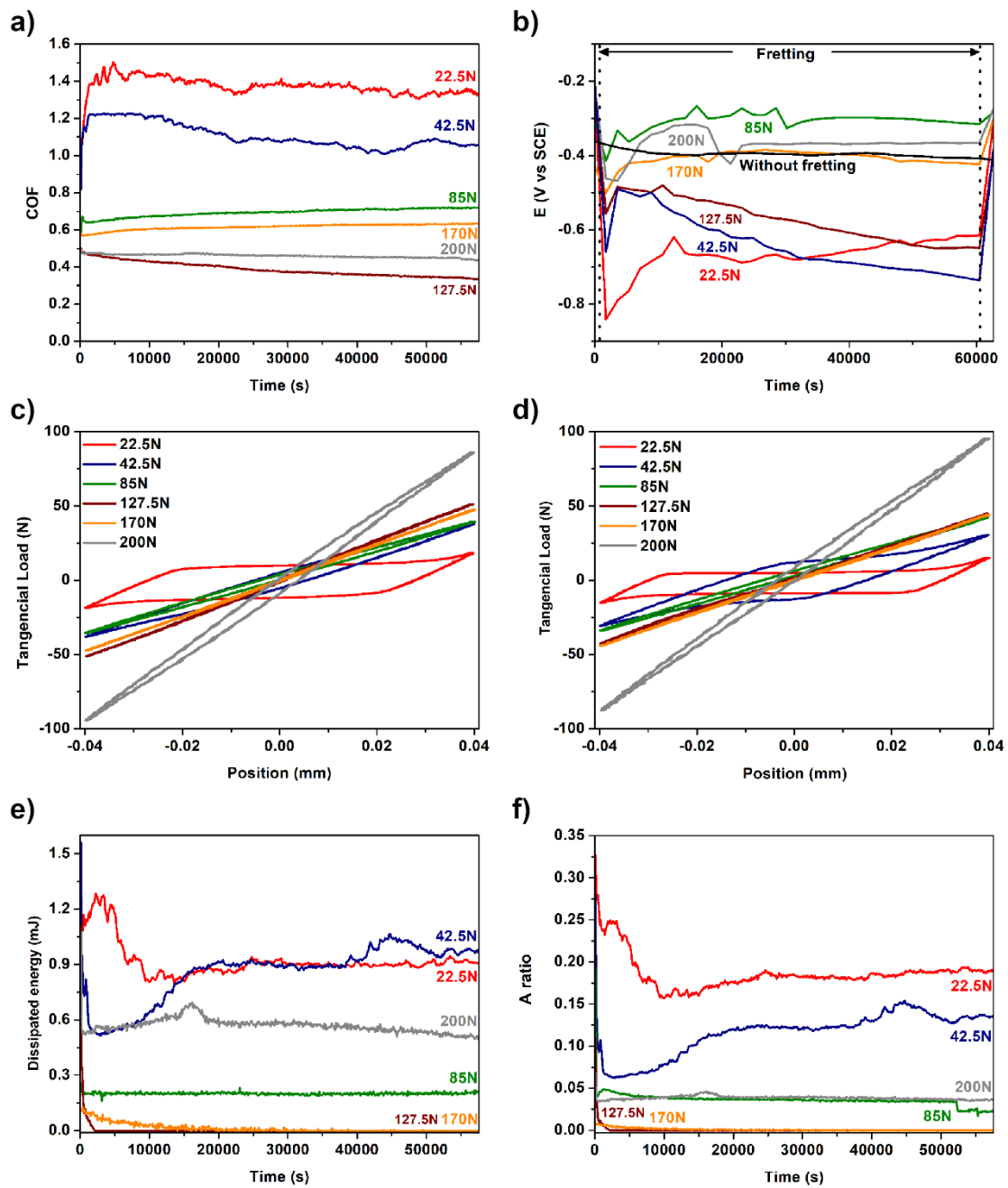
Figure 7.3. a) Coefficient of friction evolution, b) open circuit potential evolution; c) representative fretting hysteresis loops (tangential load vs displacement) for cycle 10 and d) for cycle 240; e) dissipated energy evolution and f) the A ratio evolution between Ti alloy vs highly porous Ti under fretting-corrosion tests for several loads with 0.08 mm of displacement amplitude.

Worn surfaces of highly porous Ti and Ti alloy were evaluated by SEM and optical profilometry and representative images for the respective loads under study were given in Figures 7.4 and 7.5, respectively. Highly porous Ti worn surfaces presented parallel sliding grooves due to abrasive wear together with the compacted oxidized wear debris. From 22.5 to 200 N, the intensity of the grooves and the small particles as wear debris decreased, suggesting that at lower loads, friction was more efficient. This may be linked with COF evolution, where 22.5 N presented the highest COF values (Figure 7.3a). With the ejection of wear debris, adhered and dense oxidized patches on the worn surfaces were getting thicker, surface roughness was also getting higher, leading to high COF values. At 127.5 N, Figure 7.4a presented a decrease in the number of noticeable grooves, showing smoothing of the porous structures was occurring. At 200 N, less visible degradation was noticed, pointing that a sort of polishing and smoothing of the surface was happening, due to partial slip behaviour.

Macro-pores presented loose oxidized wear debris. On porous structures, wear debris generated can go inside of the pores and can be compacted. In this way, the ejection of the wear debris into the pores can decrease the third-body abrasion that also contributed to an improved tribocorrosion performance [12].

In accordance with what was noticed in the highly porous Ti wear tracks, Ti alloy presented grooves more pronounced at lower loads, as presented in Figure 7.4b. At 22.5 N, this phenomenon was well visible, decreasing at 42.5 N where just low marks and slightly less marked grooves were visible. SEM image presented for Ti alloy at 42.5 N represented the mixed slip regime discussed above in Figure 7.3 since the bottom part of the wear track showed signs of sticking and adhesion while the rest showed a slip mechanism. At 200 N, no grooves were visible together with no substantial marks, proving an idea of sticking mechanism with small friction. At 200 N, Ti alloy surfaces presented only crystals precipitated from the electrolyte showing no wear debris formation. Ti alloys worn surfaces presented more distinguished parallel sliding grooves than porous Ti and it was previously stated that wear tracks were less noticeable in porous Ti structures than in dense structures when tribocorrosion tests were performed against a ceramic material [12]. The same trend was found for the compacted wear debris or tribolayer. These oxides compacted in a layer can play a protective role by reducing the wear due to adhesive wear but they can also be freely moving in the

electrolyte and/or they can work as third body wear. Under fretting solicitations, wear particles can also become entrapped in the fretted regions, in this way they can work as load-carrying plateau [33,34].

The fretting response from the material is linked with a regime characterized by its mechanisms of surface degradation and wear track. For example, the partial slip regime is usually associated with few amount of wear. The explanation is the low dissipated energy produced during the test where some parts of the contact remain adhered to each other and no relative motion takes place between them. Consequently, there is no wear. In this regime, only a smaller part of the contact experiences relative motion (thus low dissipated energy). Partial slip regime can be divided into two main domains: a security domain without damage and a domain where cracking appears. Usually, cracking first appears under partial slip conditions, whereas the material removal and the debris formation are mainly encountered under large displacement conditions. Gross slip regime is characterized by a high dissipated energy due to the sliding phenomena that occurs between the surfaces of the contacting bodies. Gross slip regime usually presents severe surface damage by wear due to significant material removal, with a lot of third body effects while mixed slip regime generates competition between cracking and wear [31,35,36].

EDS analysis, presented in Figure 7.4c, detected some Al and V elements in the composition of porous Ti worn surfaces, from the Ti-6Al-4V counter-face, supporting the transfer mechanism between highly porous Ti and Ti alloy.
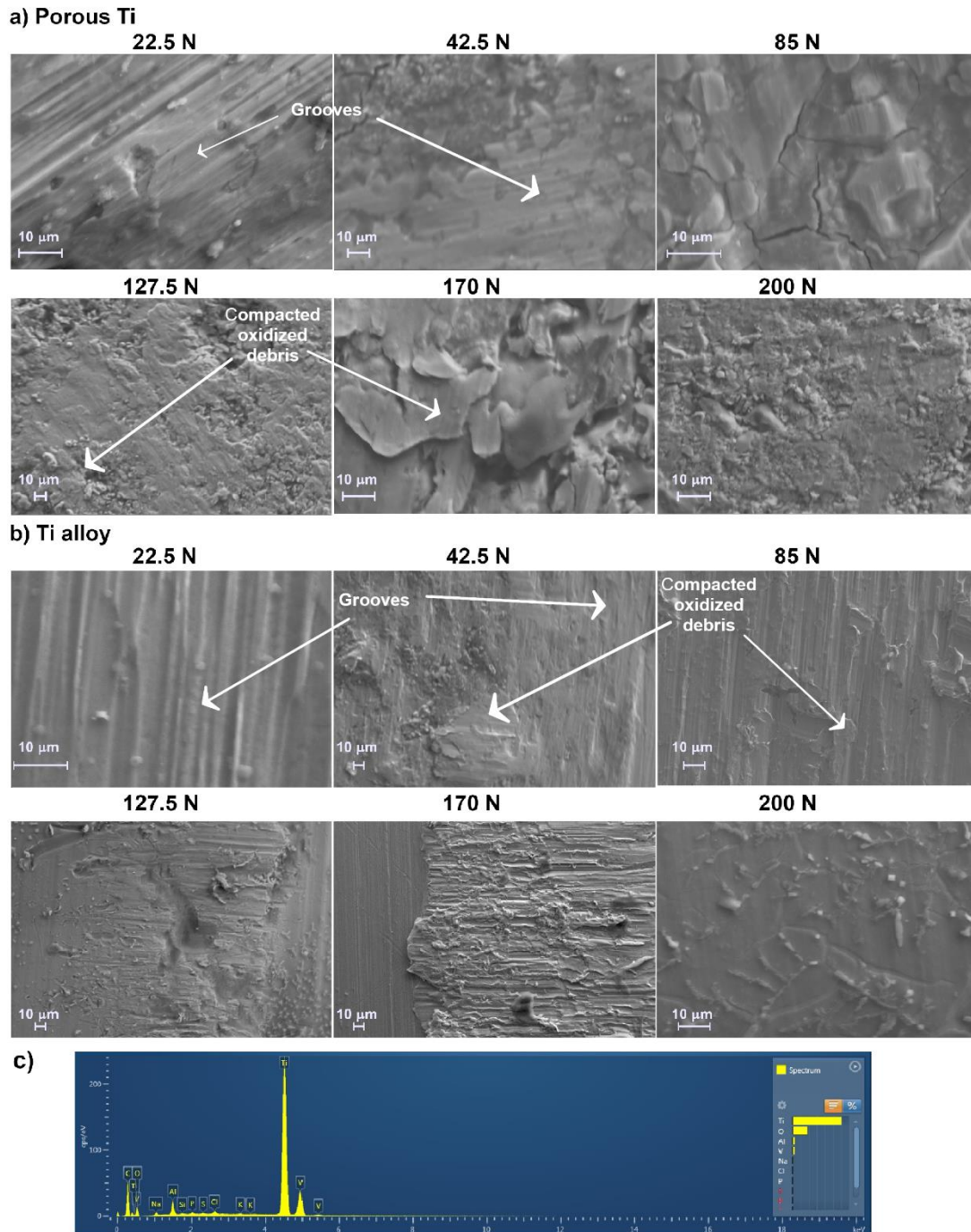
Figure 7.4. SEM images of a) highly porous Ti and b) Ti alloy worn surfaces for several loads with 0.08 mm of displacement amplitude; c) EDS spectrum obtained in the wear tracks of highly porous Ti.

A smoothing of the porous structure can also be detected in Figure 7.5. On the wear profiles of the porous structures, it was noticed material compaction and as well wear debris inside of the macro-pores, as can be seen in Figure 7.5a, for 170 N condition represented by the green isolated zones inside of the big pore coloured in blue. Highly porous Ti structures exhibited a damaged surface represented by the green parts,

surrounded by a less damaged zone coloured in red, except for 200 N. Parallel grooves for all Ti alloy images were highlighted by the optical profiles depicted in Figure 7.5b, following what was discussed above in Figure 7.4b. Once again, sticking phenomena was highlighted at 200 N, since highly porous Ti profiles showed less damage and Ti alloy profiles presented less pronounced grooves.
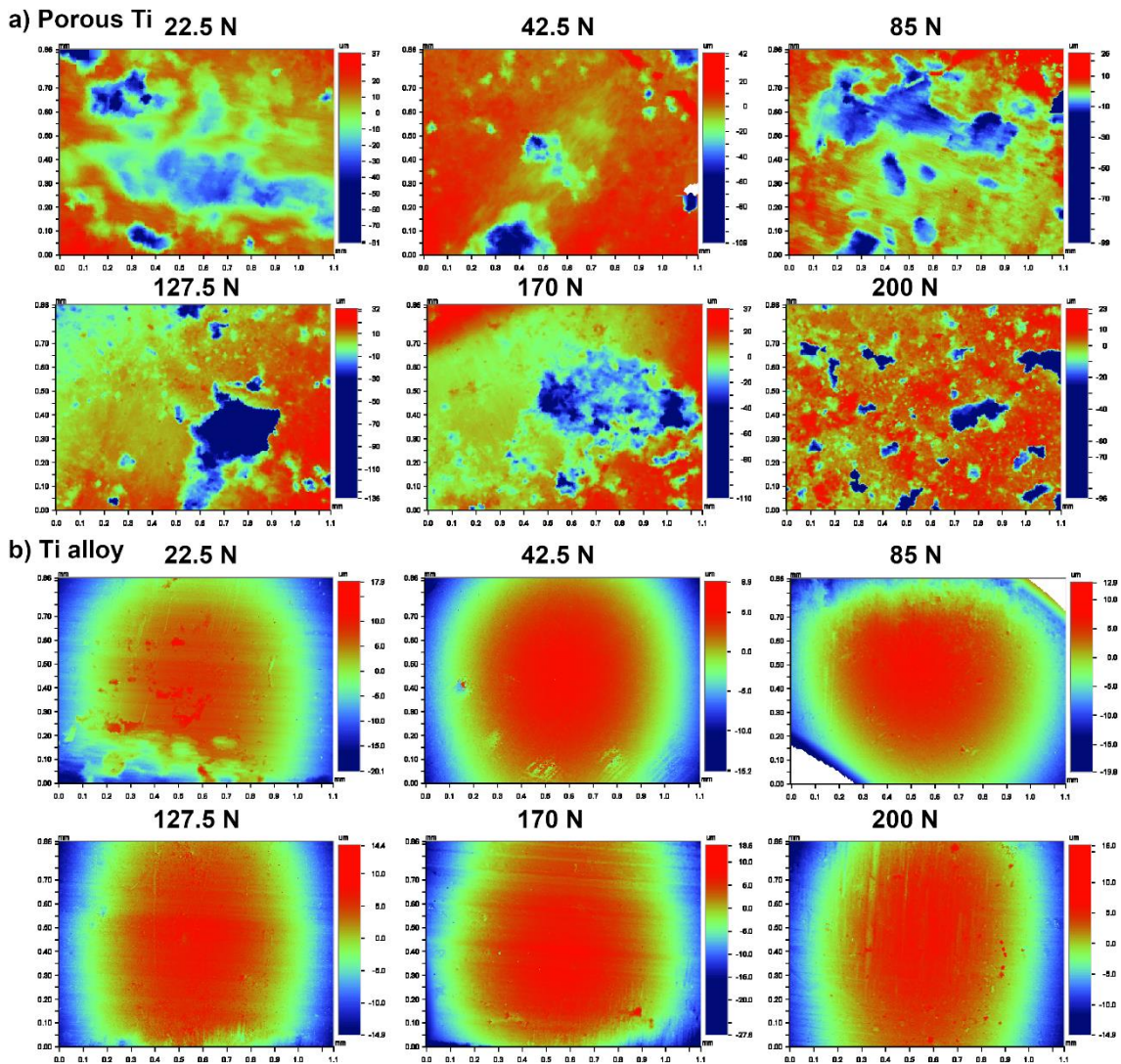
Figure 7.5. Worn surfaces images by optical profiles for a) highly porous Ti and b) Ti alloy for several loads with 0.08 mm of displacement amplitude.

The surface morphology of the highly porous Ti was preserved after 16 hours of fretting-corrosion for all the loads under study: no destruction of the structure, low wear, few/no grooves and a porous structure highlighted. As a result of microscopical and profilometric observations, together with electrochemical and fretting analysis, a

proposed fretting-corrosion mechanism of highly porous Ti against Ti alloy is illustrated in Figure 7.6. Due to the reduced contact area of the macro-porous surfaces, higher contact pressures were obtained on the contact zones leading to more severe local damage, where the most pultruded zones of the porous structures were flattened, creating wear debris. These new wear debris that were generated can be work-hardened, and/or can be mixed with the oxidized wear debris (third-bodies). Consequently, they be compacted on the worn surfaces, forming oxidized patches, whereas some of these debris may adhere on counter-body surfaces that can abrade the metal leading to the formation of grooves on the worn surfaces or move freely on the sliding surfaces, acting as third-body particles (Fig. 12a), or can go inside of the pores. For porous structures, as the load was decreasing, it seemed that the severity of abrasive wear increased.
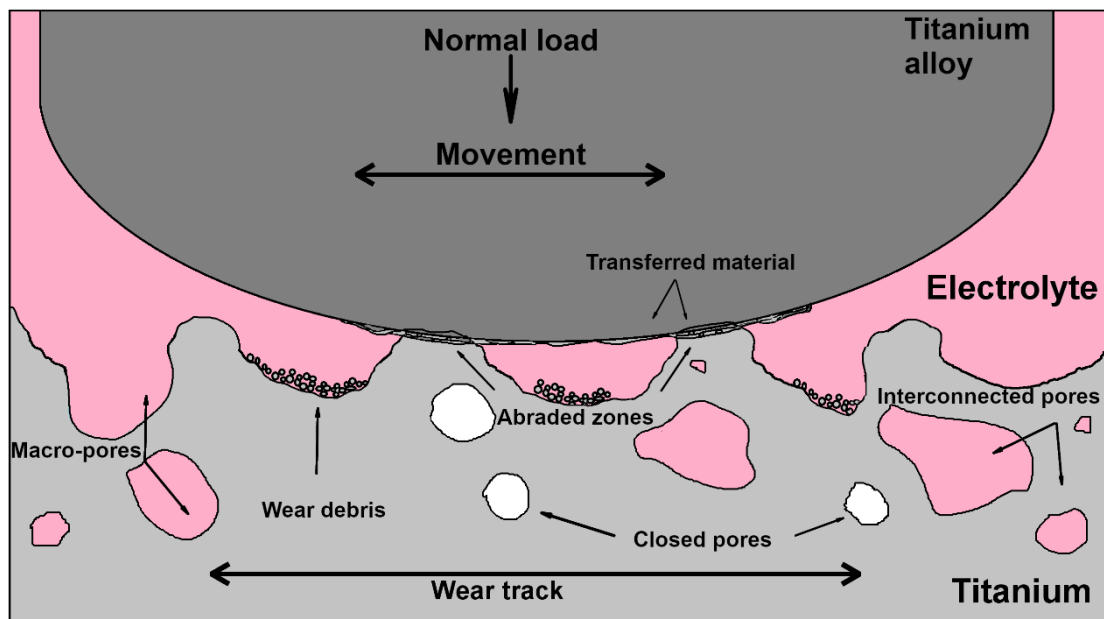
Figure 7.6. Schematic draw of the suggested fretting-corrosion mechanisms for highly porous Ti against Ti alloy.

The focus of this study was to evaluate, to the best of the authors' knowledge for the first time, the tribocorrosion behaviour of highly porous Ti against Ti alloy, simulating fretting-corrosion interfaces of implants. Depending on the load and the amplitude imposed, highly porous Ti against Ti alloy can present a different behaviour. In order to obtain a correlation between the mechanical and electrochemical responses according

to the displacement amplitude [37], Figure 7.7 presented the evolution of the 1st OCP drop when fretting started according with the A ratio. 0.02 mm as displacement amplitude was characterized by low values of the 1st OCP drop and low values of the A ratio, as presented in Figure 7.7a, showing a partial slip behaviour for all the loads under study. No significant differences can be seen between all the loads under study. In accordance with Figure 7.3, for 0.08 mm as displacement amplitude, Figure 7.7b presented that the biggest drop on OCP under fretting was the test with the extreme minimum load under study, 22.5 N, followed by 42.5 N condition. Fretting micro-motions at lower load (22.5 N) induced gross slip with high and unsteady COF values (Figure 7.3a), and presented a big OCP drop when fretting was applied (Figure 7.3b), supported by hysteresis loops (Figures 7.3c and d) with quadratic shape, that consequently expressed in high values of dissipated energy (Figure 7.3e). The A ratio (Figure 7.3f) allowed accessing that during the test, a regime transition may occur from gross slip to partial slip. Under 42.5 N, it was found a mixed slip regime, with contrary behaviour of the previous one described. According to hysteresis loops (Figure 7.3c and d), response started with partial slip and with time, the behaviour became closer to the gross slip regime, supported by the A ratio evolution (Figure 7.3f), presenting high values for dissipated energy (Figure 7.3e). For higher loads (85, 127.5, 170 and 200 N), most of the dissipated energy (Figure 7.3e) decreased back to near zero that together with the A ratio (Figure 7.3f), showed that with higher loads the response becomes more robust showing to be in a partial slip regime. No significant differences can be seen between 85, 127.5, 170 and 200 N, showing a similar response under fretting-corrosion at the interface highly porous Ti against Ti alloy, characterizing a partial slip behaviour. For 0.14 mm, the values obtained for the loads that were possible to study, presented in Figure 7.7c, showed a shift for the right side of the graph. 42.5 N presented a mixed slip regime while the rest of the load presented a partial slip regime. The transition from partial to gross slip was occurring around 0.14 mm, presenting this displacement amplitude as a threshold of the fretting-corrosion behaviour. Regarding tests with an amplitude imposed of 0.2 mm, presented in Figure 7.7d, all the loads were shifted for a higher A ratio, in comparison with the values obtained for the other amplitudes under study, with the exception of 22.5 N. This high A ratio obtained showed a gross slip behaviour for all the loads under this imposed amplitude.

174

Representative SEM images of highly porous Ti worn surfaces for 22.5 N with 0.02 mm of amplitude, 22.5 N and 42.5 N with 0.14 mm of amplitude were presented in Figure 7.7e, f and g respectively. These images were chosen in order to represent the features correspond to partial slip (Figures 7.7e and f) and gross slip regime (Figure 7.7g), presented more noticeable grooves. With the increase of the displacement amplitude, gross slip regime started to be established and consequently, one may assess the COF decreased by wear, which generated a compliant third body layer together with higher worn material removal and a shorter crack length [31,35,36].
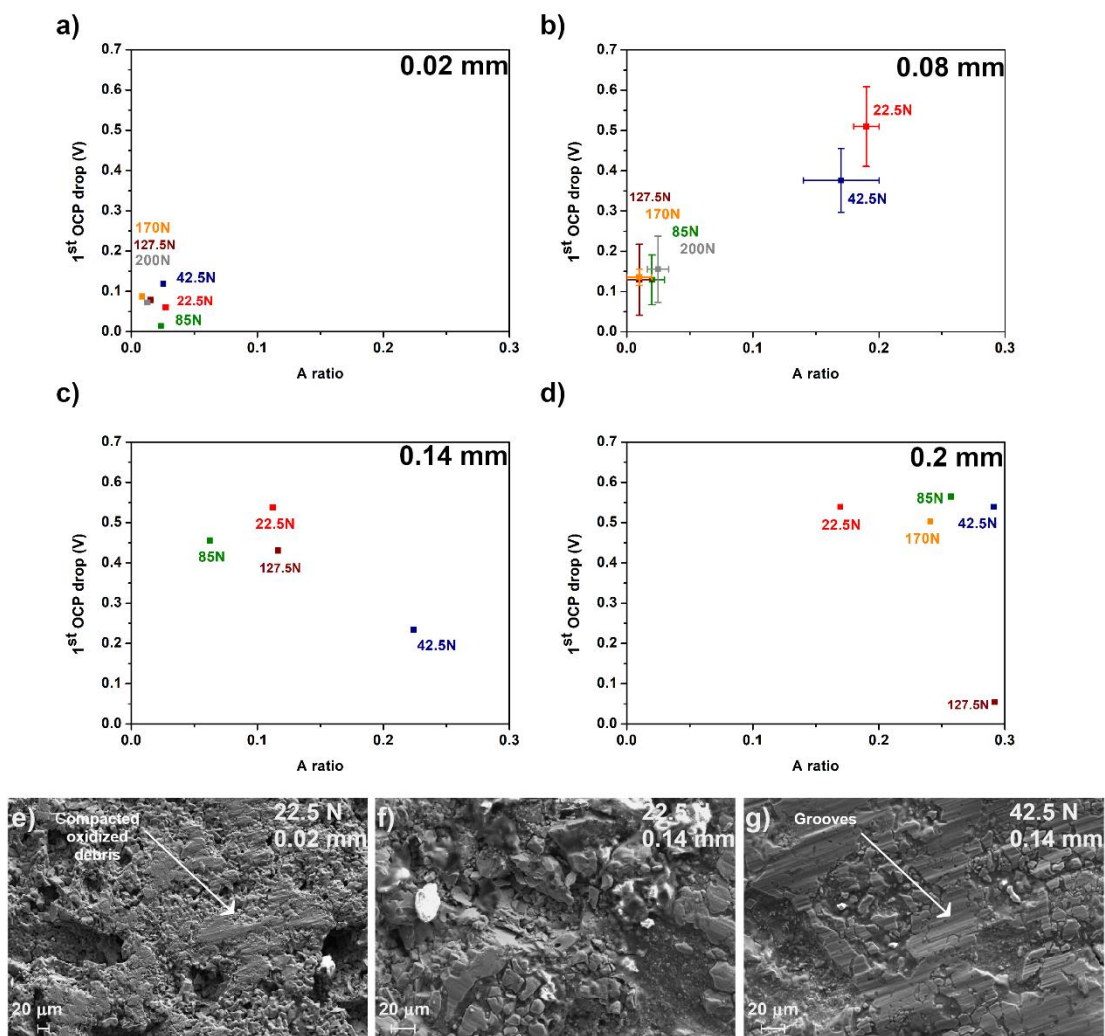
Figure 7.7. Evolution of the 1st OCP drop when fretting started according to the A ratio for the displacement amplitudes imposed: a) 0.02, b) 0.08, c) 0.14 and d) 0.2 mm; SEM images of highly porous Ti worn surfaces for e) 22.5 N with 0.02 mm of amplitude, f) 22.5 N and g) 42.5 N with 0.14 mm of amplitude.

This study presented an amplitude and load-dependent responses under fretting-corrosion solicitations between highly porous Ti and Ti alloy. Figure 7.7 allowed the construction of a schematic illustration of a fretting map in terms of contact load and displacement amplitude obtained regarding the consequences of the micro-movements between highly porous Ti against Ti alloy, presented in Figure 7.8. A fretting map is a diagram showing the relevant regimes in two variables, with regime boundaries representing critical values for the transition from one regime to another [36]. The obtained fretting map was in accordance with [38,39], where partial slip was followed by a mixed slip regime and then gross slip for higher displacement amplitudes.
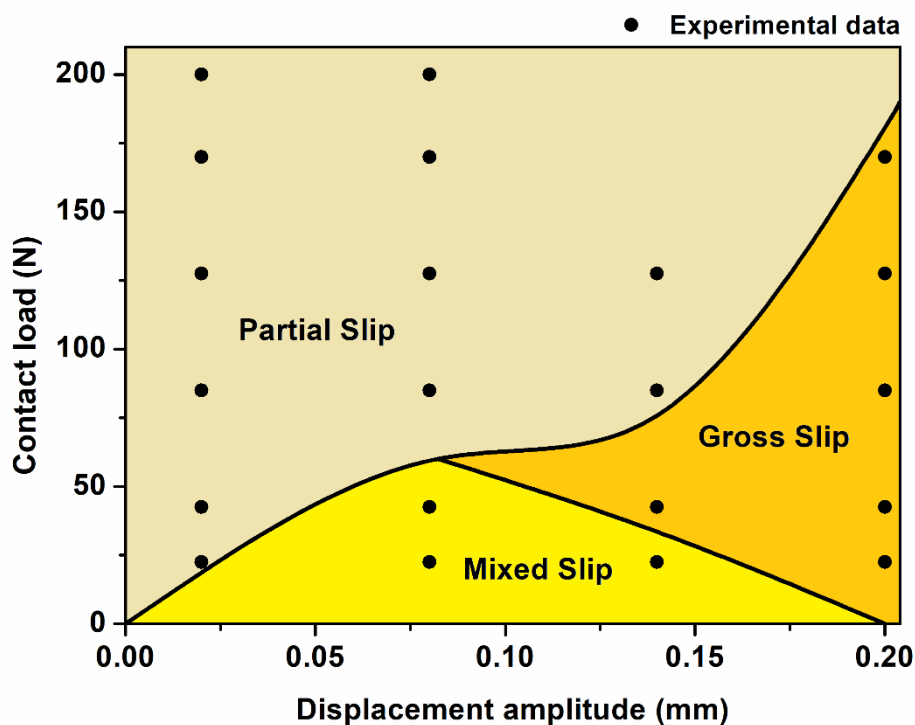
Figure 7.8. Schematic illustration of a fretting map in terms of contact load and displacement amplitude obtained regarding the consequences of the micro-movements between highly porous Ti against Ti alloy.

Open circuit potential with the mechanical data from the tangential force and displacement analysis can provide information about the properties and behaviour of materials during fretting-corrosion tests. However, there were several limitations to this study. Firstly, for 0.02, 0.14 and 0.2 mm of displacement amplitude, only one test was

performed for each load under study. In this way, a number of repetitions need to be performed in order to verify the proposed fretting map. Secondly, in the literature, master curves are presented using with the evolution of the wear rate or wear volume according to the cumulated dissipated energy [16,17,39,40], however when evaluating tribocorrosion behaviour of porous materials, this approach was not viable since it was difficult to distinguish a pore with wear damage. Besides, wear debris may go inside the pores and/or being compacted inside the pores, misguiding wear or weight loss measurements. However the A ratio vs. 1st OCP drop seems to make sense according to the tribological behaviour. Thirdly, in order to use this contact geometry approach, dense-on-porous contact, it was difficult to calculate the accurate real contact pressure. Actually, due to the surface roughness, the real contact between two counterparts was composed of many small asperity contacts. In lubricated conditions like in this study, the hydrodynamic film may stay in these small junctions and carries part of the applied normal force. In this way, the actual force applied will be reduced comparing to non-lubricated condition where the total applied normal force was carried solely by the contacting asperities [41]. Since one of the counterparts was a porous structure, it was possible that at the start of the tests, only some points were in contact, mainly due to the existence of pores. Afterwards, with the destruction of the top of the porous structure, the contact area was increasing which may lead to underestimation of the contact pressure as the porous Ti material was degraded, giving relatively lower contact pressure at the end of the test.

Even so, this study provided, to the best to the authors' knowledge, a first insight on the evaluation of porous Ti material under fretting-corrosion solicitations. These results can support the next investigations with the aim to evaluate the viability of this material for potential use in orthopaedic implants. Nevertheless, there is a need for generic standards that deal with fretting as well as test standards for specific devices [38], and these results showed that a new master curve of the A ratio vs. 1st OCP drop may be promising to study and to evaluate such complex systems.

Further investigations should focus on fatigue corrosion evaluation to study how porous Ti materials behave with crack initiation and propagation during cyclic stresses that can lead to the creation of new non-passivated surfaces in the metallic structures. This together with the study of corrosion in dynamic fluids containing proteins and

micro-organisms that can affect the electrochemical and triboelectrochemical response of porous materials is crucial, in order to mimic the *in vivo* conditions.

7.4.   Conclusions

This study complies the characterization of highly porous Ti as a potential bone substitute under fretting solicitations.

The fretting response was highly dependent on the applied load and several mechanical responses were obtained, from gross slip under low normal load until partial slip under high loads.

In order to obtain a correlation between the mechanical and electrochemical responses according to displacement amplitude, a new representative master curve was suggested: the A ratio vs. 1st OCP drop. 0.02 mm as displacement amplitude was characterized by low values of 1st OCP drop and low values of the A ratio, showing a partial slip behaviour for all the loads under study. For 0.08 mm of displacement amplitude, 22.5 N presented gross slip regime, 42.5 N a mixed slip regime and the rest of the loads presented partial slip regime. 0.14 mm was presented as a threshold amplitude for behaviour because tests with 0.2 mm, presented higher A ratio, shifting the behaviour for gross slip regime. A fretting map was built in terms of contact load and displacement amplitude regarding the consequences of the micro-movements between highly porous Ti against Ti alloy.

The surface morphology of the highly porous Ti was mostly preserved after 16 hours of fretting-corrosion solicitations. The benefits of porous titanium seem promising for replacing some metallic parts well used in dentistry and implants field.

Acknowledgements

References

[1]   M. Geetha, A.K. Singh, R. Asokamani, A.K. Gogia, Ti based biomaterials, the ultimate choice for orthopaedic implants – A review, Prog. Mater. Sci. 54 (2009) 397–425.

[2]   J. Villanueva, L. Trino, J. Thomas, D. Bijukumar, D. Royhman, M.M. Stack, M.T. Mathew, Corrosion, Tribology, and Tribocorrosion Research in Biomedical Implants: Progressive Trend in the Published Literature, J. Bio- Tribo-Corrosion. 3 (2017).

[3]   A. Bansiddhi, D.C. Dunand, Titanium and NiTi foams for bone replacement, Woodhead Publishing Limited, 2014.

[4]   A. Nouri, Titanium foam scaffolds for dental applications, Met. Foam Bone. (2017) 131–160.

[5]   A.C. Alves, R. Thibeaux, F. Toptan, A.M.P. Pinto, P. Ponthiaux, B. David, Influence of macroporosity on NIH/3T3 adhesion, proliferation, and osteogenic differentiation of MC3T3-E1 over bio-functionalized highly porous titanium implant material, J. Biomed. Mater. Res. - Part B Appl. Biomater. 107 (2019) 73–85.

[6]   A. Kumar, K. Biswas, B. Basu, Hydroxyapatite-titanium bulk composites for bone tissue engineering applications, (2014) 1–16.

[7]   F.A. España, V.K. Balla, S. Bose, A. Bandyopadhyay, Design and fabrication of

CoCrMo alloy based novel structures for load bearing implants using laser engineered net shaping, Mater. Sci. Eng. C. 30 (2010) 50–57.

[8]   J. Parthasarathy, B. Starly, S. Raman, A design for the additive manufacture of functionally graded porous structures with tailored mechanical properties for biomedical applications, J. Manuf. Process. 13 (2011) 160–170.

[9]   C. Simoneau, P. Terriault, B. Jetté, M. Dumas, V. Brailovski, Development of a porous metallic femoral stem: Design, manufacturing, simulation and mechanical testing, Mater. Des. 114 (2017) 546–556.

[10]   S. KT, L. ME, M. MT, Failure Causes in Total Hip Replacements: A Review, Austin J. Orthop. Rheumatol. 5 (2018) 1064.

[11]   A.I. Costa, L. Sousa, A.C. Alves, F. Toptan, Tribocorrosion behaviour of bio-functionalized porous Ti surfaces obtained by two-step anodic treatment, Corros. Sci. 166 (2020) 108467.

[12]   F. Toptan, A.C. Alves, A.M.P. Pinto, P. Ponthiaux, Tribocorrosion behavior of bio-functionalized highly porous titanium, J. Mech. Behav. Biomed. Mater. 69 (2017) 144–152.

[13]   L. Semetse, B.A. Obadele, L. Raganya, J. Geringer, P.A. Olubambi, Fretting corrosion behaviour of Ti-6Al-4V reinforced with zirconia in foetal bovine serum, J. Mech. Behav. Biomed. Mater. 100 (2019) 103392.

[14]   J. Geringer, D.D. Macdonald, Friction/fretting-corrosion mechanisms: Current trends and outlooks for implants, Mater. Lett. 134 (2014) 152–157.

[15]   J. Geringer, V. Fridrici, H. Ding, K. Kim, T. Taylor, L. Semetse, S. Ehsani-majd, P. Olubambi, J. Fontaine, P. Kapsa, Some Hard or Soft Coatings to Protect the Pristine Biometallic Substrates under Fretting-Corrosion Solicitations: What Should Be the Best Solution?, Lubricants. 8 (2020) 1–14.

[16]   S. Fouvry, P. Kapsa, An energy description of hard coating wear mechanisms, Surf. Coatings Technol. 138 (2001) 141–148.

[17]   S. Fouvry, P. Kapsa, H. Zahouani, L. Vincent, Wear analysis in fretting of hard coatings through a dissipated energy concept, Wear. 203–204 (1997) 393–403.

[18]   A.C. Alves, A.I. Costa, F. Toptan, J.L. Alves, I. Leonor, E. Ribeiro, R.L. Reis, A.M.P. Pinto, J.C.S. Fernandes, Effect of bio-functional MAO layers on the electrochemical behaviour of highly porous Ti, Surf. Coatings Technol. 386 (2020) 125487.

[19]   A.C. Alves, I. Sendão, E. Ariza, F. Toptan, P. Ponthiaux, A.M.P. Pinto, Corrosion behaviour of porous Ti intended for biomedical applications, J. Porous Mater. 23 (2016) 1261–1268.

[20]   G. Wang, W. Huang, Q. Song, J. Liang, Three-dimensional finite analysis of acetabular contact pressure and contact area during normal walking, Asian J. Surg. 40 (2017) 463–469.

[21]   F. Mazoochian, A. Hölzer, J. Jalali, F. Schmidutz, C. Schröder, M. Woiczinski, J. Maierl, P. Augat, V. Jansson, Finite element analysis of the ovine hip: Development, results and comparison with the human hip, Vet. Comp. Orthop. Traumatol. 25 (2012) 301–306.

[22]   M.M. Ardestani, M. Moazen, Z. Chen, J. Zhang, Z. Jin, A real-time topography of maximum contact pressure distribution at medial tibiofemoral knee implant during gait: Application to knee rehabilitation, Neurocomputing. 154 (2015) 174–188.

[23]   H. Yoshida, A. Faust, J. Wilckens, M. Kitagawa, J. Fetto, E.Y.S. Chao, Three-dimensional dynamic hip contact area and pressure distribution during activities of daily living, J. Biomech. 39 (2006) 1996–2004.

[24]   M.K. Friedrich Graef, Determination of Micromotion at the Implant Bone Interface - An In-Vitro Methodologic Study, Dentistry. 5 (2015).

[25]   M. Baxmann, S.Y. Jauch, C. Schilling, W. Blömer, T.M. Grupp, M.M. Morlock, The influence of contact conditions and micromotions on the fretting behavior of modular titanium alloy taper connections, Med. Eng. Phys. 35 (2013) 676–683.

[26]   S.Y. Jauch, G. Huber, H. Haschke, K. Sellenschloh, M.M. Morlock, Design parameters and the material coupling are decisive for the micromotion magnitude at the stem-neck interface of bi-modular hip implants, Med. Eng. Phys. 36 (2014) 300–307.

[27]   S. Holst, H. Geiselhoeringer, M. Wichmann, A.I. Holst, The effect of provisional restoration type on micromovement of implants, J. Prosthet. Dent. 100 (2008) 173–182.

[28]   J.B. Brunski, In vivo bone response to biomechanical loading at the bone/dental-implant interface., Adv. Dent. Res. 13 (1999) 99–119.

[29]   S.S. Moncler, H. Salama, Y. Reingewirtz, J.H. Dubruille, Timing of Loading and Effect of Micromotion on Bone–Dental Implant Interface: Review of Experimental Literature, J. Biomed. Mater. Res. 43 (1997) 192–203.

[30]   A. Fantetti, L.R. Tamatam, M. Volvert, I. Lawal, L. Liu, L. Salles, M.R.W. Brake,

C.W. Schwingshackl, D. Nowell, The impact of fretting wear on structural dynamics: Experiment and Simulation, Tribol. Int. 138 (2019) 111–124.

[31]   S. Fouvry, P. Kapsa, L. Vincent, Quantification of fretting damage, Wear. 200 (1996) 186–205.

[32]   R.D. Mindlin, H. Deresiewicz, Elastic Spheres in Contact Under Varying Oblique Forces, J. Appl. Mech. 20 (1953).

[33]   J. Ding, I.R. McColl, S.B. Leen, P.H. Shipway, A finite element based approach to simulating the effects of debris on fretting wear, Wear. 263 (2007) 481–491.

[34]   L. Vincent, Y. Berthier, A. Floquet, M. Godet, Fretting: Load carrying capacity of wear debris, J. Tribol. 106 (1984) 192–200.

[35]   S. Heredia, S. Fouvry, Introduction of a new sliding regime criterion to quantify partial, mixed and gross slip fretting regimes: Correlation with wear and cracking processes, Wear. 269 (2010) 515–524.

[36]   O. Vingsbo, S. Söderberg, On fretting maps, Wear. 126 (1988) 131–147.

[37]   J. Geringer, A. Boyer, S. Ehsani, V. Fridrici, P. Kapsa, K. Thorwarth, R. Hauert, T. Taylor, L. Semeste, P. Olubambi, New representative Master Curve in tribocorrosion, Applications on trunnion issue, hip joint (Paper-ID: 292821), in: Virtual EUROCORR, 2020.

[38]   R.W. Neu, Progress in standardization of fretting fatigue terminology and testing, Tribol. Int. 44 (2011) 1371–1377.

[39]   L. Ma, K. Eom, J. Geringer, T. Jun, Literature Review on Fretting Wear and Contact Mechanics of Tribological Coatings, Coatings. 9 (2019) 1–20.

[40]   P. Corne, P. De March, F. Cleymand, J. Geringer, Fretting-corrosion behavior on dental implant connection in human saliva, J. Mech. Behav. Biomed. Mater. 94 (2019) 86–92.

[41]   S. Cao, S. Mischler, Modeling tribocorrosion of passive metals – A review, Curr. Opin. Solid State Mater. Sci. 22 (2018) 127–141.

8.1. General discussion

Nature is the main inspiration for the creation of biomaterials with diverse properties. Indeed, it is in nature that it is possible to see materials with properties and hierarchical structures together with mechanisms that go beyond what materials engineering can mimic and/or produce. One of the greater examples is bone architecture that has been a struggle to achieve. Although, especially in the last decades, besides the outstanding growth with prodigious outcome in the biomedical field, there are still challenges and problems to be solved and overcome to accomplish the ultimate promising biomaterial.

The definition of biomaterial presented in Chapter 2 can be already achieved but the optimum balance resulted from all the fields of properties has not been accomplishing and the progress on the investigation must continuous. The fact that we consider a material as a biomaterial, since it was designed and studied for this function, does not mean that we can control all the interactions with the living systems in all the bodies and through all the situations where it will be used. The same was expected with the definition of biocompatibility stated in Chapter 2. The appropriated response is still under discussion since no guidance yet established in the nature of the interactions and it is still very hard to do a rigorous control of what happened since the implantation until the end of the service.

Although orthopaedic implants can be considered very successful, many patients still face two major complications: infections and aseptic loosening of the implant [1–4]. Much of the recent work in this field has focused on the design of material solutions either to prevent aseptic loosening while ignoring infection or vice versa or to promote osseointegration while ignoring microbial susceptibility. However, both solutions are required to achieve the long-term success of the implant. Therefore, it is very important that such procedures will be evaluated during the development of new orthopaedic strategies. Developing a strategy that can maintain both the anti-microbial and osseointegrative capabilities at a long-term scale is critical for the viability of the implant technologies, making the early results for engineered surface topographies quite

promising. The outcome of technologies to address all the challenges stated above simultaneously is ongoing. A clear future direction for the field is the development of multifunctional implant materials that can effectively balance osseointegration and microbial challenges. The ideal orthopaedic implant surface will likely be multifunctional, combining different technologies to simultaneously promote osseointegration while inhibiting microbial infection and stop aseptic loosening. The hope is that new understanding and new directions of research will result in patients receiving these ideal implants, thereby reducing premature implant failures and also extending overall implant lifetimes.

To achieve the main aim, a systematic and multidisciplinary approach was followed, through which new scientific knowledge was produced in research fields that were not yet explored in literature. The development of this thesis comprised several studies, which were reported in different scientific papers all interrelated with each other. In this way, this chapter is where the main results of this project, presented form Chapter 3 to Chapter 7, are discussed with the presentation of the interrelation existing between the main outcomes of each chapter together with some important topics that were additionally discussed.

Tissue like the bone has a hierarchically organized structure where pore size and porosity change from cancellous to cortical bone, and this express into distinct and peculiar mechanical properties. The bone-mimicking mechanical properties can be achieved by a promising solution of hierarchical macro-porous Ti covered by a porous oxide titanium layer with Ca, P and Sr as bioactive elements. This solution tailors the material form the nano- to the macro-scale to fruitful all the requisites of an implant. By increasing the surface area and porosity of the implant, it was possible to improve bone-ingrowth through the implant, thereby reducing micro-motion and increasing osseointegration. At the same time, through compositional or structural modification, it was possible to decrease Young's modulus of the implant to match the one of the bone. The use of porous metals for implants instead of fully dense materials can reduce the Young's modulus mismatch, and consequently, the stress-shielding problem [2,5–8]. Powder metallurgy together with the space holder technology was presented in Chapters 2, 6 and 7, as a suitable way to produce such a porous Ti structure.

However, Ti implants cannot bond to living bone directly after implantation into the host body. To achieve improved osseointegration, the composition and topography of the implant surfaces were modified. Micro-arc oxidation (MAO) process is one of the best methods for modifying the implant's surface, by creating a nano- and micro-structured TiO_2 bioactive layer on the surface due to the incorporation of bioactive elements in the oxide layer. Micro-arc oxidation can also improve electrochemical and triboelectrochemical behaviour and decrease metal ion release like presented in Chapters 2, 4, 5 and 6.

Powder metallurgy and MAO are considerable simple and low-cost techniques. More expensive materials and processing technologies do not motivate investment as easily as the simple ones and undemanding approaches that can bring immediate production. The use of technologies already existent in other areas is also an added value. MAO is also widely used in aluminium [9,10] and magnesium [11,12] based materials and is also used to improve the performance of metal materials on other application far from biomedical ones, like for the marine field [11,13].

The increasing and promising interest in the effect of Sr for bone tissue regeneration has been reflected in recently superior incorporation studies of new Sr-containing biomaterials to enhance bone repair. However, the effect of Sr concentration in *in vitro* studies was still scarce and most of the reports do not present an adequate control group or an adequate characterization. The demand for further knowledge on the Sr-enriched materials was still ongoing and that is why the main focus on Chapter 3 and 4 was to study the effect of three Sr concentrations on characterization, biological and tribocorrosion evaluations.

Like stated in Chapter 2, functionally graded materials (FGMs) are attracting attention showing that gradients in composition, morphology and porosity in a structure showed a new path of success in this field. These materials also can emphasize the promising future direction, which can lead us near to success [14]. Since it was such a complex hierarchical tailored solution, its evaluation needed to be performed separately to achieve the optimum balance between all the properties required, as well as the following discussion.

Porous Ti-based structures in all the scales (nano, micro and macro) have been studied for several body parts like mandible [15], cervical [16], hip [17], dental [18] and knee [19]. Highy porous Ti-based structures can be even used in drug-releasing purposes [20,21].

To achieve the amount of ideal porosity, one must consider the architecture of the porous structure and the pore size distribution as well as their interconnection. Moreover, pore architecture and their interconnection size were considered as important properties influencing mass transport and migration properties, vascularization potential and cellular organization. This was not only important for biologic performance but also for mechanical performance. Therefore, porosity value affects both the available surface area and the fluid transport properties which need to be finely balanced to obtain an optimized porous structure. For this purpose, the diameter of pores in porous Ti structures was evaluated, presented and discussed in Chapters 2, 5 and 6. There is still no consensus in the optimum pore size but it is well known that a wide pore size distribution is important to fulfil biological activity. More specifically, it was shown in the literature that macrophages were sensitive to the diameter of the pores since a pore size diameters above 80 µm were shown to favour the pro-inflammatory type M1 macrophage polarization within a pore structure [22]. Recently, Wo *et al.* [23] showed that macro-porous Ti structures facilitated osteoblast adhesion and differentiation when pore size was 300 µm (comparing to 500 and 800 µm) or with higher amount of porosity (58% comparing to 30%). On the other hand, proliferation was more promising with 800 µm of pore size and 58% of pore fraction. Besides amount of porosity and pore size, pore interconnection is also a major factor. The interconnection is the aperture between two adjacent pores by which cells must go through to fully colonize a porous structure. Although this parameter appears to be important regarding cell migration, the relationship between interconnection diameter and cell behaviour is poorly documented in the literature compared to the studies related to pore size and amount of porosity. Cell colonization and vascular growth across porous structures are closely linked to the diameter of the interconnections. The supply of nutrients as well as the removal of cellular wastes are also related to the parameter.

Cell penetration and cells' communication and consequently, tissue growth rate is promoted by a well interconnected porous structure [24].

Pattern, grooves and pores from the nano- to the macro-scale are known to improve biocompatibility with the body and reduce adverse reactions. Hierarchical and tailored topographical structures need to be balanced with suitable wettability and roughness since they are parameters essential for cell response [25–27]. Wettability and roughness evaluation was presented in Chapter 5 for macro-porous surfaces. Cells are sensitive to topographical parameters like roughness but also to the curvature of their substrate. Accordingly, the curved surface provided by porous structures appeared as an additional feature which will condition cell functions [24].

The need to characterize porosity is a fact. Different techniques have been used in the literature like Archimedes principle [28], helium pycnometry [29], tomography as micro-CT, like in Chapters 6 and 7, image analysis, like in Chapter 5 and 6 and electrochemical impedance spectroscopy (EIS) [30]. Recently, Giner *et al.* [30] used EIS to characterize *in vitro* osteoblast cell response in a porous Ti structure. The authors stated that techniques that are required to evaluate and monitor the renewal, differentiation and maturation of osteoblast cells in culture after different experimental conditions are generally destructive techniques, such as histology, scanning electron microscopy, fluorescence microscopy, immunohistochemistry and other biochemical assays. As an alternative approach, the authors used impedance-based cellular assays in the field of tissue engineering and regenerative medicine offer a range of methods that use microelectrodes to measure the impedance of biological systems, and thus obtain information of cellular behaviour growing on any surface or biomaterials. Giner *et al.* [30] studied and discussed the use of EIS to characterize both the porosity size of porous titanium discs produced by space holder technique and the growth of osteoblast cell cultures on the flat surface and inside of pores.

One of the main drawbacks in studying porous structures is to know the exact area of pores exposed to the electrolyte. The determination of real exposed area to the electrolyte of highly porous structures is being reported as the main difficulty in evaluating the corrosion behaviour of these structures. The raw data acquired by micro-CT, presented in Chapter 6, was used to determine the real metallic area exposed to the electrolyte of highly porous Ti samples. Because even if it is known the number of pores

that are exposed, it is hard to know if the electrolyte penetration was at the same time in the most inner pores. When placing the sample horizontally, it has been promoted the penetration inside of the pores and the creation of a more homogenous natural oxide film as stated in Chapter 6. Thus, it is believed that the knowledge of the real exposed area was a step forward to study the corrosion behaviour of highly porous Ti structures. It can be also an improvement when evaluating the biological results of such structures. Previously, porous structures similar to the ones on Chapters 6 and 7 were biologically evaluated [26] and presented promising biological outcome. On the study [26], seeding of cells was according to the geometrical area exposed and not real exposed metallic area. Future studies can investigate these promising structures with the seeding of cells according to the real exposed area that was calculated by the method based on micro-CT results. The determination of real exposed area to the electrolyte when MAO treatment is being performed is also a concern that will be discussed in the next sub-chapter.

The presence of porosity in the implant can reduce or even eliminate the problem of the Young's modulus mismatch effectively and also assure good biological fixation of the implant with the surrounding tissue. A porous structure can also help the blood circulation, the healing process of implant and reduction of the overall weight of the implant [14]. However, the problem of aseptic loosening is associated with the gaps at the bone–implant interface. Firstly, there are micromotions of the implant relative to the bone and that can lead to a progressive worsening of micromotions. At the same time, wear particles may start to interfere in direct contact between bone and implant. These wear particles may activate macrophages, initiating a cytokine signalling cascade that can lead to osteoclastogenesis and bone resorption [8]. In this way, the main novelty of Chapter 7 was the study of this micromotions on porous Ti structures.

MAO has been known to improve the biologic outcome showing treated surfaces with good biocompatibility in terms of cell attachment, proliferation and differentiation in bone tissue. Moreover, it was previously demonstrated that the relevance of bio-functionalization treatment on porous Ti macro-structures allowed the incorporation of Ca and P on the anodic layers on the most outer surface, but also into the pores, which may allow the supply of bioactive elements when necessary [26]. MAO has been demonstrated to improve corrosion, as stated in Chapter 5 and 6, and tribocorrosion responses, as stated in Chapter 4, 5 and 6.

The application of MAO layers is widely broad since has been introduced for decorative purposes, photocatalytic activity [31,32] and to aid drug release [33–35]. MAO is presented as an eco-friendly technique where the surface characteristics of metal would be altered significantly by electrochemical reactions assisted by plasma discharges, resulting in the formation of a hard, conformal, adhesive and porous inorganic layer on the metal substrate. The main mechanism characteristic from MAO process is the dielectric breakdown which makes micro-arc and micro-sparks discharges that are developed rapidly and extinguished. MAO treatment is influenced by the substrate, time of treatment, electrical parameters and electrolyte composition [36].

Regarding the substrate, there is still a lot of discussion about the preparation of samples before MAO treatment can lead to significant differences in the oxide layer formed during the treatment. Previously, it was shown that preparation of the Ti6Al4V substrates was the principal factor that determined not only the grain and pore sizes but also the morphology and topography of the coating. Consequently, the presence of the amorphous TiO_2 passive film (unpolished) resulted in thicker and more irregular oxide layer produced by MAO than when anodization was done on the bare metal surface (like polished) [37]. The authors stated that grain size and pore size of the MAO layer were determined principally by substrate preparation (unpolished *vs* polished) rather than time or electrolyte concentration. In Chapters 3, 4, 5 and 6, samples were etched in a dilute acid mixture before MAO treatment to uniform the roughness inside and outside of the pores, to remove impurities and the passive oxide layer.

The growth of the oxide layer during the time of MAO treatment is still under evaluation. Recently, Zhang *et al.* [38] presented an oxide layer after applying MAO treatment for 5 , 10 , 30 and 60 s to reveal the growth mechanism before or just after the initiation of dielectric breakdown. First, what happened was the growth of the barrier film due to its compaction that is the main protection to corrosion like stated in Chapters 5 and 6. Then, TiO_2 layer presented ultrafine pores, which evolved the grooved morphology and finally became a typical porous structure from MAO after the prolongation of oxidation periods. Zhang *et al.* [38] showed three distinctive stages with typical morphologies, namely ultrafine pores (5 s), grooved craters (10 and 30 s) and porous structure (1 and 10 min). During the early stages, the authors stated that dramatic modifications of porosity, morphology and thickness were occurring. The ultrafine pores after 5 s oxidation were originated from oxygen evolution associated with electrochemical reactions, which thus could be maintained until the end of MAO process since it was independent of the dielectric breakdown. Since the electric field may concentrate at the edge of the previously formed pores, it thus stimulated oxygen generation. As a result, ultra-fine pores could aggregate together to form the grooved craters. Along with the formation of grooved morphology, porosity continued to increase, which also caused the growth of the oxide with a dramatic increase in thickness [38].

Chapter 5 presented the study of corrosion and tribocorrosion behaviour of the hierarchical porous structures with tailored topography and chemical composition, developed by combining two-steps of anodic treatment, including the regime under micro-arc oxidation (MAO), considered as a versatile and low-cost technique. The effect of MAO on the corrosion and tribocorrosion has been already studied in the literature. However, corrosion and tribocorrosion behaviour of such surfaces having multi-scale porosity with tailored topography and chemical composition, to the best of the author's knowledge, has not been studied before. Chapter 5 provided a first and new insight into the wear–corrosion mechanisms involved in hierarchical bio-functionalized porous surfaces developed for biomedical implants. It was shown that the evolution of current during the MAO treatment did not reveal any noticeable difference between groups (plane and porous surfaces) and it was possible to state that the increased exposed area

did not affect the morphology, thickness, chemical composition and the crystalline nature of the MAO layers.

In Chapter 6, it was shown the current density evolution during MAO process regarding dense and porous Ti. Higher levels of porosity led $t_{gal/pot}$ to increase probably due to the increased exposed metallic area by the porous surfaces. The galvanostatic period is the one governing the barrier film formation that led to better corrosion behaviour and consequently, differences in the $t_{gal/pot}$, may lead to differences in the electrochemical behaviour. By increasing the duration of galvanostatic control (i.e. for longer $t_{gal/pot}$), it is considered that the thickness of the barrier film (thin and compact oxide film) increased and therefore the corrosion behaviour of bio-functionalized highly porous samples was improved. In theory, a longer galvanostatic period lead to an increase on the total charge of the system ($Q = I \times t$) which would influence the amount of oxide formed during this stage of the process. On the other hand, on the second stage (when current fall) higher currents measured are usually associated with a thinner oxide film. However, the increase of total charge did not account for a significant difference in the thickness of the MAO layer (at least on the outmost surface). Also, from the cross-sections obtained in the samples from each group, it was not possible to observe any visible effects in the compactness of the oxide. This was preceded by the problem of knowing the exposed area to the electrolyte when MAO is being performed. Moreover, different FIB cuts were performed at the outermost surface in order to understand if the macro-porosity influenced the MAO layer formation in terms of structure and thickness. As stated in the chapter, there were no significant differences on MAO layer (at least on the outmost surface) among the groups. Macro-porosity level increased the interconnectivity of the pores which may lead to a difficulty on the electrolyte to wet all the metallic area which consequently can create some heterogeneities on the MAO layer on the most inner pores. Moreover, it is important to state that it was tried to use micro-CT to understand how depth the MAO layer was formed in the most inner pores however, the MAO layer was not detected by micro-CT.

Like stated in Chapter 2, there is still no consensus on how much amount of metal ions can be tolerable in the human body [39]. In consequence, regarding the metal release from orthopaedic implants, very little is known about the size, the chemical toxicity or bioavailability of degraded implant products that are released into and

accumulate within tissues around the implant. Although the formation of nanoparticles has been speculated, their distribution and speciation are still not elucidated as well as its limited. Findings highlight the propensity for particle accumulation in the inflamed tissues around dental implants and will help guide toxicological studies to determine the biological significance of such exposures. Unfortunately, Ti particles from Ti (Grade 4) implants from several manufactures were found in peri-implant tissue in the nano- to micro-scale order in local densities of up to several ten millions per mm^3 [40]. In this way, it is required the use of an appropriate surface modification to improve the surface properties of the implant and consequently, decrease and hopefully eliminate the metal ion release [41–45]. As also stated in Chapter 5, metal ion release for macro-porous surfaces decreased after bio-functionalization by MAO, indicated that the TiO$_2$ layer formed protected the metal substrate, showing MAO treatment a valuable asset on decreasing the metal ion release.

As explained in Chapters 4 and 5, wear mechanism of MAO layer in most of the tribocorrosion conditions tested was based in a progressive removal of the higher asperities of the rough oxide. The normal load chosen for Chapters 4 and 5 was 0.5 N, corresponding to a maximum Hertzian contact pressure of 330 MPa for Ti that is already drastically above the contact pressure found in the human body for implant materials that is lower than 10 MPa [46–48]. For example, on the femoral structure, the peak pressure for normal walking is 3.26 MPa while standing up is 8.97 MPa [49]. 0.5 N was also chosen to avoid induced plastic deformation of Ti by the influence of the normal load since it was aimed to keep the applied load lower than the yield strength of Ti that can go up to 410 MPa [50]. A fretting frequency of 1 Hz was applied in order to simulate the average human gait. 1 Hz is also presented as the optimal stride frequency [51–53]. In this way, the conditions used for Chapters 4 and 5 studies are well above the ones found in the human body, showing the material response to a harsher condition that what target application requires. The same was stated in Chapter 7 for highly porous structures under fretting-corrosion solicitations.

Sr, within the group II of the periodic table of elements, follows directly calcium as alkaline earth metal. Due to its chemical and physical similarities, Sr can be accumulated in the skeleton. Sr appears as a trace element in the lithosphere and moves up into food chain. Plants absorb Sr in their environment proportionally and the animals prefer Ca in favour of Sr. Consequently, the Sr/Ca ratio is higher in plants than in animals [54,55].

Sr has been presenting functions of osteogenesis induction [56–61], osteoclastogenesis inhibition [62–64] and may have antibacterial properties [56,65]. In this way, Sr incorporation in MAO layers may be a valuable strategy to improve bone response to implants.

Sr was previously added to MAO structures [58,65–68] but the optimum level of Sr inclusion had not been elucidated. It is well known that modifying electrolyte parameters can lead to significant changes in the MAO layer, however, the knowledge of the introduction of bioactive elements and the effect of their concentrations was still very scarce. That is why the effect of three different Sr concentration was characterized and biological and tribocorrosion evaluated on Chapters 3 and 4.

The possible mechanism behind Sr activity is correlated to the activation via strontium divalent cations (Sr^{2+}) of the calcium-sensing receptor (CaR), which is expressed by bone cells. The activation of CaR triggers cell proliferation and differentiation in osteoblasts and, at the same time, apoptosis in osteoclasts, thereby promoting bone formation and reducing bone resorption. Sr can substitute Ca in the hydroxyapatite lattice, because it can have the same charge. Because of the chemical analogy with Ca, Sr is a bone seeking element and 99% of the Sr that is in the human body is on the skeleton. The incorporation of Sr^{2+} instead of Ca^{2+} in the HAP structure is reported to enhance bioactivity, biocompatibility, biodegradable rate and compressive strength compared with the traditional Sr-free HA. Indeed, several studies [55,69–73] reported the effects of Sr-HAP and Sr by itself as a promoter in the improvement of the bioactivity and biocompatibility of implants, together with an increased bone formation and less bone resorption. However, Sr concentration plays a crucial factor. As it was possible to see in Chapter 3, Sr in low concentrations did not compromise initial cell adhesion either viability and interestingly improved mineralization. However, higher

concentration of Sr showed to induce collagen secretion but with compromised mineralization, possibly due to a delayed mineralization process or induced precipitation of deficient hydroxyapatite.

The physical and chemical properties of material play an important role in the overall bioactivity of doped implants and in turn mediating cellular functions. The interplay between bioactive elements was also not yet fully clarified in the literature. Sr has been combined with a lot of elements, like Ca, P, Co F and Zn [65,74] but its effects and its ideal concentration is still under evaluation. Sr can play a role in anti-bacterial mechanisms but that was not yet well-established [75,76]. However, it was found out that silver antibacterial effect can be promoted by the presence of Sr ions. Silver and strontium combination showed promising results against bacterial strains such as methicillin-resistant *Staphylococcus aureus* (MRSA), which have developed resistance to common antibiotics [77]. It is important to develop adequate models to study the effect of Sr for antibacterial research in future studies, in order to better define the concentration on the therapeutic application of this element.

The increase on the collagen production, stated in Chapter 3, especially for the groups with higher amount of Sr (mmSr and mmmSr), opened the perspective to adapt this material to be a kind of collagen bio-stimulator in the tissues in which the mineralization is considered a side effect, for example, in soft conjunctive tissue regeneration. As stated in Chapter 4, the condition with a higher amount of Sr (mmmSr) presented a better preliminary response to tribocorrosion evaluation.

Sr has been also used with drug release solutions [78–80]. The use of Sr has been broadly applied and its doping on a TiO_2 oxide layer on porous Ti is quite promising and comprehensive.

FGMs are showing a new path to the problem of longevity and durability of artificial implants. In this project, efforts to achieve TiO_2 layer doped with Sr on a macro-porous Ti have been made. However such combination, functionally graded macro-porous doped with Sr was not achieved, because more efforts were made to produce new insights on the solutions separated. After characterization and biological and triboelectrochemical evaluation, Ti structures doped with bioactive elements on the TiO_2 layer are suggested as a promising biomaterial. By comparing with the available literature, this thesis remarkably shows that significant improvements have been

achieved. For example, by means of a simple approach, a simple and fast two-step anodic treatment was developed in Chapter 5 in order to produce macro-pores only on the surface with the incorporation of bioactive elements. The new methodology developed may bring new insights to improve already existing implant systems, or even to create new surfaces with enhanced functionalities.

This study takes along a fundamental and insightful contribution by providing new knowledge on the mechanisms behind tribocorrosive degradation of macro-porous structures that is still very scarce in the literature. This thesis brings a profound and innovative knowledge of the synergistic role of macro- and micro-pores effects. In the end, the investigations described and discussed in this thesis can contribute to develop a hard anticorrosive bioactive porous hierarchical graded structure for a durable and successful artificial load-bearing implant.

8.2. Final conclusion

The main hypothesis formulated at the beginning of this thesis, in Chapter 1, was validated since Sr incorporated in a micro-porous Ti oxide layer formed on a macro-porous Ti can improve both the biological and triboelectrochemical response of the Ti implant.

Therefore, based on the experimental approaches carried out on this work, the following conclusions are highlighted addressing the three main objectives obtained by dividing the main hypothesis:

• The incorporation of Sr did not affect significantly the pore size and morphology in the TiO_2 layer, although, it changed the chemical composition and the oxide crystal structure; biological tests revealed that lower concentrations of Sr did not compromise initial cell adhesion neither viability and interestingly improved mineralization; higher Sr concentration in the MAO electrolyte led to an increase of rutile phase within the MAO surfaces resulting in less visible mechanical damage and lower COF during tribocorrosion tests;

• A macro-porous surface structure covered with a micro-porous Ca- and P-rich oxide layer was produced using a fast and simple two-step anodic treatment; The

presence of macro-porosity did not deteriorate the bio-functionalization treatment, either chemical composition (Ca/P ratio) and layer structure;

• A macro-porous surface structure covered with a micro-porous Ca- and P-rich oxide layer exhibited a lower tendency to corrosion and more stable COF values under sliding; the electrochemical behaviour of highly porous Ti samples was improved by the bio-functionalization treatment in terms of thermodynamic and kinetics; the improved corrosion behaviour of bio-functionalized highly porous samples was mostly due to the barrier film formed under longer galvanostatic control during the MAO process; fretting response between highly porous Ti against Ti alloy was highly dependent on the applied load and several mechanical responses were obtained; the promising surface morphology of the highly porous Ti was preserved and was highlighted by its mechanical integrity under severe contact after 16 hours of fretting-corrosion solicitations.

Thus, following the main objectives of this work, within the limitations of this work, it can be concluded that macro-porous Ti with micro-porous Ti oxide layer with Ca, P and Sr can be considered as an implant material for biomedical applications.

8.3. Perspectives

Despite the number of experiments and results obtained throughout this research, there are open questions that may be deliberated for upcoming investigations. In this way, based on current findings, it is proposed to be considered for further investigation:

• Following the study in Chapter 3, the assessment of the role of Sr in anti-bacterial mechanisms and osteoclast culture;

• Evaluation of the biomechanical stability and biological response of macro-surfaces produced in Chapter 5;

• An in-depth study to define the area exposed to the electrolyte by a porous Ti structure and the oxide layer formation throughout the porous structure (micro-CT and slice-and-view FIB-SEM may be used to help to quantify the metallic area exposed to the electrolyte and to evaluate how is the oxide layer formed by MAO in the most inner pores; thermal imaging cameras may record the nature and temperature outputs from discharges, which may create temperature gradients during layer growth);

• Additional mechanical testing, including deeper evaluation on fretting corrosion, fatigue corrosion and fracture of macro-porous Ti structures;

• As reported in Chapter 2, dynamic methods like ultrasound technique to determine the Young's modulus of macro-porous Ti;

• *In vitro* evaluation of macro-porous Ti structures with TiO_2 layers doped with Sr to determine the consistency between these results and the benefits of bio-functionality on the longevity of orthopaedic implants.

References

[1]   S. Bilgen, G. Eken, Surgical Site Infection After Total Knee Arthroplasty : A Descriptive Study, Int. Multispecialty J. Heal. 2 (2016) 1–8.

[2]   F.A. España, V.K. Balla, S. Bose, A. Bandyopadhyay, Design and fabrication of CoCrMo alloy based novel structures for load bearing implants using laser engineered net shaping, Mater. Sci. Eng. C. 30 (2010) 50–57.

[3]   V. Goriainov, R. Cook, J. M. Latham, D. G. Dunlop, R.O.C. Oreffo, Bone and metal: an orthopaedic perspective on osseointegration of metals, Acta Biomater. 10 (2014) 4043–4057.

[4]   B. Zhao, A.K. Gain, W. Ding, L. Zhang, X. Li, Y. Fu, A review on metallic porous materials: pore formation, mechanical properties, and their applications, Int. J. Adv. Manuf. Technol. 95 (2018) 2641–2659.

[5]   S.Y. Min, Y. Kim, T.K. Lee, S. Seo, H.S. Jung, D. Kim, J. Lee, B.J. Lee, The effect of porosity on the elasticity of pure titanium: An atomistic simulation, Met. Mater. Int. 16 (2010) 421–425.

[6]   O. Smorygo, A. Marukovich, V. Mikutski, A.A. Gokhale, G.J. Reddy, J.V. Kumar, High-porosity titanium foams by powder coated space holder compaction method, Mater. Lett. 83 (2012) 17–19.

[7]   A. Bansiddhi, D.C. Dunand, Titanium and NiTi foams for bone replacement, Woodhead Publishing Limited, 2014.

[8]   J. Raphel, M. Holodniy, S.B. Goodman, S.C. Heilshorn, Multifunctional coatings to simultaneously promote osseointegration and prevent infection of orthopaedic implants, Biomaterials. 84 (2016) 301–314.

[9]   X. Liu, L. Zhu, H. Liu, W. Li, Investigation of MAO coating growth mechanism on aluminum alloy by two-step oxidation method, Appl. Surf. Sci. 293 (2014) 12–17.

[10]   R. Kamal Jayaraj, S. Malarvizhi, V. Balasubramanian, Optimizing the micro-arc oxidation (MAO) parameters to attain coatings with minimum porosity and maximum hardness on the friction stir welded AA6061 aluminium alloy welds, Def. Technol. 13 (2017) 111–117.

[11]   Y. Yao, W. Yang, D. Liu, W. Gao, J. Chen, Preparation and corrosion behavior in marine environment of MAO coatings on magnesium alloy, Materials (Basel). 13 (2020).

198

[12]   T.S.N. Sankara Narayanan, I.S. Park, M.H. Lee, Strategies to improve the corrosion resistance of microarc oxidation (MAO) coated magnesium alloys for degradable implants: Prospects and challenges, Prog. Mater. Sci. 60 (2014) 1–71.

[13]   A. Mathis, T. Millot, V. Branger, R. Muller, J. Gueneheux, Tribological functionalization of titanium alloys by Micro-Arc Oxidation for marine applications, MATEC Web Conf. 321 (2020) 09001.

[14]   S. Roy, Functionally graded coatings on biomaterials : a critical review, Mater. Today Chem. 18 (2020) 100375.

[15]   J. Parthasarathy, B. Starly, S. Raman, A design for the additive manufacture of functionally graded porous structures with tailored mechanical properties for biomedical applications, J. Manuf. Process. 13 (2011) 160–170.

[16]   S. Fujibayashi, M. Takemoto, T. Nakamura, T. Matsushita, T. Kokubo, K. Sasaki, S. Mori, S. Matsuda, Stand-Alone Anterior Cervical Discectomy and Fusion Using an Additive Manufactured Individualized Bioactive Porous Titanium Implant without Bone Graft: Results of a Prospective Clinical Trial, Asian Spine J. (2020).

[17]   S. Arabnejad, B. Johnston, M. Tanzer, D. Pasini, Fully porous 3D printed titanium femoral stem to reduce stress-shielding following total hip arthroplasty, J. Orthop. Res. 35 (2017) 1774–1783.

[18]   Z.J. Wally, W. van Grunsven, F. Claeyssens, R. Goodall, G.C. Reilly, Porous titanium for dental implant applications, Metals (Basel). 5 (2015) 1902–1920.

[19]   N.S. Winther, C.L. Jensen, C.M. Jensen, T. Lind, H.M. Schrøder, G. Flivik, M.M. Petersen, Comparison of a novel porous titanium construct (Regenerex®) to a well proven porous coated tibial surface in cementless total knee arthroplasty — A prospective randomized RSA study with two-year follow-up, Knee. 23 (2016) 1002–1011.

[20]   S. V. Gunther, G.T. Dambaev, T.L. Chekalkin, J.H. Kang, J.S. Kim, V.E. Gunther, Porous TiNi-based material and infrared radiation in needle-free treatment of diabetic patients, Adv. Mater. Lett. 7 (2016) 713–718.

[21]   M. Badar, M.I. Rahim, M. Kieke, T. Ebel, M. Rohde, H. Hauser, P. Behrens, P.P. Mueller, Controlled drug release from antibiotic-loaded layered double hydroxide coatings on porous titanium implants in a mouse model, J. Biomed. Mater. Res. - Part A. 103 (2015) 2141–2149.

[22]   L.R. Madden, D.J. Mortisen, E.M. Sussman, S.K. Dupras, J.A. Fugate, J.L. Cuy, K.D. Hauch, M.A. Laflamme, C.E. Murry, B.D. Ratner, Proangiogenic scaffolds as functional templates for cardiac tissue engineering, Proc. Natl. Acad. Sci. U. S. A. 107 (2010) 15211–15216.

[23]   J. Wo, S. Huang, D. Wu, J. Zhu, Z. Li, F. Yuan, The integration of pore size and porosity distribution on Ti-6A1-4V scaffolds by 3D printing in the modulation of osteo-differentiation, JABFM. 18 (2020) 1–10.

[24]   G. Lutzweiler, A.N. Halili, N.E. Vrana, The overview of porous, bioactive scaffolds as instructive biomaterials for tissue regeneration and their clinical translation, Pharmaceutics. 12 (2020) 1–29.

[25]   R. Ion, A.B. Stoian, C. Dumitriu, S. Grigorescu, A. Mazare, A. Cimpean, I. Demetrescu, P. Schmuki, Nanochannels formed on TiZr alloy improve biological response, Acta Biomater. 24 (2015) 370–377.

[26]   A.C. Alves, R. Thibeaux, F. Toptan, A.M.P. Pinto, P. Ponthiaux, B. David, Influence of macroporosity on NIH/3T3 adhesion, proliferation, and osteogenic differentiation of MC3T3-E1 over bio-functionalized highly porous titanium implant material, J. Biomed. Mater. Res. - Part B Appl. Biomater. 107 (2019) 73–85.

[27]   A.R. Ribeiro, F. Oliveira, L.C. Boldrini, P.E. Leite, P. Falagan-Lotsch, A.B.R. Linhares, W.F. Zambuzzi, B. Fragneaud, A.P.C. Campos, C.P. Gouvêa, B.S. Archanjo, C.A. Achete, E. Marcantonio, L.A. Rocha, J.M. Granjeiro, Micro-arc oxidation as a tool to develop multifunctional calcium-rich surfaces for dental implant applications, Mater. Sci. Eng. C. 54 (2015) 196–206.

[28]   X. Wang, Z. Lu, L. Jia, F. Li, Preparation and properties of low cost porous titanium by using rice husk as hold space, Prog. Nat. Sci. Mater. Int. 27 (2017) 344–349.

[29]   E. Molero, A.J. Sanchez-Herencia, R.G. das Neves, E. Gordo, B. Ferrari, Shaping strategies for porous Ti fabrication throughout colloidal chemistry, Key Eng. Mater. 704 (2016) 406–412.

[30]   M. Giner, A. Olmo, M. Hernández, P. Trueba, E. Chicardi, A. Civantos, M.Á. Vázquez, M.J. Montoya-García, Y. Torres, Use of impedance spectroscopy for the characterization of in-vitro osteoblast cell response in porous titanium bone implants, Metals (Basel). 10 (2020) 1–14.

[31]   N. Ohtsu, D. Ishikawa, S. Komiya, K. Sakamoto, Effect of phosphorous

200

incorporation on crystallinity, morphology, and photocatalytic activity of anodic oxide layer on titanium, Thin Solid Films. 556 (2014) 247–252.

[32]   X. Jiang, A. Shi, Y. Wang, Y. Li, C. Pan, Effect of surface microstructure of TiO2 film from micro-arc oxidation on its photocatalytic activity: a HRTEM study, Nanoscale. 3 (2011) 3573.

[33]   X. Xu, P. Lu, M. Guo, M. Fang, Cross-linked gelatin/nanoparticles composite coating on micro-arc oxidation film for corrosion and drug release, Appl. Surf. Sci. 256 (2010) 2367–2371.

[34]   C.M. Han, E.J. Lee, H.E. Kim, Y.H. Koh, J.H. Jang, Porous TiO2 films on Ti implants for controlled release of tetracycline-hydrochloride (TCH), Thin Solid Films. 519 (2011) 8074–8076.

[35]   P. Lu, Y. Liu, M. Guo, H. Fang, X. Xu, Corrosion and drug release properties of EN-plating/PLGA composite coating on MAO film, Mater. Sci. Eng. C. 31 (2011) 1285–1289.

[36]   A. Fattah-alhosseini, M. Molaei, K. Babaei, The effects of nano- and micro-particles on properties of plasma electrolytic oxidation (PEO) coatings applied on titanium substrates: A review, Surfaces and Interfaces. (2020) 100659.

[37]   K.H. Cheung, M.B. Pabbruwe, W.F. Chen, P. Koshy, C.C. Sorrell, Effects of substrate preparation on TiO2 morphology and topography during anodization of biomedical Ti6Al4V, Mater. Chem. Phys. 252 (2020) 123224.

[38]   X. Zhang, G. Cai, Y. Lv, Y. Wu, Z. Dong, Growth mechanism of titania on titanium substrate during the early stage of plasma electrolytic oxidation, Surf. Coatings Technol. 400 (2020) 126202.

[39]   M.T. Mathew, P. Srinivasa Pai, R. Pourzal, A. Fischer, M.A. Wimmer, Significance of tribocorrosion in biomedical applications: Overview and current status, Adv. Tribol. 2009 (2009).

[40]   K. Nelson, B. Hesse, O. Addison, A.P. Morrell, C. Gross, A. Lagrange, V.I. Suarez, R. Kohal, T. Fretwurst, Distribution and chemical speciation of exogenous micro- and nanoparticles in inflamed soft tissue adjacent to titanium and ceramic dental implants, Anal. Chem. (2020).

[41]   M. Geetha, A.K. Singh, R. Asokamani, A.K. Gogia, Ti based biomaterials, the ultimate choice for orthopaedic implants – A review, Prog. Mater. Sci. 54 (2009) 397–425.

[42]   W. Simka, A. Iwaniak, G. Nawrat, A. Maciej, J. Michalska, K. Radwański, J. Gazdowicz, Modification of titanium oxide layer by calcium and phosphorus, Electrochim. Acta. 54 (2009) 6983–6988.

[43]   H. Guleryuz, H. Cimenoglu, Surface modification of a Ti-6Al-4V alloy by thermal oxidation, Surf. Coatings Technol. 192 (2005) 164–170.

[44]   A.I. Costa, L. Sousa, A.C. Alves, F. Toptan, Tribocorrosion behaviour of bio-functionalized porous Ti surfaces obtained by two-step anodic treatment, Corros. Sci. 166 (2020) 108467.

[45]   A.C. Alves, F. Oliveira, F. Wenger, P. Ponthiaux, J.-P. Celis, L.A. Rocha, Tribocorrosion behaviour of anodic treated titanium surfaces intended for dental implants, J. Phys. D. Appl. Phys. 46 (2013) 404001.

[46]   G. Wang, W. Huang, Q. Song, J. Liang, Three-dimensional finite analysis of acetabular contact pressure and contact area during normal walking, Asian J. Surg. 40 (2017) 463–469.

[47]   F. Mazoochian, A. Hölzer, J. Jalali, F. Schmidutz, C. Schröder, M. Woiczinski, J. Maierl, P. Augat, V. Jansson, Finite element analysis of the ovine hip: Development, results and comparison with the human hip, Vet. Comp. Orthop. Traumatol. 25 (2012) 301–306.

[48]   M.M. Ardestani, M. Moazen, Z. Chen, J. Zhang, Z. Jin, A real-time topography of maximum contact pressure distribution at medial tibiofemoral knee implant during gait: Application to knee rehabilitation, Neurocomputing. 154 (2015) 174–188.

[49]   H. Yoshida, A. Faust, J. Wilckens, M. Kitagawa, J. Fetto, E.Y.S. Chao, Three-dimensional dynamic hip contact area and pressure distribution during activities of daily living, J. Biomech. 39 (2006) 1996–2004.

[50]   ASM Inc. Webpage, Http://Asm.Matweb.Com/Search/SpecificMaterial.Asp?Bassnum=MTU020. (2016).

[51]   S.J. Mason, G.E. Legge, C.S. Kallie, Variability in the length and frequency of steps of sighted and visually impaired walkers, J. Vis. Impair. Blind. 99 (2005) 741–754.

[52]   F. Danion, E. Varraine, M. Bonnard, J. Pailhous, Stride variability in human gait: The effect of stride frequency and stride length, Gait Posture. 18 (2003) 69–77.

[53]   L. Semetse, B.A. Obadele, L. Raganya, J. Geringer, P.A. Olubambi, Fretting corrosion behaviour of Ti-6Al-4V reinforced with zirconia in foetal bovine serum, J.

Mech. Behav. Biomed. Mater. 100 (2019) 103392.

[54]   V. Kliment, Determination of the Sr/Ca ratio in bones by XRFA, J. Radioanal. Nucl. Chem. 137 (1989) 265–269.

[55]   M. Bruschi, D. Steinmüller-Nethl, W. Goriwoda, M. Rasse, Composition and Modifications of Dental Implant Surfaces, J. Oral Implant. (2015) 1–14.

[56]   J. Zhou, L. Zhao, Multifunction Sr, Co and F co-doped microporous coating on titanium of antibacterial, angiogenic and osteogenic activities, Acta Biomater. 43 (2016) 358–368.

[57]   X. Lin, X. Yang, L. Tan, M. Li, X. Wang, Y. Zhang, K. Yang, Z. Hu, J. Qiu, In vitro degradation and biocompatibility of a strontium-containing micro-arc oxidation coating on the biodegradable ZK60 magnesium alloy, Appl. Surf. Sci. 288 (2014) 718–726.

[58]   W. Zhang, H. Cao, X. Zhang, G. Li, Q. Chang, J. Zhao, Y. Qiao, X. Ding, G. Yang, X. Liu, X. Jiang, A strontium-incorporated nanoporous titanium implant surface for rapid osseointegration, Nanoscale. 8 (2016) 5291–5301.

[59]   W. Liu, M. Cheng, T. Wahafu, Y. Zhao, H. Qin, J. Wang, X. Zhang, L. Wang, The in vitro and in vivo performance of a strontium-containing coating on the low-modulus Ti35Nb2Ta3Zr alloy formed by micro-arc oxidation, J. Mater. Sci. Mater. Med. 26 (2015) 203.

[60]   Z.S. Tao, W.S. Zhou, X.W. He, W. Liu, B.L. Bai, Q. Zhou, Z.L. Huang, K.K. Tu, H. Li, T. Sun, Y.X. Lv, W. Cui, L. Yang, A comparative study of zinc, magnesium, strontium-incorporated hydroxyapatite-coated titanium implants for osseointegration of osteopenic rats, Mater. Sci. Eng. C. 62 (2016) 226–232.

[61]   S. Peng, G. Zhou, K.D.K. Luk, K.M.C. Cheung, Z. Li, W.M. Lam, Z. Zhou, W.W. Lu, Strontium promotes osteogenic differentiation of mesenchymal stem cells through the Ras/MAPK signaling pathway, Cell. Physiol. Biochem. 23 (2009) 165–174.

[62]   T. Sun, Z. Li, X. Zhong, Z. Cai, Z. Ning, T. Hou, L. Xiong, Y. Feng, F. Leung, W.W. Lu, S. Peng, Strontium inhibits osteoclastogenesis by enhancing LRP6 and β-catenin-mediated OPG targeted by miR-181d-5p, J. Cell Commun. Signal. 13 (2019) 85–97.

[63]   J. Zeng, J. Guo, Z. Sun, F. Deng, C. Ning, Y. Xie, Osteoblastic and anti-osteoclastic activities of strontium-substituted silicocarnotite ceramics: In vitro and in vivo studies, Bioact. Mater. 5 (2020) 435–446.

[64]   D.P. Wornham, M.O. Hajjawi, I.R. Orriss, T.R. Arnett, Strontium potently inhibits

mineralisation in bone-forming primary rat osteoblast cultures and reduces numbers of osteoclasts in mouse marrow cultures, Osteoporos. Int. 25 (2014) 2477–2484.

[65]　J. Zhou, X. Wang, L. Zhao, Antibacterial, angiogenic, and osteogenic activities of Ca, P, Co, F, and Sr compound doped titania coatings with different Sr content, Sci. Rep. 9 (2019) 1–11.

[66]　M. Sato, P. Chen, Y. Tsutsumi, M. Shiota, T. Hanawa, S. Kasugai, Effect of strontium ions on calcification of preosteoblasts cultured on porous calcium- and phosphate-containing titanium oxide layers formed by micro- arc oxidation, Dent. Mater. J. 35 (2016) 627–634.

[67]　X. He, X. Zhang, L. Bai, R. Hang, X. Huang, L. Qin, X. Yao, B. Tang, Antibacterial ability and osteogenic activity of porous Sr/Ag-containing TiO2 coatings, Biomed. Mater. 11 (2016) 045008.

[68]　J. Yan, J.F. Sun, P.K. Chu, Y. Han, Y.M. Zhang, Bone integration capability of a series of strontium-containing hydroxyapatite coatings formed by micro-arc oxidation, J. Biomed. Mater. Res. - Part A. 101 A (2013) 2465–2480.

[69]　A.L. Oliveira, R.L. Reis, P. Li, Strontium-Substituted Apatite Coating Grown on Ti6Al4V Substrate Through Biomimetic Synthesis, J. Biomed. Mater. Res. B. Appl. Biomater. 83 (2007) 340–344.

[70]　P.J. Marie, M. Hott, D. Modrowski, C. De Pollak, J. Guillemain, P. Deloffre, Y. Tsouderos, An uncoupling agent containing strontium prevents bone loss by depressing bone resorption and maintaining bone formation in estrogen-deficient rats, J. Bone Miner. Res. 8 (1993) 607–615.

[71]　Y. Huang, H. Qiao, X. Nian, X. Zhang, X. Zhang, G. Song, Z. Xu, H. Zhang, S. Han, Improving the bioactivity and corrosion resistance properties of electrodeposited hydroxyapatite coating by dual doping of bivalent strontium and manganese ion, Surf. Coatings Technol. 291 (2016) 205–215.

[72]　K.C. Kung, T.M. Lee, J.L. Chen, T.S. Lui, Characteristics and biological responses of novel coatings containing strontium by micro-arc oxidation, Surf. Coatings Technol. 205 (2010) 1714–1722.

[73]　M. Pilmane, K. Salma-Ancane, D. Loca, J. Locs, L. Berzina-Cimdina, Strontium and strontium ranelate: Historical review of some of their functions, Mater. Sci. Eng. C. 78 (2017) 1222–1230.

204

[74]   D.-W. Zhao, C. Liu, K.-Q. Zuo, P. Su, L.-B. Li, G.-Y. Xiao, L. Cheng, Strontium-zinc phosphate chemical conversion coating improves the osseointegration of titanium implants by regulating macrophage polarization, Chem. Eng. J. (2020) 127362.

[75]   P.P. Maciel, J.A.M. Pessôa, E.L.G. de Medeiros, A.U.D. Batista, L.R.F. Figueiredo, E.S. de Medeiros, D.F. de O. Duarte, A.F. Alves, F.B. de Sousa, B.R. Vieira, R.F.B.D. Batista, D.E.C. Perez, R.R. Menezes, L.R.C. Castellano, P.R.F. Bonan, Use of strontium doping glass-ceramic material for bone regeneration in critical defect: In vitro and in vivo analyses, Ceram. Int. (2020) 0–1.

[76]   M. Chambard, D. Remache, Y. Balcaen, O. Dalverny, J. Alexis, R. Siadous, R. Bareille, S. Catros, P. Fort, D. Grossin, F. Gitzhofer, G. Bertrand, Effect of silver and strontium incorporation route on hydroxyapatite coatings elaborated by rf-SPS, Materialia. 12 (2020) 100809.

[77]   I.A.J. van Hengel, F.S.A. Gelderman, S. Athanasiadis, M. Minneboo, H. Weinans, A.C. Fluit, B.C.J. van der Eerden, L.E. Fratila-Apachitei, I. Apachitei, A.A. Zadpoor, Functionality-packed additively manufactured porous titanium implants, Mater. Today Bio. 7 (2020) 100060.

[78]   W. Hong, Q. Zhang, H. Jin, L. Song, Y. Tan, L. Luo, F. Guo, X. Zhao, P. Xiao, Roles of strontium and hierarchy structure on the in vitro biological response and drug release mechanism of the strontium-substituted bioactive glass microspheres, Mater. Sci. Eng. C. 107 (2020) 110336.

[79]   M. Khodaei, A. Valanezhad, I. Watanabe, Controlled gentamicin- strontium release as a dual action bone agent: Combination of the porous titanium scaffold and biodegradable polymers, J. Alloys Compd. 720 (2017) 22–28.

[80]   R. V. Suganthi, K. Elayaraja, M.I.A. Joshy, V.S. Chandra, E.K. Girija, S.N. Kalkura, Fibrous growth of strontium substituted hydroxyapatite and its drug release, Mater. Sci. Eng. C. 31 (2011) 593–599.